Computational Modeling of Interacting and Coalescing Surface Cracks

Application to Offshore Wind Turbine Welded Connections

Jose Mishael Chakkalakkal Joseph

Supervisor: Prof. Philippe Rigo

Co-supervisor: Dr. Pablo G. Morato

A dissertation submitted in partial fulfillment of the requirements for the degree of
Doctor of Philosophy in Engineering Sciences

Applied Sciences
University of Liège

January 2026

PhD COMMITTEE

Vincent DENOËL (*Jury Chair*)
Professor
University of Liège, Belgium

Philippe RIGO (*Promotor*)
Professor
University of Liège, Belgium

Jean-François DEMONCEAU
Professor
University of Liège, Belgium

Margaux GEUZAINE
Professor
University of Liège, Belgium

Wim DE WAELE
Professor
Ghent University, Belgium

Xiaoli JIANG
Professor
Delft University of Technology, The Netherlands

Dr. Philippe THIBAUX
Senior Structural Integrity Specialist
Applications and Solutions department, OCAS, Belgium

Dr.-Ing. habil. Moritz BRAUN
Head of the Department of Ship Reliability
German Aerospace Center (DLR) Institute of Maritime Energy Systems, Germany

To my family, for their endless love and support.

ACKNOWLEDGEMENTS

I would like to express my sincere gratitude to my supervisor, Prof. Philippe Rigo, for his helpful suggestions and encouragement throughout the research. I thank him for the opportunity to conduct this research in the Structural Engineering Department at the University of Liège.

I express my profound appreciation to Dr. Pablo G. Morato (Engineering Risk Analysis Group, Technical University of Munich, Germany) for his exceptional guidance, invaluable discussions, and unwavering support at every stage of this research. His insightful advice and constant encouragement have been instrumental in shaping the direction and quality of this work.

I gratefully acknowledge Prof. Ludovic Noels (University of Liège), whose lectures on fracture mechanics notably increased my motivation in the field of research and influenced the choice of research topic.

I express my gratitude towards Prof. Wim De Waele (University of Gent) for his support during this research through the MAXWind (MAintenance, Inspection and EXploitation Optimization of Offshore Wind Farms subjected to Corrosion-Fatigue) project.

I would also like to thank the past and present colleagues of ANAST for creating a vibrant office atmosphere.

On a more personal note, I would like to express my deepest appreciation to my wife, my two little angels, and my parents for their unwavering emotional support over the past years.

Finally, I would like to acknowledge the financial support granted by the Belgian Energy Transition Fund (FPS Economy) through the MAXWind project and FlexWind (Fatigue Life EXtension of offshore Wind foundations) project.

ABSTRACT

Offshore wind turbine (OWT) foundations operate in harsh marine environments where cyclic loading and corrosion act together to drive fatigue damage. As monopiles are the predominant foundation type for European OWTs, their fatigue deterioration must be characterized credibly to support optimized inspection and maintenance. However, reliability models that capture interaction and coalescence among multiple surface cracks under corrosion fatigue remain limited. Circumferential welds in monopile foundations can host several surface cracks; accurate determination of stress intensity factors (SIFs), including crack to crack interaction, is necessary to predict crack growth rates and assess fracture capacity. This thesis develops a computational and probabilistic framework to quantify the structural reliability of monopile welds subject to corrosion fatigue, linking high-fidelity fracture mechanics simulations with scalable surrogate modeling.

The approach integrates Paris law crack growth with SIFs computed from three-dimensional finite element analysis (FEA). Multiple interacting surface cracks are modeled with explicit treatment of interaction, coalescence, and transition to failure via through-thickness penetration or fracture toughness exceedance. The framework maintains numerical stability near coalescence and resolves realistic welded geometries to capture local stress concentrations. A multilayer perceptron (MLP) surrogate that computes SIFs along evolving crack fronts is trained on high-fidelity FEA results, enabling large-scale Monte Carlo life cycle reliability analysis. Probabilistic crack growth simulations incorporate uncertainties in initial flaw size distributions, crack growth parameters, and long-term stress ranges representative of OWT service conditions.

The framework is demonstrated on a monopile circumferential weld case with two semi-elliptical surface cracks at the weld toe and explicit weld geometry representation. Surrogate assisted evaluation of SIF histories enables efficient simulation of interaction and coalescence. Results show (i) acceleration of failure due to crack interaction and coalescence, (ii) high sensitivity of reliability to initial defect distributions and long-term stress ranges, and (iii) substantial computational speed-ups from the surrogates while retaining accuracy.

The main outcome is an interaction-aware, surrogate-enabled reliability assessment model that accounts for physical system dependencies via crack interaction and coalescence, supporting inspection planning, decision-making under uncertainty, and potential life-extension strategies for OWT assets.

TABLE OF CONTENTS

List of figures **xv**

List of tables **xix**

1 Introduction **1**
1.1 Motivation of the research 1
1.2 Objectives of the research 7
1.3 Scope of the research 8
1.4 Outline of the thesis 9
1.5 List of papers 11

2 Corrosion fatigue in offshore wind turbine monopile foundations: Insights on critical parameters **13**
2.1 Introduction 15
2.2 Mechanisms of corrosion fatigue 18
2.3 Structural steels for monopile foundations 20
2.4 Initial crack size 23
2.5 Stress intensity factor (SIF) 25
2.6 Crack growth parameters 28
2.6.1 Influence of stress ratio 32
2.6.2 Influence of residual stress 35
2.6.3 Effect of loading frequency 37
2.7 Fatigue loadings 40
2.8 Concluding remarks 42

3 Numerical fatigue modeling and simulation of interacting surface cracks in offshore wind structural connections **45**
3.1 Introduction 46
3.2 Fatigue crack growth 48
3.2.1 Crack growth modeling 48
3.2.2 Stress intensity factor computation 49

3.3 Fatigue growth, failure, and coalescence analysis of interacting cracks 51
3.3.1 Fatigue crack growth modeling of multiple surface cracks 51
3.3.2 Interaction factor and coalescence of adjacent cracks 53
3.3.3 Fatigue failure definition 54
3.4 Fatigue analysis and multiple crack interaction in a finite thickness plate 55
3.4.1 Comparative study of numerically computed stress intensity factors and interaction effects 55
3.4.2 Fatigue crack growth of multiple interacting surface cracks 58
3.5 Fatigue analysis of interacting surface cracks in offshore wind structural connections 60
3.5.1 Case study definition 60
3.5.2 Results and discussion 63
3.6 Concluding remarks 68

4 Propagation of Interacting Cracks in Offshore Wind Welded Structures through Numerical Analysis 71
4.1 Introduction 71
4.2 Fatigue crack growth and stress intensity factor 74
4.2.1 Crack growth modeling 74
4.2.2 Stress intensity factor for weld-toe surface cracks 75
4.2.3 Long-term stress range 77
4.2.4 Initial crack size and crack growth parameters 78
4.3 Fatigue analysis of interacting surface cracks in offshore wind welded connections . 79
4.3.1 Case study description 79
4.3.2 Results and discussion 81
4.4 Conclusions 83

5 Probabilistic fatigue analysis of offshore wind monopile welds with interacting and coalesced cracks using MLP surrogates 85
5.1 Introduction 86
5.2 Background 89
5.2.1 Fatigue crack growth modeling 89
5.2.2 SIF computation 91
5.2.3 Surrogate modeling 92
5.3 Problem formulation and methodological framework 93
5.3.1 Problem statement and research gap 93
5.3.2 Proposed methodological framework 94
5.4 Case study: Offshore wind welded monopile foundation 97
5.4.1 Geometry, material, and loading conditions 98
5.4.2 Finite element modeling strategy 100

5.4.3 Model implementation and probabilistic inputs 101
5.5 Results and Discussion 105
5.5.1 Validation of MLP Surrogates 105
5.5.2 Probabilistic fatigue analysis 109
5.6 Conclusions 114
Appendix A1 XFEM formulation 115
Appendix A2 Mesh refinement algorithm around the crack front 118
Appendix A3 Validation of FEA results 118

6 Conclusions and outlook **121**
6.1 Concluding remarks 121
6.2 Suggestions for further research 123

References **125**

LIST OF FIGURES

1.1 Illustration of an offshore wind turbine on a monopile foundation. 2
1.2 A fabricated monopile for an offshore wind farm. 3
1.3 Representation of a system with "n" components; (a) Series system, and (b) Parallel system. 4
1.4 Organization of the PhD thesis. 10

2.1 A typical large-diameter monopile fabricated for an offshore wind farm in the German North Sea. 16
2.2 Different stages of corrosion fatigue process initiated from corrosion pits. 19
2.3 Typical microstructures of different S355 steel grades. 22
2.4 Semi-elliptical surface crack in a finite thickness plate. 24
2.5 Consolidated Paris law curves for S355 base metal in air. 30
2.6 Consolidated Paris law curves for S355 base metal in seawater. 31
2.7 Fatigue crack growth in S355 structural steel in air environment. 33
2.8 Crack growth rates in heat-affected zone (HAZ) at different stress ratios. 34
2.9 Transverse residual stress in three CT samples along the crack direction before pre-cracking. 36
2.10 Comparison of fatigue crack growth rate in air and seawater for different frequency of cyclic loads. 39

3.1 Representation of geometry and nomenclature for multiple and coalesced surface cracks, idealized with a semi-elliptical shape. 48
3.2 Overarching iterative procedure for numerically computing the stress intensity factor and growth of interacting surface cracks, also considering coalesced cracks and fatigue failure. 52
3.3 Plate and crack front geometry corresponding to the model implemented in the finite thickness plate setting. 55
3.4 Graphical representation of the crack front finite element mesh (top) and stress field results, σ_Z, (bottom). 56
3.5 Comparative analysis of calculated stress intensity factors in a finite thickness plate under tension. 57

3.6 Comparative study of crack interaction factors retrieved from the proposed numerical method and those published in the literature. 58
3.7 Fatigue crack growth predictions retrieved for a single semi-elliptical crack and two interacting semi-elliptical cracks in a finite thickness plate. 59
3.8 Graphical representation of the finite element mesh generated for the investigated offshore wind substructure. 62
3.9 Comparative study of stress intensity factors computed for a monopile substructure at critical crack front points. 64
3.10 Investigation of the interaction effects observed on a pair of surface cracks in an offshore wind structural connection. 65
3.11 Fatigue growth of interacting surface cracks in the investigated offshore wind structural connection. 66
3.12 Influence of the stress ratio on the number of cycles to failure observed in the studied offshore wind structural connection. 67

4.1 Graphical representation of a typical offshore wind turbine monopile foundation . . . 79
4.2 Propagation of interacting cracks and independent single crack under expected stress range loading. 82
4.3 Propagation of interacting cracks and independent single crack under equivalent stress range loading. 83

5.1 Polar coordinate system defining the θ field in the vicinity of the crack front. 92
5.2 Schematic of toroidal surfaces surrounding the crack front Γ used for the computation of SIF using $G-\theta$ method. 92
5.3 Computational workflow for reliability estimation. 97
5.4 Schematic of a typical offshore wind turbine monopile foundation indicating longitudinal and circumferential welds. The investigated circumferential weld geometry and dimensions are highlighted. 99
5.5 Finite element models developed for the offshore wind monopile foundation. 101
5.6 Architecture of the multilayer perceptron (MLP) surrogate model used for SIF prediction. 102
5.7 Parity of MLP-predicted versus FE-computed SIF range (ΔK) for the interacting two crack surrogate at $\beta = 0.003$ radians. 106
5.8 Parity of MLP-predicted versus FE-computed SIF range (ΔK) for the interacting two crack surrogate at $\beta = 0.009$ radians. 107
5.9 Parity of MLP-predicted versus FE-computed SIF range (ΔK) at three crack front locations for the post-coalescence single semi-elliptical crack configuration. 108
5.10 Parity of MLP-predicted versus FE-computed SIF range (ΔK) at three crack front locations for the single semi-elliptical crack at a fixed angular offset $\beta = +0.0015$ radians configuration. 108

5.11 Comparison of FE-based and MLP-based crack growth predictions over 20 years for five random samples. 109
5.12 Time evolution of probability of failure (P_f) for the interacting cracks, single offset crack, two single cracks in series, and two single offset cracks with coalescence (all at $\beta = 0.003$ radians). 110
5.13 Coalescence statistics for interacting and offset + coalescence configurations at $\beta =$ 0.003 radians. 112
5.14 Probability of failure (P_f) versus time for interacting cracks with angular separation of $\beta = 0.003$ radians and $\beta = 0.009$ radians. 112
5.15 Coalescence statistics for interacting cracks at two angular separations. 113
A1.1 Representation of a semi-elliptical crack on a plate using XFEM where the semi-elliptical crack is introduced into an existing mesh. 115
A1.2 Schematic representation of finite elements enriched by XFEM intersected by a curved crack. 116
A1.3 Schematic representation of crack geometry using normal and tangent level set functions. 117
A3.1 Normalized stress intensity factor as a function of position along the crack front for semi-elliptical surface cracks in wide plates subjected to unit tensile stress. 120

LIST OF TABLES

1.1 Crack interaction, coalescence, and crack propagation modeling studies across different domains. 5

2.1 Maximum permitted chemical composition (in weight %) and typical mechanical properties for structural steels commonly used in OWT foundations. 20
2.2 Representative plate grades used in European OWT monopile projects. 21
2.3 Chemical composition of offshore steel grades (wt.%), including only major elements. 23
2.4 Paris law parameters (C and m) for S355 steel in air and seawater environments. . . . 32

3.1 Material and crack growth parameters considered in the finite thickness plate numerical experiments. 56
3.2 Material and crack growth parameters considered in the offshore wind structural connection setting. 61

4.1 Initial crack size (a_0) and crack growth parameters (C) calibrated from Class D S-N curves in seawater with cathodic protection. 80

5.1 Random variables and deterministic constants adopted in the case study (calibrated from Class D S-N curve in seawater with cathodic protection). 99
5.2 Input ranges for interacting two crack MLP surrogates. 103

CHAPTER 1

INTRODUCTION

1.1 Motivation of the research

Over the past decade, offshore wind energy has rapidly evolved into a key renewable resource, crucial to limiting carbon emissions and achieving global climate goals. This growth has been driven by technological advances, cost reductions, and enhanced supply chains, which have resulted in the widespread adoption of offshore wind in various markets. However, designing robust and reliable support structures for offshore wind turbines (OWTs) remains a significant challenge. These large steel foundations, often monopiles, operate in harsh marine environments under cyclic loads from wind, waves, and currents. Consequently, they are susceptible to fatigue and corrosion fatigue, which degrade structural integrity over time. In particular, corrosion fatigue poses a serious threat because the synergistic interaction of cyclic loading and corrosive reactions accelerates crack initiation and propagation compared to either mechanism acting alone [1, 2].

Monopile foundations dominate shallow-water installations due to their relatively simple fabrication and installation processes [3]. They are manufactured by rolling and bending large, thick steel plates and then welding them together in longitudinal and circumferential directions [4] (see Figs. 1.1 and 1.2). These welds, essential to their manufacture, form crack-prone locations, with circumferential welds at risk of surface cracking initiated by inherent flaws and exacerbated by corrosion. Despite the widespread use of coatings, cathodic protection, and corrosion allowances, localized corrosion, such as pitting and microbial corrosion, can still occur, causing increased stress concentrations and accelerating the fatigue process [5]. Furthermore, the trend toward larger turbine sizes and deeper water installations further magnifies the complexity of fatigue loading on fixed foundations [6]. As rotor diameters and hub heights increase, the support structures are subjected to higher cyclic loads from wind, waves, and currents, while also being exposed to more severe environmental conditions. This increased exposure can shorten the service life of critical welded connections unless more advanced design and maintenance strategies are used. Given that an OWT support structure can account for up to one-third of the total cost of an offshore wind project [7], ensuring its long-term reliability is essential for cost-effective operation and for reducing the levelized cost of energy. Therefore, robust structural reliability models are required to predict service life,

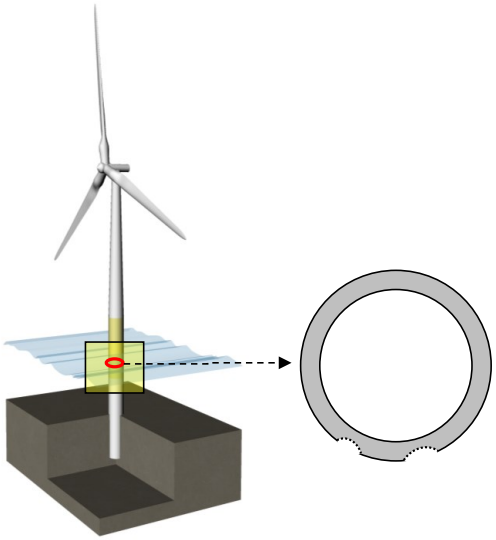

Fig. 1.1 Illustration of an OWT on a monopile foundation. The red color band highlights a circumferential weld; these welded connections concentrate cyclic stresses and are prone to corrosion fatigue crack initiation. Two surface cracks are represented on the cross-section of the monopile.

schedule inspections, and plan maintenance activities throughout the operational lifespan of the turbine.

In this context, rational structural reliability modeling becomes critical, especially since OWT support structures can be viewed as complex systems composed of multiple interdependent components that may deteriorate and fail under harsh marine conditions. For example, fatigue hotspots–hereafter referred to as components–located at the joints of an OWT jacket foundation or along the circumferential welds of an OWT monopile foundation are subject to combined cyclic loading from wind, waves, and currents. Over time, these loading conditions, along with concurrent corrosion processes, degrade structural integrity and increase the probability of failure. Consequently, optimal system-level representations of these components are essential to reduce the overall risk of structural failure and to guide maintenance actions.

From a reliability perspective, an element (hereafter also called component or hotspot) is any part treated as a whole in the analysis and not decomposed further for the case at hand [9]. The system is the collection of such elements, and its reliability depends on the reliability of the individual elements, their number, and their mutual arrangement. In complex structures, such as OWT monopile foundations with many welded locations, the large number of potential hotspots means that even highly reliable elements can, in combination, lead to a non-negligible system failure probability if arrangement and dependencies are not considered. Hence, thoughtful structural arrangement and realistic system representations are essential to achieve accurate reliability estimates [9].

In the literature, simplified system modeling approaches often begin with fundamental configurations such as series and parallel systems, as shown in Fig. 1.3. In a series system, failure of any single component leads to the failure of the entire system, thereby limiting the maximum achievable

Fig. 1.2 A fabricated monopile for an offshore wind farm [8]. The alternating light and dark bands reveal the individual rolled steel cans that are joined by circumferential welds. This underscores the number and scale of potential fatigue hotspots in a full-size monopile structure.

reliability to that of its weakest component. By contrast, a parallel system functions as long as at least one component remains operational, increasing redundancy and thus boosting overall reliability. Another common approach is the k-out-of-n system, in which any k out of n components need to work for the system to function. This broader framework includes the series (when k=n) and the parallel systems (when k=1 and n>1). While these idealized system representations are useful for illustrating basic principles, welded OWT foundations generally require more nuanced system representations that account for interactions among hotspots, coalescence[1], and site-specific deterioration, which this thesis addresses.

Despite the existence of various reliability modeling approaches, many studies oversimplify the representation of OWT support structures by treating their critical components—or "hotspots"—as independent, either neglecting interactions among multiple hotspots (or cracks) or considering only one component at a time [10–13]. Interacting cracks alter local stress intensity factors (SIFs) through shielding or amplification effects [2] [14], thereby reducing or accelerating crack growth [15]. Interaction can also change crack growth directions [16–18] and may lead to coalescence into larger defects [19–22], causing accelerated crack growth and earlier through-thickness penetration. Evidence from the aerospace, nuclear, and oil & gas communities shows that coalescence and proximity effects can significantly shorten fatigue life relative to independent-crack assumptions, particularly under complex loading spectra and corrosive environments [16, 20, 23–31]. Therefore, the possibility of multiple

[1] the process by which two or more cracks join together to form a larger crack, often accelerating structural failure.

[2] changes in the local stress intensity factor at a crack tip caused by nearby cracks, which can either reduce (shield) or increase (amplify) crack growth rates.

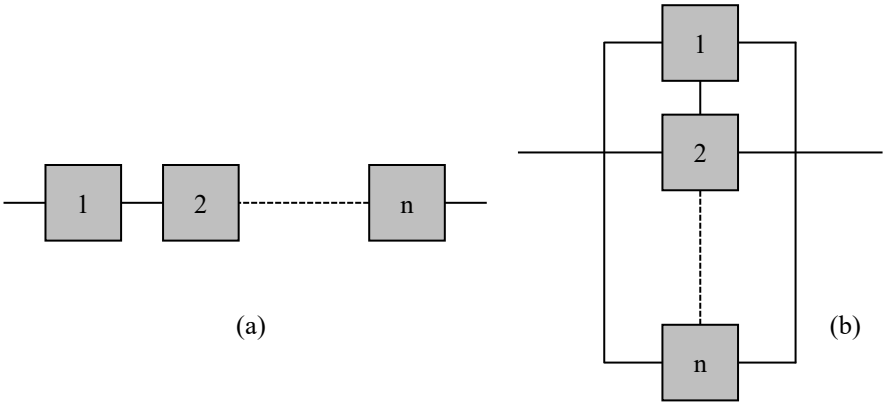

Fig. 1.3 Representation of a system with "n" components; (a) Series system, and (b) Parallel system.

surface cracks at OWT monopile circumferential welds should be considered explicitly in fatigue reliability estimation. Ignoring crack interactions results in biased reliability estimates and suboptimal inspection intervals. Table 1.1 summarizes prior works on crack interaction and coalescence across different application domains, highlighting which studies address interaction, coalescence, and crack growth. As seen in Table 1.1, OWT focused studies typically rely on closed-form analytical SIF expressions which are based on semi-elliptical surface cracks in flat plates [32, 33] and rarely treat interaction and coalescence in a probabilistic analysis.

In addition to closed-form SIF solutions, structural integrity standards such as BS7910 provide geometry-based interaction criteria for adjacent flaws based primarily on geometric proximity and re-characterization rules (i.e., replacing two nearby surface cracks by an equivalent single flaw for assessment) [33]. While these rules are valuable as practical screening procedures, they do not quantify the local, position-dependent SIF redistribution along the crack fronts that governs interaction-driven changes in crack growth. In fact, BS7910 notes that flaw interaction criteria are not normally required for fatigue assessment. However, if there is uncertainty as to whether flaws are separate, they should be combined, or specific calculations should be carried out [33]. Additionally, different standards (e.g., BS 7910, R6, ASME XI, and GB/T 19624-2019) adopt different assumptions for assessing multiple cracks and for treating interaction prior to coalescence. This highlights that geometry-based rules are not necessarily transferable across assessment contexts [43]. Moreover, the significance of interaction (e.g., interaction factors and the most adverse SIF conditions along the crack front) can be sensitive to loading mode and the through-thickness stress distribution, which suggests that geometry-based screening rules may not consistently capture the most adverse interaction condition under all loading modes [44]. For these reasons, this thesis evaluates interaction directly through high-fidelity numerical SIF computations and models coalescence using a small geometric tolerance on crack front separation, chosen to be consistent with the mesh resolution and solver capabilities used in the respective case

Table 1.1 Crack interaction, coalescence, and crack propagation modeling studies across different domains.

Ref.	Interaction	Coalescence	Crack growth	Crack dimension	SIF source	Analysis	Application
[3]	✗	✗	✓	1D	Exp.	Det.	OWT
[4]	✗	✗	✓	2D	Emp. & FEA	Det.	OWT
[10–13, 34]	✗	✗	✓	1D	Emp.	Prob.	OWT
[12, 35]	✗	✗	✓	2D	Emp.	Prob.	OWT
[14]	✓	✗	✗	1D	SIM	Det.	Plate
[15]	✓	✗	✓	1D	FEA	Det.	Airframe
[17, 18]	✓	✓	✓	1D	Exp. & FEA	Det.	Plate
[19, 25]	✓	✓	✓	2D	FEA	Det.	Plate
[20, 22]	✓	✓	✓	2D	Exp. & FEA	Det.	Plate
[23]	✓	✗	✗	2D	Emp. & FEA	Det.	Pressure vessel
[24]	✓	✓	✓	2D	Exp.	Det.	Plate
[36]	✓	✓	✓	2D	FEA	Det.	Plate
[37]	✓	✓	✓	2D	FEA	Det.	Pipeline
[38]	✓	✗	✓	1D	FEA	Prob.	Plate*
[39]	✓	✓	✓	2D	FEA	Det.	Fairlead#
[40]	✗	✗	✓	1D	FEA & NN	Prob.	Plate
[41]	✗	✗	✓	1D	FEA & NN	Prob.	Stiffened panel
[42]	✗	✗	✓	2D	FEA & NN	Det.	Tubular joint

Legend: ✓ addressed; ✗ not addressed. *Abbreviations*: SIM - singular integral method; FEA - finite element analysis; Det. - deterministic; Prob. - probabilistic; Exp. - experiments; Emp. - closed-form empirical expressions; NN - neural network. *A laboratory-scale hexagonal tension specimen with four simultaneous fatigue cracks, designed to mimic system-level properties of marine structures. #Fairlead refers to the structural connection point on a floating offshore wind turbine platform where mooring lines attach.

studies. This enables explicit representation of physical system dependencies—namely SIF coupling[3], crack interaction, and coalescence—within a probabilistic deterioration modeling framework.

At the design stage, fatigue in offshore structures is commonly assessed using S-N curves and cumulative damage (e.g., Palmgren-Miner's rule), which are efficient and well suited for standardized details and loading definitions in design standards [45]. However, the applicability of S–N curves is largely constrained to structural configurations and loading conditions comparable to those used in their experimental calibration, and they do not explicitly represent an evolving physical damage state. This limitation becomes critical for inspection and maintenance planning, because inspection outcomes are naturally expressed in terms of detectable flaw sizes and their evolution, which cannot be incorporated directly within a conventional S–N framework. Linear elastic fracture mechanics (LEFM) provides a complementary and more general framework by modeling fatigue deterioration

[3]the condition in which the stress intensity factors of multiple cracks are interdependent, meaning that growth of one crack affects the driving force of another.

through crack growth laws driven by the stress intensity factor (SIF) range, thereby enabling remaining life estimation and inspection/maintenance decisions to be linked directly to predicted crack sizes [32, 45]. In marine and offshore engineering communities, fatigue deterioration is often modeled using standard fracture mechanics laws (e.g., the Paris law) [3, 10–12, 32, 46, 47] that rely on multiple parameters. In marine environments, these parameters are highly uncertain:
(i) initial crack sizes at welds (depend on fabrication processes and inspection outcomes) [48–50],
(ii) crack growth parameters (e.g., Paris law coefficients) that vary by material grade, welding procedure, and environment [51–54], and
(iii) long-term stress ranges influenced by wind–wave loading spectra and site conditions [32].
Additional factors can also influence fatigue crack growth in welded structures, including residual stresses, weld geometry variability, material mismatch, crack closure effects, and environmental variability affecting corrosion fatigue behavior. In this thesis, the probabilistic analyses focus on uncertainty in initial crack size, crack growth parameters, and long-term stress range, while the influence of weld geometry is investigated through explicit weld-resolved modeling. Broader treatment of residual stress and other sources of uncertainty is outlined within the scope and future extensions.

Large datasets exist for crack growth parameters in OWT steels under corrosion fatigue conditions [3, 51–56]. However, these data are highly scattered, making deterministic use of single parameter values unsafe (overly conservative or non-conservative, depending on context). In this thesis, a comprehensive examination and comparison of the crack growth parameters reported for OWT monopile foundation steels under corrosion fatigue conditions is carried out. This supports a probabilistic framework that propagates the associated uncertainties over the lifetime of OWT monopile foundations, especially when interacting, coalescing surface cracks are present.

Additionally, deterioration modeling in many OWT fatigue assessments has relied on simplified formulas proposed by industrial standards [32, 33] to account for weld effects on SIFs [12, 46] via magnification factors[4] (M_k). While these formulas are efficient, they can introduce unnecessary conservatism due to their basis on the magnification factors proposed by Bowness and Lee [57] for 3D T-butt joints. However, M_k factors for plate-to-plate butt welds—similar to those found on OWT monopile foundations—differ from those for single T-butt joints [58]. The percentage differences can reach up to 63.8% for axial loading and 97.4% for bending. Therefore, an approach is adopted in this thesis by explicitly modeling the weld geometry in the crack growth computations. However, this approach is not viable for probabilistic analysis due to the substantial computational cost and extended simulation time. Therefore, the previous approach is extended by integrating finite element analysis (FEA) with explicit weld geometry and surrogate modeling for the probabilistic analysis. This extended approach enables the recovery of most of the accuracy benefits at a fraction of the computational cost.

Building on this rationale, advanced data-driven methods are increasingly used to capture the nonlinear and time-dependent nature of crack growth [40, 59, 60]. For example, recurrent neural

[4] the ratio of the stress intensity factor for a crack in a welded plate or plate with attachment to the corresponding stress intensity factor for the same crack in an idealized plate without attachment.

networks can be trained using high-fidelity crack growth simulations that account for varying load histories and material properties [59]. These simulations can then be used to create efficient surrogate models that accurately replicate the progression of cracks [41, 42, 61]. Similarly, Gaussian process models have been used to compute SIFs for surface cracks in offshore pipelines [62, 63]. Once validated, these surrogate models can be integrated into probabilistic analyses, enabling the rapid computation of the probability of failure of complex structural systems under corrosion fatigue conditions. Such data-driven approaches bridge the gap between detailed simulation and system-level reliability assessment. They help to optimize inspection intervals, manage uncertainties, and reduce operational risks and maintenance costs.

Although surrogate models for SIF prediction and crack growth simulations are gaining interest, they have rarely been implemented to represent crack interaction and coalescence scenarios. Moreover, while surrogate models for SIF prediction exist, their integration into full crack growth simulations and, crucially, into system-level probability of failure estimation remains rare. This thesis advances that integration by training surrogates on high-fidelity 3D FEA datasets and deploying them inside probabilistic simulations. This approach provides a computationally feasible method for conducting extensive Monte Carlo or advanced sampling studies, while maintaining the physics derived from detailed FEA, which would otherwise be impractical at fleet or farm scales.

1.2 Objectives of the research

The main goal of this thesis is to develop rational, system-level structural reliability models representative of OWT support structures. The focus is on the circumferential weld connections of monopile foundations that are susceptible to fatigue deterioration. These models facilitate optimized inspection and maintenance planning by explicitly capturing interactions among structural components.

The following objectives are defined to achieve the main goal of the thesis.

- **Objective 1:** To critically review and synthesize the state-of-the-art knowledge on corrosion fatigue crack growth in OWT monopile foundations.
- **Objective 2:** To develop and validate a numerical methodology for modeling the fatigue growth of multiple interacting surface cracks in OWT structural connections, incorporating crack interaction effects, coalescence behavior, and fracture mechanics-based fatigue failure criteria.
- **Objective 3:** To extend numerical modeling of fatigue crack propagation by explicitly integrating detailed weld geometry effects into simulations, and to investigate their influence, along with crack interaction, coalescence, and loading conditions, on fatigue life predictions for welded connections in monopile foundations.
- **Objective 4:** To develop a surrogate modeling framework for efficient and accurate prediction of stress intensity factors for interacting and coalesced surface cracks scenarios, and to integrate

this model into probabilistic fatigue crack growth simulations for quantifying system-level probability of failure in offshore wind monopile structures.

1.3 Scope of the research

In this thesis, structural components correspond to fatigue hotspots as defined in Section 1.1. The proposed methodology is applied to welded monopile foundations of OWT structures (see Fig. 1.1). However, this methodology can be generalized and extended to other types of steel structures that experience similar fatigue-related degradation mechanisms, such as offshore tubular joints. In the case studies presented in this thesis, two structural components are considered explicitly. This is due to the high computational demands associated with modeling systems with a large number of components. However, the framework is designed to allow for the addition of more components as more computational resources become available.

Regarding weld representation, the numerical studies consider an idealized circumferential butt-weld profile based on a representative geometry reported in the literature [7]. The purpose is not to reproduce a specific as-built weld, but to quantify how including a realistic weld reinforcement (relative to flat-plate idealizations) affects SIFs, interaction/coalescence behavior, and fatigue life predictions within a consistent modeling framework. Weld geometry in practice exhibits significant variability (e.g., reinforcement height/width, bevel shape, misalignment), which can alter local stress concentrations and crack driving forces. A systematic sensitivity analysis and stochastic modeling of weld profile parameters are therefore identified as important extensions of the present work.

In addition, residual stresses and other welding-related uncertainties (e.g., misalignment, material heterogeneity, and potential crack closure influences) can affect crack driving forces and growth rates. These effects are not treated as stochastic inputs in the present probabilistic case studies; incorporating residual stress fields and additional uncertain parameters into the reliability framework is identified as an important extension.

For computational tractability in the three-dimensional fracture mechanics simulations, the case studies adopt a constant amplitude load representation derived from long-term fatigue loading models used in offshore standards. Specifically, a representative stress range is obtained from long-term stress range descriptions (e.g., a two-parameter Weibull model) or from equivalent constant amplitude stress ranges consistent with code based formulations [32, 64]. This representative stress range is converted to an equivalent bending moment using beam theory relations for the monopile, and is then applied in the finite element model to drive the crack growth analysis.

Beyond the use of commercial and open-source finite element solvers, this thesis relies on in-house computational developments to enable repeatable crack growth and reliability studies at scale. These developments include:

(i) automated generation and management of parametric crack configurations;

(ii) adaptive meshing/refinement workflows (including interfaces to mesh refinement tools) to maintain accuracy as cracks evolve;

(iii) post-processing routines to extract SIFs from energy release rate outputs under plane-stress and plane-strain assumptions;

(iv) numerical integration tools for Paris law crack growth using both explicit schemes (Euler method) and adaptive time-stepping (e.g., Runge-Kutta methods); and

(v) probabilistic simulation workflows for Monte Carlo estimation of failure probabilities.

These tools are integrated into the analysis pipeline used across the case studies reported in the thesis.

1.4 Outline of the thesis

This thesis follows a paper-based structure, in which each chapter—except for Chapter 1 (Introduction) and Chapter 6 (Conclusions and outlook)—corresponds to a published or under-review research paper. All chapters are formatted consistently to ensure readability and coherence. In these papers, the author takes primary responsibility for conceptualization, methodology, formal analysis, data collection, results interpretation, and original manuscript preparation. The contributions of co-authors are explicitly listed at the end of each chapter. Addressing the objectives defined in Section 1.2, the thesis organization is illustrated in Fig. 1.4.

This thesis is structured so that each chapter contributes a specific step along the pathway from physics-based crack modeling to system-level probability of failure estimation. Chapter 2 quantifies and organizes the key uncertain parameters associated with crack growth (*Objective 1*). Chapter 3 establishes and validates the deterministic multiple crack modeling methodology (*Objective 2*). Chapter 4 increases the physical fidelity by explicitly incorporating weld geometry into the finite element model (*Objective 3*). Finally, Chapter 5 integrates these elements—validated multi-crack mechanics, high-fidelity weld-resolved data, and quantified uncertainties—into a surrogate-enabled probabilistic framework to estimate system-level failure probabilities (*Objective 4*).

The following paragraphs describe the specific contributions and linkages of each chapter in more detail.

Chapter 2 provides an in-depth review of corrosion fatigue in offshore wind turbine monopile support structures. It synthesizes existing data on crack propagation in corrosive environments relevant to monopile structural steels, emphasizing the influence of material properties, initial crack size, crack growth parameters, and stress histories. The chapter also highlights the uncertainties associated with these parameters and their implications for structural integrity assessments. This chapter shows that the experimental results are highly scattered, necessitating stochastic modeling of these parameters in real applications. It underscores the need for probabilistic analysis, as presented in Chapter 5, by

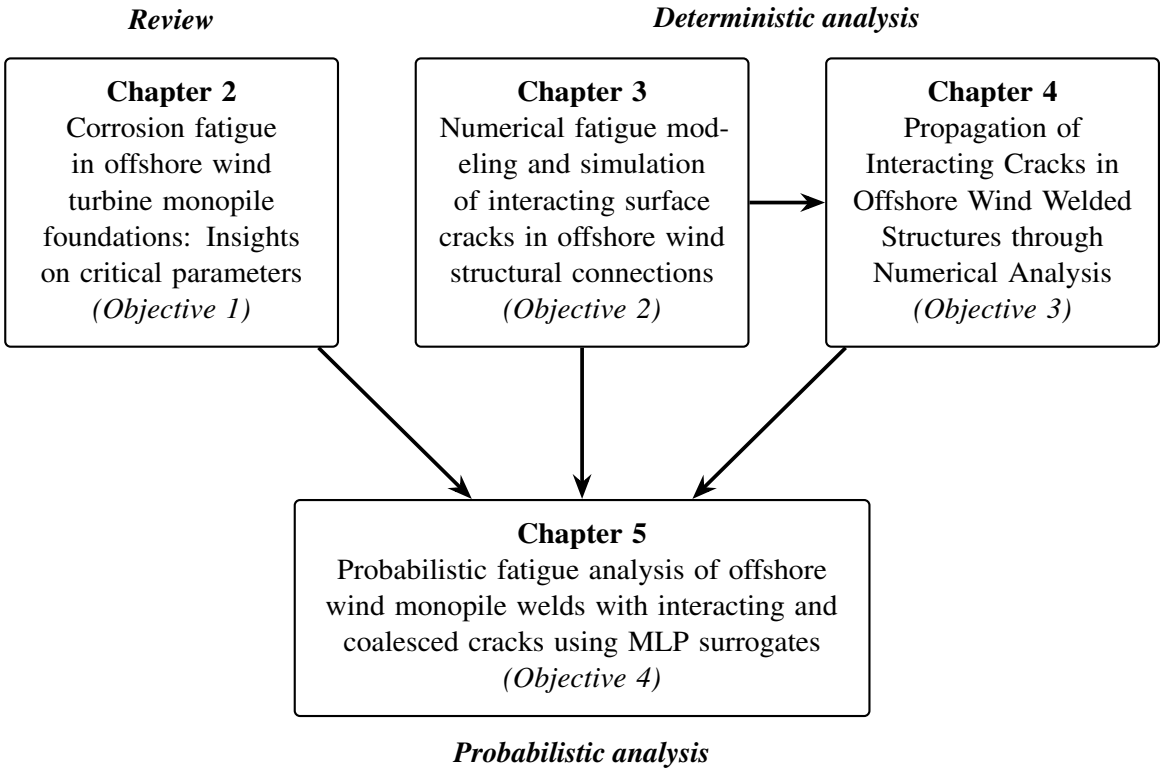

Fig. 1.4 Organization of the PhD thesis. Arrows indicate data/knowledge flow used for surrogate training (Chapter 3→ Chapter 5, and Chapter 4→ Chapter 5) and uncertainty integration (Chapter 2→ Chapter 5).

accounting for uncertainties associated with initial crack size, crack growth parameters, and long-term stress ranges.

A numerical methodology for modeling the fatigue crack growth of multiple surface cracks in offshore structural components is introduced in Chapter 3. The approach accounts for critical phenomena such as crack interaction, coalescence, and through-thickness propagation. The methodology is demonstrated through a numerical case study involving the fatigue propagation of surface cracks in the monopile foundation of an offshore wind turbine. The validated deterministic crack growth and interaction/coalescence handling methodology developed here provides the basis for the simulation framework extended in Chapter 4 and the physical modeling concepts applied in Chapter 5.

Chapter 4 extends the methodology developed in Chapter 3 by explicitly incorporating weld geometry into the finite element model of the monopile foundation. This enhancement allows for a more accurate assessment of the influence of weld profiles on fatigue life predictions, particularly in the presence of interacting and coalescing surface cracks. The simulations in this chapter validate the finite element modeling approach with explicit weld geometry, which is subsequently adopted in Chapter 5 to generate high-fidelity SIF datasets for surrogate training and validation.

Chapter 5 integrates all developments from Chapters 2 to 4 into a single framework. It presents a probabilistic fatigue reliability analysis enabled by a surrogate modeling framework. The surrogate model is trained on high-fidelity three-dimensional finite element simulations and is used to efficiently predict stress intensity factors during crack growth. This approach significantly reduces computational cost while maintaining accuracy, making it suitable for large-scale Monte Carlo simulations. The methodology is applied to assess the structural reliability of a circumferential welded connection in a monopile foundation of an offshore wind turbine.

1.5 List of papers

The following papers are included in this thesis to accomplish the research objectives:

- **Paper 1:** Mishael, J., Morato, P.G., and Rigo, P. (2025). Corrosion fatigue in offshore wind turbine monopile foundations: Insights on critical parameters. *Marine Structures*. Submitted.
- **Paper 2:** Mishael, J., Morato, P.G., and Rigo, P. (2023). Numerical fatigue modeling and simulation of interacting surface cracks in offshore wind structural connections. *Marine Structures*. 92. 103472.
- **Paper 3:** Mishael, J., Morato, P.G., and Rigo, P. (2024). Propagation of Interacting Cracks in Offshore Wind Welded Structures through Numerical Analysis. In *Proceedings of the Thirty-fourth International Ocean and Polar Engineering Conference* (*ISOPE 2024*). 3116-3123.
- **Paper 4:** Mishael, J., Morato, P.G., and Rigo, P. (2025). Probabilistic fatigue analysis of offshore wind monopile welds with interacting and coalesced cracks using MLP surrogates. *Theoretical and Applied Fracture Mechanics*. Submitted.

The following additional contributions, also pertaining to the thematic of rational reliability models, are achieved during the research period. However, they are not included in this thesis as they are not essential to the core of the thesis line.

- **Paper 5:** Mishael, J., Giro, F., Morato, P.G., and Rigo, P. (2022). System Structural Reliability Modelling for Offshore Wind Welded Connections. In *The 18th European Academy of Wind Energy (EAWE) PhD Seminar on Wind Energy*.
- **Paper 6:** Giro, F., Mishael, J., Morato, P.G., and Rigo, P. (2022). Inspection and Maintenance Planning for Offshore Wind Support Structures: Modelling Reliability and Inspection Costs at the System Level. In *Proceedings of the ASME 2022 41st International Conference on Ocean, Offshore and Arctic Engineering (OMAE 2022), Volume 2: Structures, Safety, and Reliability*.

CHAPTER 2

CORROSION FATIGUE IN OFFSHORE WIND TURBINE MONOPILE FOUNDATIONS: INSIGHTS ON CRITICAL PARAMETERS

Paper 1: Mishael, J, Morato, PG, and Rigo, P (2025). Corrosion fatigue in offshore wind turbine monopile foundations: Insights on critical parameters. *Marine Structures*. Submitted.

Abstract: Offshore wind turbine foundations are vulnerable to fatigue damage due to cyclic loads experienced during their service life. Fatigue cracks commonly initiate from preexisting flaws, which may be introduced during manufacturing, transportation, or installation, and can progressively grow to an unstable condition leading to structural failure if left uncontrolled. Additionally, the harsh marine environment significantly increases damage through corrosion. The corrosion-assisted crack growth mechanism can become amplified under cyclic loading due to the synergistic interaction between fatigue loads and corrosive conditions. The extent of such damage depends on multiple factors, including material properties, initial crack size, crack growth parameters, residual stresses, and more. This paper provides a comprehensive review of corrosion fatigue in offshore wind turbine monopile support structures. It synthesizes existing data on crack propagation in corrosive environments and emphasizes the critical influence of these parameters and their uncertainties on the assessment of structural integrity.

Nomenclature

a	Crack depth of a semi-elliptical surface crack [mm].
c	Surface half-length of a semi-elliptical crack [mm].
$2c$	Surface length of a semi-elliptical crack [mm].
T	Plate (wall) thickness [mm].
a_0, c_0	Initial crack depth and initial surface half-length [mm].

a/c	Crack aspect ratio.
N	Number of load cycles [cycle].
$\Delta\sigma$	Applied stress range [MPa].
σ_y	Yield (0.2% proof) strength [MPa].
UTS	Ultimate tensile strength [MPa].
K	Stress intensity factor (SIF) [MPa$\sqrt{\text{m}}$].
ΔK	Stress intensity factor range in a cycle [MPa$\sqrt{\text{m}}$].
$K_{\max}$	Maximum stress intensity factor in a cycle [MPa$\sqrt{\text{m}}$].
$K_{\min}$	Minimum stress intensity factor in a cycle [MPa$\sqrt{\text{m}}$]
ΔK_a	Stress intensity factor range at crack depth [MPa$\sqrt{\text{m}}$].
ΔK_c	Stress intensity factor range at surface point of crack [MPa$\sqrt{\text{m}}$].
ΔK_{th}	Threshold stress intensity factor range for crack growth [MPa$\sqrt{\text{m}}$].
ΔK_{eff}	Effective stress intensity factor range (closure-corrected) [MPa$\sqrt{\text{m}}$].
K_r	Residual-stress intensity factor [MPa$\sqrt{\text{m}}$].
$Y(a,c)$	Geometry/shape correction function for stress intensity factor.
M_k	Weld magnification factor on stress intensity factor.
α	Membrane-stress fraction of total stress ($0 \leq \alpha \leq 1$).
$\frac{da}{dN}$	Crack growth rate (in depth) [m/cycle].
C, m	Paris law coefficients in $da/dN = C(\Delta K)^m$.
J	J-integral (energy release rate) [N/m].
$\dot{J}$	Time derivative of J [N/(m·s)].
$\dot{\Delta K}$	Time derivative of ΔK [MPa$\sqrt{\text{m}}$/s].
R	Stress ratio, $R = \sigma_{\min}/\sigma_{\max}$.
f	Loading frequency [Hz].
$Q(\Delta\sigma)$	Exceedance probability of a stress range.

q Weibull scale parameter for stress ranges [MPa].

h Weibull shape parameter for stress ranges.

P_f Probability of failure.

2.1 Introduction

Addressing modern societal and environmental concerns, offshore wind stands out as one of the most preferred solutions due to its potential for large-scale deployment and significant reductions in levelized cost, especially in the last decade [65]. An essential factor for realizing this potential lies in the design and cost of offshore wind turbine (OWT) foundations, which differ significantly from their onshore counterparts. These foundations not only play a pivotal role in ensuring structural stability but also represent 15% of the capital investment in shallow waters (10–20 m). Moreover, present and future wind farm projects envisage wind turbines installations on deeper waters (40-50 m) with associated life-cycle cost of wind turbine substructure reaching up to 30% of the total investment [66].

The substructures of OWT, which include the foundation and tower, must withstand combined loads from wind, waves, and sea currents throughout their service life. Among the different foundation types in shallow water, monopiles become the preferred solution in Europe due to their relatively simple fabrication and installation process [67]. Typical monopile diameters range from 3 to 7 m, with wall thicknesses between 30 mm and 125 mm [7], and they are considered economically viable for water depths up to 30 m [68]. Fig. 2.1 shows a typical large diameter monopile that was fabricated for an offshore wind farm in the German North Sea [69]. To meet the demands of larger turbines and deeper waters, the development of even larger diameter monopiles is currently underway. These structures are manufactured by rolling and longitudinally welding thick steel plates to form cylindrical sections, which are then circumferentially welded together [4]. The welded joints, particularly the ring welds, often become critical locations for fatigue crack initiation due to microstructural and chemical variations across the base metal (BM), heat-affected zone (HAZ), and weld metal (WM), resulting from the rapid thermal cycles of submerged arc welding [7]. These issues are further complicated by the fact that post-weld treatments are typically not applied in monopile fabrication due to size and cost concerns [3, 70, 71], leaving residual stresses and material-property gradients contributing to fatigue susceptibility. Experimental evidence indicates that HAZ is the primary site for fatigue crack initiation, exhibiting lower fatigue resistance compared to BM [72–75]. Crack initiation in the HAZ typically propagates into BM following a through-thickness path [3, 54, 76]. Recent seawater corrosion fatigue tests reveal significantly increased crack growth rates from the monopile's inner to outer surfaces [3]. Consequently, post-weld heat treatments to release residual stress have significant potential for extending monopile service life.

Corrosion is another damage mechanism that affects the OWT monopile foundations during their service life. Usually, the external surface of the monopile is protected from corrosion using coatings and cathodic protection (CP) systems. The inner side of the monopile foundations, however,

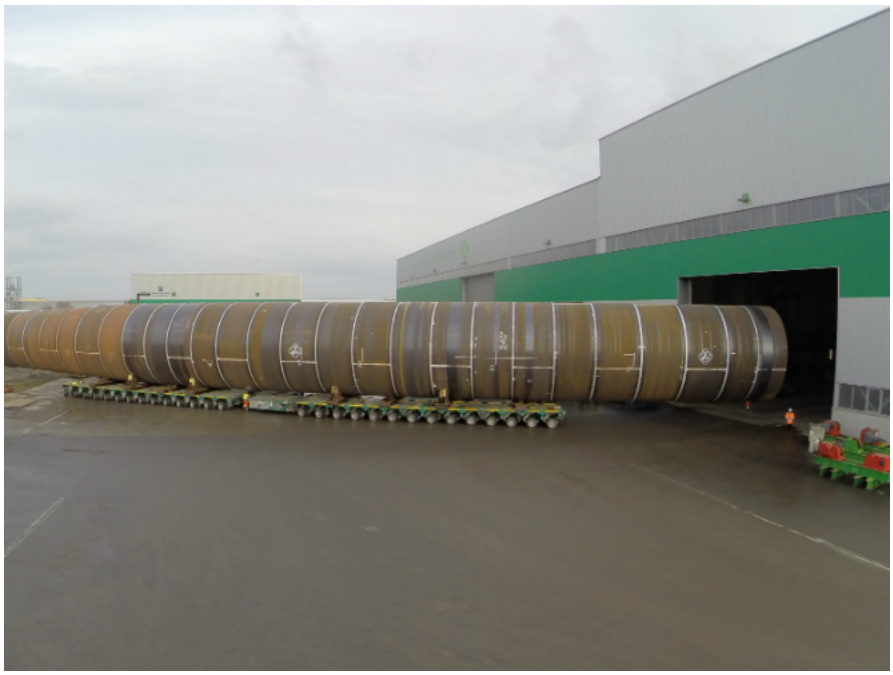

Fig. 2.1 A typical large-diameter monopile fabricated for an offshore wind farm in the German North Sea [69]. The alternative light and dark bands reveal the individual cylindrical sections formed by rolling steel plates, which are then joined by circumferential welds to achieve the full length of the monopile.

is not protected by coatings or CP because low corrosion rates are expected in a closed compartment [77]. Nevertheless, inspections revealed that the inside of the monopile foundations is severely affected by uniform corrosion and localized forms of corrosion such as pitting, accelerated low-water corrosion (ALWC), and microbiologically influenced corrosion (MIC) [77, 78]. Corrosion degrades material properties, enhances surface roughness, and creates localized pits that act as critical stress concentration sites that can initiate fatigue cracks. The interaction between corrosion and fatigue loads amplifies crack growth and reduces the service life of the monopile if not properly treated.

Extensive corrosion fatigue research exists for aerospace components [79–84] and oil & gas offshore platforms [85–92]. However, similar detailed data for large-diameter welded monopiles specific to OWTs remains limited. Current design standards for OWT foundations largely rely on DNV [32, 45, 93] guidelines developed originally from data on slender, small-diameter piles subjected to relatively few load cycles [94]. In contrast, modern OWTs often experience more than 10^9 stress cycles due to combined wind and wave loading at critical welds over the course of their typical 20-year service life [95]. This discrepancy introduces significant uncertainty in fatigue assessments due to limited corrosion fatigue data specifically tailored for monopile steel grades, weld geometries, and environmental conditions. Recent experimental campaigns have started addressing these gaps, but the findings remain scattered, lacking a comprehensive framework.

Traditionally, fatigue assessment of welded offshore structures, including monopile foundations, relies on nominal stress life (S-N) approach combined with the Palmgren-Miner cumulative damage rule [45]. While this method is straightforward for initial design stages but lacks explicit capability to monitor and predict crack evolution. Fatigue assessment based on fracture mechanics (FM), particularly linear elastic fracture mechanics (LEFM), explicitly tracks crack initiation and growth, offering precise predictions of crack propagation under cyclic loading. One of the key parameters in LEFM is the stress intensity factor (SIF), usually represented by the symbol K, which quantifies the stress distribution at crack tips. Crack propagation behavior is typically modeled using Paris law, which is expressed as:

$$da/dN = C(\Delta K)^m \tag{2.1}$$

where, da/dN represents the crack growth rate, ΔK is the SIF range, and C and m are material-specific constants. LEFM thus facilitates detailed characterization of crack evolution, enabling informed decisions regarding inspection intervals and maintenance actions, crucial for reliability assessments in OWT monopile foundations.

The effectiveness of LEFM based fatigue life assessment is inherently tied to several critical parameters. Initial crack sizes, typically defined from weld imperfections or derived from periodic inspection data, form the baseline for crack growth analyses. The SIF, directly influenced by loading conditions and crack geometry, dictates the rate of crack advancement. Additionally, experimentally determined crack growth rates are highly sensitive to environmental influences and operational loading conditions. Residual stresses introduced during fabrication processes, particularly welding, further impact fatigue performance by accelerating or mitigating crack propagation. Integrating these parameters within LEFM facilitates detailed fatigue life predictions, thereby empowering decision-makers with improved capabilities for scheduling inspections, implementing proactive maintenance, and optimizing overall structural reliability and economic efficiency.

The probabilistic FM approach further strengthens the reliability assessment by explicitly accounting for uncertainties inherent in material properties, loading conditions, initial crack sizes, inspection capabilities, and modeling methods [96]. This probabilistic approach, recommended by classification societies such as DNV for offshore structures [32], has become increasingly valuable for establishing inspection schedules and managing maintenance strategies effectively. Nonetheless, widespread implementation of probabilistic FM approaches demands accurate quantification of these uncertainties through appropriate statistical distributions.

Recognizing the critical role of parameters such as initial crack sizes, crack growth rates, material properties, and long-term stress ranges as well as their associated uncertainties, this review synthesizes existing data relevant to corrosion fatigue in OWT monopile foundations. By consolidating and critically evaluating this information, this review aims to improve fatigue life predictions, support risk informed inspection planning, and guide cost effective maintenance strategies. Thereby, it contributes to enhancing the structural integrity and economic viability of monopile foundations in aggressive marine environments.

2.2 Mechanisms of corrosion fatigue

As previously stated in the introduction, metallic structures in service conditions, particularly OWT foundations, are exposed to harsh environments, which makes them susceptible to corrosion. The fatigue damage resulting from the combined effects of cyclic loading and aggressive environmental conditions is broadly termed as corrosion fatigue (CF). Such damage may manifest in one of two ways: as a simple superposition of fatigue cracking and corrosive degradation, or as a complex synergistic interaction between these two phenomena. The synergistic interaction between corrosion and fatigue has been demonstrated to significantly accelerate material degradation and is a key contributor to the premature failure of engineering structures [2]. According to the American Society for Testing and Materials (ASTM), corrosion fatigue may be defined as a sequence of damage stages to metal that occurs with accumulated loading cycles in aggressive environments. This evolution is the result of interactions between irreversible cyclic plastic deformation and localized chemical or electrochemical reactions [1].

Numerous factors influence CF behavior, which can be categorized into mechanical, metallurgical, and environmental factors [85, 86, 97]. Maximum stress [98], SIF [99], cyclic stress or stress intensity range [100], loading frequency and waveform [101–104], load interactions under variable amplitude loading [101, 105], stress state and residual stresses [102, 106–108], and crack size and geometry in relation to component dimensions [109] are examples of mechanical variables. The distribution of alloying elements, impurities, microstructure, and crystal structure [110, 111], mechanical working, applied heat treatments [112], alloy composition [113], and intrinsic mechanical properties like strength and fracture toughness [55] are all examples of metallurgical influences. Environmental factors include pH [114, 115], electrochemical potential [113, 116, 117], temperature [118–120], and the effectiveness of coatings or corrosion inhibitors [121]. Due to this complexity, research on CF typically focuses on a limited number of relevant factors because it is economically not feasible and practically challenging to incorporate all influencing parameters.

Corrosion fatigue crack initiation mechanisms in aqueous environments are commonly classified into four main categories: (1) pitting corrosion, where pits formed from corrosive attack become nucleation sites for cracks; (2) preferential dissolution, areas with higher plastic deformation corrode preferentially; (3) oxide film rupture, where cyclic deformation breaks protective oxide films, exposing fresh metal to the environment; and (4) surface energy reduction due to environmental species adsorption, promoting micro-crack propagation [85]. Among these mechanisms, stress concentration from corrosion pits was initially proposed to explain accelerated crack initiation under CF [122–124]. Preferential dissolution also contributes significantly, particularly targeting freshly exposed metallic surfaces from cyclic slip step fractures [98, 125–128]. Rupture of oxide films can similarly accelerate crack initiation, particularly in materials like copper, aluminum, and stainless steel, known for forming protective oxide layers upon exposure to air [129, 130]. Additionally, the reduction in surface energy due to adsorption of environmental species can also facilitate early-stage crack formation [125]. However, no single mechanism alone can explain CF crack initiation. The dominant

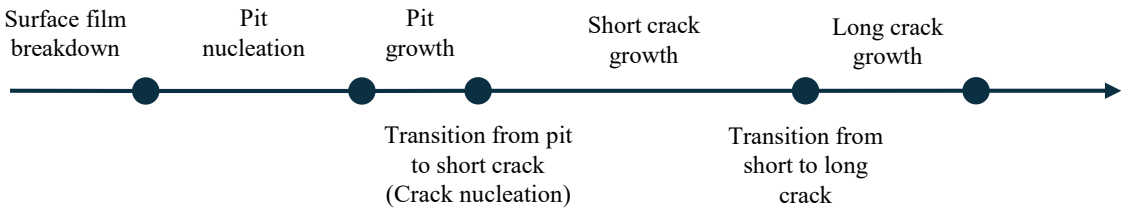

Fig. 2.2 Different stages of corrosion fatigue process initiated from corrosion pits. Adapted from [140].

initiation mechanism varies with specific combinations of material and environmental conditions, indicating a high sensitivity of CF behavior to context.

In OWT monopile foundations, the CF crack initiation process is predominantly attributed to localized pitting corrosion in critical regions such as circumferential welds toes or geometric discontinuities [131]. This localized corrosion begins with the breakdown of protective surface films, forming pits that grow until they reach a critical size. These pits then serve as nucleation points for fatigue cracks [39, 124, 132–136]. Crack initiation and early growth can be significantly increased when multiple corrosion pits occur closely together, leading to complex interactions and elevated local stress concentrations.

Despite clear evidence of the critical role of corrosion pits in fatigue crack initiation, deterministic modeling approaches face considerable challenges in accurately characterizing the pit to short crack and short to long crack transition phases. Traditional deterministic fatigue life predictions, such as fatigue S-N curves, often do not fully capture the inherent variability in pit formation, early crack nucleation, and interactions between multiple pits. Therefore, structural reliability and probabilistic modeling frameworks have gained prominence as essential tools to bridge this gap [137–139]. These approaches allow explicit incorporation of uncertainties in pit size, shape, distribution, and interactions, thereby offering more robust predictions of fatigue life and structural integrity.

Typically, deterministic CF models aim to determine the fatigue life of base material and welded components by considering the combined corrosion and fatigue degradation mechanisms. The CF crack growth process initiated predominantly from pitting involves multiple sequential stages, as shown in Fig. 2.2. Initially, localized pits form and act as crack nucleation sites, evolving into short cracks, and eventually transitioning into long cracks. Understanding and accurately modeling this transition to long crack growth is essential for structural integrity assessments. The subsequent crack propagation behavior under cyclic loading conditions is typically analyzed using fracture mechanics approaches such as Paris' law or similar fatigue crack growth relationships.

As mentioned earlier, pitting CF significantly affects crack initiation, growth, and ultimately the structural longevity of OWT monopiles [2]. To accurately predict CF life at weldments in OWT support structures, fatigue S-N curves must incorporate effects of pit size and morphology explicitly [131]. Although recent research efforts have addressed corrosion pits within fatigue life predictions of monopile foundations [141, 142], a comprehensive understanding of transition phases—from pits

Table 2.1 Maximum permitted chemical composition (in weight %) and typical mechanical properties for structural steels commonly used in OWT foundations [145–147].

Steel grade	C	Mn	P	S	Si	σ_y (MPa)	UTS (MPa)	Typical application
S235	0.22	1.60	0.05	0.05	0.05	235	360–510	boat landings, ladders, etc.
S275	0.25	1.60	0.04	0.05	0.05	275	370–530	platforms, J-tubes, etc.
S355	0.23	1.60	0.05	0.05	0.05	355	470–630	monopile body, flange connections, etc.
S460	0.12	1.60	0.025	0.015	0.50	460	520–670	high-stress welded joints

to short cracks and from short to long cracks—remains incomplete. Furthermore, current fracture mechanics models typically lack holistic integration of the complex, synergistic effects of mechanical, metallurgical, and environmental variables that characterize CF in OWT monopile foundations.

2.3 Structural steels for monopile foundations

Monopile foundations for OWTs are fabricated almost exclusively from low-alloy structural steels covered by the European standards EN 10025 (general structural steel) and EN 10225 (weldable offshore steel). It is expected that these steels will also be used for the support structures of future generations of wind turbines [143]. The most frequently used strength classes—S235, S275, S355, and S460—have minimum yield strengths of 235–460 MPa and are supplied in plate thicknesses extending beyond 100 mm [144]. The chemical and mechanical properties of these steels are summarized in Table 2.1.

Structural steel grade S355 has become the reference material for primary monopile structures. Its moderate carbon equivalent allows for multi-pass submerged arc welding without excessive preheating, while still providing adequate fracture toughness under North Sea conditions. Consequently, it is featured in most recent CF studies [3, 7, 54–56, 70, 103] and industrial deployments [148–150]. Lower-strength S275 and higher-strength S460 are also used, although more selectively, when fabrication logistics or weight savings justify their use.

Industrial practice confirms the widespread use of these structural steel grades. As summarized in Table 2.2, steel orders for wind farms in Europe, including Arkona, Hornsea, Borssele, and many others, use S235/S275 plates for secondary elements and S355 for primary structures. Additionally, S420 and S460 are used in places where reducing weight or increasing section modulus is necessary [144, 148]. In some of the offshore wind projects, the plate thickness ranged from 70 to 100 mm and individual contracts exceeded 100 kt of steel. Such usage reflects the trend towards larger wind turbine ratings and the drive to minimize offshore welding.

Usually, offshore structural steels are specified with suffixes representing specific chemical and mechanical processing conditions aimed at improving mechanical properties. Most listed steel grades carry offshore-specific suffixes—such as G7, G8 or G10, indicating progressively stricter Charpy

and crack-tip opening displacement (CTOD) toughness requirements, or the Z35 suffix denoting verified through-thickness ductility ($\geq$35% reduction of area). Additionally, steels are primarily delivered in thermo-mechanically processed (+M) condition, which underscores the importance of low-temperature toughness and weldability requirements for steels that can withstand the working conditions in the North Sea. The steel grades in Table 2.2 follow the naming convention recommended by standards such as EN 10025 and EN 10225. The prefix *S* identifies structural steels; the subsequent number (e.g., 235, 355, 460) states the guaranteed 0.2% proof stress for sections not exceeding 16 mm in thickness. Impact-toughness classes are denoted by letters (*JR*, *J0*, *J2*, or *K2*), representing minimum absorbed energies of 27 J (40 J for *K2*) at test temperatures of +20, 0, -20, and -20 °C, respectively. In the case of offshore steel grades, these letters are substituted with *G*. The designation of the steel grade is completed by adding the processing symbols; *+N* for normalized material, *+M* for thermo-mechanically controlled-processed (TMCP) plate, and an optional *L* for low-temperature variants (e.g., S355ML). For example, S355 G10+M Z35 specifies a TMCP plate that meets the most strict offshore toughness class and has verified through-thickness ductility. Commercial mills can supply steel plates up to 250 mm thick in the +N class and up to 150 mm thick in the +M class, respectively [151, 152].

Most CF design curves historically trace back to laboratory experiments conducted on BS4360 50D steel in the 1970s and 1980s [154]. BS4360 Grade 50D is equivalent to the modern S355 J2+N hot-rolled normalized steel [153, 155, 156]. It contains higher levels of carbon and sulfur and exhibits a coarse ferrite-pearlite microstructure (see, Fig. 2.3). Modern offshore steels, such as S355 G10+M

Table 2.2 Representative plate grades used in European OWT monopile projects [144, 148]. Grade selection reflects project-specific needs, with S460 used for weight savings in larger turbines and S235/S275 for less critical secondary components.

Project	Country	Steel grades	Thickness (mm)	Tonnage (kt)
Arkona	DE	S355 G7+M, S355 G8+M (Z35), S420 G1+M, S420 G2+M (Z35), S460 G2+M (Z35)	70–104	52.25
Borkum Riffgrund 2	DE	S355 J0, S355 ML, S355 G9+M, S355 G10+M, S420 ML, S460 G2+M	20–95	40.80
Borssele I & II	NL	S275 ML, S355 ML, S355 J2+N	30–108	104.80
Borssele III & IV	NL	S355 G7+M, S355 G8+M, S355 ML, S460 G2+M, S460 ML	12.7–88	69.60
Hornsea 1	UK	S275 ML, S355 ML	30–102	303.93
Hornsea 2	UK	S275 ML, S355 ML, S355K2+N, S355J0, S355 JR, S355 J2, S355 J2+N, S355 G10+N	18–110	224.00
Northwester 2	BE	S355 NL, S355 G10+M, S355 ML	8–100	25.40
Saint–Nazaire	FR	S235 JR+N, S355 ML, S355 G8+M, S460 G2+M, S420 ML	20–135	76.40

"Z35" denotes plates qualified for $\geq$ 35 % through-thickness reduction of area.

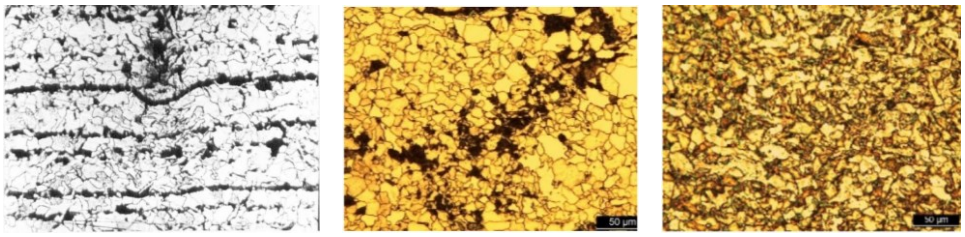

(a) BS4360 50D (b) S355J2+N (c) S355G10+M

Fig. 2.3 Typical microstructures of different steel grades at the same magnification (50 μ*m*): (a) BS4360 50D steel [76], (b) S355 J2+N steel [153], both containing coarse ferrite–pearlite grains; and (c) S355 G10+M steel [153], containing refined (fine) ferrite–pearlite grains.

and S460 G2+M, are produced via TMCP, which yields a refined ferrite-pearlite microstructure (see, Fig. 2.3) and significantly lower impurity levels [110, 153, 157]. TMCP refines grain size, which lowers the ductile-to-brittle transition temperature and enhances strength, formability, and fracture toughness compared to its coarse-grained equivalents [151, 158–161]. The refined microstructure of TMCP steels significantly influences CF performance. Grain refinement deflects crack paths and increases crack face roughness, thereby elevating threshold SIFs (ΔK_{th}) and lowering Paris law crack growth constants compared to normalized steels [53, 153, 162]. Consequently, TMCP is widely adopted in advanced offshore structural steels, including the S355 M series used in monopile fabrication [151], as it improves the resistance to CF crack initiation and propagation. Therefore, applying historical datasets that are based on BS4360 50D steel for the life predictions of modern TMCP steels gives lower ΔK_{th} values and higher crack growth rates, resulting in conservatively short fatigue life predictions. Current CF design practices for monopiles adhere to standards like DNV [45], which need to be updated to reflect the enhanced performance characteristics of modern TMCP structural steels.

The advantages of microstructural refinement described above become especially crucial in the marine environment. The offshore environment, characterized by seawater's high chloride content and cyclic wind and wave loading at low frequencies (0.1–0.3 Hz), accelerates CF crack growth compared to air. Such severe environmental conditions necessitate advanced steel grades featuring refined microstructure. Over the past decade, several research groups started addressing the lack of contemporary data by producing new corrosion fatigue crack growth (CFCG) data for modern TMCP offshore steels and representative weldments [7, 54, 55, 103]. Their findings generally confirm that microstructural refinement, lower impurity levels, and verified through-thickness ductility contribute to higher ΔK_{th} values and reduced Paris-law constants. However, there remains considerable scatter among the published results. To quantify and understand this scatter, it is useful to compile precise chemical compositions from recent experiments and directly compare them with the standardized specification limits listed in Table 2.1. A compilation of these experimental compositions is provided in Table 2.3.

Table 2.3 Chemical composition of offshore steel grades (wt.%), including only major elements.

Steel	Element									%E	σ_y	UTS	Ref
	C	Mn	Ni	Si	Cu	Cr	P	Mo	S		(MPa)	(MPa)	
S355 J2+N	0.160	1.420	0.300	0.380	0.400	0.300	0.013	0.080	0.006	20.0	355[2]	470[2]	[51]
S355 ML	0.053	1.520	0.320	0.270	0.240	0.028	0.012	0.007	0.001	35.0	478	518	[55]
S355 G10+M	0.060	1.570	0.334	0.271	0.241	0.034	0.013	0.006	0.001	38.0	435	545	[155]
S355 G8+M	0.050	1.520	0.320	0.270	0.240	0.030		0.010		35.0	447	549	[103]
S355	0.100	0.640	0.095	0.150	0.380	0.076	0.022	0.014	0.041	22.0	419	732	[163]
S355 NL	0.140	1.230	0.290	0.280	0.310	0.008	0.013		0.004	27.7	400	557	[164]
S355 NL	0.130	1.110	0.270	0.240	0.250	0.006	0.011		0.005	30.2	405	516	[164]
S355 J2+N	0.150	1.420	0.009	0.230	0.014	0.047	0.009	0.004	0.004		355[1]	470[1]	[165]
S355 J2+N	0.170	1.540	0.040	0.040	0.080	0.020		0.004	0.004	30.7	385	531	[166]

[1] The values are not explicitly specified in [165]. Instead, they are taken from [167], which is cited therein, for plates under 16 mm thickness. [165] performed experiments on 15 mm thick plates.

[2] The values specified in [51] are based on the minimum required by [167].

The available data clearly shows that significant variability exists among steels of the same nominal grade used within the offshore wind industry. This variability introduces aleatory uncertainty into CFCG data, and hence in fatigue life estimations, due to variations in material properties that cannot be eliminated through manufacturing controls alone. These differences directly affect the steel's ability to resist crack initiation, propagation, and failure under cyclic loading conditions and corrosive environment. Considering the harsh operational environment of offshore monopiles, which regularly experience multi-axial, variable-amplitude loadings from wave, wind, and turbine operation, quantifying and understanding these uncertainties is critical for reliably predicting fatigue life. Therefore, future research should focus on systematically quantifying these uncertainties through controlled experiments and probabilistic modeling. Furthermore, the development of CFCG models specifically calibrated for modern TMCP steel grades will considerably reduce conservatism and enhance fatigue life predictions for offshore monopile foundations.

2.4 Initial crack size

The initiation and subsequent propagation of fatigue cracks in welded structures significantly depend on the initial size and characteristics of existing defects. Such initial cracks are inherently random in nature, influenced by various factors including material properties (such as inclusions and particles), manufacturing processes (introducing scratches or dents), loading and environmental conditions (mainly corrosion), as well as geometric features like holes and sharp corners. More importantly, the crack growth may be negligible if the initial cracks are sufficiently small, particularly when considering the lower SIF ranges within crack growth rate diagrams (da/dN versus ΔK) for specific materials [168]. Typically, fatigue cracks exhibit irregular shapes and orientations [24]. For analysis, however, they are commonly idealized as semi-elliptical surface flaws with depth a and surface half-length c (total surface length $2c$), as recommended by industrial standards [32, 33]. Fig. 2.4 illustrates this geometry on a finite thickness plate.

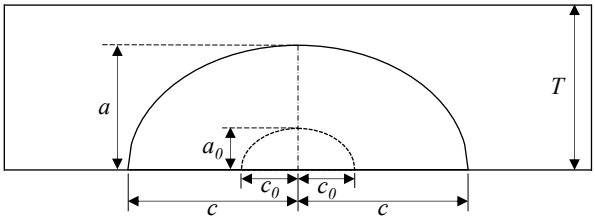

Fig. 2.4 Semi-elliptical surface crack in a finite thickness plate. The dashed semi-ellipse denotes the initial crack with depth a_0 and surface half-length c_0 (total surface length $2c_0$) at $N = 0$. The solid semi-ellipse shows the current crack depth a and surface half-length c (total surface length $2c$) after N cycles. T is the plate thickness.

The initial crack size, usually represented by a_0 (initial depth) and c_0 (initial surface half-length) at $N = 0$ (N, number of stress cycles), profoundly influences fatigue life predictions and significantly affects the applicability of the LEFM approach. Researchers and industry standards typically recommend initial crack depths (a_0) ranging from 0.1 mm to 0.5 mm for fatigue analysis. For example, BS7608 [169] recommends initial crack sizes between 0.1 mm and 0.25 mm at the weld toe of flaw-free welded joints, whereas the ABS standard [48] specifies a conservative initial crack depth of 0.5 mm for surface cracks initiating from weld-base material transitions. Radaj et al. [49] suggested a minimum initial crack depth of 0.15 mm and surface crack lengths ($2c_0$) ranging from 0.45 to 0.75 mm for effective application of LEFM. Lassen and Recho [50] recommended an initial crack size of 0.1 mm, motivated by limitations in detecting smaller cracks during routine in-service inspections. Similarly, Skoglund and Leander [170] concluded that an initial crack depth of 0.1 mm, coupled with an initial aspect ratio (a_0/c_0) of 0.2, provides realistic fatigue strength estimates for fillet-welded structures, consistent with earlier observations by Koenigsberger and Fisher [171], and Albrecht and Friedland [172].

Despite well-established recommendations, the determination of initial crack sizes involves considerable uncertainty, primarily due to inherent variability in manufacturing quality and operational environments. In welded joints, fatigue crack initiation periods are often deemed negligible since weld defects, such as undercuts, slag inclusions, and surface spatters, inherently serve as crack initiation points [173, 174]. Historically, initial crack sizes have been characterized by measuring defect distributions directly from welded structures. For example, analyses of weld defects in offshore structures yielded mean initial crack depths ranging approximately between 0.11 and 0.38 mm, typically represented by exponential distributions [175–179]. However, this method presents challenges due to its labor-intensive nature and limited transferability across different welding procedures, materials, and structural geometries.

Another critical consideration when selecting initial crack sizes is the largest crack that may escape detection during non-destructive inspections (NDI), as such undetected defects directly influence the reliability of fatigue assessments [176]. The detection limit of NDI techniques is inherently probabilistic, influenced by several factors, including the inspection method, the operator's expertise,

material characteristics, and the accessibility of structural components [177]. Consequently, deterministic crack sizes corresponding to specific probabilities of detection (PoD) are generally selected for practical fatigue analyses, emphasizing the probabilistic nature of initial crack definitions.

In practice, initial crack sizes are frequently defined through calibration of probabilistic crack propagation models to experimental fatigue (S-N) data [180–182]. The initial crack size distributions are adjusted until the predicted fatigue failure probabilities match observed empirical outcomes from fatigue tests. These calibrated crack sizes are often termed "fictitious," as they do not necessarily represent physically measurable defects, but rather serve as model parameters accounting for simplifications inherent to LEFM methods, such as assuming isolated cracks and overlooking crack coalescence phenomena [183]. Furthermore, these calibrated initial crack sizes are typically based on the as-welded condition, necessitating updates to account for real-world inspection results and potential repair interventions [181, 183].

Recent studies continue to adopt exponential distributions to characterize initial crack sizes, particularly for inspection and maintenance planning purposes in offshore wind structures [12, 35, 46, 47]. Amirafshari et al. [184] comprehensively reviewed available weld defect size data, updating earlier datasets with modern welding technologies such as hybrid laser welding, which demonstrated lower defect rates compared to conventional arc welding methods. Their findings indicate significant improvements in welding quality and reduced defect occurrences compared to historical data, suggesting potential updates in initial crack size distributions for contemporary offshore and ship structures.

Finally, another notable approach for defining initial crack sizes is the equivalent initial flaw size (EIFS) method, extensively used in aerospace but less commonly applied within the offshore industry [124]. The EIFS method involves measuring cracks at a known stage of structural life and performing a backward analysis to estimate the original flaw size at the onset of propagation [168, 185]. While the EIFS is not physically measurable, it functions effectively as a model calibration parameter facilitating fatigue life estimation under similar operational conditions [186]. The offshore industry could benefit from broader adoption of EIFS techniques, particularly for more precise fatigue life predictions and enhanced structural integrity assessments.

2.5 Stress intensity factor (SIF)

The accurate determination of SIFs is critical in LEFM based crack propagation analyses, as the SIF governs the stress field near the crack tip and thus directly influences crack growth behavior. In welded structures, including OWT monopile foundations, SIF calculations become inherently complex due to their dependency on several factors, including global structural geometry, local weld geometry, crack configuration, residual stress states, and loading conditions [187]. Consequently, even seemingly simple weldments require detailed analytical or numerical evaluations to ensure accurate SIF predictions, accounting comprehensively for geometrical and loading complexities.

SIFs for welded joints are commonly computed using established analytical solutions derived from finite element analyses (FEA) of standardized crack geometries. Widely adopted expressions, such as those proposed by Newman and Raju [188, 189], describe the SIF of surface cracks in finite plates under tension and bending loads. The standards DNV [32] and BS 7910 [33] reference these solutions, integrating them into fatigue assessment guidelines for cruciform, butt, and T-butt welds. To address weld-specific features, Maddox [190] introduced the concept of the magnification factor (M_k), defined as the ratio of SIF in a welded structure to that of an equivalent plane plate. Bowness and Lee [57] extended this approach specifically for semi-elliptical cracks in T-butt joints, providing equations widely utilized in industry standards.

Despite their utility, standard SIF solutions typically assume simplified conditions and fixed crack geometries, potentially overlooking complex weld features and crack interactions found in practical scenarios. Zhao et al. [191] demonstrated this limitation by studying fatigue crack propagation in longitudinal fillet welded joints using FEA, highlighting the necessity of numerical analyses for structures not adequately described by existing analytical solutions. Similarly, Lie et al. [58] reported significant discrepancies between M_k factors for plate-to-plate butt welds and standard T-butt joints, emphasizing deviations up to 97.4% under bending loading conditions. These discrepancies underline the necessity for careful consideration when applying generic solutions to specific structural configurations.

Additionally, the SIF in welded joints is influenced not only by global structural geometry but also significantly by local weld geometry parameters, such as weld toe radius, weld angle, and reinforcement dimensions [192–194]. Investigations by Nguyen and Wahab [192] and Ferreira and Branco [193] explicitly demonstrated how variations in weld profile parameters significantly alter fatigue characteristics, influencing SIF magnitudes and thus fatigue life. Schork et al. [194] further emphasized that among weld geometry parameters, the weld toe radius and flank angle are particularly influential on SIF near endurance limits. Recently, Kolios et al. [195] utilized advanced laser scanning combined with FEA, showing that accurate modeling of local weld geometry could substantially enhance fatigue predictions for OWT monopile weldments, with stress concentration factors (SCF) varying notably between 1.1 and 1.65 depending on weld quality. As local stress concentrations directly influence the SIF, such variations in SCF also affect the SIF magnitude and, consequently, the predicted fatigue crack growth.

To distinguish fatigue-related fracture mechanics from static cases, the SIF range (ΔK) is used instead of the single-valued SIF (K). While K describes the crack tip stress field for a specific loading condition, ΔK, defined as the difference between the maximum and minimum SIFs ($K_{\max} - K_{\min}$), quantifies the cyclic loading range and governs crack growth under fatigue. The reader is directed to [196] for a detailed theoretical background on the concept and formulation of the SIF.

The quantitative determination of the SIF range (ΔK), essential for fatigue crack growth modeling, is expressed analytically as:

$$\Delta K = Y(a,c)\,\Delta\sigma\,\sqrt{\pi a}, \tag{2.2}$$

where $\Delta\sigma$ is the applied stress range, $Y(a,c)$ is a shape factor reflecting crack geometry and local loading conditions, and a and c denote crack depth and surface half-length, respectively.

Once ΔK is available at the deepest point (ΔK_a) and at the surface point (ΔK_c), the crack depth and surface half-length over a block of ΔN cycles can be written as:

$$a(N+\Delta N) = a(N) + \int_N^{N+\Delta N} C\left[\Delta K_a\right]^m dN, \tag{2.3}$$

$$c(N+\Delta N) = c(N) + \int_N^{N+\Delta N} C\left[\Delta K_c\right]^m dN. \tag{2.4}$$

where ΔK_a and ΔK_c depend on the evolving crack geometry and loading history.

In practical applications, especially for welded joints subject to combined membrane and bending loading, DNV [32] proposes expressions for ΔK at these locations, explicitly accounting for the relevant factors:

$$\Delta K_a = \Delta\sigma\left[\alpha Y_{\mu a} M_{k\mu a} + (1-\alpha) Y_{ba} M_{kba}\right]\sqrt{\pi a}, \tag{2.5}$$

$$\Delta K_c = \Delta\sigma\left[\alpha Y_{\mu c} M_{k\mu c} + (1-\alpha) Y_{bc} M_{kbc}\right]\sqrt{\pi a}, \tag{2.6}$$

where subscripts μ and b denote membrane and bending stress components, respectively, α represents the ratio of membrane to total stress and M_k factors quantify stress amplification due to local weld geometry effects [57]. These closed-form solutions are invaluable for rapid assessments but have inherent limitations in capturing detailed interactions between stress distribution changes and crack geometry evolution during propagation.

Another significant aspect in assessing fatigue crack growth is accounting for the interaction and possible coalescence of multiple adjacent surface cracks, common in welded joints subject to fatigue. Crack interaction effects significantly modify local SIF values, potentially accelerating crack propagation and affecting fatigue life predictions. Kamaya [22, 197], Bell and Vosikovsky[198], and To et al. [199] provided experimental evidence that semi-elliptical surface cracks initiating along weld toes often coalesce, forming dominant larger cracks with accelerated growth rates. Experimental and numerical studies by Madia et al. [200] further emphasized that SIFs for interacting cracks differ significantly from those of isolated cracks, necessitating advanced numerical simulations to accurately predict fatigue life.

Numerical methods such as FEA have proven crucial for accurately computing SIFs in complex weld geometries and crack configurations, including crack interaction phenomena. For example, comprehensive studies by Newman and Raju [188, 189, 201], Navid et al. [202], and Kirkhope et al. [203] leveraged numerical analyses to generate widely used SIF solutions for various structural configurations. More recently, authors [204, 205] employed detailed three-dimensional finite element modeling to directly capture local weld geometry effects on semi-elliptical weld toe cracks in offshore monopile foundations, thus avoiding simplified parametric equations and enhancing prediction accu-

racy. These numerical approaches, though computationally intensive, provide unmatched precision in complex real-world applications.

The computational cost of detailed three-dimensional FEA poses challenges for probabilistic fatigue assessments requiring numerous simulations. To overcome this limitation, recent developments have focused on surrogate modeling approaches, such as Gaussian process regression, to efficiently predict SIFs based on a limited set of high-fidelity FEA results. Keprate et al. [63], Leng et al. [206], and Kaloop et al. [207] successfully demonstrated the efficacy of surrogate models for predicting SIF in offshore structures. These models significantly reduce computational expense while maintaining high accuracy, with prediction errors typically below 2%. However, existing research primarily addresses single crack scenarios on idealistic simple structural geometries. The application of surrogate models to predict SIFs for interacting multiple cracks, a realistic and critical condition for offshore structures, remains largely unexplored. Additionally, small errors in SIF prediction based on surrogate models can accumulate over successive crack growth increments, resulting in significant deviations in fatigue life estimation. This sensitivity underscores the importance of high surrogate model fidelity when predicting SIF and careful uncertainty quantification in long-term crack propagation simulations.

Other approaches, including the weight function method, provide flexible and effective solutions for estimating SIFs induced by external loads and residual stresses. Shen and Glinka [208] as well as Goyal and Glinka [209] demonstrated its effectiveness by integrating stress distributions along potential crack planes obtained from FEA. Dong and Guedes Soares [210] further validated this approach for weld toe cracks, accounting explicitly for local stress singularities and offering improved fatigue life predictions aligned with experimental observations. These numerical-analytical hybrid methods offer practical alternatives, particularly useful in cases where purely numerical modeling may be prohibitively costly or complex.

It can be summarized that, the accurate computation of SIFs for welded structures involves careful consideration of local and global geometric features, weld imperfections, residual stresses, and loading conditions. While analytical solutions and standard equations provide practical tools for initial fatigue assessments, the complexities of crack interaction and detailed weld geometries often necessitate advanced numerical simulations or hybrid numerical-analytical approaches. Emerging surrogate modeling techniques offer a promising way to balance computational efficiency and predictive accuracy. This is particularly relevant for complex fatigue assessments involving multiple interacting cracks, which is an area that requires further research.

2.6 Crack growth parameters

Identifying and using the appropriate crack growth parameters is also essential for accurately estimating the fatigue life of welded joints. The crack growth parameters C, and m are material dependent and usually derived from crack propagation experiments. These parameters depend on multiple factors, such as stress ratio, residual stress, environmental conditions, loading frequency, and corrosion. This

section reviews the influence of these factors on the crack growth behavior of structural steels used to fabricate OWT monopiles, with a focus on recent findings and recommended practices.

Recommendations regarding the parameters to use in LEFM-based fatigue crack propagation modeling are specified in industrial standards [32, 33, 48, 211]. Hobbacher [211] stated that the fatigue life estimate using the LEFM approach can be carried out with appropriate parameters and the calculations should be verified at known structural details; on the other hand, DNV [32] and ABS [48] propose that the assumptions for the fracture mechanics analysis model can be calibrated by comparison with the S-N model. In contrast, British Standards [33] recommends values for crack growth parameters that are appropriate for various materials and environments by putting forth a simple linear or more accurate bi-linear model to depict the crack propagation in welded structures. Hobbacher [212] showcased that there exists a large scatter in crack propagation data for different welded joints and recommended to use an upper bound line for practical applications. However, in practical scenarios it is important to use the crack propagation parameters relevant to the specific material, loading and environmental conditions under consideration. Recently many researchers focused on deriving C values for widely used structural steel grades for OWT monopile foundations. These investigations are motivated by the fact that the available fatigue crack growth data for steels in air and seawater environments are several decades old and may not be appropriate for structural integrity assessment of OWT foundations, which are fabricated using modern materials and welding technologies [54]. Additionally, the crack growth data suggested in offshore standards is based on the characteristics that are representative of typical offshore structures in the oil & gas industry.

The recent literature emphasizes the critical role of environmental conditions, notably seawater, on fatigue crack growth behavior of structural steels such as S355, which are extensively utilized for fabricating OWT monopile foundations. Mehmanparast et al. [54], through the Structural Life Integrity for Corrosion (SLIC) inter-laboratory testing program, established comprehensive fatigue crack growth data for S355G8+M steel, covering BM and HAZ in air and seawater environments. The SLIC results show that for a given value of ΔK, the fatigue crack growth rate, da/dN, is on average around 2 times higher in seawater compared to air for both BM and HAZ. This is less than the crack acceleration factor in seawater compared to air recommend by BS7910 [33]. Additionally, the SLIC results reinforced the validity of bi-linear models, as recommended by BS 7910 [33], for both air and seawater environments for BM. They also concluded that the simplified Paris-law model suggested by BS7910 [33] provide a good estimate of fatigue crack growth behavior for HAZ in air and seawater.

Moreover, Igwemezie et al. [155] conducted experimental studies highlighting that crack propagation is significantly accelerated in seawater relative to air environments. They observed that TMCP grades, specifically S355G10+M, demonstrated lower crack growth rates in air compared to normalized-rolled steels. Additionally, comparison between different TMCP grades showed that the S355G10+M has higher resistance to fatigue crack growth in air than the S355G8+M steel grade, especially at lower values of SIF range. However, this advantage diminishes in seawater environments, reinforcing the notion that environmental effects often dominate fatigue crack growth behaviors, overshadowing microstructural benefits. They quantified environmental reduction factors (ERF),

which is the ratio of fatigue endurance in air to that in the marine environment, approximately in the range of 1.5–3.4 with an average of 2.31, and ERF is reduced with increasing SIF range. In other words, seawater nearly doubles the crack growth rates compared to air, depending upon the SIF levels. They also compared their results with BS7910 [33], and concluded that the current BS7910 [33] air curve satisfactorily and conservatively defines the upper fatigue crack growth rate bound for all investigated S355 steels. However, for the seawater, the BS7910 [33] curves are much more conservative for the S355 steels considered in their study. The increase in conservativeness will results in the reduction of the lifespan of OWTs.

Similar conclusions were reached by Saeed et al. [56], who experimentally assessed crack growth rates in welded joints of S355NL structural steel. Their results indicated a clear distinction between short and long crack propagation behaviors in air and seawater. Short cracks in the HAZ exhibited more pronounced sensitivity to seawater compared to air, with crack growth rate even reaching 3.5 at lower ΔK values. This acceleration in crack growth can be attributed to the effects of corrosion in the seawater environment. However, once the crack reaches the long crack region, the ratio of crack growth in seawater to air decreases to 2.2 at the transition point of the two-stage crack growth curve, decreasing further to 1.5 as the notch advances toward fracture. Their findings underscore the importance of capturing both the initiation and propagation phases of cracks in CF assessments. This highlights the inadequacy of single-stage Paris law models, particularly when representing fatigue crack growth in HAZ.

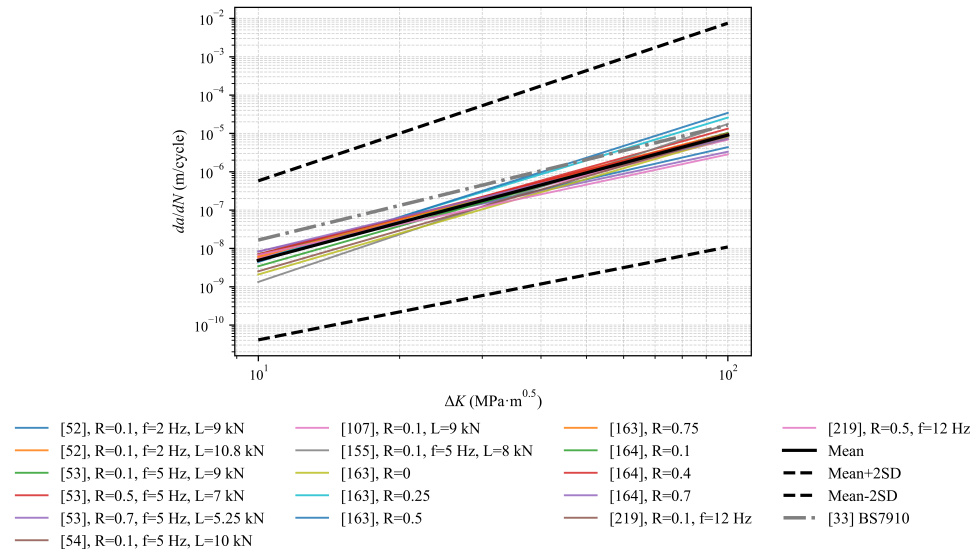

Fig. 2.5 Consolidated Paris law curves for S355 base metal in air. Parameters from literature are plotted as $da/dN = C(\Delta K)^m$. The mean and mean $\pm$ 2SD envelopes are also shown. The BS 7910 lines are shown for reference, but are excluded from the statistics. Legend entries: R (stress ratio), f (frequency in Hz), and L (load applied in kN).

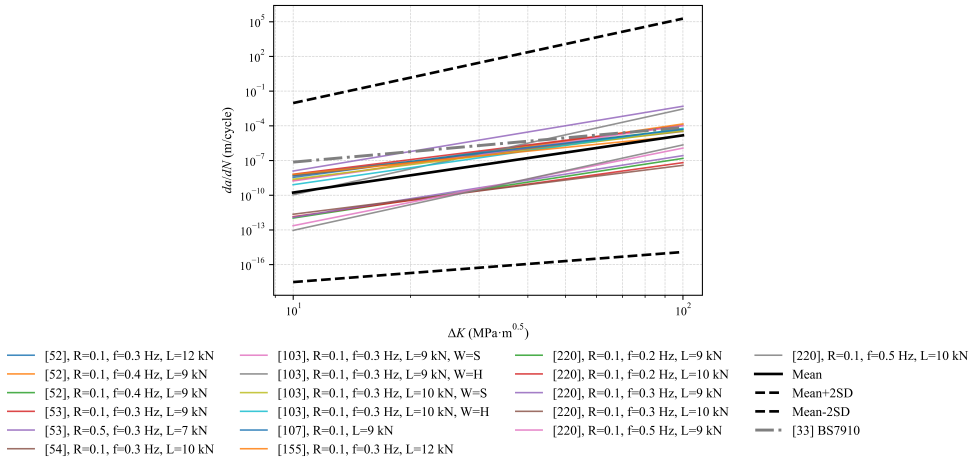

Fig. 2.6 Consolidated Paris law curves for S355 base metal in seawater. Parameters from literature are plotted as $da/dN = C(\Delta K)^m$. The mean and mean $\pm$ 2SD envelopes are also shown. The BS 7910 lines are shown for reference, but are excluded from the statistics. Legend entries: R (stress ratio), f (frequency in Hz), L (load applied in kN) and W (waveform: S = sine, H = hold).

Figs. 2.5 and 2.6 consolidate Paris law parameters available in literature for S355 base metal in air and seawater, respectively, plotted as $da/dN = C(\Delta K)^m$. To provide practical reference curves when project specific data are unavailable, the plots include Mean, Mean$\pm$2SD envelopes. Across both plots the individual literature lines are nearly parallel, indicating broadly similar slopes m, while most of the spread comes from C. In air (Fig. 2.5) the datasets cluster tightly: the Mean curve sits close to the center of the cloud, and the Mean-2SD / Mean+2SD envelopes bracket the vast majority of lines. This compact band reflects the relative insensitivity of crack growth in air to frequency and test details. In seawater (Fig. 2.6) environment the cloud widens and a few steeper lines appear. This is consistent with environmental acceleration and the influence of loading details, such as waveform, and mean stress. The wider scatter indicates that, when project-specific data are unavailable, a larger epistemic margin should be applied to seawater fits.

The BS7910 [33] reference lines tend to sit toward the upper portion of the compiled trends. In air, the BS7910 line generally tracks the upper half of the literature band, typically lying between the mean and mean+2SD envelopes, which is consistent with its intended conservative use. In seawater, the BS7910 line again falls near the upper envelope. For some datasets, it overpredicts relative to contemporary measurements. This is consistent with reports that BS7910 seawater parameters can be markedly conservative for modern S355 grades and test conditions. The figures suggest using the mean curves as representative inputs when no data exist, reserving mean plus two standard deviations (mean+2SD) as an explicit conservative bound, and using the BS7910 line when a standards-based upper bound is required.

Table 2.4 presents the mean and mean+2SD values of crack growth parameters for BM, HAZ, and WM in air and seawater. In air, BM shows compact scatter with a mean of approximately 3.3. In seawater, both the slope and dispersion increase (BM mean of approximately 5.0, with mean+2SD

Table 2.4 Paris law parameters (C and m) for S355 steel in air and seawater environments. Legends: BM- base metal, HAZ- heat-affected zone, WM- weld metal, and SD- standard deviation.

Environment	Location	Number of data	C		m	
			Mean	Mean+2SD	Mean	Mean+2SD
Air	BM	17	2.62×10^{-12}	4.45×10^{-11}	3.27	4.11
	HAZ	11	5.22×10^{-13}	4.36×10^{-11}	3.63	4.81
	WM	5	2.94×10^{-12}	1.37×10^{-10}	3.15	4.13
Seawater	BM	18	1.90×10^{-15}	4.68×10^{-10}	4.95	7.30
	HAZ	5	4.60×10^{-13}	1.50×10^{-11}	4.09	5.15
	WM	2	2.44×10^{-15}	4.39×10^{-15}	5.71	5.73

While using the parameters in $da/dN = C(\Delta K)^m$, units corresponding to da/dn and ΔK are m/cycle and MPa$\sqrt{\text{m}}$, respectively.

reaching 7.3), which is consistent with environmentally assisted acceleration. HAZ and WM exhibit similar trends, but with smaller sample sizes. Their mean + 2SD values should therefore be treated as indicative upper bounds rather than precise design inputs. In practice, the mean values offer representative parameters when project specific data are unavailable. Mean + 2SD provides an explicit conservative option for screening or sensitivity studies, particularly in seawater, where epistemic uncertainty is larger.

In addition to environmental effects, some mechanical factors also influence the CF behavior of OWT monopile foundations. They are discussed in the following sections.

2.6.1 Influence of stress ratio

Mean stress effects on crack growth rates are generally described with respect to the cyclic stress ratios used during testing. The stress ratio (R-ratio), defined as the ratio of minimum to maximum cyclic stress, substantially influences crack growth rates in structural steels exposed to corrosive marine environments. Mean stress, or stress ratio, is a variable that influences the fatigue crack behavior of materials in both air and seawater, but its effect depends on material type, specimen geometry, and loading state [154]. An increase in mean stress typically results in an increase in crack growth rates, but the magnitude of this effect depends on the crack growth region, material, and environment [213]. At lower stress intensity factor ranges in a seawater environment, crack growth rates may be higher, lower, or similar to those measured in an air environment [154]. This also depends on the degree of crack closure imposed at the crack tip, which is influenced by the loading ratio [214]. At increased stress ratios, the influence of seawater on crack growth rates may be significantly greater than in air. This is probably due to a larger crack tip exposure area or crack opening displacement that occurs at higher stress ratios [154]. The effects of mean stress have been studied under different environmental conditions and for various materials [53, 118, 163, 164, 215]. These investigations have revealed a range of crack growth responses with increasing R-ratios.

Thorpe et al. [118] conducted experiments on BS4360 50D steel under free corrosion conditions and observed increased crack growth rates with increasing stress ratio across all ranges of ΔK.

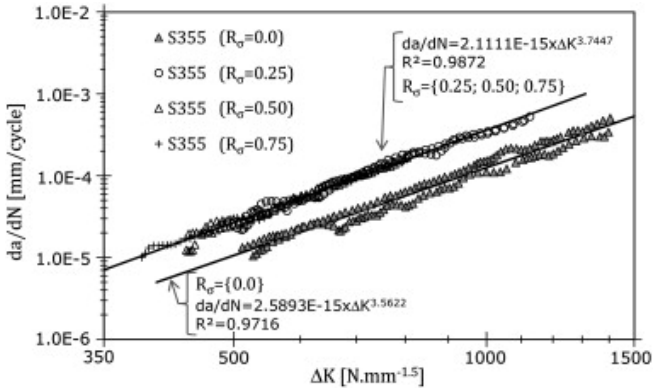

Fig. 2.7 Fatigue crack growth in S355 structural steel in air environment [163].

Additionally, the effect saturated at $R = 0.5 - 0.7$, giving an upper bound of approximately six times the mean crack growth rate observed in air. They also found no effect of stress ratio on crack growth in air. When tested in natural seawater at various electrode potentials, BS4360 50D steel exhibited significant acceleration of crack growth rates at lower stress intensity factor ranges ($\Delta K < 25$ MPa$\sqrt{\text{m}}$) and stabilization at higher ratios ($R \geq 0.5$) [118]. This relationship between R-ratio and crack growth in seawater highlights the critical role of mean stress effects, particularly at low ΔK, where seawater exposure dramatically increases crack growth compared to air.

However, different crack growth behavior has been reported in other studies. The increase in crack growth rate with increasing positive R-ratios tends to be small in the Paris law region [216]. This is confirmed by the results of Appleton [215] on BS4360 50D steel in 3% NaCl solution, which showed no effect of R-ratio apart from experimental scatter. Adedipe et al. [154] suggested that differences in temperature and seawater environment between the experiments may be the reason for the different behaviors reported by Thorpe et al. [118] and Appleton [215].

Recent experiments on modern structural steels such as S355, used in OWT monopile applications, show that crack propagation rates increase as the stress ratio changes from 0 to positive values [163]. Jesus et al. [163] conducted fatigue crack growth experiments on S355 structural steel under four different stress ratios (0, 0.25, 0.5, 0.75). Similar crack propagation rates were observed for all positive stress ratios. The results can be seen in Fig. 2.7. This behavior is consistent with a crack closure effect occurring between $R = 0.0$ and $R = 0.25$. At lower R-ratios, partial crack closure occurs, reducing the effective stress intensity factor range, whereas higher R-ratios sustain fully open crack tips, resulting in higher propagation rates.

Albuquerque et al. [164] performed a detailed study of the influence of stress ratio on fatigue crack growth behavior in S355NL steel, investigating BM, WM, and HAZ using thick compact tension specimens. Experiments were conducted at three stress ratios ($R = 0.1$, 0.4, and 0.7). The results for the BM showed a clear and expected trend: the crack growth rate increased with increasing R-ratio, which is in line with the behavior reported by Jesus et al. [163] for similar steels.

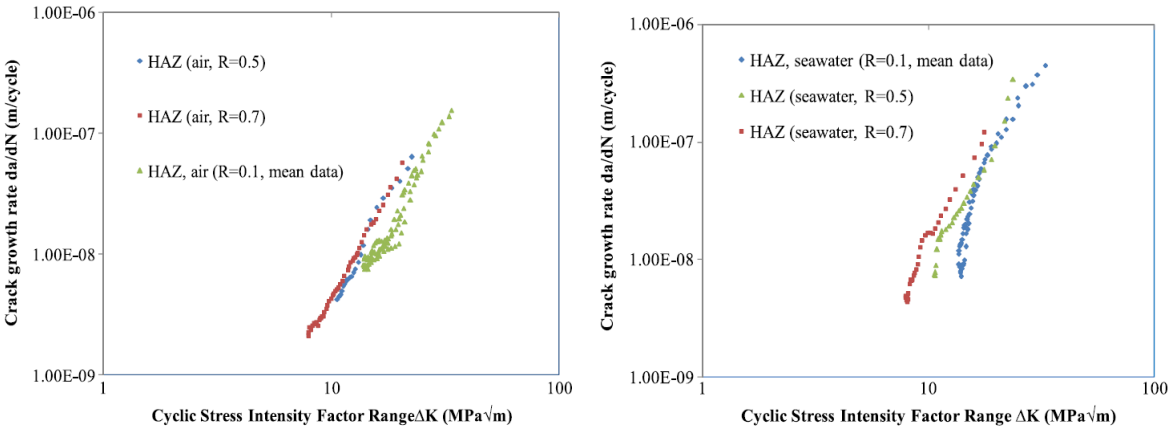

Fig. 2.8 Crack growth rates in heat-affected zone (HAZ) at stress ratios, 0.1, 0.5, and 0.7: (a) in air, and (b) in seawater [53].

However, the WM and HAZ specimens exhibited more complex crack growth behavior, primarily due to the influence of residual stresses. Higher loads were required to propagate cracks in the WM and HAZ compared to the BM during pre-cracking and the initial stages of fatigue tests. Additionally, the da/dN versus crack length curves for WM and HAZ showed a decrease in crack growth rate as the crack length increased under constant amplitude loading in the beginning of the tests. This unusual trend was attributed to residual stress fields, which led to significant crack closure effects, temporarily restricting crack advance.

However, once the opening load and crack closure effects were accounted for—by evaluating the effective SIF range (ΔK_{eff})—the fatigue crack growth rates for WM and HAZ specimens aligned closely with those of the BM. In all material conditions, higher R-ratios ultimately resulted in increased crack growth rates, although the difference between $R = 0.4$ and $R = 0.7$ was relatively small, and closure-corrected data followed the same Paris law behavior.

Experimental work of Adedipe et al. [53] provides valuable insights into how stress ratio (R) and environment interact to influence fatigue crack growth rates in S355J2+N steel, particularly in the heat-affected zone (HAZ). The study systematically compared crack growth rates in air and seawater at R-ratios of 0.1, 0.5, and 0.7, capturing both mechanical and environmental influences. Their results are shown in Fig. 2.8.

It can be seen from Fig. 2.8 (a) that at the lowest stress ratio ($R = 0.1$), the da/dN vs. ΔK curve exhibits a clear bi-linear relationship, with a distinct transition from delayed to accelerated crack growth as ΔK increases. This bi-linear behavior at low R is indicative of significant crack closure effects, where partial closure at the crack tip limits the effective driving force for crack advance, particularly at low ΔK. This phenomenon can also be seen in Fig. 2.7 at low R values. However, as the stress ratio increases to $R = 0.5$ and $R = 0.7$, the bi-linear form disappears and the curves become nearly linear on a log-log scale, indicating that crack closure effects are largely eliminated at higher

R due to greater crack tip opening. Moreover, the crack growth rates at $R = 0.5$ and $R = 0.7$ are very similar, suggesting that once a sufficiently high stress ratio is reached, further increases in mean stress have minimal additional effect on crack propagation in air for HAZ material. Across all tested ΔK values, higher R-ratios lead to moderately higher crack growth rates compared to $R = 0.1$, but typically not exceeding a factor of two. It is also notable that the ΔK range for higher R-ratios is shifted to lower values due to the reduction in load range at increased minimum loads.

Fig. 2.8 (b) shows the influence of stress ratio on the crack growth rate in a corrosive environment. It can be seen that the influence of mean stress on crack growth is amplified by environmental effects. Crack growth rates in free-corrosion seawater are generally higher at increased R-ratios compared to $R = 0.1$, with the most pronounced differences observed in the intermediate ΔK range (13–18 MPa$\sqrt{m}$). In this range, crack growth at $R = 0.7$ is about twice that at $R = 0.5$, and approximately four times greater than at $R = 0.1$. However, at higher ΔK values, the difference between the R-ratio curves diminishes: the $R = 0.7$ curve approaches that for $R = 0.1$, and similarly, the $R = 0.5$ curve converges towards $R = 0.1$. This trend is attributed to the accumulation of corrosion debris within the crack and the increasing rates of material removal by corrosion at high crack opening displacements, which can limit further acceleration of crack growth even under high mean stress. The findings align with earlier observations by Appleton [215], who noted that corrosion products can dominate the crack environment under free-corrosion conditions and restrict the access of seawater to the crack tip.

The synergistic effect of high mean stress and corrosive environment on the crack growth can be seen by comparing both Fig. 2.8 (a) and Fig. 2.8 (b) together. Crack growth rates in seawater at higher R-ratios are significantly elevated across the entire ΔK. Crack growth rates in seawater being two to three times faster than in air for equivalent R values. Notably, the acceleration in crack growth with increasing R is more rapid at lower ΔK values in seawater, reflecting the dominant role of the corrosive environment when the crack is fully open. This environmental enhancement is especially prominent at high mean stress, as increased crack opening displacement allows more aggressive seawater ingress and reduces resistance to crack propagation. As ΔK increases, the difference between air and seawater narrows, but the seawater data consistently remain above the air data for the same R.

Overall, the stress ratio significantly impacts crack growth behavior of S355 steels, particularly in corrosive environments. It must be carefully considered when evaluating fatigue performance and selecting Paris law parameters for design and assessment.

2.6.2 Influence of residual stress

Residual stresses induced by the welding process have a significant impact on both fatigue crack initiation and propagation in structural steels [217]. Xin and Veljkovic investigated the influence of residual stress on fatigue crack initiation in butt-welded plates made of high strength steels [217]. Their results showed that residual stresses affect both the crack initiation location and the overall fatigue behavior of welded plates. Models that included residual stress gave better agreement with fatigue test results than residual stress-free models. The effective value of the stress intensity factor

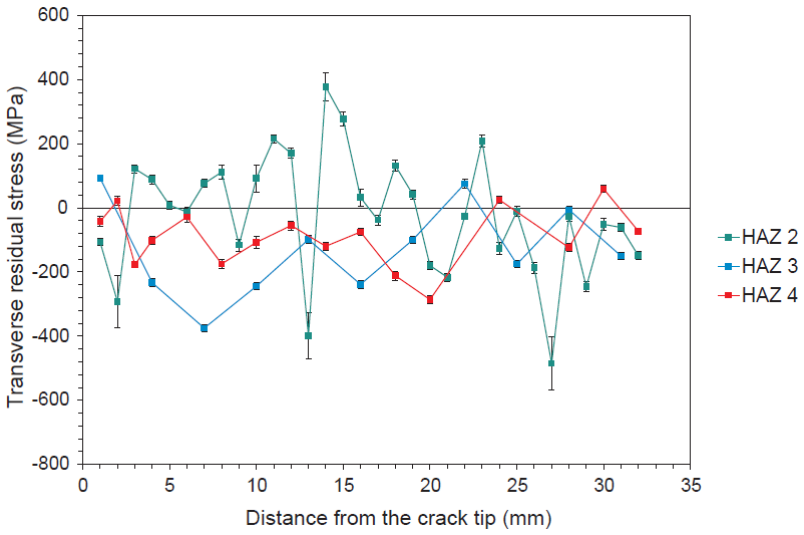

Fig. 2.9 Transverse residual stress in three CT (compact tension) samples along the crack direction before pre-cracking [70].

can differ significantly depending on whether residual stresses are considered [107]. Residual stresses can be either compressive or tensile, and their effects on crack initiation and propagation are different. Compressive residual stresses can slow or even stop fatigue crack growth [218], while tensile residual stresses accelerate crack growth and reduce the fatigue life of the structure.

For relatively thick materials, such as those used for monopile fabrication, both tensile and compressive residual stresses are likely to be present. In these cases, the overall through-thickness distribution of residual stress should be considered when evaluating their effect on crack growth rates [154].

Jacob et al. [71] showed that the longitudinal residual stress in monopile welded plates is much greater—almost seven times higher—than in compact tension (CT) samples. They also reported that the transverse residual stresses at circumferential welds in monopiles can be very large, sometimes approaching the yield strength of the material (see Fig. 2.9). Such high residual stresses can accelerate crack initiation and growth under corrosion fatigue loading. The maximum residual stress after welding may reach the yield strength, and in the worst case, tensile residual stress near the yield point will promote crack initiation, rapid propagation, and even fracture [71].

Fig. 2.9 shows the measured transverse residual stress as a function of distance from the crack tip for three different HAZ samples. It can be seen that the residual stresses at the crack tip are typically around +100 MPa or -100 MPa, with peak values ranging from +400 MPa to -400 MPa. The residual stress is mainly compressive for samples HAZ3 and HAZ4, whereas for sample HAZ2, the residual stress varies between tensile and compressive regions [70].

The measured transverse residual stresses, as shown in Fig. 2.9, can be both compressive and tensile, with values reaching up to +/-400 MPa along the crack path. These results demonstrate that the stress state around welds in monopile structures is complex and can significantly impact crack

initiation and propagation. The results also indicate that small laboratory specimens do not always accurately represent the effects of the larger, more varied residual stresses present in actual monopile welds. This should be carefully considered when using laboratory data to predict the behavior of real structures.

The presence of these residual stresses significantly influences the effective threshold stress intensity factor range and thus affects both crack initiation and early crack growth. Locked-in welding residual stresses and their redistribution during crack growth can alter the stress ratio, mean stress, and the effective stress intensity factor range. Therefore, to properly characterize the fatigue behavior of monopile welded structures, it is important to use realistic residual stress values, which are typically much higher than those found in laboratory-scale CT specimens [71].

Xin and Veljkovic [107] further investigated the effect of weld-induced residual stress on fatigue crack growth in S355 steel. Their numerical results showed that tensile residual stresses significantly increase crack growth rates in both air and seawater. They also found that the crack growth exponent (m) is always higher in seawater, and including residual stresses leads to higher m values. Crack growth parameters based on elastic-plastic fracture mechanics (EPFM), such as the J-integral, crack tip opening displacement (CTOD), and crack tip opening angle (CTOA), are more accurate than those calculated from linear elastic fracture mechanics (LEFM). Their findings highlight the importance of including residual stress effects in fatigue life predictions.

Pedrosa et al. [219] focused on plasticity-induced crack closure and its influence on fatigue crack growth predictions. Using the UniGrow model, which is based on elastic-plastic crack tip stresses and strains, they emphasized the need to use effective stress intensity factors (ΔK_{eff}) rather than nominal values. ΔK_{eff} combines the applied stress intensity factor range (ΔK_{app}) and the residual stress intensity factor (K_r), where K_r is negative for compressive residual stresses. This approach accounts for how reversed plastic deformation changes the relationship between the SIF and the actual stress–strain field. They found that higher applied SIF leads to higher residual stress intensity factors, and higher stress ratios reduce the residual stress intensity factor. Accounting for crack closure explained observed differences in fatigue crack growth rates at different stress ratios under residual stress.

Due to the uncertainties in weld-induced residual stresses, it can be challenging to fully account for their influence on crack growth behavior in welded structures. However, it is crucial to account for the variability and magnitude of residual stresses for an accurate prediction of fatigue life in offshore wind monopile weldments.

2.6.3 Effect of loading frequency

The loading cycle frequency influences corrosion fatigue crack growth. In an inert environment such as air, loading frequency has little to no effect on the fatigue crack growth rate [118]. However, the introduction of a corrosive environment creates frequency sensitivity in many material–environment combinations. Thorpe et al. [118] found that loading at lower frequencies in a corrosive environment

on BS4360 50D steel caused more damage than when the experiment was conducted in air. This can be attributed to the fact that, at lower frequencies, the crack tip is exposed to the environment for a longer time during each loading cycle [52]. In offshore structures, the realistic impact of corrosion on fatigue crack growth is only visible when crack growth tests are performed at sufficiently low frequencies, where time-dependent corrosion mechanisms can meaningfully interact with fatigue processes. Depending on the test frequency, the fatigue crack growth behavior of steel in a marine environment can be dominated by fatigue, corrosion, or a combination of both [220]. At higher frequencies, the influence of corrosion diminishes and crack growth rates converge to those in air [118], whereas at lower frequencies, the corrosive effect becomes more pronounced.

Experimental data from Appleton [215] provide detailed insight into the frequency dependence of crack growth rates under both free corrosion and cathodic protection conditions on BS4360 50D steels used in offshore structures. In tests performed under free corrosion in 3% NaCl, the fatigue crack growth rate (da/dt) increased systematically with frequency across the measured stress intensity factor range (ΔK). At a given ΔK, crack growth rates were highest for tests conducted at 5 Hz, followed by 1 Hz and 0.167 Hz, with the separation between these curves becoming more pronounced at higher ΔK values. This demonstrates that higher frequencies accelerate fatigue crack propagation in corrosive environments, likely due to reduced time for passive film regeneration at crack tip and more persistent mechanical disruption of corrosion products.

The influence of frequency is even more striking under cathodic protection. Appleton's results show that at low frequencies (0.05 Hz and 0.167 Hz), cathodic protection (-1.0 V SCE) is highly effective, suppressing crack growth rates to low values across the ΔK range. However, as frequency increases to 1 Hz and 5 Hz, the protective effect diminishes rapidly, and crack growth rates rise steeply—especially at higher ΔK. At 5 Hz, the growth rates under cathodic protection approach those observed in free corrosion, indicating that at high cyclic frequencies, mechanical and hydrogen-assisted processes can dominate over electrochemical suppression mechanisms. This frequency threshold effect underscores the limited effectiveness of cathodic protection in mitigating corrosion fatigue when rapid cyclic loading is present.

Experimental investigations by Adedipe and Brennan [51] and Adedipe et al. [52] provide further insights into the effect of loading frequency on corrosion fatigue crack growth rates in modern offshore structural steels. Their work on S355J2+N, a widely used offshore wind monopile steel, involved direct comparisons of crack growth rates in air (at 2–5 Hz) and in seawater (at 0.3–0.4 Hz). The results consistently demonstrated that, in air, the fatigue crack growth rate is largely insensitive to the loading frequency across the tested range similar to the results reported by Thorpe et al. [118]. Crack growth curves at 2 Hz and 5 Hz almost perfectly overlapped, confirming that higher-frequency testing in air does not influence Paris law parameters and is therefore suitable for efficient laboratory assessment by reducing the experimental time.

In a corrosive seawater environment, however, crack growth rates were systematically higher—by a factor of approximately two—compared to air at the same ΔK, reflecting the dominant influence of corrosion on crack advance. Nevertheless, when seawater tests were performed at three close

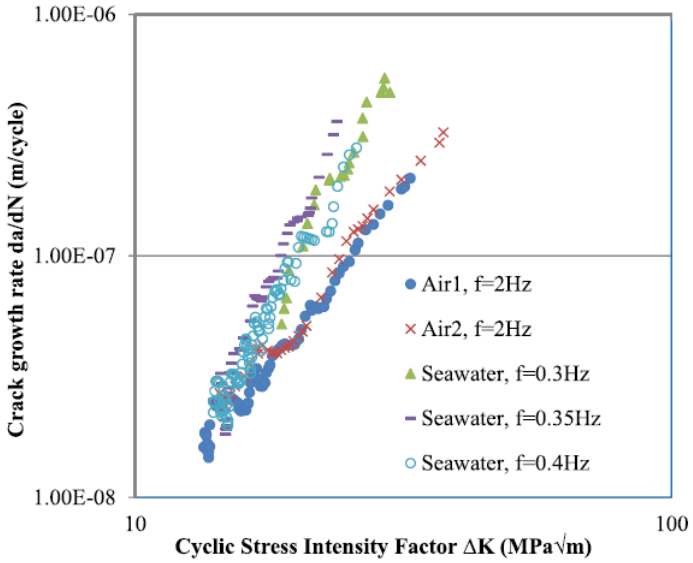

Fig. 2.10 Comparison of fatigue crack growth rate in air and seawater for different frequency of cyclic loads [52].

frequencies (0.3, 0.35, and 0.4 Hz), the crack growth rates showed no consistent trend or substantial frequency sensitivity within this range; all curves closely tracked each other, and the increase in crack growth rate at lower frequencies (e.g., 0.3 Hz vs. 0.4 Hz) was marginal and not systematic. Notably, at low ΔK values (threshold region), crack growth rates in air and seawater were nearly identical, indicating that the environmental effect on fatigue crack propagation is negligible at early stages, but becomes more pronounced at higher ΔK, where corrosion-assisted mechanisms dominate. These results are shown in Fig. 2.10.

These findings are highly consistent with the trends reported by Appleton for BS4360 50D steel [215], where frequency effects on corrosion fatigue crack growth are minimal within practical offshore loading frequency ranges, and environmental influence overwhelmingly governs the fatigue behavior. Both sets of studies underscore that, while environmental exposure accelerates crack growth in marine steels, small variations in loading frequency near typical offshore operational values (0.3–0.5 Hz) have little impact on crack growth rate. This highlights that crack growth models for offshore wind monopiles should focus on environmental and material factors, with frequency only becoming a major parameter when much lower or higher frequencies are considered.

Recently, Igwemezie and Mehmanparast [103] showed the frequency and waveform dependence of CFCG in modern marine structural steels relevant to offshore wind monopile foundations. Their experiments on S355J2+N (normalized-rolled) and TMCP subgrades S355G8+M and S355G10+M under free corrosion in artificial seawater revealed that, within the operational frequency range typical for offshore wind structures (0.2–0.5 Hz), frequency alone exerts little influence on the crack growth rate in the Paris law region. Instead, the waveform of cyclic loading was found to be the important factor. For all frequencies and load levels studied, a constant amplitude sinewave produced

consistently higher CFCG rates than a trapezoidal waveform, even reaching up to a factor of three. This trend was most pronounced at lower frequencies (0.2 Hz) and higher loads, and diminished with increasing frequency or at lower stress intensity factor ranges. They concluded that using sinewave Paris law constants for structural reliability assessment is likely to be a conservative approach for CF life prediction in offshore wind monopile steels.

More recently, Ryan and Mehmanparast [220] performed experiments on S355G10+M in seawater at low frequencies (0.2–0.5 Hz), and found that traditional fracture mechanics parameters such as ΔK, $K_{\max}$ (maximum SIF), or even the J-integral are not sensitive to the small frequency changes relevant for offshore structures. This is because these parameters are cycle-dependent and do not account for the time-dependent nature of corrosion. They introduced new time-dependent parameters—$\Delta\dot{K}$ and $\dot{J}$—which are the time derivatives of the stress intensity factor and J-integral, respectively. When crack growth rates were plotted against these time-dependent parameters, the frequency dependence became much clearer: at lower frequencies, the crack growth rate was higher, and the effect was more evident under higher loading. They further proposed a new model for predicting corrosion fatigue crack growth rates at different frequencies using short-term air data, thus avoiding the experimental challenges of long-duration, low-frequency corrosion fatigue testing. This model, when calibrated, provides a practical and robust approach to incorporate frequency effects in life prediction of OWT steels.

In summary, frequency effects on CFCG in offshore steels are most pronounced at lower frequencies, where corrosion processes can meaningfully interact with fatigue mechanisms. However, within the typical operational frequency range for offshore wind monopiles (0.2–0.5 Hz) [52, 103], the influence of frequency is often less significant than that of the environment and waveform.

Despite recent advancements in the understanding and modeling of fatigue crack growth in offshore wind monopile steels through laboratory experiments, significant gap remains between the experimental results and real world performance. To improve crack growth parameter selection and reduce uncertainty in fatigue life predictions, more experimental data is needed, especially for modern materials and realistic welded geometries subjected to variable loading and harsh environmental conditions. Further research should also address the effects of complex loading spectra, long-term environmental exposure, and the combined effects of residual stress, stress ratio, and corrosion.

2.7 Fatigue loadings

The fatigue reliability assessment of OWT monopile foundations requires comprehensive consideration of uncertainties associated with fatigue loads. Marine structures experience complex and variable loads predominantly induced by wave and wind actions, leading to complicated stress distributions and fatigue damage processes. Accurate prediction and modeling of these stress conditions and associated uncertainties is crucial for reliable fatigue life estimation [221, 222].

Fatigue damage in marine structures, including OWT monopiles, predominantly arises from wave-induced cyclic stresses. Common engineering practice often simplifies the representation of

these stresses using statistical distributions rather than explicit time-domain stress histories. Typically, short-term stress responses under a particular sea state are modeled as narrow-banded Gaussian processes, frequently approximated by Rayleigh distributions, with corrections for wider-banded processes. These short-term distributions aggregate into long-term stress range distributions, typically represented by statistical functions such as Weibull or generalized gamma distributions [223–225].

The prediction of these short-term responses is influenced by multiple uncertainties, including the choice of spectral models, wave scatter diagrams, and heavy weather maneuvering conditions. Long-term wave statistics provided by classification societies, often presented as joint probability distributions of significant wave heights and mean wave periods (wave scatter diagrams), underscore significant variations in fatigue life predictions due to statistical uncertainty. Studies utilizing hindcast data have demonstrated marked variability in crack growth predictions when different wave statistics were employed, highlighting the critical role of statistical uncertainty in stress consideration [179, 226].

OWTs experience dynamic responses that differ significantly from traditional offshore platforms, largely due to additional wind-induced stresses. Studies show that wind-induced cyclic stresses can constitute more than 60% of the fatigue damage in multi-planar tubular joints of jacket-type OWTs, leading to over 7×10^7 stress cycles per year [95]. The dynamic responses of OWT structures necessitate sophisticated coupled hydro-aero-elastic modeling, which can account for complex interactions between wind, waves, and structural vibrations [227].

In practice, offshore structures seldom experience simple constant amplitude loading. Real operational conditions involve spectrum loading with variable amplitudes and sequences, which complicate fatigue assessments. While fatigue crack growth data under constant amplitude loading are essential as reference points due to simplicity and comparability, real-world applications require incorporating load interactions and spectrum loading into fatigue life predictions. Unfortunately, fully capturing these interaction effects in laboratory conditions remains challenging due to practical constraints [154, 228].

Nevertheless, studies indicate negligible load interaction effects in some steel grades, such as ABS EH36, when tested under constant amplitude and spectrum loading conditions. This suggests that, under certain conditions, constant amplitude fatigue data can reliably estimate crack growth behavior [228]. Thus, the literature recommends cautious extrapolation of constant amplitude test results to predict real structural behavior when considering specific material-environment-load combinations.

The representation of long-term loading conditions using probabilistic methods significantly enhances fatigue reliability estimates. Offshore industry standards recommend representing long-term stress ranges using two-parameter Weibull distributions when detailed stress histories are unavailable [32, 93]. The exceedance probability of stress ranges under this method is mathematically defined as:

$$Q(\Delta\sigma) = exp\left[-\left(\frac{\Delta\sigma}{q}\right)^h\right] \tag{2.7}$$

where, Q represents the probability of exceedance of a stress range $\Delta\sigma$, while q and h denote Weibull scale and shape parameters, respectively. This approach facilitates efficient probabilistic fatigue analyses and reliability assessments without the need for resource-intensive numerical simulations [32].

An alternative simplified approach suggested by Eurocode 3 is the equivalent constant amplitude stress range, converting variable amplitude loading scenarios into a single stress range that yields equivalent fatigue life under Palmgren-Miner's rule. This method simplifies the analytical process, making it particularly useful in the absence of detailed loading data, while maintaining a sufficient level of reliability in fatigue predictions [229].

Incorporating probabilistic models for the long-term stress range in fatigue reliability assessments allows systematic consideration of uncertainties in load characterization, structural response, and material fatigue properties. Studies employing these probabilistic methods demonstrate that accurate characterization of long-term stress distributions significantly reduces conservatism in fatigue life predictions, enhancing both safety and economic efficiency in structural designs of OWT foundations [12, 47, 205].

An accurate assessment of the fatigue life of OWT monopile foundations requires detailed load analyses that reflect realistic operational scenarios, such as complex load interactions and variable amplitude effects. These stress conditions, along with factors such as stress ratio, loading frequency, and waveform shape, are critical to fatigue crack growth, particularly in corrosive marine environments. As discussed in the section 2.6, these variables interact with corrosion mechanisms, necessitating the development of modeling approaches that integrate load characterization and material degradation processes.

2.8 Concluding remarks

This paper summarizes the existing knowledge on the corrosion fatigue behavior of OWT monopile foundation steels and emphasizes the need for a better understanding of crack growth behavior in the base metal (BM), heat-affected zone (HAZ), and weld metal (WM) under realistic operational conditions. A key finding from compiling CF crack growth parameters for S355 steels is the significant variation in Paris law constants reported in different studies, often due to variations in microstructure, environment, frequency, stress ratio, residual stress, and testing conditions. Consequently, corrosion fatigue life assessments for monopiles must transition from single "characteristic" values to explicit uncertainty quantification and probabilistic FM analysis. The following conclusions can be drawn from the paper:

- Future corrosion fatigue assessments should prioritize generating crack growth data specific to modern thermo-mechanically processed (TMCP) steels, rather than relying solely on historical datasets, to accurately reflect their improved microstructure and reduce conservatism.

- Due to the observed variability in Paris-law crack growth parameters, C and m should be modeled as random variables with distributions that are conditioned on the material zone (BM/HAZ/WM) and the environment (air/seawater). These distributions should be propagated in probabilistic FM (e.g., Monte Carlo or reliability methods) instead of relying on single upper-bound or mean curves.

- Accurately defining realistic initial crack size distributions, especially for weldments in monopile foundations, remains essential to improve probabilistic fatigue life predictions and reliability-based inspection planning. Use distributions informed by weld defect data and inspection capability (PoD), and adopt EIFS or calibrated "fictitious" flaws when appropriate for aligning FM predictions with observed S-N behavior.

- Analytical solutions for stress intensity factors (ΔK) offer valuable approximations, but advanced numerical simulations combined with surrogate modeling techniques are necessary to realistically capture weld geometry complexities, residual stresses, and interactions between multiple cracks.

- Account for weld-induced residual stresses explicitly. Laboratory CT specimens under-represent the magnitude and through-thickness variability seen in monopiles. Use realistic residual stress fields and, where possible, effective driving forces (e.g., ΔK_{eff}) that reflect crack closure/opening.

- Reflect the predominance of environmental effects at service-relevant frequencies: within 0.2–0.5 Hz, frequency alone often has a minor influence compared to seawater; waveform can matter and should be reflected in parameter selection and uncertainty bounds.

- While laboratory experiments following ASTM guidelines offer valuable benchmarks, significant uncertainty remains about their representativeness to real-world monopile conditions. Designing experiments that incorporate thick sections, realistic weld details, representative residual stresses, corrosive conditions, and multiple surface cracks can help bridge this gap. These experiments can enable the calibration of model-form uncertainty for monopile applications.

Authorship Contribution Statement

Mishael, J: Conceptualization, Methodology, Literature Review, Data Curation, Writing – Original Draft, Visualization. **Morato, P. G.**: Conceptualization, Methodology, Writing – Review & Editing, Supervision **Rigo, P.**: Supervision, Project Administration.

Acknowledgement

The authors gratefully acknowledge the financial support provided by the Belgian Energy Transition Fund (ETF) through the MAXWind project.

Declaration of generative AI in the writing process

During the preparation of this paper, the author(s) utilized ChatGPT, an AI tool developed by OpenAI, to assist in rewriting sentences for enhanced clarity and comprehension. Following the use of the tool, the author(s) thoroughly reviewed and edited the generated content as necessary to ensure its accuracy and alignment with the paper's objectives. The author(s) take full responsibility for the final content of this publication.

CHAPTER 3

NUMERICAL FATIGUE MODELING AND SIMULATION OF INTERACTING SURFACE CRACKS IN OFFSHORE WIND STRUCTURAL CONNECTIONS

Paper 2: Mishael, J, Morato, PG, and Rigo, P (2023). Numerical fatigue modeling and simulation of interacting surface cracks in offshore wind structural connections. *Marine Structures*. 92. 103472. DOI: 10.1016/j.marstruc.2023.103472

Abstract: The structural integrity of marine structures is significantly influenced in many practical applications by their fatigue behavior, especially when dealing with dynamically sensitive structural systems, e.g., offshore wind substructures. The propagation of cracks found in structural components can be estimated through fracture mechanics-based methods, in which the crack growth under cyclic loading is mainly driven by the stress intensity factor (SIF). To simplify the computation of the SIF, closed-form solutions are often suggested in industrial standards, yet their applicability is limited to specific geometries and loading conditions. Overcoming the aforementioned constraints, we propose here a general methodology for numerically simulating the SIF and growth of multiple cracks by computing the SIF of adjacent cracks in an integrated finite element analysis, in which interaction effects are implicitly considered. In our proposed method, the coalescence of bordering cracks is also adequately modeled and fatigue failure is defined based on fracture mechanics principles. With the objective of enabling an efficient SIF computation, we also provide the necessary modeling details for the appropriate implementation of the corresponding finite element analysis. The proposed methodology is then tested and validated in a finite thickness plate under cyclic loading setting, whereas in a more practical case study, we investigate the fatigue analysis of interacting surface cracks in an offshore wind structural connection. The results emphasize the importance of considering interaction effects and crack coalescence when simulating the fatigue evolution of structural details in practical applications, and within the study, specific insights are additionally provided for the fatigue analysis of offshore wind structural components. With respect to the investigated fatigue failure criteria, the results show that a through-thickness limit state might yield slightly conservative fatigue

life estimates compared to the fatigue limit that results when failure is defined based on the material fracture toughness.

3.1 Introduction

The integrity of marine structures, and other engineering systems, is detrimentally affected over the course of their service life by deterioration mechanisms and mechanical stressors. In a harsh marine environment, welding defects steadily propagate under cyclic loading, and fatigue thus becomes a main structural failure mode. In the marine and offshore engineering communities, the fatigue damage is typically quantified through Miner's rule at the design stage [45], and when combined with operational data, damage accumulation computations can also yield remaining life estimates [230, 231]. The aforementioned methods can only be applied to structural details with particular geometries and subjected to loading conditions similar to the experimental test specimens employed for the generation of specific SN curves. In a more general modeling approach, the fatigue life of marine structures can, instead, be estimated through linear elastic fracture mechanics (LEFM). Since the outcome of fracture mechanics analysis corresponds to the crack size, inspection and maintenance strategies can also be informed based on computed crack growth simulations. Specifically, LEFM crack growth rate is mainly driven by the applied cyclic loading and resulting stress field near the crack tip, considering specific crack geometrical details, all analytically cast in a parameter denoted stress intensity factor (SIF) range. Industrial standards recommend modeling crack growth through Paris' law, where the SIF range is weighted with empirically determined parameters in order to compute the crack growth rate [32, 45].

In practical applications beyond idealized geometrical and loading conditions, crack growth simulations demand a more general SIF computation. This has motivated the scientific community into developing SIF solutions and investigating surface crack growth in finite and infinite bodies through both numerical methods and experiments [3, 188, 189, 201–203, 232, 233]. Newman and Raju (N-R) [188], for instance, explore finite thickness plates under tension and provide SIF solutions for a wide range of cracks relying on finite element (FE) simulations. Also based on analysis conducted via finite element method (FEM), the SIF solution for hollow cylinders under tension and bending is introduced by [201] and an empirical solution is proposed by [189] for calculating the SIF of surface cracks in a plate under tension or bending. The reported expression is still widely used in engineering practice due to its simplicity of application. Besides FE simulations, Navid et al. [202] and Kirkhope et al.[203] have developed SIFs for semi-elliptical surface cracks in thick-walled pressurized cylinders relying on boundary integral methods.

Most developed SIF solutions are formulated for single cracks, yet multiple adjacent surface cracks can be often found in typical structural components and interaction effects among them can be experienced depending on their dimensions, geometry, and applied loading. In structures subjected to fatigue and stress corrosion cracking (SCC), interaction effects should be carefully considered [22]. During their evolution, the SIFs associated with multiple contiguous cracks are directly influenced

by the common stress field and lead to crack shapes and growth rates different than those resulting from single crack growth simulations. In some cases, cracks propagating under cyclic loading might coalesce into a single large crack if contiguous cracks are sufficiently close, thus inducing a much faster crack propagation [22]. The SIF and growth of interacting surface cracks have been widely investigated mainly through numerical methods, e.g., FEM [20, 36, 44, 234–236], finite element alternating method [23, 197, 237], body force method [238, 239], and coupled line-spring boundary element method [240]. The objective of some experimental and numerical studies is the investigation of coplanar semi-elliptical crack interaction and coalescence in plate specimens [20, 22, 24, 25], whereas some of them only focus on the interaction of two-dimensional cracks and disregard crack coalescence [241, 242]. In the experiments conducted by Leek and Howard [24], crack coalescence can be observed even if the main objective of the study is the exploration of interaction and growth of coplanar and non-coplanar surface cracks in a plate under tension or bending.

More recently, there has been an increased interest in fatigue crack growth methods for marine structures, needed for the development of rational prognosis approaches [3, 4, 38, 155, 233, 236, 242] as well as inspection and maintenance planning schemes [11–13, 46, 47, 243]. Counting a few exceptions, research studies considering crack interaction effects cannot, however, be easily found [38, 241, 242]. An early investigation conducted by Okawa et al. [241] explored, for example, the propagation of multiple cracks on a three-dimensional stiffened panel, a representative ship structural element, relying on FE simulations along with experiments. More recent experiments, performed by Zhang and Collette [38, 242], include the testing of a hexagonal specimen under tensile load in an effort to reproduce the characteristics of complex marine structures undergoing fatigue degradation, e.g., crack-to-crack interaction, component interdependence, redundant load paths, and non-binary failure states. Note that the aforementioned studies [38, 241, 242] model the crack growth as one dimensional.

With respect to the definition of fatigue failure, the structural integrity assessment of oil & gas pipelines as well as nuclear energy assets has been primarily based on leak-before-break (LBB) analysis [244], evaluating whether a crack is likely to cause a stable detectable fluid leak before resulting in a catastrophic failure [33]. However, a crack subject to cyclic loading can further grow beyond the through-thickness limit. Even if the structural load bearing capacity and strength are severely compromised, additional remaining fatigue life might be still expected and should, therefore, be considered when studying offshore wind structural components [95].

According to the literature survey summarized before, one can conclude that an integrated fatigue analysis capable of accounting for surface crack interaction effects demands a generic modeling approach, especially when dealing with practical engineering applications, e.g., fatigue deterioration of marine and civil structural components. In this work, we propose a general methodology for numerically computing the SIF and growth of interacting surface cracks and we define a fatigue failure criterion stemming from fracture mechanics principles. By evaluating the SIF of multiple cracks in a common finite element model, the applicability of the proposed approach is not limited to specific geometries and loading conditions while the resulting crack growth implicitly considers interaction

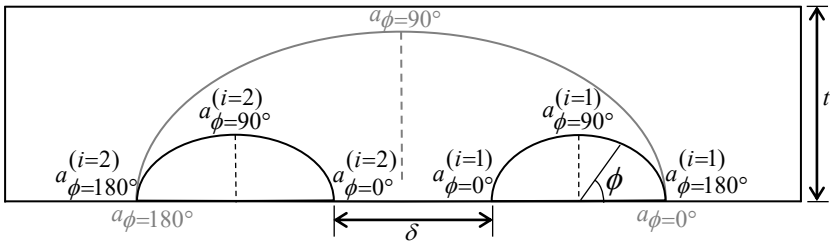

Fig. 3.1 Representation of geometry and nomenclature for multiple and coalesced surface cracks, idealized with a semi-elliptical shape. The distance between cracks and their angular location are denoted as δ and ϕ, respectively. The critical points at the maximum crack depth (i.e., $a_{\phi=90°}$) and length (i.e., $a_{\phi=0°}$ and $a_{\phi=180°}$) are also indicated in the image.

effects. Coalesced cracks, formed from two closely spaced propagating cracks, are also adequately treated in our method. In order to efficiently execute the corresponding finite element analysis (FEA), we additionally provide detailed implementation recommendations, including geometry re-characterization and finite element meshing suggestions. The validity and applicability of the proposed crack growth methodology are thoroughly tested in a finite-thickness plate setting and in a practical case study of an offshore wind structural connection subject to cyclic loading, drawing valuable insights for the modeling and analysis of marine structures. In the conducted numerical experiments, the interaction effects observed in a wide range of explored surface crack geometries are additionally interpreted.

The remainder of the paper is structured as follows: an overview of crack growth theoretical and modeling aspects is provided in Section 3.2, whereas the proposed methodology for numerically simulating the growth of interacting cracks is described in detail in Section 3.3. The definition of the numerical experiments and the discussion of the results can be found in Sections 3.4 and 3.5, for the case of a finite thickness plate and an offshore wind structural connection under cyclic loading, respectively. Finally, concluding remarks are additionally outlined in Section 3.6.

3.2 Fatigue crack growth

3.2.1 Crack growth modeling

Surface cracks are typically irregular with respect to their shape and orientation [24]. However, they can be often assumed for the ease of modeling as semi-elliptical in shape with axes defined according to crack length and depth dimensions, as suggested by industrial standards, e.g., BS7910 [33]. To further illustrate this, Fig. 3.1 depicts the geometry of multiple surface cracks, with each crack front location spanning from 0° to 180°.

As explained in Section 3.1 and suggested in industrial standards [32, 33, 45], the crack growth of offshore structural details can be modeled via Paris' law, as:

$$\frac{da_\phi}{dn} = C_\phi(\Delta K_\phi)^m \tag{3.1}$$

where a_ϕ stands for the crack size at a specific angle ϕ, e.g., depth or length, n corresponds to the stress cycles, ΔK_ϕ represents the SIF range, and C_ϕ along with m stand for material and environmental empirical parameters. Due to the free-surface layer effect [21], caused by the variation of the three-dimensional stress state around the crack tip and resulting in a slower crack growth along the surface direction than in interior crack locations, the specification of equal material constants, C_ϕ, around the crack front may lead to inaccurate results. Also, the influence of the tension-bending aspect ratio should be carefully considered [245, 246]. Focusing on critical crack locations and assuming a semi-elliptical profile, a coupled Paris-based crack growth was proposed by Newman and Raju [189]:

$$\frac{da}{dn} = C_a(\Delta K_a)^m; \qquad \frac{dc}{dn} = C_c(\Delta K_c)^m \tag{3.2}$$

where a and c represent the surface crack depth and length, C_a and C_c correspond to crack growth parameters, ΔK_a and ΔK_c refer to the SIF range at the maximum depth and surface points of a surface crack, respectively. Assuming a semi-elliptical profile is preserved during the crack evolution, it is reasonable to evaluate the SIF and crack growth at critical locations, i.e., maximum depth and surface points, yet the SIF and crack growth can be easily quantified anywhere else through numerical methods. The material constant, C_a, is typically obtained through experiments conducted with standard specimens under preferably plane strain conditions, whereas the constant, C_c, can be computed by following the relation recommended by Newman and Raju [189]:

$$C_c = 0.9^m C_a \tag{3.3}$$

The above-stated relation yields more accurate results than simply establishing $C_c = C_a$ [21]. Note that the reference values for C_a and m can be found in industrial standards, e.g., BS7910 [33]. While conducting a crack growth simulation, one also needs to take into account that a crack propagates only if the SIF range exceeds a certain threshold, ΔK_{th}. This threshold value can be found in industrial standards or can alternatively be determined via experimental tests or numerical simulations. According to Davenport [247], the threshold SIF is defined as a function of the fracture toughness, K_C, maximum SIF, K_{max}, and stress ratio, R, all interconnected through a relationship.

3.2.2 Stress intensity factor computation

In order to compute the crack growth evolution following conventional fracture mechanics principles, one needs to calculate the SIF range, ΔK, analytically defined as:

$$\Delta K = \Delta\sigma Y(a,c)\sqrt{\pi a} \tag{3.4}$$

where $\Delta\sigma$ corresponds to the applied stress range weighted by a factor, Y, so as to account for local geometrical and loading conditions, and specified as a function of both crack depth, a, and crack length, c. Closed-form analytical solutions for computing the SIF range can be found in the literature, yet they are normally applicable only to standardized and idealized crack geometries under simplified loading conditions. For most practical problems, the validity of available analytical ΔK solutions is limited. For instance, a typical closed-form solution applicable for a surface crack in a finite plate subjected to membrane and bending loads is expressed as [32]:

$$\begin{aligned} \Delta K_c &= \Delta\sigma \left[\alpha Y_{\rho c} M_{k\rho c} + (1-\alpha) Y_{bc} M_{kbc}\right] \sqrt{\pi a} \\ \Delta K_a &= \Delta\sigma \left[\alpha Y_{\rho a} M_{k\rho a} + (1-\alpha) Y_{ba} M_{kba}\right] \sqrt{\pi a} \end{aligned} \tag{3.5}$$

where the subscripts ρ and b stand for membrane and bending stress components. The factor α corresponds to the ratio between membrane and total stress and M_k represents the stress magnification factor accounting for the stress concentration due to weld local geometrical effects. The geometric factors $Y_{\rho c}$, Y_{bc}, $Y_{\rho a}$, Y_{ba}, and stress magnification factors $M_{k\rho c}$, M_{kbc}, $M_{k\rho a}$, M_{kba} can be computed through the parametric equations listed in BS7910 [33].

Without being limited to specific crack geometries and/or loading conditions, numerical methods can be instead used for the direct calculation of the SIF range. Indeed, most SIF range closed-form solutions are obtained via FEA [4, 188, 201, 233]. Specifically, the SIF along a crack front can be estimated from the local distribution of stress, strain, and displacements retrieved from FE simulations. For example, Raju and Newman [188] rely on nodal forces normal to the crack plane and ahead of the crack front in order to evaluate the SIF values, whereas Soboyejo et al. [20] estimate SIF at several points surrounding a crack front by applying the principle of virtual work. Accounting for stress singularities, Yoshimura et al. [234] calculate SIFs through the displacement extrapolation method, also incorporating quarter-point finite elements, while other proposed research works rely on the virtual crack closure integral technique [235]. SIF values along the crack front can also be computed through the application of the J-integral approach, leveraging on its path-independent principles and avoiding the modeling of additional quarter-point elements for the simulation of the stress singularity at the crack-tip [21, 36, 44]. Alternatively, SIF values can be calculated via the interaction integral method [248, 249], yielding also more accurate results than stress and displacement extrapolation techniques. Derived from the J-integral, the interaction integral is a two-state integral that combines two admissible solutions (i.e., the actual field and a customary auxiliary field) of a boundary value problem. The reader is directed to [250] for a more complete description of the interaction integral and its application to fracture mechanics problems.

The surface and through-thickness cracks in solid bodies can be modeled via FEM by following multiple strategies and relying on various elements types, e.g., in [44, 197, 201, 233–235, 251]. The application of these modeling techniques for crack propagation applications is, however, challenging due to the fact that the crack geometry must be iteratively re-characterized during the analysis. Addressing the aforementioned concerns, we propose here a versatile and generalized modeling

approach for treating surface crack fronts within a fatigue growth analysis. In terms of implementation, the finite element mesh mainly includes three element types. The crack front region features 15-node quadratic wedge elements formed by the condensation of 20-node quadratic brick elements and surrounded by 20-node quadratic brick elements arranged in a 6-element-thick layer, which are chosen by verifying that at least 6 contours are available for the computation of SIFs. This selection should be conducted based on the results obtained from a sensitivity analysis in which the number of elements along the crack front is systematically modified for a wide range of aspect ratios and relative crack depths. To automatically generate the mesh during the analysis, cracks are embedded in a region with 10-node quadratic tetrahedron elements, whereas linear 8-node brick elements are included elsewhere in the modeled structure. To better capture local geometrical details as well as to yield a realistic deformation, high dimensional elements can be included near the crack front with a relatively fine mesh, while areas far from the crack front can be efficiently modeled with a coarse mesh composed of linear elements. As previously mentioned, the stress state ahead of the crack front causes a free surface layer effect [21]. Generally, the three-dimensional stress state at interior crack front locations can be assumed to be under a plane strain condition, which smoothly transitions to plane stress for points close to the surface. To account for this free surface layer effect, free surface points are hence assumed to be under plane stress, while points located in any other position along the crack front are assumed to be under plane strain.

3.3 Fatigue growth, failure, and coalescence analysis of interacting cracks

3.3.1 Fatigue crack growth modeling of multiple surface cracks

Following the principles described in Section 3.2.1, the crack propagation can still be computed separately for each considered crack front location, even if the corresponding SIFs should be retrieved from an integrated numerical analysis. By assigning each crack with its specific SIF range, the fatigue growth of multiple surface cracks can then be formulated as:

$$\frac{da_{\phi}^{(i)}}{dn} = C_{a_{\phi}} (\Delta K_{a_{\phi}}^{(i)})^m \tag{3.6}$$

where a_{ϕ} represents the crack size along the crack front as a function of the angle ϕ, as shown in Fig. 3.1. The superscript, $i \in \{1,2,...,N\}$, merely enumerates the set of N considered interacting surface cracks. As mentioned in Section 3.2.1, an informative crack growth description can be achieved by focusing on three crack front angles, i.e., inner surface ($\phi = 0°$), maximum depth ($\phi = 90°$), and outer surface ($\phi = 180°$) points. During the geometric modeling of propagating semi-elliptical cracks, one should consider that their combined interaction effect renders different SIFs at each location, e.g., $\Delta K_{a_{\phi=0°}}$ and $\Delta K_{a_{\phi=90°}}$, thus resulting in an asymmetrical crack front shaped as two-quarter ellipses, instead of the conventionally assumed semi-elliptical shape [24]. Moreover, the

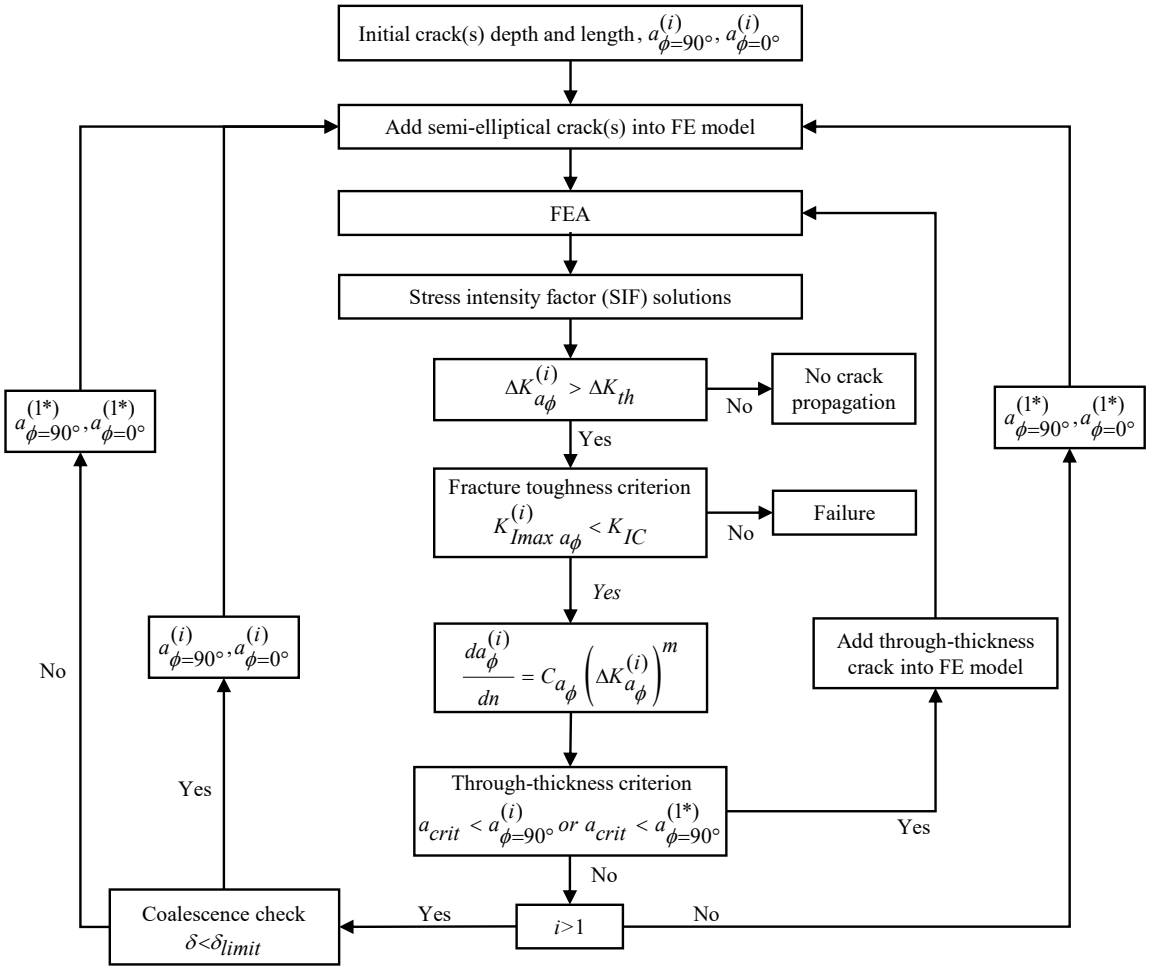

Fig. 3.2 Overarching iterative procedure for numerically computing the stress intensity factor and growth of interacting surface cracks, also considering coalesced cracks and fatigue failure. Note that a re-characterized coalesced crack is specifically denoted as $a^{(1^*)}$.

geometrical description of surface crack fronts should be modified after a coalescence is produced and/or once a crack grows up to the structural detail's thickness. Under applied cyclic loading, adjacent surface cracks propagate closer to each other until, at a certain point, they may coalesce into one larger crack [22]. From that moment, the growth can be modeled as a single coalesced crack [36]. Besides, the crack front should also be adapted when a crack reaches the structural detail's thickness, as previously mentioned. Consequently, the fatigue growth and SIFs must be subsequently recomputed at each time step. Encompassing all the aforementioned remarks, we propose an iterative procedure for modeling fatigue growth of interacting semi-elliptical cracks while also accounting for coalescence and through-thickness propagation. The overarching numerical approach is described in Fig. 3.2.

At the initial stage, crack dimensions and locations, applied stress range and annual stress cycles, as well as crack growth parameters should be specified. Based on the provided initial settings, the finite element model is generated and executed, rendering the SIF at the analyzed crack front points. If the resulting SIF range is above the crack propagation threshold (i.e., $\Delta K_{a_\phi} > \Delta K_{th}$) and if the SIF falls below the fracture toughness-based failure limit (i.e., $K_{Imax a_\phi} < K_{IC}$), the crack propagation is then computed via numerical methods, e.g., Runge-Kutta, according to Eq. 3.6 for multiple interacting cracks, $a^{(i)}$, or according to Eq. 3.2 for a coalesced crack, $a^{(1^*)}$. From there, the iterative loop proceeds again to the finite element model construction step based on the newly calculated crack dimensions, and the crack is further re-characterized if the crack separation distance is below the specified limit (i.e., $\delta < \delta_{limit}$) and/or if a crack depth exceeds the structural component wall thickness (i.e., $a_{\phi=90^\circ} > a_{crit}$). Note that the crack initiation phase is not explicitly considered in the proposed methodology. Typically, offshore wind welded connections do not undergo post-processing treatments [3], and the initial crack sizes found are often large enough to propagate under fatigue [45, 252]. In applications where the crack initiation should be accounted for, the introduced methodology can still be applied for computing the crack growth during the propagation stage. In that case, the crack initiation phase should be estimated separately.

3.3.2 Interaction factor and coalescence of adjacent cracks

When computing the fatigue growth of multiple adjacent cracks, their interaction should be adequately considered within the calculation of the SIF, since a combined behavior may result in either shielding or enhancement effects depending on the relative location and orientation of the analyzed cracks. Formally, the interaction between two cracks can be expressed through a factor, γ, as [44]:

$$\gamma(\phi) = \frac{\Delta K^{\delta}(\phi)}{\Delta K^{\delta=\infty}(\phi)} \tag{3.7}$$

where ΔK^{δ} stands for the SIF range retrieved from a surface crack in which the interaction effect is accounted for, and $\Delta K^{\delta=\infty}$ corresponds to the SIF range resulting from a single surface crack with the same geometry and under the same loading conditions. Evidently, the interaction factor varies along crack front locations, formally described by the parametric angle, ϕ, as depicted in Fig.3.1. The explicit computation of SIFs resulting from multiple interacting cracks can be implemented through the interaction integral method, as described in Section 3.2.2.

Once two adjacent cracks come sufficiently close to each other during their propagation, they may coalesce into a single combined crack, often shaped differently than an idealized semi-elliptical profile. If two semi-elliptical cracks coalesce, the resulting combined crack forms a re-entrant 'dented' portion at the contact point [22]. Due to the higher SIF at the re-entrant crack front points, their growth evolution is substantially faster than anywhere else along the crack front, rapidly leading to a single combined semi-elliptical crack [20, 24]. It is, therefore, reasonable to still model the coalesced crack as a semi-ellipse with geometrical dimensions derived from the interacting cracks before reaching

the coalescence phase. The depth of this newly conceived surface crack can be assumed equal to the largest depth between the two adjacent cracks at the coalescence stage, whereas the crack length can be considered as the sum of their surface crack lengths. Although this geometrical re-characterization might result in an overestimation of the actual crack growth, the simplicity of the proposed approach significantly facilitates the implementation of the crack propagation under interaction while also accounting for a potential crack coalescence. Once the combined crack is re-defined, the fatigue growth of the coalesced crack can still be predicted through Eq. 3.2.

3.3.3 Fatigue failure definition

Through-thickness criterion

A surface crack propagates through the thickness of a structural detail following the minimum release energy path and may ultimately reach its wall thickness, in which case, it is denoted as through-thickness crack. According to industrial standards recommendations [33], the shape of a through-thickness crack can still be assumed semi-elliptical and its growth can be computed via Paris' law (Eq. 3.1), even if its width (minor axis) might be longer than the wall thickness itself. Following a through-thickness criterion, g_{th}, the fatigue failure limit state can be defined as the point in which the crack depth, $a_{\phi=90^\circ}$, exceeds the wall thickness, a_{crit}, formulated as:

$$g_{th} = a_{crit} - a_{\phi=90^\circ} \tag{3.8}$$

The fatigue failure event then corresponds to the probability of the limit state being equal or less than zero, i.e., P $[g_{th} \leq 0]$.

Fracture toughness criterion

While through-thickness cracks exhibit reduced structural capacity, they can still hold significant residual fatigue life [95] and alternative fatigue failure criteria can hence be established. Stemming from fracture mechanics principles, fatigue failure can be defined as the point in which the SIF at the crack tip exceeds the material fracture toughness, K_C, which is specified according to the applied fatigue loading mode(s) and also influenced by the wall thickness. Generally, higher toughness is observed in (thin) specimens under plane-stress whereas (thick) specimens under plane-strain are characterized with lower toughness. In practice, the fracture toughness is conservatively defined as the measured value under plane-strain condition, widely available in industrial standards for fatigue loading mode I, denoted as K_{IC}. Following a probabilistic approach, the fracture toughness can be described as a three-parameter Weibull distribution [253]. As mentioned previously, the failure of a structural detail under applied cyclic stress can be determined when the SIF computed from the maximum stress (σ_{max}) exceeds the fracture toughness, K_{IC}. The maximum SIF, K_{Imax}, varies with respect to specific stress ratios, $R = \sigma_{min}/\sigma_{max}$ (i.e., the ratio between the minimum and maximum

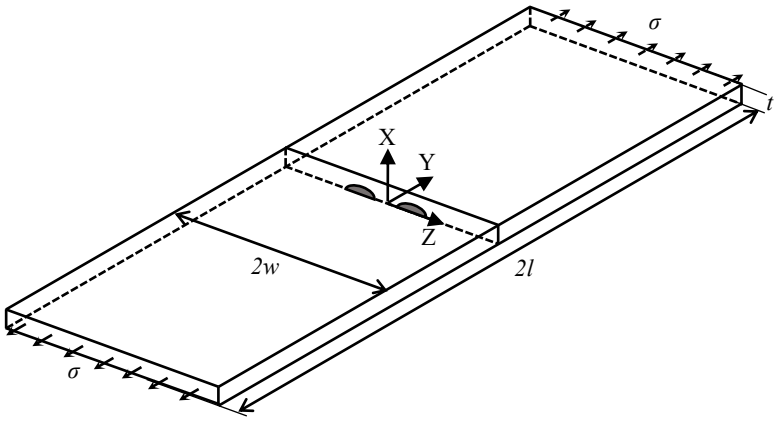

Fig. 3.3 Plate and crack front geometry corresponding to the model implemented in the finite thickness plate setting, also indicating the coordinate system and relevant terminology.

applied stress), and K_{Imax} can then be computed as:

$$K_{Imax} = \frac{\Delta K}{1-R}, \tag{3.9}$$

and the fracture toughness failure limit state can be formulated as:

$$g_K = K_{IC} - K_{Imax} \tag{3.10}$$

3.4 Fatigue analysis and multiple crack interaction in a finite thickness plate

3.4.1 Comparative study of numerically computed stress intensity factors and interaction effects

With the objective of testing the numerical approach proposed in Sections 3.2.2 and 3.3.2, we compute and compare with existing results both SIFs and interaction factors in a finite thickness plate under tension. The definition of the plate geometry is mainly inspired by the work carried out by Coules [44], yet the dimensions of the specimen are intentionally reduced in order to decrease computational requirements. Specifically, the plate is modeled with thickness, $t = 1$ mm, width, $2w = 500$ mm, and total length, $2l = 800$ mm, along the tensile loading direction, as shown in Fig. 3.3. All studied cracks are assumed semi-elliptical in shape and are subjected to 1 MPa tensile load. Additionally, the material parameters are listed in Table 3.1, where the crack growth parameters are directly taken from published fracture mechanics standards [33]. In future research directions, the proposed crack growth methodology could be cast in a probabilistic approach, in which the crack growth parameters

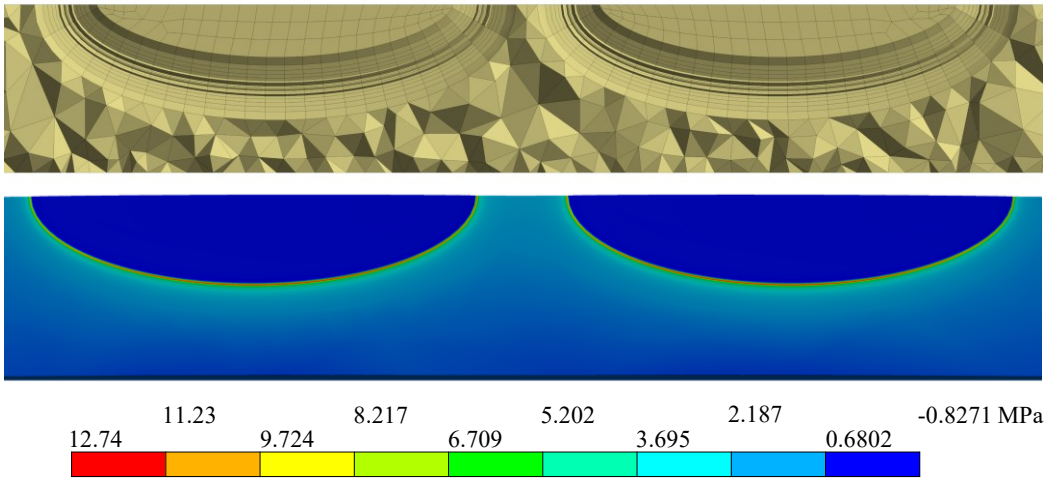

Fig. 3.4 Graphical representation of the crack front finite element mesh (top) and stress field results, σ_Z, (bottom) corresponding to a typical simulation from the finite thickness plate case study. In this particular case, the plate is subjected to a tensile loading of 1 MPa.

can be carefully calibrated following a reliability-based comparative analysis or defined based on experimental tests.

With respect to the implemented finite element settings, the full plate featuring two semi-elliptical cracks is modeled, and to minimize computational time, fine elements with a size of approximately 1 mm are meshed near the crack tip region, whereas coarser elements ranging from 1 mm to 25 mm are meshed elsewhere. For illustration purposes, a reproduction of the crack fronts generated mesh as well as the corresponding stress field are shown in Fig. 3.4. Further finite element modeling details are explained in Section 3.2.2. In the first comparative analysis, we examine the SIFs at the surface ($\phi = 0°$) and deepest ($\phi = 90°$) points of a semi-elliptical crack with varying a/t ratio and constant, $a/c = 0.4$. In Fig. 3.5, the obtained results are represented along with the empirical solutions and finite element results reported by Newman & Raju (N-R) [188, 189]. Note that SIF solutions for semi-elliptical cracks in finite thickness plates are presented by [188] and [189] as normalized SIF values, $K_I/(\sigma\sqrt{\pi a/Q})$. To enable a direct comparison, the retrieved SIFs are equally normalized with respect to $(\sigma\sqrt{\pi a/Q})$, where Q stands for the shape factor of an ellipse, calculated as the square

Table 3.1 Material and crack growth parameters considered in the finite thickness plate numerical experiments.

Parameter	Value
Young's modulus, E	210 GPa
Poisson's ratio, ν	0.3
C [1]	$3.318 \cdot 10^{-12}$ [24]
m	3.056 [24]

[1] The units corresponding to da/dn and ΔK are m/cycle and MPa$\sqrt{\text{m}}$, respectively.

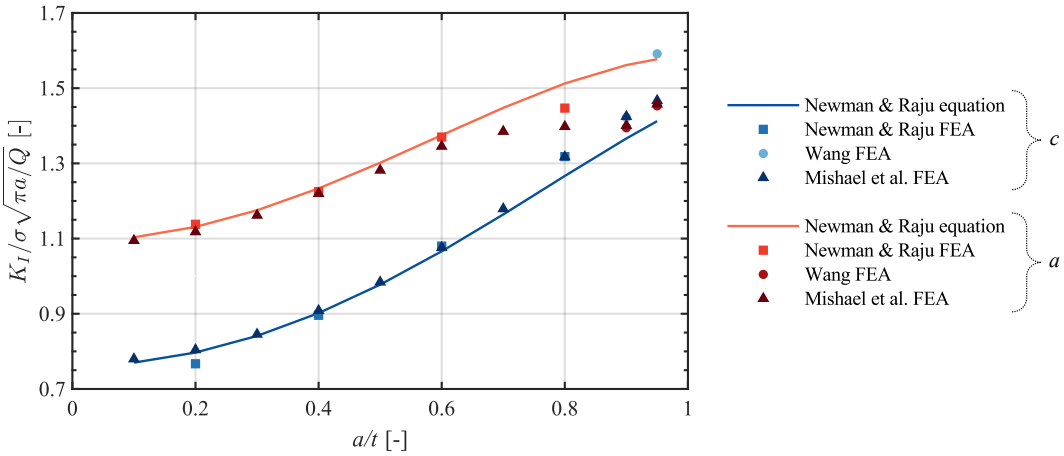

Fig. 3.5 Comparative analysis of calculated stress intensity factors in a finite thickness plate under tension, contrasting the results obtained with the proposed numerical approach against published empirical and finite element solutions [188, 189, 232]. The normalized stress intensity factor, $K_I/(\sigma\sqrt{\pi a/Q})$, is represented as a function of the crack depth by thickness ratio, a/t, at the critical crack front points a and c of a semi-elliptical surface crack with a crack depth by length ratio, $a/c = 0.4$.

of the complete elliptic integral of the second kind [189]:

$$Q = 1 + 1.464\left(\frac{a}{c}\right)^{1.65} \quad \text{for} \quad \left(\frac{a}{c}\right) \leq 1 \tag{3.11}$$

The results show that the SIFs computed from the numerical simulations are in good agreement with Newman & Raju empirical solutions and finite element-based results, except for points characterized with large a/t ratios. This discrepancy can be attributed to the limited applicability of N-R empirical solutions for a/t greater than 0.8. To further verify the computed SIFs, the results are also compared with the SIFs retrieved by Wang [232] through three-dimensional FEA for deeper cracks ($a/t = 0.9$ and $a/t = 0.95$). In this case, the difference between the compared normalized SIFs is very small, as shown in Fig. 3.5. Besides noticing that SIFs increase for higher a/t ratios, one can also observe that N-R empirical solution yields higher SIFs for deeper crack locations and lower SIFs for surface points.

Considering now the interaction effects of identical semi-elliptical cracks, we study and compare the interaction factors retrieved from our numerical simulations against the work conducted by Coules [44]. As seen in Fig. 3.6, the compared interaction factors are overall in good agreement, with an error below 1.7% in all considered settings. Based on the reported interaction factors, one can also conclude that the SIFs along a crack front will not be symmetrical. Besides, the interaction factor is very sensitive with respect to the crack separation at the inner surface point ($\phi = 0°$), yet this effect is almost negligible at the outer surface point ($\phi = 180°$). And, as expected, there always exists more

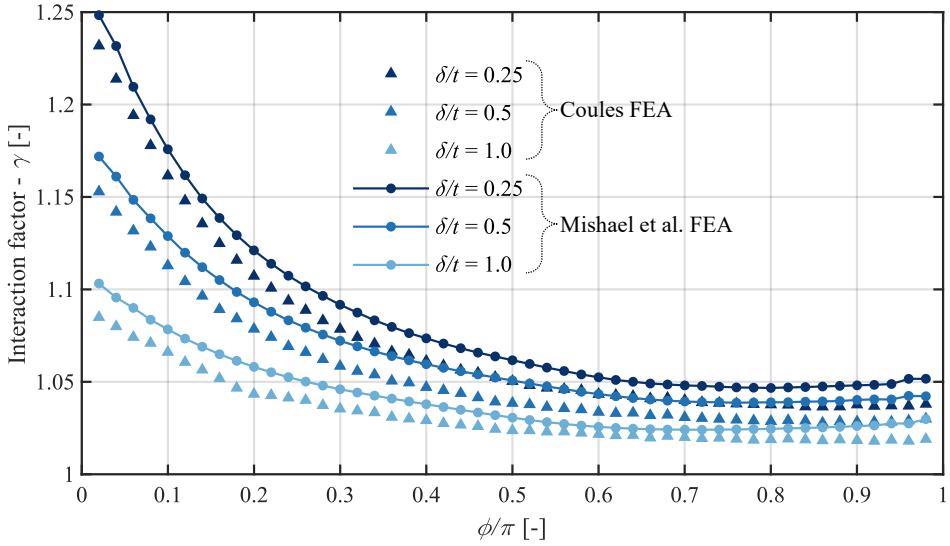

Fig. 3.6 Comparative study of crack interaction factors retrieved from the proposed numerical method and those published in the literature [44], all investigated in a finite thickness plate under tension. The interaction factor, γ, is represented as a function of the crack angular location, ϕ, for a set of crack separation distance by thickness ratios, δ/t, a constant crack depth by length ratio, $a/c = 0.4$, and a fixed crack depth by thickness ratio, $a/t = 0.5$.

interaction at the inner surface point than that at the deepest and outer surface points, with generally higher interaction factors for short crack separation distances.

3.4.2 Fatigue crack growth of multiple interacting surface cracks

In order to verify the proposed methodology for fatigue growth of multiple interacting cracks (Section 3.3.1), an additional numerical experiment is conducted here in a plate subjected to tensile loading, testing various crack front settings and comparing the results with experiments reported in the literature. In this case, the plate geometry and experimental crack growth conditions are modeled following Leek and Howard [24], whose work also examines the fatigue crack growth of interacting surface cracks in a finite thickness plate under tensile, as well as bending loading. In particular, the dimensions of the plate are specified with thickness, $t = 20$ mm, width, $2w = 100$ mm, and length, $2l = 580$ mm. Both modeled surface cracks are assumed equal and with a semi-elliptical shape, and a 100 MPa tensile load with a stress ratio, $R = 0.2$, is applied to the plate, following Leek and Howard's [24] experiments. For convenience, crack geometrical parameters are reported via non-dimensional numbers, i.e., crack aspect ratio (a/c), relative crack depth (a/t), and distance between cracks (δ/t). The material and crack growth parameters specified in the simulations are tabulated in Table 3.1, which correspond to A508 steel exposed to air, and the finite element model is meshed following the same considerations as those described for the SIF comparative study. Note that Leek and Howard [24] considered equal growth parameters for crack length and depth, i.e., $C_c = C_a = C$.

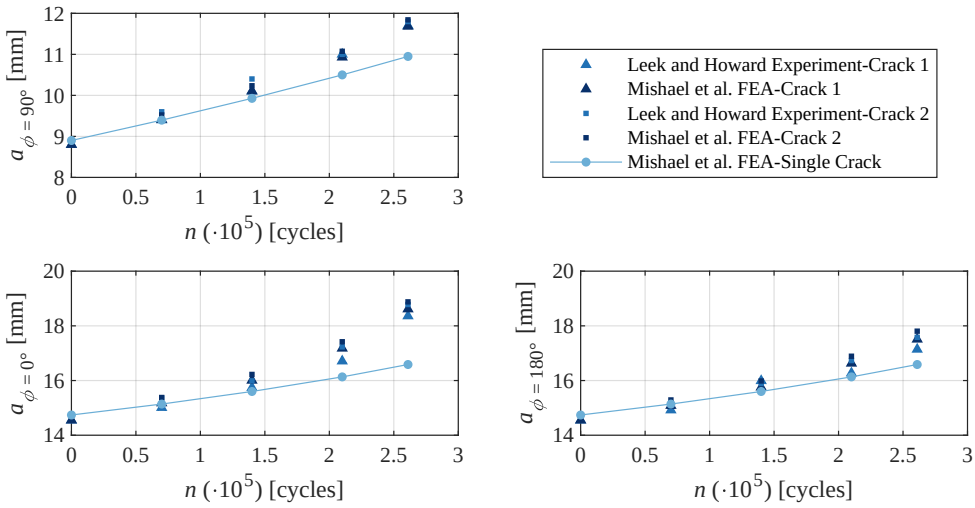

Fig. 3.7 Comparative analysis of fatigue crack growth predictions retrieved from a single semi-elliptical crack and two interacting semi-elliptical cracks in a finite thickness plate, comparing the crack growth estimated by the proposed numerical method with results reported in the literature [24]. Specifically, the fatigue crack growth evolution is represented as a function of the applied stress cycles for the critical crack front points, $a_{\phi=0^\circ}$, $a_{\phi=90^\circ}$, and $a_{\phi=180^\circ}$.

The fatigue crack evolution corresponding to our proposed numerical approach and the experimental dataset reported by Leek and Howard [24] is represented in Fig. 3.7. In the illustration, the crack growth is studied at the crack depth, $a_{\phi=90^\circ}$, along with the inner and outer surface points, $a_{\phi=0^\circ}$ and $a_{\phi=180^\circ}$, resulting from two interacting surface cracks. As observed in the comparative figure, a good agreement is reached between the crack growth evolution resulting from the proposed numerical approach (Section 3.3.1) and existing experimental results, with an error less than 3% in all examined settings.

Furthermore, the fatigue crack growth of a single semi-elliptical crack is also illustrated in Fig. 3.7 so as to directly observe the consequence of neglecting combined interaction effects. As shown in the figure, disregarding the influence of a nearby crack induces a discrepancy in the resulting crack growth evolution, especially at the inner surface point. As explained previously, the crack interaction will render two distinct SIFs at the inner and outer surface points, which in turn, leads to a different crack growth evolution at those points, and hence the surface crack geometry might no longer hold an idealized semi-elliptical shape [24]. Note that in order to simplify the fatigue crack growth analysis, the surface cracks are here re-characterized as semi-elliptical cracks.

3.5 Fatigue analysis of interacting surface cracks in offshore wind structural connections

The goal of this practical case study is to apply the proposed methodology for modeling the fatigue evolution of interacting surface cracks in offshore wind structural connections, demonstrating the importance of adequately considering the combined crack interaction effects when analyzing the fatigue deterioration experienced by a structural detail. Similar to the previous case study, a set of semi-elliptical crack geometries and configurations are here analyzed, all of them categorized through non-dimensional parameters, i.e., a/c, a/t, and δ/t.

3.5.1 Case study definition

Monopile geometry, material and crack growth parameters

Adhering to marine structural design practices [4], the studied 30-m monopile substructure is assumed to be installed over a water depth of 20 m with outer radius, $r_{out} = 3$ m, and wall thickness, $t = 100$ mm [254]. During the manufacturing process of a monopile substructure, cylindrical steel plates ('cans') are usually assembled along the longitudinal direction. In this case, the monopile substructure consists of five cylindrical steel plates, each with a length of 6 m. The examined structural detail corresponds to the monopile circumferential connection located at a distance of 12 m from the seabed. In the experiments, the monopile substructure material is specified as S355 structural steel, a widely used material in the offshore wind industry [155]. All material properties are further tabulated in Table 3.2. Note that a service life of 20-25 years is typically considered for offshore wind substructures [230, 255].

In agreement with defects commonly found on marine welded structures [101], the initial crack depth is assumed as $a_{\phi=90^\circ} = 0.3$ mm, with an aspect ratio, $a/c = 0.4$ [4]. The initial crack dimensions can also be determined based on a calibration process where the structural reliability results are aligned with those obtained from a corresponding Miner's rule analysis [12, 32]. In the numerical experiments, the separation between cracks is considered as $\delta/t = 0.01$ with the exception of a setting in which the separation is modeled as $\delta/t = 0.5$, in order to observe the behavior exhibited by non-interacting cracks. In terms of crack growth parameters, the simplified Paris-law constants recommended by BS7910 [33] for base metal (BM) in seawater are selected for the conducted crack growth simulations, since the investigated cracks are located at a depth of 8 m from the mean sea level, as explained previously. The crack growth parameters can alternatively be specified according to a calibration study with the objective of reaching similar structural reliability estimates as those resulting from a corresponding Miner's rule analysis [12, 32]. Note that industrial standards also account for corrosion-related effects by suggesting specific crack growth parameters for either air or seawater environments. Also following industrial recommendations [33, 253], the fracture toughness is specified as $K_{IC} = 35$ MPa$\sqrt{\text{m}}$ and the threshold SIF range, ΔK_{th}, is specified as zero, which corresponds to the standardized

Table 3.2 Material and crack growth parameters considered in the offshore wind structural connection setting.

Parameter	Value
Young's modulus, E	210 GPa
Poisson's ratio, ν	0.3
C_a [1,2]	$2.3 \cdot 10^{-12}$ [33]
m	3 [33]
K_{IC}	35 MPa$\sqrt{\text{m}}$ [253]

[1]The units corresponding to da/dn and ΔK are mm/cycle and MPa$\sqrt{\text{mm}}$, respectively.
[2]The value corresponds to an upper bound on the stated crack growth parameters.

value for BM and heat-affected regions on a free-corrosive seawater environment. All relevant crack growth parameters are listed in Table 3.2.

Finite element model

Avoiding boundary effects on the computed SIFs, the FE domain comprises the 30-m examined monopile, modeled as a single cylindrical structure. To speed up the simulations and adequately define the studied crack growth geometries, the model is divided into six distinct mesh regions. Longitudinally, the monopile includes 3 mesh regions spanning over 0-11 m, 11-13 m, and 13-30 m, respectively, as shown in Fig. 3.8(a). Additionally, the previously defined longitudinal regions are split vertically into two areas bounded by an XZ plane. Following the recommendations provided in Section 3.2.2, three element types are selected for generating the FE mesh, with elements size varying from 0.01 m near the crack front location to 0.25 m elsewhere. Specifically, regions far from the crack front (e.g., 0-11 m and 13-30 m half-cylindrical sections) are meshed with 8-node linear brick elements, whereas the half-cylindrical section where the crack is located is meshed with 10-node quadratic tetrahedron elements, as shown in Fig. 3.8(b).

With the assistance of the semi-elliptical crack object available on ANSYS' fracture module package [256], the surface cracks are adequately modeled. In this case, the crack fronts are meshed with 15-node quadratic wedge elements, resulting from a previously executed condensation process, and surrounded by a layer of 6-element-thick quadratic brick elements characterized by 20 nodes. In this study, specific details on the weld geometry and residual stress effects are not incorporated into the finite element model, as such details might not always be available to the designer/analyst. After two cracks coalescence, they are replaced by a single semi-elliptical crack with their combined geometrical properties, and if a semi-elliptical crack reaches its wall thickness, it is then re-characterized as a straight through-thickness crack, yet is meshed with a reduced number of crack front elements. For illustration purposes, the cross-sectional view of two examined semi-elliptical cracks is displayed in Fig. 3.8(c). To compute the SIF, the FE solver carries out an integration via the interaction integral method over the ring of elements (contours) that enclose the analyzed crack front. Since numerical

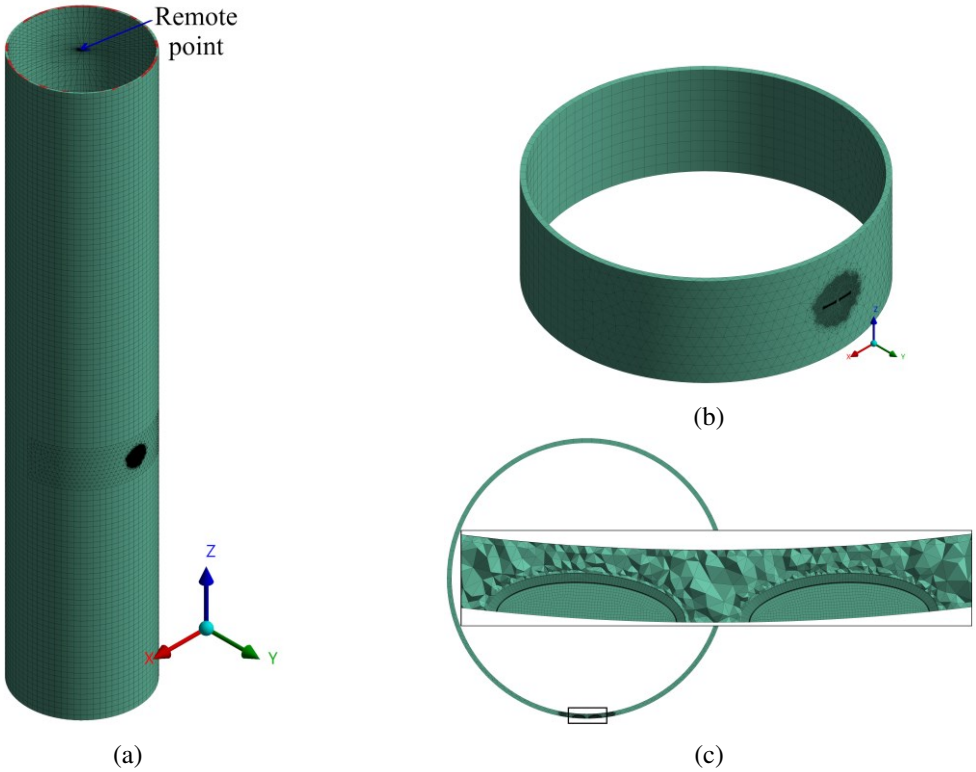

Fig. 3.8 Graphical representation of the finite element mesh generated for the investigated offshore wind substructure with particular focus on: (a) full monopile model, (b) crack fronts surrounding region, and (c) cross-sectional area showcasing the finite element types selected for modeling the examined adjacent semi-elliptical cracks.

variations can be expected in resulting SIF solutions when a limited number of contours is considered, six contours are here selected for the evaluation of SIFs based on the results observed in an additionally conducted convergence analysis.

Loading and boundary conditions

The investigated surface cracks are analyzed under mode I fracture mode, being a critical fatigue failure mode experienced by offshore wind structural components. A bending moment, induced in practice by wind and wave combined loads, is thus applied at the top of the FE model through a coupled remote point that conveys the applied bending moment to all connected FE nodes via multi-point constraint (MPC) equations, as can be seen in Fig. 3.8(a). Following industrial standard recommendations [45], the considered long-term stress range is described by a two-parameter Weibull distribution, here assumed with scale parameter, $q = 9.29$, and shape parameter, $h = 0.8$. With the objective of reducing the computational effort involved in crack growth simulations, the expected value of the long-term stress range distribution can be directly specified in the considered crack propagation law, corresponding in this case to a stress range of 10.5 MPa. This approach yields an

estimation of the expected crack growth over a certain period of time. By following this scheme, potential overloads and/or other load sequence effects are, however, not accounted for. In future research works, the effect of this simplification in terms of accuracy and computational requirements could be further investigated. It should be noted that the specified stress range will not yield a fatigue life in agreement with the one that would result from a Miner's rule damage accumulation analysis defined as a function of the long-term Weibull distribution. Alternatively, one can also calculate and rely on an equivalent damage stress range, i.e., a constant-amplitude stress range that yields the same fatigue damage as when considering the long-term stress range distribution.

The above-mentioned loading is applied to the analyzed monopile circumferential weld ring, whereas a set of corresponding stress ratios, R, is also studied. This specified stress range is in line with values reported in the literature based on wind and wave collected data from a monitored offshore wind farm located in the North Sea [7]. To further simplify the FE computation, the monopile structure is assumed fixed to the seabed by restricting in the model all degrees of freedom at the bottom. The combination of the selected clamped boundary condition and the applied bending moment produces a crack-opening effect on the studied structural details.

3.5.2 Results and discussion

Comparative study: single crack SIF solutions

In this setting, we compare the SIF solutions resulting from our proposed numerical approach with the results published by Bocher et al. [233], all calculated for a semi-elliptical surface crack in a monopile substructure under bending. On the left side of Fig. 3.9, the normalized SIFs are showcased for a semi-elliptical crack with aspect ratio $a/c = 0.4$ and varying a/t ratios, which correspond to monopile dimensions $r_{out}/t = 30$. The results from the analysis indicate a good agreement between both compared SIFs with a mean error of 1.5% and a maximum error of 2% for all tested a/t values. In the figure, one can also observe that the highest SIFs result from deep crack points for all examined a/t values, whereas SIFs are generally higher with increasing crack depths for both $a_{\phi=0^\circ}$ and $a_{\phi=90^\circ}$ points.

An additional configuration is investigated here for a monopile substructure with wall thickness, $t = 75$ mm, that corresponds in this case to $r_{out}/t = 40$, and the retrieved SIFs are also compared with those reported by Bocher et al. [233]. The normalized SIFs at the deepest and the surface points for a semi-elliptical crack with relative crack depth, $a/t = 0.2$, and varying a/c ratios are represented on the right side of Fig. 3.9. Also in this case, both compared SIFs are in overall good agreement, except for a few surface crack points with configuration $a/c > 0.6$, where a slight discrepancy can be observed. These results are reasonable since a similar trend is already reported by Raju and Newman [201] for surface cracks in pipes subjected to bending loading.

A closer inspection of Fig. 3.9 reveals that, at the specific setting $a/c = 0.4$ and $a/t = 0.2$, SIFs slightly decrease for lower outer radius to thickness ratios. This can be generally attributed to a structural strength reduction with decreasing outer radius-to-thickness ratio, r_{out}/t.

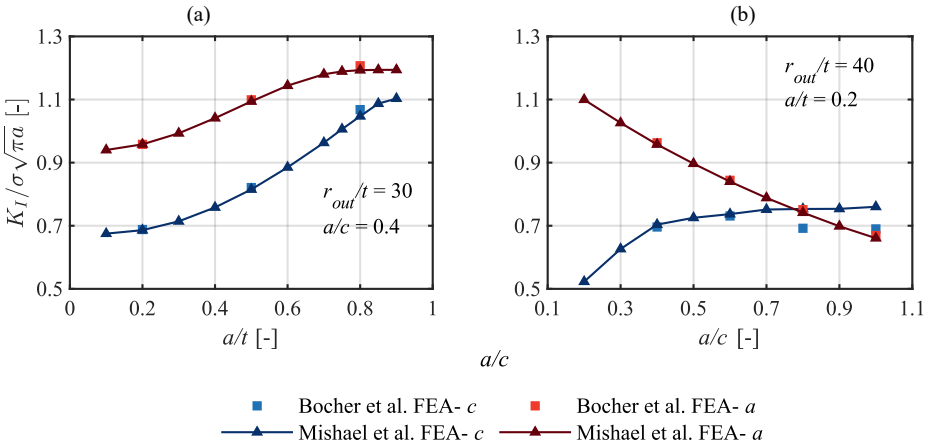

Fig. 3.9 Comparative study of stress intensity factors computed for a monopile substructure at critical crack front points, c and a, benchmarking the values estimated with the proposed numerical method against those published in the literature [233]. The normalized stress intensity factor, $K_I/(\sigma\sqrt{\pi a})$, is investigated in two different settings: (a) semi-elliptical crack with varying crack depth by thickness ratio, a/t, and featuring a crack depth by length ratio, $a/c = 0.4$, and outer monopile radius by thickness ratio, $r_{out}/t = 30$, and (b) semi-elliptical crack with varying crack depth by length ratio, a/c, and featuring a crack depth by thickness, $a/t = 0.2$, and outer monopile radius by thickness ratio, $r_{out}/t = 40$.

Crack interaction effects

In this study, the interaction effects on a pair of interacting surface cracks in a monopile substructure are investigated. The interaction factor, γ, along the crack front of two semi-elliptical surface cracks is shown in Figs. 3.10(a) and 3.10(c), whereas Figs. 3.10(b) and 3.10(d) showcase the interaction factor for semi-circular cracks. At the outer surface and deepest points, the interaction factor is not significantly influenced by the distance between surface cracks, δ, while the interaction factor at inner surface points clearly increases for lower δ. Specifically, the interaction factor at the inner surface point is approximately 30% higher when δ/t decreases from 2 to 0.10, yet the interaction factor for the same case only increases around 5.4% and 4.4% at the deepest and outer surface points, respectively.

One can additionally observe in the figures that the maximum interaction factor can be found at the inner surface point and decreases along the front for cracks with aspect ratio $a/c = 0.4$, whereas the lowest interaction factor can be seen at the deepest point for cracks with an aspect ratio of 1.0. This can be explained by the higher interaction experienced at the outer semi-circular crack points, $a/c = 1$, and considering that inner and outer surface points are closer than for the case of semi-elliptical cracks with aspect ratio, $a/c = 0.4$. Due to the resulting higher SIFs in deeper cracks, one can also notice that higher interaction factors can be found for increasing crack depth ratios, a/t, for all tested points along the crack front.

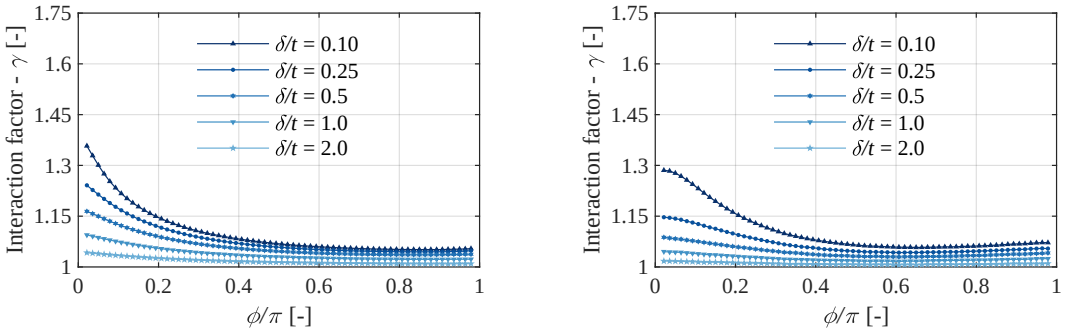

(a) $a/t = 0.5$ and $a/c = 0.4$ (b) $a/t = 0.5$ and $a/c = 1.0$

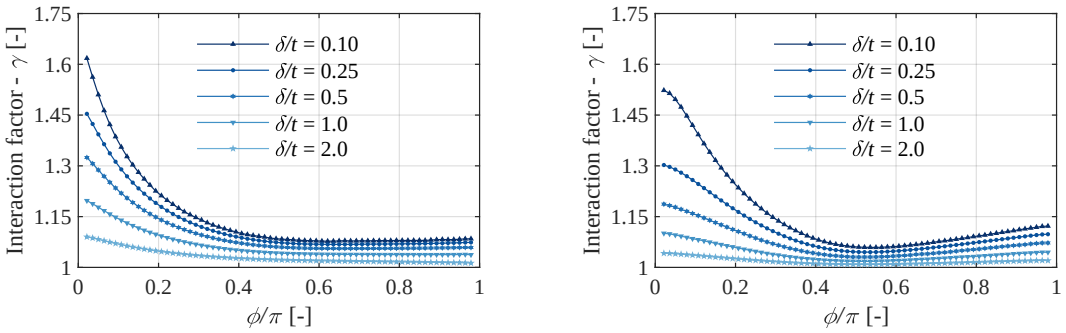

(c) $a/t = 0.8$ and $a/c = 0.4$ (d) $a/t = 0.8$ and $a/c = 1.0$

Fig. 3.10 Systematic investigation of the interaction effects observed on a pair of surface cracks in an offshore wind structural connection. The interaction factor, γ, is represented as a function of the angular ratio, ϕ/π, for varying crack separation distance by thickness ratio, δ/t, in four settings: (a) semi-elliptical cracks with aspect ratio, $a/c = 0.4$, and crack depth by thickness ration, $a/t = 0.5$, (b) semi-circular cracks with aspect ratio, $a/c = 1$, and crack depth by thickness ration, $a/t = 0.5$, (c) semi- elliptical cracks with aspect ratio, $a/c = 0.4$, and crack depth by thickness ration, $a/t = 0.8$, and (d) semi-circular cracks with aspect ratio, $a/c = 1$, and crack depth by thickness ration, $a/t = 0.8$.

Fatigue growth analysis of multiple interacting surface cracks

In this final analysis, we investigate the fatigue growth of two identical interacting surface cracks in a circumferential connection of an offshore wind monopile substructure. Following the methodology proposed in Section 3.3, the fatigue evolution, coalescence, and failure of two interacting surface cracks are numerically computed. As explained in the theoretical sections, the interacting cracks are replaced by a single combined crack at the coalescence stage and a straight through-thickness crack is modeled once the wall thickness is reached (see Sections 3.3.2 and 3.3.3). The fatigue evolution that results from a pair of interacting semi-elliptical cracks is depicted in Fig. 3.11, where the growth of a single crack is also reported for comparison purposes. Additionally, Fig. 3.11 also represents the single crack fatigue life resulting from an analysis based on SIFs computed according to the parametric equations stated in [189]. Note that the previously mentioned parametric equations do not explicitly account for weld effects [32]. To also consider the influence of specific weld details, a

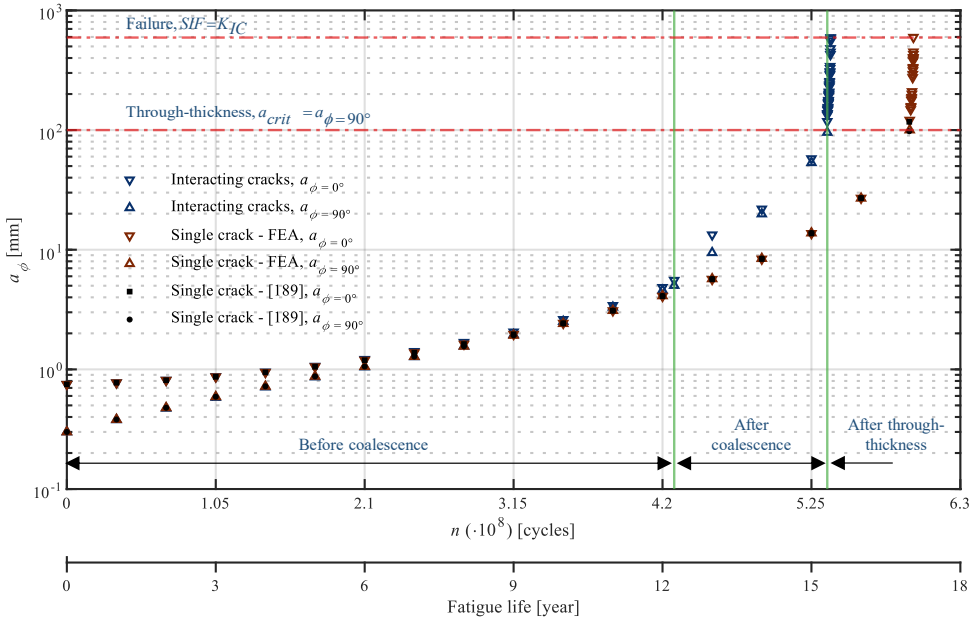

Fig. 3.11 Fatigue growth of interacting surface cracks in the investigated offshore wind structural connection. The propagation of two interacting cracks and a single crack at the critical points $a_{\phi=0°}$ and $a_{\phi=90°}$ are represented as a function of the applied stress cycles, also showcasing the transition to a coalesced crack and the through-thickness stage. Both fracture toughness- and through-thickness-based failure criteria are also indicated with red dashed lines. Note that a stress ratio, $R = 0.1$, is specified in this particular analysis.

magnification factor can be specified [57] or the weld geometry can be directly incorporated into the finite element model.

At an early crack growth stage, both surface cracks grow almost independently, seemingly like non-interacting cracks, since the distance between them is still significant at that point. In a further crack growth stage, the distance between the investigated cracks decreases, and an interaction combined effect can then be observed. In contrast, the studied single surface crack naturally grows up to the wall thickness without any interaction effect, thus demonstrating the importance of integrated crack growth numerical modeling. Also in Fig. 3.11, a good agreement can be observed between the growth of a single crack resulting from numerically computed SIFs and the growth obtained based on published SIFs. In the figure, one can observe that the crack aspect ratio continuously increases under the influence of the interaction effect during the course of the crack growth until the coalescence phase is reached. At that point, the coalesced crack grows faster than the previous pair of interacting cracks, since higher SIFs are found at the crack depth and surface points, induced by the resulting higher crack area and aspect ratio. Interestingly, the already coalesced crack grows with an increasing aspect ratio until it reaches the wall thickness, following a similar behavior as the previously examined pair of interacting cracks.

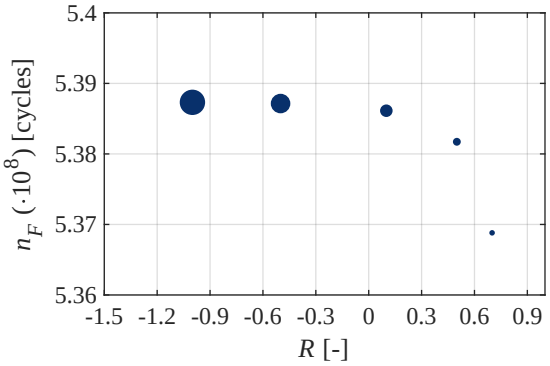

Fig. 3.12 Influence of the stress ratio on the number of cycles to failure observed in the studied offshore wind structural connection. The number of cycles to failure, n_F, and represented as a function of the stress ratio, R. The size of the markers indicates the magnitude of the stress intensity factor range, ΔK, at fatigue failure.

A closer inspection of Fig. 3.11 reveals that a single crack (i.e., disregarding interaction effects) exceeds the wall-thickness after $5.94 \cdot 10^8$ cycles, while only $5.36 \cdot 10^8$ cycles are required for the case of interacting cracks, thus resulting in a fatigue life reduction of approximately 9.8%. Assuming the component experiences around $3.5 \cdot 10^7$ cycles per year [46], the fatigue life reduction can be estimated as approximately 1.66 years, hence demonstrating the importance of considering interaction effects within the fatigue analysis. The point at which the crack penetrates the monopile thickness, the crack length size represents only 1.4% of the monopile's circumference for the interacting cracks case. As explained previously, the semi-elliptical crack is then re-characterized, at that stage, as a straight through-thickness crack. At the through-thickness phase, the structural connection still holds additional residual structural strength to further withstand the applied bending moment. Considering an applied stress ratio $R = 0.1$, the results show that the structural detail can resist up to approximately $2.4 \cdot 10^6$ stress cycles after reaching the through-thickness stage and before the SIF exceeds the fracture toughness. At that fatigue failure stage, the crack length arrives up to around 6.3% of the monopile circumference. As seen in Fig. 3.11, the crack(s) grow rapidly from the through-thickness stage to the fatigue failure, which only represents a small fraction of the total fatigue life. However, it should be noted that this observed behavior is case-dependent, specifically influenced by material properties and loading conditions.

Evidently, the stress ratio (R) directly influences the fatigue failure of a structural detail since the maximum SIF is defined as a function of R, as stated in Eq. 3.9. Note that a lower SIF range can lead to fatigue failure in high stress ratio settings. To further investigate this, the influence of the stress ratio on the number of stress cycles to failure is shown in Fig. 3.12. As expected, the number of cycles to failure decreases for high stress ratios. One can thus conclude that a higher stress ratio might induce a more rapid structural failure and this should be adequately considered when formulating the fatigue failure limit state.

3.6 Concluding remarks

A general methodology for numerically modeling the stress intensity factor (SIF) and growth of surface cracks is proposed in this paper, accounting for interaction effects caused by adjacent cracks as well as a potential coalescence of two bordering cracks. In contrast to available SIF closed-form solutions, the introduced modeling approach is not constrained to specific geometrical and/or loading conditions. Since the fatigue crack growth is driven by the SIF, numerically computed via a finite element model where multiple cracks can be jointly analyzed, crack interaction effects are implicitly considered. As opposed to through-thickness fatigue failure criteria, which are mainly pertinent to pipeline safety applications, fatigue failure is here defined based on fracture mechanics principles.

The proposed methodology is tested in a finite thickness plate setting, a typical case study within the fracture mechanics community, and the resulting SIFs as well as the computed crack growth predictions are in close agreement with those reported in the literature. From a more practical standpoint, our approach is also applied to a case study of an offshore wind structural connection under cyclic loading. The results from the conducted numerical experiments highlight the importance of adequately modeling crack interaction effects in practical engineering scenarios. Even if two surface cracks are not initially very closely spaced and thus only a minor interaction is experienced at that moment, a significant interaction behavior may still be expected at a later crack propagation stage. Also based on the reported results, one can conclude that the coalescence of two contiguous cracks might drastically accelerate their propagation, hence resulting in a very short fatigue life. With respect to fatigue failure criteria, this study shows that a through-thickness limit state can often be slightly conservative, and instead a fracture toughness-based fatigue failure can be formulated, especially when dealing with thick structural details.

Evidently, the computational requirements needed for numerically simulating the fatigue propagation in a structural component noticeably increase with the number of collectively considered cracks, and the fatigue analysis becomes substantially more complex if the propagation direction under mutual crack interaction is accounted for. Further research efforts might focus on the development of surrogate models based on, for example, Gaussian processes or artificial neural networks, in order to efficiently calculate SIF predictions. In that case, the fatigue crack growth analysis of multiple interacting cracks could be implemented through a probabilistic approach, ultimately providing a stochastic physics-based deterioration model that can be integrated with asset management planning methods.

Authorship contribution statement

Mishael, J: Conceptualization, Methodology, Software, Validation, Formal analysis, Investigation, Writing - Original Draft, Writing - Review & Editing, Visualization. **Morato, P. G.**: Conceptualization, Methodology, Validation, Formal analysis, Writing - Review & Editing, Supervision. **Rigo, P.**: Supervision, Project administration.

Declaration of competing interest

The authors declare that they have no known competing financial interests or personal relationships that could have appeared to influence the work reported in this paper.

Acknowledgement

The authors gratefully acknowledge the financial support provided by the Belgian Energy Transition Fund (ETF) through the MAXWind project.

CHAPTER 4

PROPAGATION OF INTERACTING CRACKS IN OFFSHORE WIND WELDED STRUCTURES THROUGH NUMERICAL ANALYSIS

Paper 3: Mishael, J, Morato, PG, and Rigo, P (2024). Propagation of Interacting Cracks in Offshore Wind Welded Structures through Numerical Analysis. In *Proceedings of the Thirty-fourth International Ocean and Polar Engineering Conference* (*ISOPE 2024*). 3116-3123.

Abstract: This study investigates the behavior of interacting surface cracks at the circumferential weld toe of monopile-supported offshore wind turbines. Relying on a numerical model that explicitly considers weld profiles, we explore the impact of crack interaction and loading scenarios on crack propagation. Our findings reveal that, initially, surface cracks grow independently, resembling single crack behavior. However, a pronounced interaction effect accelerates their growth as cracks propagate further, potentially leading to crack coalescence, high stress intensity factors, and reduced fatigue life. Consequently, this work highlights the need for integrating specific weld geometry representation in numerical models, as neglecting this can lead to significantly inaccurate fatigue life estimates in typical practical applications. Moreover, this study points out the challenge in accessing representative crack growth material parameters, vital for accurately evaluating the fatigue life of structural connections in offshore wind turbines.

4.1 Introduction

The structural integrity of marine structures and other engineering systems is adversely influenced over their operational lifespan by deterioration mechanisms and mechanical stressors. In harsh marine environments exposed to corrosive agents such as saltwater and atmospheric contaminants, welding defects found in marine structures steadily propagate under cyclic loading induced by waves and other dynamic forces, making fatigue one of the main structural failure modes. In marine and offshore engineering communities, the fatigue assessment of welded structures is usually performed by relying

on nominal stress S-N curves [45], yet the applicability of such S-N curves is constrained to structural configurations and loading conditions analogous to those in the original experimental setup.

A comprehensive modeling strategy entails the adoption of a linear elastic fracture mechanics (LEFM) approach for predicting the fatigue life of welded structures, particularly in scenarios that deviate from the experimental specimens used to establish conventional S-N curves. The crack growth modeled via LEFM is mainly governed by the stress intensity factor (SIF). This factor represents the stress field near the crack tip, derived from the crack size/geometry and applied loading. The fatigue crack growth of welded offshore steel structures can be modeled by a power law that establishes the relation between crack propagation rate, da/dN, and SIF range, ΔK [32, 45]. Naturally, suitable SIF solutions should be computed to yield accurate fatigue life predictions.

In real-world scenarios, welded sections often develop cracks because of the variation in material properties that is caused by the rapid heating and cooling cycles experienced during typical welding processes [7]. Due to the variation in material properties, the characterization of the stress field surrounding cracks originated from welded joints is a challenging task, where weld quality should be carefully considered, e.g., weld geometry, initial defects, residual stresses, and surrounding environment. Initial defects, commonly found near weldments, can rapidly propagate when subjected to cyclic loads owing to the local stress concentration at discontinuities. Consequently, the crack propagation prevails over the crack initiation phase [187].

Additionally, the interaction between adjacent cracks and their potential coalescence should also be accounted for when predicting welded joints' fatigue life. Structural components often exhibit multiple adjacent surface cracks, and their behavior is influenced by various factors such as size, relative position, geometry, and applied stress. These interactions commonly hold significance in structures subjected to fatigue and stress corrosion cracking [197]. Fatigue crack initiation and propagation experiments carried out for welded T-joints in offshore structural elements show that semi-elliptical cracks initiate along weld toes and may progressively coalesce, forming combined cracks [198]. To study the influence of specimen thickness, stress distribution, and environment on the fatigue crack shape evolution, To et al. [199] performed fatigue tests of welded T-plate, pipe-plate, and tubular joints. Their experimental campaign indicates that multiple cracks initiate along the weld toe early in the fatigue life, subsequently growing and potentially reaching coalescence, thereby resulting in a dominant crack. Similarly, Madia et al. [200] show that micro-cracks at weld toe propagate individually and simultaneously until they eventually coalesce with neighboring cracks. As adjacent cracks approach each other, the interdependence of the stress field and SIFs lead to pronounced growth rates and complex crack shapes. Quantifying fatigue growth of adjacent surface cracks and their coalescence thus demands accounting for their mutual interactions. While SIF values for conventional welded joints are reported in standards such as BS7910 [33]; suitable SIF solutions cannot, however, be easily found for structures with specific weld configurations, geometry, and/or loading conditions.

Since the nucleation of cracks along a weld toe is related to its notch geometry and the existence of micro-notches, weld toe local geometry at the weld toe plays a prominent role in the initiation of surface cracks [200]. Weld geometry can be characterized by defining the weld toe angle, weld

toe radius, width of weld reinforcement, height of reinforcement, and plate thickness. The effects of different welded geometry parameters on the fatigue life of welded joints are investigated by various researchers. For instance, Nguyen and Wahab [192] investigated the effect of welding parameters on the SIF of welded joints. They developed an analytical model to predict the fatigue strength of welded joints subjected to the co-influence effect of butt-weld geometry parameters and demonstrated how weld profile geometry factors have a significant impact on the SIF. The effects of welding geometry on the fatigue properties of T-weld and cruciform joints loaded in tension and in bending were studied by Ferreira and Branco [193] using finite element analysis. Plate thickness and welded toe radius were found to be the most significant factors influencing the fatigue characteristics of welded joints. Bowness and Lee [57] proposed a set of equations for estimating weld toe magnification factors for semi-elliptical cracks in T–butt joints by considering different parameters such as crack depth and aspect ratios, attachment footprint, weld angle, and weld toe radius. The equations together with plain plate solutions of Newman and Raju [189] can be used to compute the SIF solutions of T-butt joints. The fatigue life simulation results for butt welded joints by Schork et al. [194] indicate that the effects of weld geometry become more significant toward the endurance limits. Furthermore, the effects of flank angle and toe radius are more significant than the effects of excess weld metal height within the simulated range. Recently, Kolios et al. [195] proposed an approach based on combined three-dimensional laser scanning technology and finite element analysis (FEA) to accurately compute the stress concentration factor (SCF) in offshore welded structures specifically for circumferential weldments in offshore wind turbine (OWT) monopile foundations. They found that, depending on weld quality, the SCF at the weld toe varies significantly and ranges between 1.1 and 1.65. Additional fatigue testing using large dog-bone samples taken from 90 mm thick weldments showed cracks were initiated at areas of maximum stress concentration. Effective assessment of fatigue strength requires accurate modeling of the weld geometry as it influences the fatigue strength of welded joints.

In addition to the geometry at the weld toe, fatigue crack propagation is influenced by initial defect size and crack growth parameters too. The size and nature of weld defects significantly contribute to the initiation and subsequent propagation of cracks. Weld imperfections, such as slag inclusion at the weld toe, exist in all welded joints and act as pre-existing cracks and stress-raisers [187]. The identification and usage of appropriate crack growth parameters is also essential for the estimation of fatigue life of welded joints. Recommendations regarding the parameters to use in LEFM-based fatigue crack propagation models are specified in industrial standards [32, 33, 48, 211]. Hobbacher [211] states that fatigue life estimates using LEFM approaches can be carried out with appropriate parameters and the calculations should be verified at known structural details; on the other hand, ABS [48] and DNVGL [32] propose that the assumptions for fracture mechanics analysis models can be calibrated by comparison with S-N models. In contrast, BS7910 [33] recommends values for crack growth parameters that are appropriate for various materials and environments through a simple linear or bi-linear model to estimate the crack propagation in welded structures.

In a recent study, we propose a methodology that leverages three-dimensional finite element (FE) analysis to compute the SIF at any point along crack fronts, enabling a direct assessment of

crack propagation under interaction effects [204]. A noteworthy feature of this methodology is its ability to adequately model the coalescence of adjacent cracks. Building upon this foundation, this work expands the scope by investigating the influence of welding effects on the progression of multiple adjacent cracks, specifically those located in circumferential welds commonly found in monopile-supported OWTs. A key addition is the explicit modeling of weld profiles within the underlying three-dimensional FE analysis. Additionally, we adopt a calibration approach based on industrial S-N curves to account for variability in crack growth parameters and initial crack size. This reliability-based calibration approach adheres to the methodology introduced by Hlaing et al. [46] to determine crack growth parameters and initial crack size. Furthermore, we examine the impact of long-term stress range on crack propagation by comparing two approaches: (i) long-term stress range modeled as the expected value of a two-parameter Weibull distribution [32], and (ii) long-term stress range assumed as the equivalent stress range [64]. In a practical case study, we investigate the propagation of two interacting surface cracks at the circumferential weld toe of a monopile-supported OWT, showcasing the effectiveness of our proposed approach.

4.2 Fatigue crack growth and stress intensity factor

4.2.1 Crack growth modeling

Adhering to LEFM principles, crack propagation rate da/dN, can be numerically computed by solving the following ordinary differential equation:

$$\frac{da}{dN} = f(\Delta K, R, C), \tag{4.1}$$

where N represents the number of cycles, $R = \sigma_{min}/\sigma_{max}$ denotes stress ratio, i.e., minimum to maximum applied stress, and C is a material parameter usually derived from experimental data. Relevant industrial standards recommend Paris' law formulation for modeling fatigue crack growth in offshore structures [32, 33]. Following Paris' law, two-dimensional crack growth can be calculated by solving a system of ordinary differential equations [189]:

$$\frac{da}{dN} = C_a(\Delta K_a)^m; \tag{4.2}$$

$$\frac{dc}{dN} = C_c(\Delta K_c)^m, \tag{4.3}$$

where a and c are the crack depth and length of a surface crack idealized with semi-elliptical shape, ΔK_a and ΔK_c denote the stress intensity factor range at the crack deepest and surface points, and material and environmental effects are accounted for through the deterministic variables C_a, C_c, and m. To model crack growth retardation along the surface, Newman and Raju [189] propose the use of distinct crack growth parameters, C_a, and C_c, each of which related to crack growth along the depth and surface directions, respectively. A relation between C_a, and C_c can be assumed as:

$$C_c = 0.9^m C_a \tag{4.4}$$

where C_a and m parameters can be read from industrial standards [33] or through calibration with respect to structural reliability estimates computed via damage accumulation Miner's rule [32, 46].

If two or more surface cracks interact with each other, the stress intensity factors (SIFs) along their crack fronts become interdependent, thereby resulting in a combined crack growth propagation. In that case, the fatigue crack growth of multiple surface cracks can still be formulated by following Paris' law, yet specific SIF(s) should be considered for each crack:

$$\frac{da^{(i)}}{dN} = C_a(\Delta K_a^{(i)})^m; \tag{4.5}$$

$$\frac{dc^{(i)}}{dN} = C_c(\Delta K_c^{(i)})^m, \tag{4.6}$$

where the superscript $i \in \{1, 2, \ldots, n\}$represents an individual crack i out of n considered interacting surface cracks, and their combined propagation can be computed by numerically integrating da over a specific number of cycles, N, relying on methods such as Runge-Kutta.

Another aspect that demands careful consideration in interacting crack propagation modeling is the coalescence of multiple cracks. Interacting cracks may coalesce into a single crack during their growth as soon as their crack tips merge. During their coalescence, the crack shape largely deviates from the semi-elliptical profile that existed before coalescence. The coalesced crack forms a re-entrant (dented) portion at the contact point of the coalescing semi-elliptical surface cracks [22]. Because of the greater SIF at the re-entrant portion, the re-entrant part of the coalesced crack front grows at a faster rate than the other areas, resulting in the formation of a semi-elliptical crack shape for the coalesced crack [24]. Therefore, the coalesced crack can be modeled as a semi-elliptical surface crack with dimensions obtained from the combined geometry of the interacting cracks. It can also be assumed that the length of the new surface crack is equal to the sum of the lengths of the two previously interacting surface cracks, with its depth equal to the deepest crack before coalescence. Then, the crack growth can be calculated following Eqs. 4.2 and 4.3. This approach provides an initial estimate of crack growth under interaction and coalescence, even if the assumed crack re-characterization may lead to an overestimation of the actual crack growth.

4.2.2 Stress intensity factor for weld-toe surface cracks

As previously mentioned, the computation of fatigue crack growth requires an accurate estimation of stress intensity factor range, ΔK, which is analytically defined as:

$$\Delta K = \Delta\sigma Y(a,c)\sqrt{\pi a}, \tag{4.7}$$

where $\Delta\sigma$ corresponds to the applied stress range weighted by a shape factor, Y, that accounts for local geometrical and loading conditions, and is specified as a function of both crack depth, a, and

crack length, c. Evaluating SIF range in practical scenarios presents a challenge due to its dependence with the crack depth and length, which undergoes continuous change during crack propagation. Nonetheless, existing works in literature offer closed-form analytical solutions that are predominantly applicable to standardized and idealized crack geometries under simplified loading conditions. For instance, a typical closed-form solution for the SIF range for surface cracks in a welded finite plate subjected to membrane and bending loading is formulated in [32] as:

$$\Delta K_a = \Delta\sigma \left[\alpha Y_{\mu a} M_{k\mu a} + (1-\alpha) Y_{ba} M_{kba}\right] \sqrt{\pi a} \tag{4.8}$$

$$\Delta K_c = \Delta\sigma \left[\alpha Y_{\mu c} M_{k\mu c} + (1-\alpha) Y_{bc} M_{kbc}\right] \sqrt{\pi a} \tag{4.9}$$

where the subscripts μ and b stand for membrane and bending stress components. The factor α corresponds to the ratio between membrane and total stress and M_k represents the stress magnification factor accounting for the stress concentration due to local weld geometrical effects [57]. The geometric factors $Y_{\mu a}$, Y_{ba}, $Y_{\mu c}$, Y_{bc}, and stress magnification factors $M_{k\mu a}$, M_{kba}, $M_{k\mu c}$, M_{kbc} can be computed using the parametric equations listed in [33].

The parametric equations recommended by industrial standards [32, 33] are based on the magnification factors proposed by Bowness and Lee [57] for 3D T-butt joints. However, M_k results for plate-to-plate butt welds differ from those for single T-butt joints [58]. The percentage difference in values is as high as 63.8% for axial loading cases and 97.4% for bending loading cases. In addition, the intricate nature of cracked geometries and the complexity of service loads in practical scenarios render direct analytical solutions unattainable.

In contrast, numerical methods, such as finite element method (FEM), have proven useful for obtaining stress intensity factors in complex structures with irregular crack geometries. For instance, accepted stress intensity factor solutions for surface cracks on finite-thickness plates, hollow cylinders, and circular rods can be obtained via finite element analysis [188, 201]. Another approach involves combining numerical methods with existing solutions of weld geometry magnification factors proposed by standards such as DNVGL [32]. This will reduce the computational effort required to perform numerical simulations, especially when detailed information about weld geometry is not readily available. However, the efficacy of this approach relies on the determination and applicability of suitable weld geometry magnification factor solutions.

In this work, a three-dimensional FE model, following the approach proposed in our previous work [204], is extended by considering the weld geometry, thus avoiding the need for parametric equations to compute the weld toe magnification factor (M_k) in practical scenarios, e.g., plate-to-plate butt-welded connections in offshore wind turbine monopile foundations. The accurate computation of SIF requires the development of appropriate finite element models that can represent semi-elliptical weld-toe cracks. Building upon our recent work on the finite element modeling scheme for semi-elliptical surface cracks [204], we propose an alternative approach to model semi-elliptical weld-toe cracks. Recognizing the significance of the weld toe radius in creating a curved geometry near the

weld toe, we adopt a modeling strategy that employs 10-node quadratic tetrahedral elements. These elements are chosen for their ability to accurately capture the complex features of surface cracks, especially in regions with curved geometries. Considering 10-node tetrahedral elements ensures an effective representation of the weld toe, addressing the challenges posed by its curved nature and contributing to the overall effectiveness of the FE model. They are also capable of automatically adapting to variations in crack dimensions during crack propagation. The semi-elliptical cracks located at the weld toe, along with their crack fronts, are carefully modeled using these quadratic tetrahedral elements. 8-node linear brick elements are used for creating a structured mesh for the remaining part of the model. The modeling procedure ensures that at least six contours are available for the computation of SIF through the interaction integral method. Reasonably refined elements are used to model the semi-elliptical cracks, and sufficiently fine mesh is set up along the crack front to avoid the use of quarter-point elements.

4.2.3 Long-term stress range

The stress range influences the stress intensity factor, as shown in Eq. 4.1, and therefore, it is essential to consider long-term loading conditions in fatigue crack growth computations. For crack growth computations, offshore industrial standards [32, 255] recommend using a long-term stress range described by a two-parameter Weibull distribution if long-term stress range data for the structure are not available. The exceedance probability derived from a two-parameter Weibull distribution can be represented as:

$$Q(\Delta\sigma) = exp\left[-\left(\frac{\Delta\sigma}{q}\right)^{h}\right], \tag{4.10}$$

where Q stands for the probability of exceedance corresponding to the stress range $\Delta\sigma$, while q and h are Weibull scale and shape parameters, respectively. The scale and shape parameters can be obtained from standards [45]. To reduce the computational effort associated with three-dimensional finite element analysis, the expected value of the long-term stress range distribution is often employed in SIF computations. This approach provides a representative value that can be used to estimate the effects of long-term loading without the need for detailed and resource-intensive analyses.

An alternative approach for representing the long-term stress range is to use the equivalent constant amplitude stress range suggested in Eurocode 3 [64], which is defined as the stress range that would result in the same fatigue life as the spectrum of variable amplitude stress ranges when the comparison is based on Palmgren-Miner's rule. The advantage of this approach lies in its ability to simplify the fatigue analysis by transforming variable amplitude loading scenarios into an equivalent constant amplitude, facilitating a more straightforward assessment of structural fatigue life. A simplified procedure for the determination of equivalent constant amplitude stress range is reported in Eurocode 3 [64].

4.2.4 Initial crack size and crack growth parameters

The initial crack size influences the crack propagation life and plays a key role in the applicability of the LEFM approach. The calculated number of cycles is very sensitive to the dimensional parameters of the initial crack, especially for the crack depth [212]. Theoretical initial crack sizes can be determined by performing curve fitting based on experimental fatigue test data and crack growth parameters [212]. The initial crack size reported by researchers and suggested by standards varies between 0.1 and 0.5 mm. For instance, the crack size recommended by BS7608 [169] ranges between 0.1 and 0.25 mm at the weld toe of flaw-free welded joints, whereas ABS standard [48] suggests an initial crack depth of 0.5 mm for surface cracks starting from the transition between weld and base material. Radaj et al. [49] suggest an initial crack depth greater than 0.15 mm and a surface crack length ($2c$) greater than 0.45-0.75 mm for the application of the LEFM approach. An initial crack depth of 0.1 mm is suggested by Lassen and Recho [50] based on the inability for detecting cracks smaller than 0.1 mm during in-service inspections using non-destructive inspection techniques.

Crack growth parameters, C and m, are material dependent and usually derived from crack propagation experiments. They depend on many factors such as stress ratio, residual stress, environmental conditions, temperature, corrosion, among others. Hobbacher [212] shows that there exists a large scatter in crack propagation data for different welded joints and recommended to set up an upper bound line for practical applications. However, in practical applications it is important to use the crack propagation parameters relevant to the specific material, loading, and environmental conditions under consideration. Mehmanparast et al. [54] performed fatigue crack growth tests in air and seawater on S355G8+M steel, a widely used material in the fabrication of offshore wind monopile structures. Specifically, they proposed crack growth parameters for base metal as well as heat-affected zones in air and seawater (free-corrosion) environments. The investigation was motivated by the fact that available fatigue crack growth data for steels in air and seawater environments are several decades old and may not be appropriate for structural integrity assessment of offshore wind turbine foundations, which are fabricated using modern materials and welding technologies. In addition, crack growth data reported in offshore standards is based on the characteristics that are representative of typical offshore structures in the oil and gas industry. Instead of directly relying on material parameters listed in standards, it is also possible to estimate them by performing a calibration analysis that minimizes the difference in structural reliability with respect to estimates computed via Palmgren-Miner's rule [12, 32, 46].

This calibration process can be conceptualized as an optimization problem with the objective of minimizing the difference in estimated failure probabilities resulting from representative S-N data and the considered fracture mechanics model. Failure probability over time should be considered because, while fracture mechanics models compute crack growth evolution, S-N data only provides information about the failure or survival of the considered hotspot due to fatigue damage [32]. The reader is advised to refer to [12] for more information on the procedure to carry out the fracture mechanics parameter calibration based on a probabilistic approach. Alternatively, unknown fracture

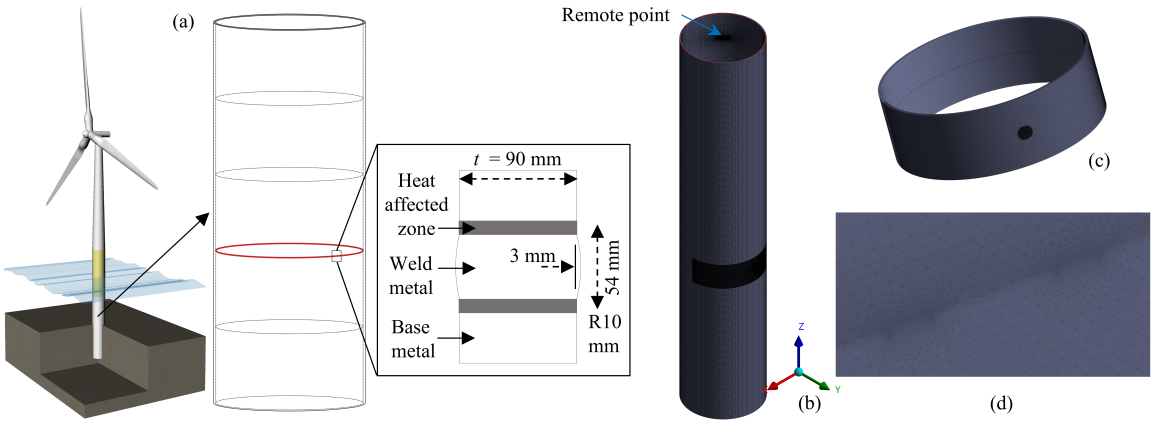

Fig. 4.1 Graphical representation of a typical offshore wind turbine monopile foundation, illustrating the studied weld geometry and its dimensions. (a) The examined surface cracks are located at the circumferential weld toe marked with a solid red line, (b) monopile FE model representation, also showcasing the remote point where the bending moment is applied, (c) local mesh near the circumferential weld region, and (d) refined mesh representation at the semi-elliptical cracks' location.

mechanics parameters can also be calibrated following a deterministic approach, by adjusting crack growth parameters so that through-thickness failure is reached at the same time as fatigue damage failure computed via Palmgren-Miner's rule and representative S-N data.

4.3 Fatigue analysis of interacting surface cracks in offshore wind welded connections

4.3.1 Case study description

In this case study, we investigate the influence of weld geometry, crack growth parameters, and long-term stress range approximations on the fatigue growth of interacting surface cracks that can be found in typical offshore wind monopile welded connections. We compare the propagation of two interacting cracks at the toe of a circumferential weld utilizing different methods to compute SIFs: (i) a finite element model considering both geometric and weld details, (ii) a finite element model where only geometric details are considered and relying on Bowness and Lee [57] parametric equations to account for weld magnification effects, and (iii) computing geometric effects via Newman and Raju [189] parametric equations along with Bowness and Lee [57] magnification factors. Additionally, all experiments are compared against the growth of an independent single crack, where crack interaction effects are neglected.

The subject of the study is a 30-m monopile substructure with a 3-m outer radius and a 90-mm wall thickness, t, installed in a water depth of 20 m. The examined structural detail corresponds to a monopile circumferential welded connection located at 12 m height from the seabed. The geometry of the weld and its dimensions are shown in Fig. 4.1. The monopile substructure is assumed to be

Table 4.1 Initial crack size (a_0) and crack growth parameters (C) calibrated from Class D S-N curves in seawater with cathodic protection. The units corresponding to da/dN and ΔK are mm/cycle and MPa$\sqrt{}$mm, respectively.

Calibrated parameters	a_0[mm]	C (mean)	C (standard deviation)	Approach
Expected stress range– 4.739 MPa				
a_0	2.8191	$3.4268 \cdot 10^{-13}$ [32]	0.22 [32]	Probabilistic
a_0 and C	0.5785	$8.5643 \cdot 10^{-13}$	0.56	Probabilistic
a_0	6.5797	$3.4268 \cdot 10^{-13}$ [32]	-	Deterministic
a_0 and C	0.6895	$1.3239 \cdot 10^{-12}$	-	Deterministic
Equivalent stress range– 17.052 MPa				
a_0	0.0037	$3.4268 \cdot 10^{-13}$ [32]	0.22 [32]	Probabilistic
a_0 and C	0.1525	$3.8667 \cdot 10^{-14}$	0.56	Probabilistic
a_0	0.0059	$3.4268 \cdot 10^{-13}$ [32]	-	Deterministic
a_0 and C	0.5929	$3.0871 \cdot 10^{-14}$	-	Deterministic

made from S355 structural steel, which is a widely used material for the fabrication of offshore wind foundations [54]. The modulus of elasticity and Poisson's ratio are specified as $2.1 \cdot 10^5$ MPa and 0.3, respectively. While not implemented in this work, one can additionally consider distinct material properties near the region of the weld, e.g., base metal, weld metal, and heat-affected zone. Adhering to typical practical scenarios [255], we set a service life of 20 years, in which the analyzed details experience approximately $7 \cdot 10^7$ stress cycles per year, caused by dynamic wind and wave loads [257].

Following the process suggested by industrial standards [45], initial crack size and crack growth parameters are calibrated as explained in the methodological section, considering a class D S-N curve, which is applicable to details exposed to seawater and equipped with cathodic protection. All resulting crack parameters are listed in Table 4.1, categorized according to the followed calibration approach (i.e., deterministic, or probabilistic), and based on the determined long-term stress range approximation. While it is interesting to observe the variation of the resulting crack parameters depending on the imposed assumptions, only the parameters calculated via the deterministic approach are considered in the experiments. This decision is made by considering computational efficiency and with preference on parameters that can be found in typical scenarios, as detailed in the previous section. An alternative approach one could instead adopt would be adjusting crack parameters according to the mean values resulting from the probabilistic calibration approach.

To study potential crack interaction effects, we model two identical surface cracks idealized with semi-elliptical geometries and separated by a distance-to-thickness ratio, $\delta/t = 0.09$, where δ is the distance between the semi-elliptical crack centers. The investigated surface cracks are analyzed under mode I fracture mode, which represents a critical fatigue failure mechanism commonly experienced by offshore wind structural components. To simulate the experienced combined wind and wave loads,

a bending moment is applied at the top of the monopile FE model through a coupled remote point, as shown in Fig. 4.1.

Based on industrial standard recommendations [45, 64], we examine two long-term stress range approximations in the numerical experiments, i.e., expected stress range and equivalent stress range, both explained in the previous section. The magnitudes of the considered stress ranges are 4.739 MPa and 17.052 MPa for expected and equivalent stress range, respectively. Furthermore, the monopile is assumed fixed to the seabed by restricting in the model all degrees of freedom at the bottom. The combination of a clamped boundary condition and applied bending moment induces a crack-opening effect at the investigated circumferential weld connection.

4.3.2 Results and discussion

The fatigue propagation experienced by a pair of interacting semi-elliptical cracks at the circumferential weld toe of a monopile foundation is illustrated in Fig. 4.2, where the growth of an independent single crack is also represented for comparison purposes. The investigated surface cracks grow almost independently during the early propagation stage since they are still far from each other, thus following the same path as an independent single crack. The stress field around each crack, at this initial phase, aligns with that of a single crack without inducing any notable stress concentration in the surrounding region. However, an interaction effect can be observed as the cracks continue to propagate over time, thereby resulting in a more pronounced crack growth compared to that of an independent crack. This interaction effect naturally becomes more prominent as the cracks draw closer to each other. The proximity of cracks induces a mutual influence, causing the stress fields around the cracks to overlap and interact. This phenomenon results in a collective rise in stress levels, marking the departure from stress distributions observed during the early, independent growth stage. This increase in stress levels is the primary cause for the pronounced crack growth observed in the later stage. Stress concentration zones induced by the cracks proximity further amplify the applied loading at the crack tips, leading to higher stress intensity factors (SIFs), thereby accelerating propagation of interacting surface cracks. When surface cracks draw near enough to each other, they coalesce into a single combined crack and continue to propagate until the end of the structural component's lifetime. The increased growth at this final stage can be attributed to elevated SIFs at both crack depth and surface points, which are induced by the increased crack area and aspect ratio that results from coalescence.

As shown in Fig. 4.2, the growth evolution of the investigated interacting cracks is clearly influenced by the weld profile, thus showing the importance of explicitly modeling weld effects in fatigue numerical simulations. As seen in the figure, cracks grow faster when weld geometry effects are considered, compared to the case where the weld geometry is not explicitly represented in the FE model. Interestingly, Fig. 4.2 also illustrates that accounting for weld geometry effects through Bowness and Lee magnification factors [57] substantially overestimates crack growth in our numerical experiments. This behavior is observed for both interacting and independent cracks. A good agreement is, however, reached between the growth of a single crack derived from numerically

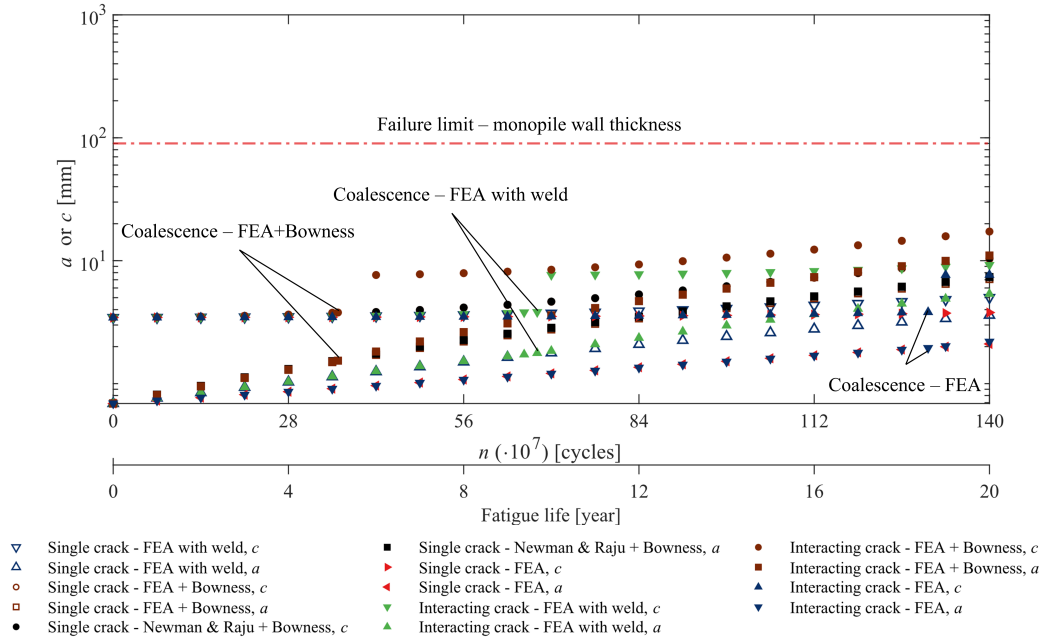

Fig. 4.2 Propagation of interacting cracks and independent single crack under expected stress range loading for all investigated methods.

computed SIFs and those based on published SIFs [189] if weld geometry effects are computed with Bowness and Lee magnification factors [57] in both cases. This result verifies that the observed discrepancy is caused by the method used to account for weld effects. Specifically, the growth of an independent single crack significantly differs when SIFs are computed with either a FE model where the circumferential weld profile is incorporated or a FE model along with Bowness and Lee magnification factors [57].The difference in crack growth between these two modeling approaches is approximately 50% for both crack depth and surface points at the end of the service life of the studied monopile foundation.

Furthermore, the outcome from crack propagation numerical simulations for the case where long-term loading is approximated by an equivalent stress range is represented in Fig. 4.3. In this scenario, the discrepancy in the propagation of a single independent crack from a FE model where the circumferential weld is incorporated and the predicted growth when relying on parametric equations reaches up to 55% at the end of service life. A shift is, however, observed between the expected and equivalent stress range loading scenarios, mainly because the calibrated crack growth parameters are not equal, as shown in Table 4.1. The difference in the calibrated parameter values for all considered cases in Table 4.1 raises concern for effectively predicting the fatigue life of monopile foundations. Rational fatigue life predictions rely on crack growth parameters related to specific materials used in the offshore wind industry. Given that S-N curves currently available in standards mostly correspond to materials that are commonly used in the oil & gas industry, further research is needed to establish

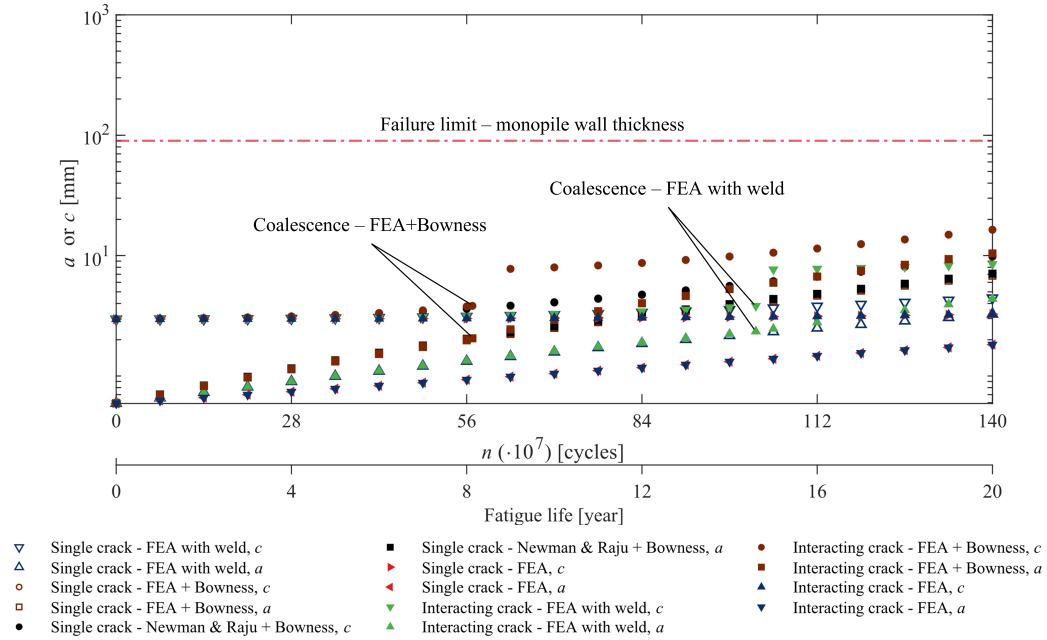

Fig. 4.3 Propagation of interacting cracks and independent single crack under equivalent stress range loading for all studied methods.

representative crack growth parameters for materials commonly employed in the offshore wind industry.

4.4 Conclusions

This study investigates the propagation of interacting surface cracks in circumferential welded connections of monopile-supported offshore wind turbines. Our findings highlight the importance of explicitly incorporating the geometry of weld profiles when numerically computing stress intensity factors. Relying simply on closed-form magnification factors may otherwise potentially lead to inaccurate fatigue life estimates in practical scenarios. Besides, the implementation of crack growth methods for evaluating the integrity of offshore wind structural connections is currently hindered by the unavailability of representative crack growth parameters. Future research directions are envisaged toward the development of probabilistic crack growth methods that account for variability in material parameters and initial crack size, while also effectively modeling crack interaction effects in offshore wind welded connections.

Authorship contribution statement

Mishael, J: Conceptualization, Methodology, Software, Validation, Formal analysis, Investigation, Writing - Original Draft, Writing - Review & Editing, Visualization. **Morato, P. G.**: Conceptualization,

Methodology, Validation, Formal analysis, Writing - Review & Editing, Supervision. **Rigo, P.**: Supervision, Project administration.

Acknowledgements

The authors gratefully acknowledge the financial support provided by the Belgian Energy Transition Fund (ETF) through the MAXWind project.

CHAPTER 5

PROBABILISTIC FATIGUE ANALYSIS OF OFFSHORE WIND MONOPILE WELDS WITH INTERACTING AND COALESCED CRACKS USING MLP SURROGATES

Paper 4: Mishael, J, Morato, PG, and Rigo, P (2025). Probabilistic fatigue analysis of offshore wind monopile welds with interacting and coalesced cracks using MLP surrogates. *Theoretical and Applied Fracture Mechanics*. Submitted.

Abstract: Fatigue-induced surface cracks govern the long-term integrity of marine structures, especially when dealing with dynamically sensitive systems such as offshore wind substructures. Crack growth rates in fracture mechanics models are controlled by the stress intensity factor (SIF), but the closed-form SIF expressions provided in industrial standards apply only to simple geometries and loading conditions. Full three-dimensional (3D) finite element analyses (FEA) can supply accurate SIFs for arbitrary crack shapes under interaction and coalescence, yet the computational cost is prohibitive for large Monte Carlo simulations, particularly when multiple semi-elliptical cracks evolve and reshape their fronts during growth.

We develop a computational framework that replaces repeated high-fidelity finite element (FE) evaluations with three regime-specific families of multilayer perceptron (MLP) surrogates, trained on 3D extended finite element (XFEM) simulations: (i) two interacting semi-elliptical crack states at prescribed angular separations, (ii) post-coalescence single crack states, and (iii) single offset crack states. In the present case this corresponds to four individual networks: two interacting crack MLPs (for $\beta = 0.003$ and 0.009 radians) and one network each for the post-coalesced and single offset crack regimes.

The surrogates reproduce SIF ranges at key crack front positions with coefficients of determination $R^2 \approx 1.0$ and small absolute errors (typically below 0.1 MPa$\sqrt{\text{mm}}$ for interacting cracks), while reducing the cost of each SIF evaluation from FE time scales to milliseconds. These surrogates allow for a probabilistic fatigue analysis of an offshore wind monopile weld with multiple interacting surface cracks, using thousands of realizations. The resulting Monte Carlo study provides the probability of fatigue failure by following the through-thickness failure criterion. This approach treats the ensemble

of interacting cracks as an implicit system, capturing their dependencies within the surrogate and avoiding the simplifications of series/parallel or k-out-of-n models. This interaction-aware method offers a practical route to assessing the fatigue reliability of offshore structural components realistically.

5.1 Introduction

Offshore wind turbines (OWTs) are critical components of renewable energy infrastructure, with monopile foundations widely used to support these structures. These foundations experience cyclic loading from environmental forces such as wind and waves, leading to fatigue damage over time. Fatigue deterioration typically manifests through the initiation and propagation of surface cracks, potentially extending through the thickness of structural components. In non-redundant systems like monopile foundations, fatigue-induced cracking can result in significant structural failure and loss of power production. Therefore, accurate and reliable fatigue assessments are essential for ensuring structural integrity and sustained operational performance.

Traditional fatigue reliability assessments within marine and offshore engineering communities often rely on the S-N approach outlined in industry standards [32, 45]. However, linear elastic fracture mechanics (LEFM) offers a more versatile framework, explicitly modeling crack initiation, propagation, and the effects of inspection and maintenance actions. Fatigue crack growth in LEFM is governed by a differential equation of the form $da/dN = f(\Delta K, R)$, where ΔK denotes the stress intensity factor (SIF) range and R is the stress ratio. Accurate fatigue crack growth predictions depend critically on precise evaluations of ΔK as it characterizes the stress field near the crack tip, influenced by crack dimensions, geometry, and loading conditions.

SIFs for welded joints are commonly derived from analytical solutions obtained via FEA of standardized crack geometries. Widely used formulations, such as those proposed by Newman and Raju [188, 189], define SIFs for surface cracks in finite plates under tensile and bending loads. Industry standards incorporate these solutions into fatigue assessment guidelines for cruciform, butt, and T-butt welds [32, 33]. To account specifically for welded joint features, Maddox [190] introduced a magnification factor (M_k), representing the ratio between the SIF of a welded structure and an equivalent plain plate. Bowness and Lee [57] expanded this concept explicitly for semi-elliptical cracks in T-butt joints, providing widely adopted equations.

However, standard SIF solutions typically assume simplified conditions and fixed crack geometries, potentially overlooking complex weld features and realistic crack interactions. Zhao et al. [191] highlighted these limitations by investigating fatigue crack propagation in longitudinal fillet welded joints using numerical analyses, underscoring the necessity of advanced FEA for accurately modeling structures inadequately described by existing solutions. Similarly, Lie et al. [58] reported significant discrepancies (up to 97.4%) between standard magnification factors for plate-to-plate butt welds and T-butt joints under bending loads, emphasizing caution when applying generic SIF solutions to specific configurations.

Furthermore, multiple adjacent surface cracks commonly found in welded joints complicate fatigue analyses due to their interactions and potential coalescence, which significantly amplify local SIFs and accelerate crack propagation. Studies by Kamaya [22, 197], Bell and Vosikovsky [198], and To et al. [199] provided experimental evidence that semi-elliptical surface cracks often coalesce, forming larger cracks with enhanced growth rates. Madia et al. [200] reinforced that interacting cracks produce distinctly different SIFs compared to isolated cracks, further necessitating advanced numerical simulations for accurate fatigue predictions.

Numerical methods, particularly detailed 3D FEA, have been essential for accurately computing SIFs in complex weld geometries and crack configurations, including crack interactions. Extensive studies by Newman and Raju [188, 189, 201], Navid et al. [202], Kirkhope et al. [203], and recently Mishael et al. [204, 205], illustrate the capability of numerical modeling to directly capture local weld geometry and crack interaction effects, surpassing simplified analytical solutions. Despite their accuracy, comprehensive 3D FEA remains computationally demanding, limiting its use in probabilistic analyses that necessitate numerous simulations, particularly in the case of interacting cracks and coalescence.

Extended finite element method (XFEM) has gained attention for modeling several discontinuities in 3D complex geometries as it allows the modeling of the crack geometry independent of the underlying mesh, and completely avoids the need for re-meshing in crack growth problems. The method is based on the partition of unity concept of conventional finite element method (FEM) [258, 259]. The XFEM method enriches the conventional FEM mesh by special shape functions to take into account the displacement and discontinuity. Many researchers employed XFEM to simulate fracture behavior. For instance, crack modeling in isotropic and bi-material media using XFEM is described in Sukumar and Prevost [260]. They also showcased the implementation of the modeling of discontinuous fields using XFEM within a general purpose finite element code. Huang et al. [261] presented the numerical applications using Sukumar and Prevost's methodology. The modeling of cracks with multiple branches, multiple holes and cracks emanating from holes is presented in Daux et al. [262]. The implementation is based on using the same enrichment functions for the cracks (discontinuous and tip functions) and the enrichment scheme is developed based on the interaction of the discontinuous geometric features with the mesh. More recently, Moghaddam et al. [39] employed XFEM to study the crack growth rate of single and multiple cracks originating from corrosion pits on a fairlead connection of a mooring cable to the floating offshore wind turbine.

To address the computational challenges associated with the detailed 3D FEA, recent developments have focused on surrogate modeling approaches, such as Gaussian process regression, to efficiently predict SIFs based on a limited set of high-fidelity numerical simulations. Keprate et al. [63], Leng et al. [206], and Kaloop et al. [207] successfully demonstrated the efficacy of surrogate models for predicting SIF in offshore structures, reducing computational expense significantly while maintaining high accuracy. Sobotka and McClung [263] used Gaussian process regression to develop surrogate SIF models for straight through cracks in C-section geometries. Zhang et al. [264] employed artificial neural networks modeled with XFEM to predict mixed mode SIFs in composite materials.

Seghier et al. [265] used neuro-fuzzy inference system models to create surrogate SIF models that outperformed the equations proposed in BS7910 for semi-elliptical crack in finite thickness plate in terms of accuracy. He et al. [266] demonstrated the efficiency of Kriging-based Monte Carlo methods over response surface methods for mixed-mode fatigue crack growth analyses. Recently, Merrell et al. [267] combined fracture mechanics knowledge with interpretable machine learning via genetic programming for symbolic regression (GPSR) to develop a framework for the automated creation of handbook SIF solutions. The GPSR equations outperformed the Raju-Newman equations in accuracy, evaluation time, and equation complexity. Although these methods have been successful in addressing single crack scenarios, their application to predict SIFs for multiple interacting cracks, a realistic and critical condition, remains largely unexplored, presenting a critical research gap.

From a structural fatigue reliability point of view, in order to account for structural and loading uncertainties, a feasible solution is to couple reliability theory with FEM [268, 269]. However, the challenge in structural reliability computation is to limit the calls to the numerical models [270] to reduce the total simulation time. This is because fatigue crack growth analysis involves more complex computations and the evaluation of the failure probability may require very time-consuming computations. The crack interaction and coalescence create further complexities in the computations. Therefore, directly incorporating 3D FEA into probability computation is not feasible. However, in structural reliability, surrogate models like Kriging, combined with Monte Carlo simulation (MCS), reduce computational costs while addressing uncertainties in input parameters [266, 270–273]. Methods such as adaptive response surfaces [271], ANN-based FORM [272], and Kriging-based MCS [266, 270] enhance efficiency in probabilistic fatigue analysis, yet their application to multiple interacting cracks remains limited. Therefore, there remains a critical need for efficient yet accurate computational frameworks that can combine high-fidelity numerical simulations with surrogate-based reliability analysis to capture the effects of crack interaction and coalescence.

This study addresses the aforementioned research gap by proposing a novel fatigue reliability framework applied to an offshore wind turbine monopile foundation. The framework integrates high-fidelity 3D XFEM simulations with multilayer perceptron (MLP) surrogate models to efficiently predict SIFs for multiple interacting and coalescing semi-elliptical surface cracks. The trained surrogates are embedded within a Monte Carlo–based probabilistic crack growth analysis, enabling efficient yet accurate evaluation of the probability of failure with respect to critical crack depths. Furthermore, a system-level reliability formulation is introduced to implicitly capture the transition between interacting and coalesced cracks—effectively bridging local crack behavior and global structural reliability. Unlike existing approaches limited to isolated cracks or analytical SIF expressions, the present framework explicitly accounts for crack interaction and coalescence through data-driven surrogates that retain XFEM-level accuracy while remaining computationally tractable for large-scale probabilistic simulations. In summary, regime-specific MLP surrogates for ΔK are developed and embedded in a reliability workflow that combines the fidelity of numerical fracture mechanics with the efficiency of machine learning–based uncertainty quantification.

The remainder of this paper is structured as follows: Section 5.2 presents the theoretical background, Section 5.3 outlines the proposed computational framework, Section 5.4 describes the offshore wind monopile case study, Section 5.5 discusses and interprets the results, and Section 5.6 summarizes the key findings and future research directions.

5.2 Background

5.2.1 Fatigue crack growth modeling

Surface cracks in structural components often exhibit complex geometries and orientations [24]; however, semi-elliptical approximations are widely adopted in engineering practice to simplify modeling efforts, as recommended by industrial standards such as BS7910 [33]. Crack growth in offshore structural components is typically described using Paris' law [32, 33, 45], which relates crack propagation rates to the stress intensity factor (SIF) range:

$$\frac{da}{dN} = C_a(\Delta K_a)^m, \quad \frac{dc}{dN} = C_c(\Delta K_c)^m, \tag{5.1}$$

where a and c denote crack depth and length respectively, N is the number of loading cycles, ΔK_a and ΔK_c are the SIF ranges at the crack's deepest point and surface intersection, respectively, and C_a, C_c, and m are material- and environment-dependent constants. Due to three-dimensional stress state variations near the surface [21], cracks propagate differently along depth and length, making it inaccurate to assume identical constants ($C_a = C_c$). Hence, a practical relationship is given by Newman and Raju [189]:

$$C_c = 0.9^m C_a. \tag{5.2}$$

In practical modeling, each point along the crack front has an individual SIF. Thus, crack propagation is described locally:

$$\frac{da_\phi^{(i)}}{dN} = C_\phi \left[\Delta K_\phi^{(i)}\right]^m, \tag{5.3}$$

where a_ϕ represents crack dimension at a specific angle ϕ, and superscript (i) distinguishes among multiple interacting cracks. Typically, key locations along the crack front surface intersections ($a_{\phi=0^\circ}$ and $a_{\phi=180^\circ}$), denoted hereafter as cL and cR, and the maximum depth ($a_{\phi=90^\circ}$), denoted as a suffice for fatigue analysis. Here, c (without subscript) continues to denote the semi-ellipse surface half-length parameter of the crack geometry, whereas cL and cR are denote the left and right surface points on the crack front. As cracks evolve, their shapes may deviate significantly from idealized

semi-elliptical profiles, particularly when adjacent cracks interact and coalesce [22, 24, 36]. Such interactions necessitate frequent geometrical updates in numerical models.

The numerical computation of fatigue crack growth involves significant challenges primarily due to the computational complexity associated with accurately determining the SIF. High-fidelity methods such as FEM or the XFEM [274–276] are commonly used for evaluating SIF distributions. Conventional FEA methods require frequent remeshing to capture evolving crack geometries, leading to high computational costs. XFEM alleviates some of these issues by eliminating explicit crack front remeshing [274]. Typically, two primary strategies exist within FE-based crack growth simulations: (i) specifying a fixed increment of crack growth (da) and subsequently determining the corresponding elapsed cycles (dN), or (ii) setting a constant number of loading cycles (dN) and calculating the resulting crack increment (da) at each step. Both approaches have drawbacks: initially, the crack increments might be smaller than numerical errors, causing inaccuracies, whereas at advanced stages of crack growth, large increments can lead to numerical instability. Thus, adaptive increment schemes—based either on maximum permissible crack increments or predefined cycle counts adjusted dynamically according to crack growth rates—are recommended to balance computational efficiency, accuracy, and stability [277, 278]. However, FE-based crack growth simulations remain computationally intensive, particularly when analyzing large numbers of loading cycles, often in the order of 10^8 cycles [279].

From a continuous perspective, crack growth from cycle N to $N+\Delta N$ can be represented in an integral form:

$$a_{\phi}^{(i)}(N+dN) = a_{\phi}^{(i)}(N) + \int_{N}^{N+dN} C_{\phi} \left[\Delta K_{\phi}^{(i)}(z)\right]^{m} dz. \tag{5.4}$$

This integral is approximated numerically using methods such as Euler's method or higher-order techniques like fourth-order Runge-Kutta (RK4) [204, 205, 279]. Euler's method is computationally straightforward but has limitations concerning stability and accuracy. RK4 provides significantly better accuracy by evaluating intermediate crack propagation states within each integration step, making it highly suitable for accurately capturing fatigue crack evolution [204, 205]. However, direct coupling of RK4 with high-fidelity FEA methods, necessary for SIF evaluations, is computationally prohibitive due to repeated expensive simulations for each intermediate step, particularly in probabilistic analyses involving numerous realizations.

To overcome this computational challenge, this study adopts an efficient surrogate modeling approach. Specifically, a multilayer perceptron (MLP) surrogate model, trained using a limited set of high-fidelity FEA simulations, efficiently estimates SIF values at critical crack front locations (e.g., deepest point, surface intersections). Consequently, numerical integration via RK4 can be performed externally without repetitive FEA computations, drastically improving computational efficiency and enabling practical probabilistic analyses. The surrogate-based RK4 approach effectively approximates the integral formulation described above, bridging the continuous integral concept and practical discretizations in a clear, computationally feasible manner. Further details about the MLP model and

its integration with the RK4 method for probabilistic crack growth simulations are elaborated in the following sections.

5.2.2 SIF computation

As outlined in the introduction, the SIF is the principal parameter governing fatigue crack growth analyses. Conventional FEM can provide reliable SIF estimates for a single stationary crack, but they become impractical when the crack grows, multiple cracks are present, or many alternative crack shapes must be assessed: each new configuration requires regeneration of a fresh, topology conforming mesh, an effort that becomes even more complicated when the future crack path is unknown. Moreover, classical FEM relies on special quarter-point elements to reproduce the near-tip stress singularity, further complicating the model generation.

XFEM eliminates these bottlenecks by enriching the displacement approximation so that both discontinuities and singular fields are represented independently of the underlying mesh. This allows cracks to cut directly through finite elements [274, 275]. XFEM has proven especially effective for 3D problems with complex, unpredictable crack trajectories. It delivers high accuracy even on coarse or moderately refined meshes because the enrichment functions embed the asymptotic crack-tip behavior in the solution space [279]. A brief summary of XFEM formulation is provided in Appendix A1. However, this versatility comes at extra computational cost. High-cycle fatigue studies may require 10^3–10^8 load cycles and thus a very large number of nonlinear solution steps [279].

In this study, we use XFEM to compute SIFs of semi-elliptical surface cracks. We employ Code_Aster, an open source finite element software developed by EDF R&D for performing high-fidelity fracture simulations, providing the training data for the surrogate models described in Section 5.2.3. Accurate values of ΔK are essential, because any systematic error propagates through the Paris law integration (Eq. (5.4)) and increases uncertainty in service life and probability of failure predictions. XFEM allows for an extensive campaign of design experiments with minimal preprocessing effort. This is possible because XFEM keeps the background mesh unaltered while varying the crack geometry. This advantage is unattainable with conventional FEM.

The $G-\theta$ method employed in Code_Aster is used to extract SIFs by post-processing XFEM simulations. It is based on domain integral formulation, where the energy release rate (G) is obtained by taking the Lagrangian derivative of the potential energy with respect to a virtual crack extension velocity field, θ [280]. In this method, the θ field is defined in the vicinity of the crack front using a local coordinate system consisting of directions tangent to the crack faces and normal to the crack front as shown in Fig. 5.1. To avoid inaccuracies from stress singularities near the crack front, two concentric toroidal surfaces with inner radius R_{int} and outer radius R_{ext} around the crack front Γ define the integration domain (see Fig. 5.2). The θ field is constructed such that it is constant within the inner torus ($0 \leq r < R_{int}$), decreases linearly between inner and outer tori ($R_{int} \leq r \leq R_{ext}$), and vanishes beyond $r > R_{ext}$. A sensitivity analysis was performed to ensure that the computed energy release rate

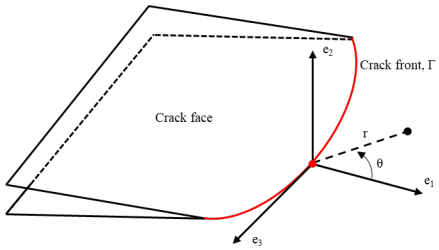

Fig. 5.1 Polar coordinate system defining the θ field in the vicinity of the crack front.

was independent of the size of the torus. In our study, we selected $R_{ext} = 6h$ and $R_{int} = 4h$, where h is the element size near the crack front.

Although the present study considers predominantly Mode I loading, the general relationship between the total energy release rate and the stress intensity factors for all three modes is:

$$\Delta G = \frac{\Delta K_I^2}{E'} + \frac{\Delta K_{II}^2}{E'} + \frac{1+\nu}{E}\Delta K_{III}^2 \tag{5.5}$$

where ΔK_I, ΔK_{II}, and ΔK_{III} denote the Mode I (opening/normal to the crack plane), Mode II (in-plane shear/sliding), and Mode III (out-of-plane shear/tearing) SIF ranges, E is the Young's modulus, and ν is Poisson's ratio. The effective modulus, $E' = E$ for plane stress, and $E' = E/(1-\nu^2)$ for plane strain conditions, respectively. Plane stress condition is assumed at the surface points and plane strain condition is considered at the deepest point of the crack front.

5.2.3 Surrogate modeling

Surrogate modeling provides an efficient means to approximate computationally intensive numerical models by constructing data-driven mappings between inputs and outputs. In essence, a surrogate acts as a reduced-order representation of the underlying high-fidelity model, enabling rapid evaluations once trained. In fatigue crack growth analysis, where the computation of SIFs through FEA demands substantial resources, surrogates offer a practical alternative that preserves the essential physics of the system while drastically reducing computational effort [63, 206, 265]. By interpolating or regressing

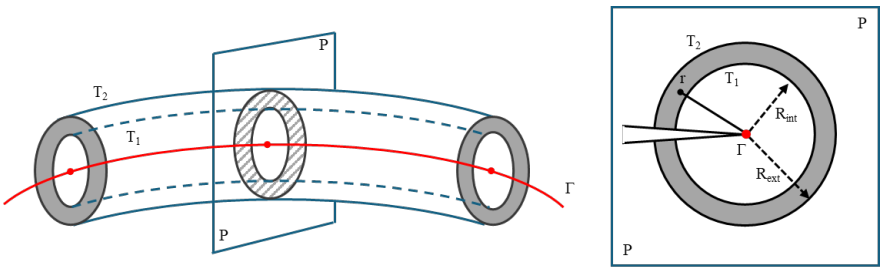

Fig. 5.2 Schematic of toroidal surfaces surrounding the crack front Γ used for the computation of SIF using $G-\theta$ method [280].

on strategically sampled data from high-fidelity simulations, these models provide near-instantaneous SIF predictions over a wide range of geometrical and loading configurations.

Among various surrogate modeling techniques, such as polynomial response surfaces, Gaussian processes or Kriging, artificial neural networks, particularly multilayer perceptrons (MLPs), have gained prominence for problems involving highly nonlinear and high-dimensional relationships. An MLP consists of sequential layers of interconnected neurons that transform input features through nonlinear activation functions, allowing the network to approximate arbitrary continuous mappings between inputs and outputs. This hierarchical architecture enables the model to capture intricate dependencies between geometric variables (e.g., crack depth, surface half-length, and crack separation) and resulting fracture responses (e.g., ΔK at crack front points), which are often intractable for conventional analytical formulations.

For crack growth simulations, the relationship between input parameters and SIFs is inherently nonlinear, influenced by local geometry, interaction effects, and boundary conditions. Traditional regression-based surrogates struggle to reproduce such complexity without a prohibitive number of terms or sampling points. MLPs, in contrast, learn these nonlinearities directly from data through gradient-based optimization, making them particularly suitable for surrogate-assisted fatigue analyses. Several studies have demonstrated their superior performance in capturing multi-variable dependencies in structural mechanics and fracture problems, achieving low prediction errors across wide parametric ranges [264].

A key challenge in surrogate modeling lies in balancing model expressiveness with generalization capability. Overly complex networks may overfit the training data, while under specified architectures fail to capture the necessary physics. Effective surrogate development thus requires a well-designed training dataset that spans the physically relevant parameter space, ensuring robustness across diverse crack configurations, including interacting and coalesced states. Techniques such as regularization, dropout, and cross-validation can further mitigate overfitting and enhance model stability during extrapolation. Once trained, the MLP surrogate allows the efficient evaluation of ΔK at crack front locations, eliminating the need for repeated XFEM computations. This makes it possible to integrate the Paris law affordably into subsequent probabilistic analyses, whether through Euler or Runge–Kutta (RK4) schemes.

5.3 Problem formulation and methodological framework

5.3.1 Problem statement and research gap

The accurate assessment of fatigue life in offshore wind turbine monopile foundations remains a critical challenge, driven by the complex interplay of cyclic loading, weld imperfections, and multiple interacting surface cracks. Traditional fatigue reliability methods often rely on closed-form SIF formulations derived from industrial standards, which, although computationally efficient, are generally restricted to idealized single crack scenarios under simplified geometries and loading

conditions. These formulations fail to account for the nonlinear effects of crack interactions and coalescence—phenomena frequently observed in welded joints where adjacent defects amplify local SIFs and accelerate crack growth [24, 200]. Such limitations become particularly critical in offshore environments, where multiple defects induced by welding or corrosion are common, and dynamic loading from waves and wind exacerbates fatigue damage at structural hotspots.

Existing surrogate modeling approaches, including Gaussian process regression and polynomial-based response surfaces, face challenges in capturing the abrupt SIF variations that arise during crack coalescence. While effective for single crack problems, these methods often struggle with high-dimensional input and output states, limiting their adaptability to the evolving geometries of interacting cracks. Consequently, alternative strategies capable of efficiently learning complex nonlinear dependencies are required. Multilayer perceptrons (MLPs), with their hierarchical architecture and capacity to approximate nonlinear mappings, offer a promising pathway to overcome these limitations.

Although three-dimensional XFEM simulations provide detailed insights into crack front behavior, their high computational cost makes them impractical for probabilistic analyses such as Monte Carlo simulations (MCS), which require thousands of model evaluations to quantify uncertainty in crack growth and failure probabilities. This restriction hinders realistic reliability assessments that capture the true behavior of interacting cracks, leaving a significant methodological gap.

The need for a robust and computationally scalable solution is underscored by the potentially severe consequences of underestimating failure risk in offshore wind structures. Neglecting crack interactions can result in non-conservative reliability estimates, compromising safety and operational longevity—especially during mid-life stages when coalescence events become more likely. This study is therefore motivated by the absence of a unified surrogate framework capable of seamlessly handling both pre- and post-coalescence regimes within a probabilistic context. The proposed approach addresses this gap by integrating MLP-based surrogates trained on high-fidelity XFEM datasets with a state-adaptive crack growth framework, thereby enabling efficient and accurate reliability analysis of welded monopile foundations under realistic multi-crack conditions.

5.3.2 Proposed methodological framework

System state and input definition

The proposed framework defines the system state to encapsulate the evolving geometry and spatial relationships of multiple semi-elliptical surface cracks within a welded offshore detail, providing the foundation for surrogate-based fatigue reliability analysis. The state is represented by parameters describing the dimensions and positions of the cracks, along with their proximity. This enables the model to track changes as the cracks interact and potentially coalesce over time. This flexible representation accommodates both pre- and post-coalescence scenarios and is coupled with loading conditions that reflect the dynamic stresses experienced by the structure.

The input space for surrogate prediction is constructed from geometric features and loading variables carefully selected to capture the dominant factors influencing SIFs. These inputs are

normalized and structured to ensure robustness and generalization across interacting pairs, coalesced cracks, and isolated offset cracks. Multiple specialized MLP surrogates are employed, each tailored to a specific crack regime—interacting, post-coalescence, and single offset configurations—allowing the system to adapt its SIF predictions based on the current state. This modular structure supports the integration of surrogate models into a probabilistic crack growth simulation, where the inputs drive ΔK prediction at critical crack front locations, forming the foundation for accurate fatigue life assessment.

The definition of the system state and inputs further enables a comparative analysis of crack interaction effects, isolating the influence of coalescence on reliability. By incorporating a diverse range of crack geometries and loading scenarios, the input design ensures that the MLP surrogates can handle the nonlinear transitions associated with crack merging—an aspect that remains challenging for traditional analytical models. This setup establishes the groundwork for large-scale MCS to quantify time-dependent failure probabilities, comparing configurations with and without crack interactions.

Crack evolution and coalescence handling

Crack growth is governed by the Paris law, as described in Section 5.2.1, with propagation rates computed at three critical front points—the deepest point and two surface intersections—and integrated over the number of cycles N using a fourth-order Runge–Kutta (RK4) scheme. This higher-order integration method accurately captures crack evolution by evaluating intermediate states within each step, enhancing numerical stability and precision over long-term simulations. At each RK4 sub-step, SIF ranges (ΔK) are dynamically queried from the appropriate MLP surrogate, selected according to the current crack state (interacting or coalesced), thereby eliminating the need for repeated high-fidelity XFEM evaluations and substantially reducing computational overhead. The surrogate inherently captures interaction effects through its training data, ensuring seamless SIF predictions that reflect evolving crack geometry and proximity.

Coalescence is detected by monitoring the minimum separation (δ) between the adjacent surface points of the two semi-elliptical cracks. When δ falls below a threshold of 0.02 mm—determined based on mesh resolution and consistency with XFEM training data—the cracks are deemed coalesced. At this stage, an equivalent semi-elliptical crack is defined by geometric continuity, enveloping the maximum depth and total surface span of the original cracks. The same equivalent-ellipse construction is used to trigger the surrogate switch and to ensure continuity of the system limit-state; see Section 5.4.3 for the limit-state definition. The system state vector is then updated to represent this single crack, and the surrogate mapping automatically transitions to the post-coalescence mode. This approach ensures a continuous evolution of ΔK values without artificial discontinuities in the RK4 integrator, preserving numerical stability and capturing the nonlinear SIF changes associated with the coalescence event. Such consistency is essential for reliable fatigue life predictions and downstream reliability evaluation.

Computational workflow

The computational workflow orchestrates the integration of the proposed framework into a unified process for fatigue reliability assessment. The procedure begins with the initialization of crack geometry and loading conditions, establishing the baseline system state for crack growth simulation. The RK4 scheme then iteratively advances the crack front, dynamically querying the relevant MLP surrogate to obtain ΔK at each step without requiring additional XFEM computations. Coalescence detection and geometric updating occur automatically, ensuring a continuous evolution of the system state throughout the simulation.

Subsequently, uncertainties in initial crack dimensions, material parameters, and loading conditions are propagated through the surrogate-based model. Random samples are generated to represent these uncertainties, and the Paris law is integrated via RK4 for each realization, forming the basis for probabilistic evaluation. Limit-state functions are then assessed to estimate the probability of failure over the structure's lifetime. This workflow supports both deterministic and probabilistic analyses, combining computational efficiency with high-fidelity. It forms the foundation for the MCS ensemble described in the following subsection.

The complete surrogate-assisted probabilistic fatigue framework is summarized schematically in Fig. 5.3, which highlights the integration of MLP-based SIF prediction, RK4 crack growth, coalescence handling, and MCS-driven reliability evaluation.

Probabilistic analysis

The probabilistic analysis framework quantifies the time-dependent reliability of offshore wind monopile foundations by explicitly accounting for uncertainties in crack growth, material properties, and environmental loading. The uncertain parameters—including initial crack dimensions, crack growth parameters, and stress range—are modeled as random variables that influence the evolution of the crack state. These uncertainties are propagated through the surrogate-based RK4 integration, which efficiently predicts ΔK at each time step and enables the simulation of diverse crack trajectories over the structure's service life.

MCS is employed to evaluate the probability of failure, leveraging its robustness in handling the nonlinear and path-dependent nature of fatigue crack propagation. A large ensemble of realizations is generated, and failure probabilities are obtained by evaluating limit-state functions, such as through-thickness penetration. The use of MLP surrogates that dynamically switch between interacting and coalesced crack regimes eliminates the computational bottleneck associated with repeated finite element evaluations, allowing the simulation to scale efficiently to thousands of samples.

By embedding surrogate-driven crack growth within the MCS framework, the proposed methodology enables comprehensive system-level reliability assessment of welded monopile foundations. The framework's modularity allows for the incorporation of additional uncertainty sources or alternative failure definitions while maintaining computational feasibility. This unified, state-adaptive surrogate

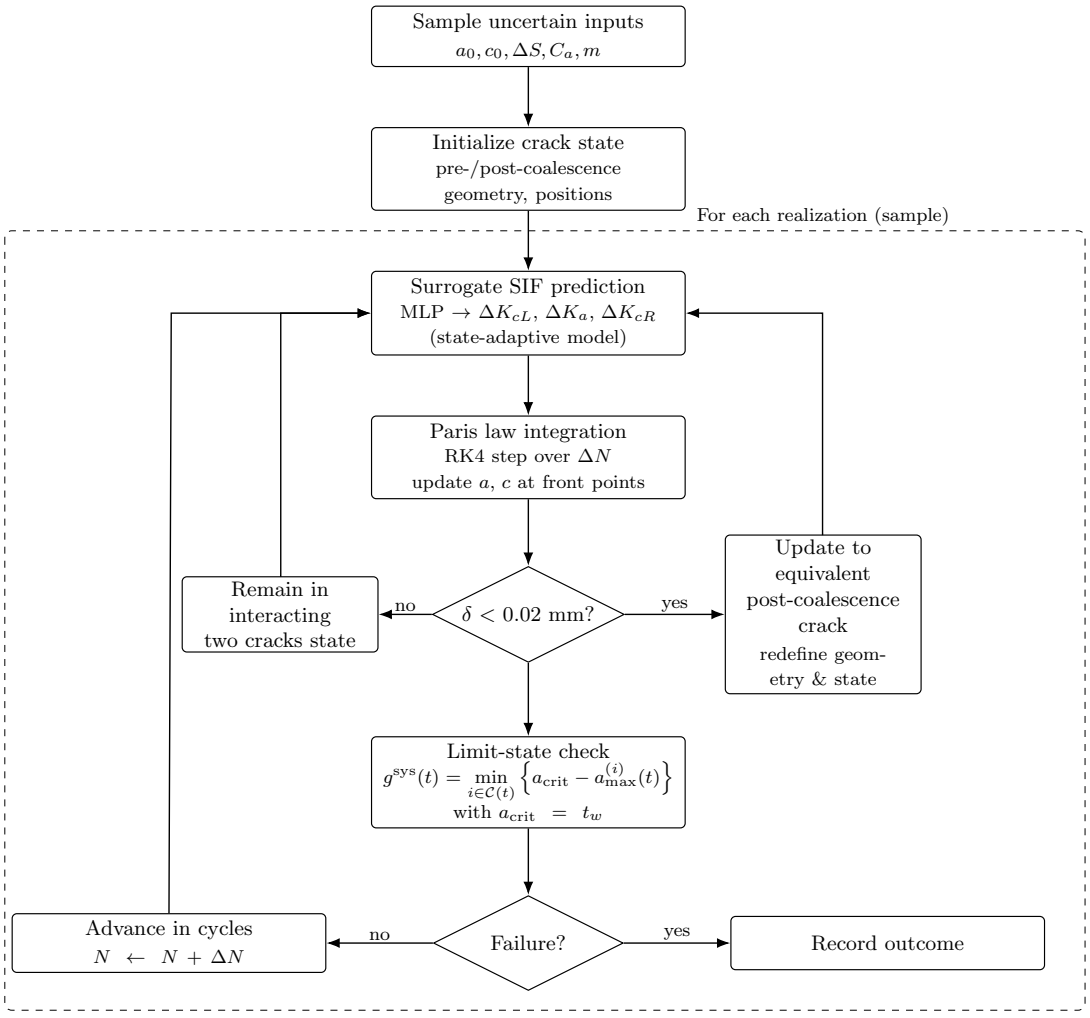

Fig. 5.3 Computational workflow integrating state-adaptive MLP-based stress intensity factor (SIF) prediction, Runge–Kutta (RK4) crack growth integration, coalescence detection, and Monte Carlo simulation (MCS) for reliability estimation.

framework bridges high-fidelity simulation and probabilistic fatigue reliability analysis, forming the basis for the case study presented in Section 5.4.

5.4 Case study: Offshore wind welded monopile foundation

This case study evaluates the fatigue reliability of a welded circumferential connection in an offshore wind turbine monopile using the surrogate-based probabilistic framework described in Section 5.3.2. Five configurations are analyzed:

(i) two interacting semi-elliptical surface cracks placed symmetrically about the $+Y$ axis at the weld toe with an angular separation $\beta = 0.003$ radians (9 mm center-to-center),
(ii) a single semi-elliptical crack at an angular offset $\beta = 0.0015$ radians, providing an isolated configuration with comparable geometry and loading,
(iii) two single offset cracks positioned at $\beta = \pm 0.0015$ radians, each modeled using the single offset MLP surrogate and evaluated as a series system, i.e. system failure occurs when either crack reaches the critical depth,
(iv) two single offset cracks positioned at $\beta = \pm 0.0015$ radians that are allowed to coalesce once the surface separation δ between their adjacent tips falls below the threshold defined in Section 5.3.2; prior to coalescence both cracks are propagated using the single offset surrogate and the two component limit-state, and after coalescence an equivalent semi-elliptical crack is propagated using the post-coalescence single crack surrogate, and
(v) two semi-elliptical cracks configuration with a wider angular separation, $\beta = 0.009$ radians, simulated using the interacting two crack surrogate trained for this spacing as a sensitivity case to examine how the probability of failure varies with crack separation.

To ensure consistency, identical random seeds are employed across these configurations so that initial crack sizes, crack growth parameters, and stress ranges are matched sample-wise, isolating the effects of crack interaction, coalescence treatment, and angular separation on fatigue reliability.

The fixed angular separation value (β=0.003 radians) adopted for the interacting crack MLP surrogate is to facilitate a controlled comparison with the single crack scenario while maintaining consistency in the stress field around the $+Y$ axis. Within the interacting case, the surrogate-based crack growth model automatically transitions to the post-coalescence single crack regime when the surface separation δ falls below the prescribed threshold (0.02 mm), ensuring continuity in the evolution of the ΔK.

The subsequent sections describe the numerical setup of the case study, including the monopile geometry, boundary conditions, and probabilistic inputs used to train and evaluate the surrogate models prior to their validation and reliability analyses discussed in Section 5.5.

5.4.1 Geometry, material, and loading conditions

The structure under study is a 30 m monopile with a 3 m outer radius (R_o) and a 90 mm wall thickness (t_w), installed in a water depth of 20 m. The examined detail is a circumferential welded connection located 12 m above the seabed; its geometry and dimensions are shown in Fig. 5.4. The monopile is assumed to be made of S355 structural steel, commonly used for offshore foundations [155], with modulus of elasticity $E = 2.1 \cdot 10^5$ MPa and Poisson's ratio $\nu = 0.3$. While not implemented here, distinct properties for base metal, weld metal, and heat-affected zone could be considered in future work.

Consistent with practical scenarios [255], a service life of 20 years is assumed, during which the detail experiences approximately $7 \cdot 10^7$ stress cycles per year due to combined wind and wave loading

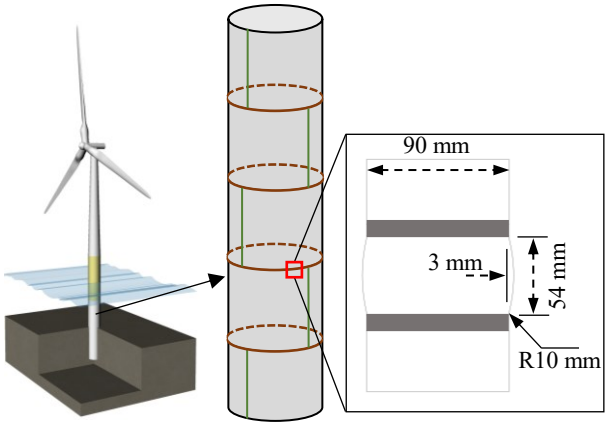

Fig. 5.4 Schematic of a typical offshore wind turbine monopile foundation indicating longitudinal and circumferential welds. The investigated circumferential weld geometry and dimensions are highlighted.

[257]. Following industrial practice [45], crack growth parameters are calibrated from a Class D S-N curve representative of seawater with cathodic protection, using the procedure as in [12]. The resulting parameters are listed in Table 5.1 and they are adopted in the probabilistic analysis.

Based on industrial standard recommendations [45], the long-term stress range (ΔS) is approximated using a two-parameter Weibull distribution. The Weibull scale (q) and shape (h) parameters are also provided in Table 5.1. Furthermore, the monopile is assumed fixed to the seabed by restricting all degrees of freedom at the bottom (clamped condition) in the model. The applied global bending moment acting with a clamped base produces predominant Mode I opening at the circumferential weld toe where the cracks are introduced.

Table 5.1 Random variables and deterministic constants adopted in the case study (calibrated from Class D S-N curve in seawater with cathodic protection).

Variables	Distribution	Mean (Median)	Std (CoV)
a_0 [mm]	Exponential	0.5785	–
a_0/c_0	Deterministic	0.2 [32]	–
$\log C_a$ [1]	Normal	-27.7860	0.5619
q	Normal	4.1833	(0.25)
h	Deterministic	0.8 [32]	–
m	Deterministic	3.0	–
N_c [cycles per year]	Deterministic	$7 \cdot 10^7$ [281]	–

[1] Units of da/dN and ΔK are mm/cycle and MPa$\sqrt{\text{mm}}$, respectively.

5.4.2 Finite element modeling strategy

A global 3D solid FE model of the monopile, including the explicit weld profile at 12 m above the seabed (see Fig. 5.4), is employed to capture stiffness distribution and stress transfer through the thickness. Linear hexahedral elements are used away from the weld to maintain computational economy, with a target in-plane mesh size of ~ 600 mm and at least three elements through the 90 mm wall to resolve bending. In the weld vicinity, the mesh is refined to ~ 100 mm and tetrahedral elements are used to represent the curvature introduced by the weld geometry.

A kinematically coupled reference node is attached to the top face so that an imposed bending moment induces a rigid-body rotation of the coupled nodes. The moment is transmitted as an equilibrated traction field over the face rather than as a concentrated couple, yielding a clean pure-moment section without any shear. The base is fully clamped, producing opening stresses at the weld toe where cracks are introduced. This configuration ensures that the applied global bending moment induces predominantly Mode I opening at the crack locations.

Following standard submodeling practice [282], a local submodel is extracted around the circumferential weld to resolve near-tip fields and compute SIFs efficiently. The submodel employs quadratic tetrahedral elements and displacement-driven boundary conditions obtained by projecting global model displacements onto the submodel cut surfaces. This approach reproduces the global kinematics locally while allowing refined meshing only where required. Opposing faces of the global and local models are meshed with matching node densities to minimize interpolation error, and nodal displacements are mapped consistently onto the submodel boundaries. The submodel mesh is refined with a characteristic element size ranging from 2.65 mm at the weld toe to 80 mm in the far field. The characteristic size represents the maximum edge or diagonal length of individual 3D elements. This refinement provides accurate resolution of near-tip fields while maintaining computational efficiency in the surrounding regions. The global and local finite element models used in the analysis are illustrated in Fig. 5.5.

Semi-elliptical surface cracks are placed at the weld toe using a cylindrical coordinate system with the Z-axis along the monopile length and the X–Y plane defining the cross-section. The two semi-elliptical cracks lie on the outer surface of the monopile at radius R_o, centered symmetrically about the Y-axis at angular offsets $\pm\beta/2$ in the X–Y plane. Hence, the crack centers are located at $\big(\pm R_o \sin(\beta/2),\ R_o \cos(\beta/2),\ z_{\text{weld}}\big)$, where z_{weld} denotes the height of the weld along the monopile length. For the post-coalesced single crack configuration, the semi-elliptical surface crack is positioned at the intersection of the weld toe and the positive Y-axis, i.e., on the outer radius R_o of the monopile at coordinates $(0,\ R_o,\ z_{\text{weld}})$.

The accuracy of the SIFs obtained from the FE analyses is ensured through a systematic mesh refinement scheme around the crack front. The refinement procedure defines a target element size near the crack tip (h_c) as the minimum of two characteristic lengths: one related to crack depth and another to crack-tip separation. The depth-based size decreases proportionally with crack depth to maintain an approximately constant number of elements (typically 6–8) across the radial extent of

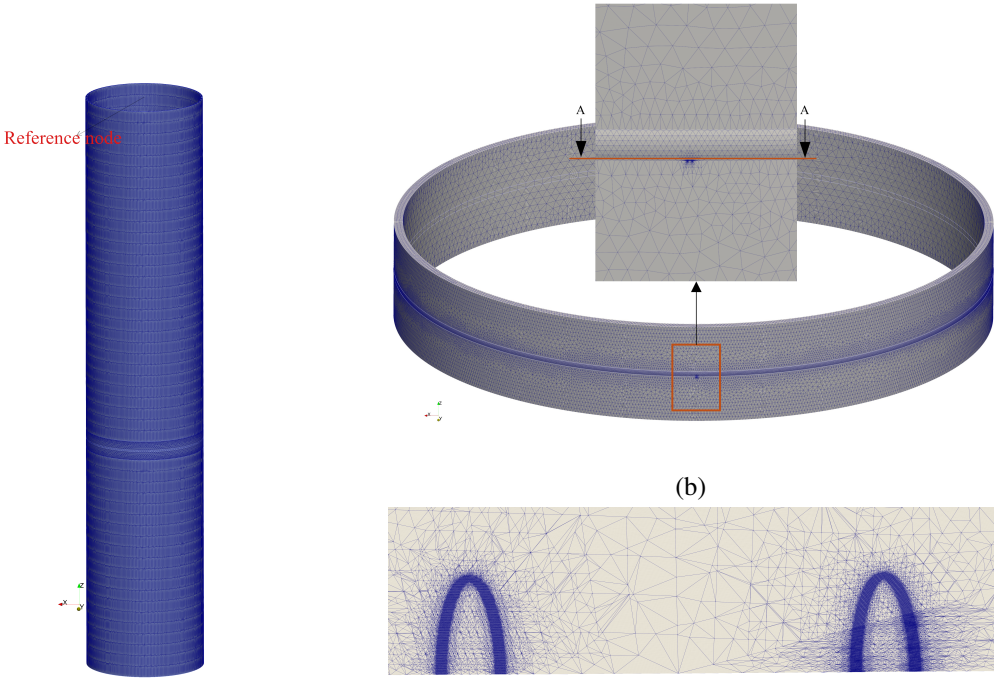

(a) (b) (c)

Fig. 5.5 Finite element models developed for the offshore wind monopile foundation: (a) global model capturing the overall stiffness distribution and boundary conditions; (b) refined submodel around the circumferential weld showing the detailed mesh near the weld toe with a zoomed view of the weld region; and (c) sectional view along A-A illustrating the adjacent semi-elliptical crack fronts.

the crack front. When two cracks are in close proximity, an additional constraint ensures at least four elements between adjacent crack tips, with a lower bound imposed on h_c to prevent excessive refinement. Starting from an initial coarse mesh size (h_0), successive uniform refinements are applied according to $h = h_0/2^n$, where n is the smallest integer satisfying $h \leq h_c$. This hierarchical refinement provides a balanced compromise between accuracy and computational efficiency while maintaining sufficient element density to capture the stress singularity at the crack front. The complete refinement procedure is summarized in Appendix A2. Fig. 5.5 (c) illustrates the locally refined mesh distribution in the vicinity of the semi-elliptical crack fronts. The refined mesh near the crack front enables accurate evaluation of SIFs, which are computed along each semi-elliptical front using the G–θ method described in Section 5.2.2. Additional finite element validation exercises confirmed the reliability of the computed SIFs, as presented in Appendix A3.

5.4.3 Model implementation and probabilistic inputs

The proposed framework is implemented by integrating regime-specific MLP surrogates with MCS to evaluate fatigue reliability. Three crack regimes are represented: (i) two interacting semi-elliptical surface cracks, (ii) a post-coalescence single semi-elliptical crack, and (iii) a single offset semi-

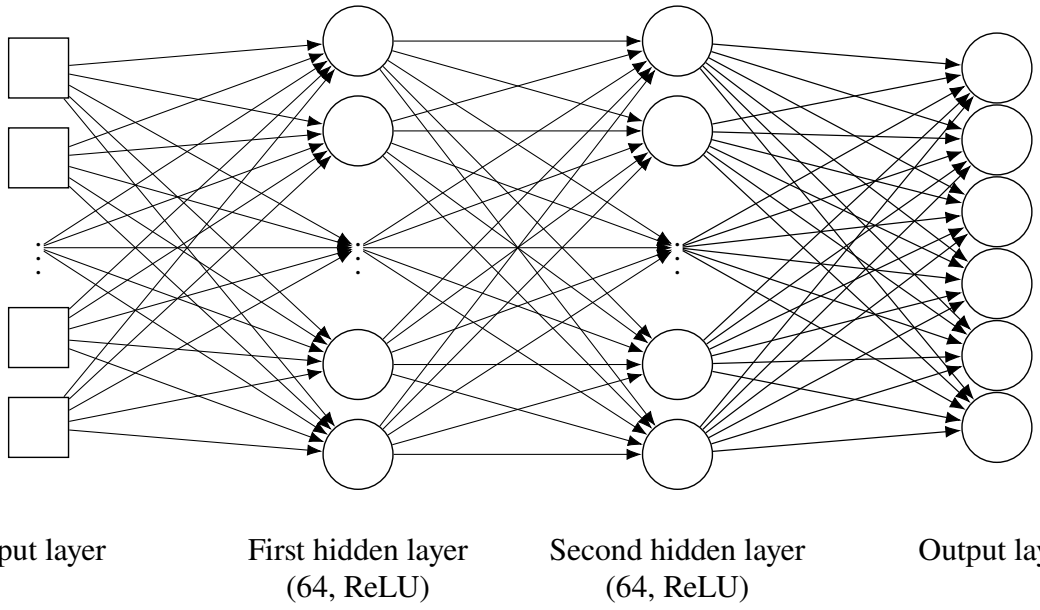

Fig. 5.6 Architecture of the multilayer perceptron (MLP) surrogate model used for SIF prediction. Each network consists of an input layer, two hidden layers with 64 neurons and ReLU activation functions, and an output layer. The input and output dimensions vary with the crack configuration: (i) 6 inputs and 6 outputs for two interacting semi-elliptical cracks at a prescribed angular separation (two specialized networks for $\beta = 0.003$ and $\beta = 0.009$ radians), (ii) 3 inputs and 3 outputs for the post-coalescence single crack, and (iii) 3 inputs and 3 outputs for the single offset crack.

elliptical crack. For the interacting regime, two specialized MLPs are trained, one for each prescribed angular separation ($\beta = 0.003$ and $\beta = 0.009$ radians). In total this yields four distinct MLPs grouped into three regimes: two interacting crack networks (for $\beta = 0.003$ and 0.009 radians) and one network each for the post-coalesced and single offset crack configurations. These models predict ΔK at three locations on the crack front (left surface point, deepest point, and right surface point). All networks share the same architecture, with two hidden layers of 64 neurons and ReLU (Rectified Linear Units) activations, but they are tailored to the specific input–output dimensions of each crack regime. The MLP architecture used is shown in Fig. 5.6.

For the two semi-elliptical cracks MLPs (one for $\beta = 0.003$ radians and one for $\beta = 0.009$ radians), the input vector includes the crack depths and half-lengths $\{a^{(1)}, c^{(1)}, a^{(2)}, c^{(2)}\}$, the long-term stress range (ΔS), and the bending moment (M) deterministically computed from ΔS via Euler's beam theory (6 inputs in total). For a given angular separation β the crack center coordinates and separation are fixed by the monopile geometry, so they are not included as explicit features. We retain both ΔS and M in the input to improve numerical conditioning and to make the learned mapping robust to minor changes in how the load is parametrized. The outputs are the six ΔK values at the three front points for each crack: $\{\Delta K_{cR}^{(1)}, \Delta K_{a}^{(1)}, \Delta K_{cL}^{(1)}, \Delta K_{cR}^{(2)}, \Delta K_{a}^{(2)}, \Delta K_{cL}^{(2)}\}$. For the coalesced and single offset MLPs, the inputs reduce to three variables $\{a^{(1)}, c^{(1)}, \Delta S\}$, and the outputs to $\{\Delta K_{cR}^{(1)}, \Delta K_{a}^{(1)}, \Delta K_{cL}^{(1)}\}$.

Table 5.2 Input ranges for the interacting two crack multilayer perceptron (MLP) surrogates for the two prescribed angular separations $\beta = 0.003$ and $\beta = 0.009$ radians.

β [radians]		$a^{(1)}$ [mm]	$c^{(1)}$ [mm]	$a^{(2)}$ [mm]	$c^{(2)}$ [mm]	ΔS [MPa]	M [N-mm]
0.003	Min	7.66×10^{-3}	3.83×10^{-2}	6.39×10^{-3}	3.20×10^{-2}	1.17	2.84×10^{9}
	Max	1.48	6.78	1.58	6.95	10.09	2.46×10^{10}
0.009	Min	1.24×10^{-2}	6.20×10^{-2}	7.68×10^{-3}	3.02×10^{-2}	1.00	2.44×10^{9}
	Max	4.65	2.16×10^{1}	5.10	2.14×10^{1}	10.46	2.54×10^{10}

Training data for the interacting two crack MLPs are tailored to the monopile case study rather than constructed as a generic, geometry-independent design of experiments. For each prescribed angular separation ($\beta = 0.003$ and $\beta = 0.009$ radians), candidate crack geometries are generated by sampling initial crack sizes and stress ranges from the probabilistic models shown in Table 5.1. The samples are then filtered to ensure physically meaningful and numerically resolvable states. Both cracks remain strictly shallower than the wall thickness; aspect ratios a/c are within a realistic range representative of weld-toe surface flaws; and crack depths are bounded below by the smallest value for which the XFEM model yields stable SIFs ($a_{\min} \approx 8.27 \times 10^{-4}$ mm). This sampling strategy concentrates the training data on the region of the input space most relevant to the monopile weld without relying on prior knowledge of failure probabilities.

After filtering, the interacting datasets contain 1803 samples for $\beta = 0.003$ radians and 2805 samples for $\beta = 0.009$ radians. In both cases, an 80:20 split is used for training and testing, and an internal 80:20 split of the training set is reserved for early-stopping validation. The input ranges for the interacting surrogates are summarized in Table 5.2. For the coalesced and single-offset models, 2800 training and 250 test samples are generated using Latin hypercube sampling (LHS), with inputs $a^{(1)} \in [1.26 \times 10^{-4},\ 85]$ mm and $\Delta S \in [0.48,\ 8.68]$ MPa, and $c^{(1)}$ computed from the aspect ratio $a^{(1)}/c^{(1)} \in [0.1,\ 0.9]$.

The main hyperparameters of the MLPs are the number of hidden layers, the number of neurons per layer, the activation function, and the optimization settings (learning rate, weight decay, batch size, and early-stopping patience). Preliminary trials were carried out on a subset of the interacting crack data with 1–3 hidden layers and 32–128 neurons per layer. The architecture with two hidden layers of 64 neurons and ReLU activation was found to provide the best compromise between prediction accuracy, robustness, and training time. Deeper or wider networks only marginally improved validation loss, but increased the risk of overfitting and computational cost, whereas smaller networks systematically underfitted the SIF response.

For all regimes, the networks are trained with a stochastic, adaptive gradient-based optimizer with decoupled weight decay, using a learning rate of 10^{-3} and weight decay 10^{-4}. Batch size of 256 samples and a mean squared error (MSE) loss function are adopted. An internal validation set is used to monitor training; early stopping with a patience of 120 epochs is applied, and the model

parameters corresponding to the minimum validation loss are retained for subsequent testing and reliability analyses.

All input and output variables are standardized to have zero mean and unit variance based on the training set statistics before entering the network, and the corresponding scaling parameters are stored together with the trained weights so that the same transformation is applied consistently during crack growth and Monte Carlo simulations.

To ensure reproducibility, the pseudo-random number generators that control the training-testing data splits, parameter initialization, and mini-batch shuffling are initialized with fixed seeds. The final trained weights, scaling parameters, and metadata (feature order, target names, and architecture settings) are archived. Rerunning the training procedure with the same data and seeds produces the same surrogate models used in this paper.

The trained MLPs are validated against held-out FE data, achieving high predictive accuracy (see Section 5.5). For the interacting two crack surrogates the test sets yield $R^2 \approx 0.998$–1.000 with mean absolute errors (MAE) in the range of 0.025–0.048 MPa$\sqrt{\text{mm}}$. Meanwhile, the coalesced and single-offset surrogates attain $R^2 \geq 0.999$ with MAE of approximately 0.28–0.34 MPa$\sqrt{\text{mm}}$. These surrogates replace the need for repeated FE evaluations by providing ΔK estimates in milliseconds, which is critical for large MCS ensembles.

The limit-state function relates the evolving crack depth to a prescribed critical size, defining failure consistently across interacting and coalesced regimes. The local welded detail is treated as a system comprising two components (two interacting surface cracks). System failure is declared when either crack reaches or exceeds the critical depth, taken as the monopile wall thickness ($a_{\text{crit}} = t_w$). Accordingly, the system-level limit-state is expressed as

$$g^{\text{sys}}(t) = \min_{i \in \mathscr{C}(t)} \{a_{\text{crit}} - a_{\max}^{(i)}(t)\}, \tag{5.6}$$

where $\mathscr{C}(t)$ denotes the set of existing cracks at time t, two separate cracks prior to coalescence and one equivalent crack thereafter.

A negative value of $g^{\text{sys}}(t)$ indicates failure. Once the surface separation δ between the two cracks falls below the coalescence threshold ($\delta < 0.02$ mm), a single equivalent semi-elliptical crack is defined and the limit state reduces to $g^{\text{sys}}(t) = a_{\text{crit}} - a(t)$. The equivalent semi-ellipse is constructed by geometric continuity, enveloping the maximum depth and the total surface span of the two fronts. Thus at coalescence time, t_{coal}, the system limit-state smoothly reduces to the single-component form, with no jump in $g^{\text{sys}}(t)$ (i.e., $g^{\text{sys}}(t) = a_{\text{crit}} - a(t)$ for $t \geq t_{\text{coal}}$). This formulation ensures a consistent transition across the pre- and post-coalescence regimes and provides a clear criterion for evaluating the probability of failure within the MCS framework.

5.5 Results and Discussion

This section quantifies the accuracy of the proposed surrogates and examines their implications for crack growth and structural reliability.

First, we validate the MLP-predicted ΔK at the three crack front locations against held-out FE data for all regimes (two interacting cracks, post-coalescence single crack, and single offset crack). Secondly, we verify that surrogate-driven Paris law integrations reproduce FE-driven crack growth trajectories when both are advanced using an explicit Euler scheme. To isolate surrogate fidelity from coalescence logic, this test is performed using two semi-elliptical crack samples that do not coalesce within the service life of the structure.

Finally, we quantify system-level reliability by performing large-scale Monte Carlo analysis with adaptive RK4 integration of Paris law. Five configurations are examined, consistent with the case study definition in Section 5.4:

(i) two interacting semi-elliptical cracks at $\beta = 0.003$ radians,
(ii) a single semi-elliptical crack at $\beta = +0.0015$ radians,
(iii) two single offset cracks at $\beta = \pm 0.0015$ radians, each propagated with the single-offset surrogate and evaluated using the two-component system limit-state of Eq. 5.6,
(iv) two single offset cracks at $\beta = \pm 0.0015$ radians that are propagated with the single-offset surrogate until the surface separation δ falls below the coalescence threshold, after which a single equivalent crack is evolved with the post-coalescence surrogate under the same system limit-state, and
(v) two interacting semi-elliptical cracks with a wider separation $\beta = 0.009$ radians for spacing sensitivity.

Identical random seeds are used across all simulations so that differences in predicted $P_f(t)$ isolate the effects of crack interaction, coalescence treatment, and angular separation captured by the surrogates.

5.5.1 Validation of MLP Surrogates

The performance of the two interacting semi-elliptical crack surrogates is validated in Figs. 5.7 and 5.8, which show parity plots for the six ΔK outputs for the $\beta = 0.003$ and $\beta = 0.009$ radians models, respectively. In both cases, the test points cluster tightly around the 45° line, with no systematic bias across the range of SIFs relevant for the monopile case study. For $\beta = 0.003$ radians, the overall test-set errors are root mean square error (RMSE) = 0.052 MPa$\sqrt{\text{mm}}$, mean absolute error (MAE) = 0.032 MPa$\sqrt{\text{mm}}$ and $R^2 = 0.999$, with per-output MAE values between 0.025 and 0.038 MPa$\sqrt{\text{mm}}$. For $\beta = 0.009$ radians, the overall test-set errors are RMSE = 0.060 MPa$\sqrt{\text{mm}}$, MAE = 0.038 MPa$\sqrt{\text{mm}}$ and $R^2 = 0.9993$, with per-output MAE values between 0.030 and 0.048 MPa$\sqrt{\text{mm}}$. Across both separations, the interacting surrogates thus achieve R^2 values in the range of 0.998–1.000 and MAE levels typically below 0.05 MPa$\sqrt{\text{mm}}$, which is sufficient for reliability-level crack growth simulations.

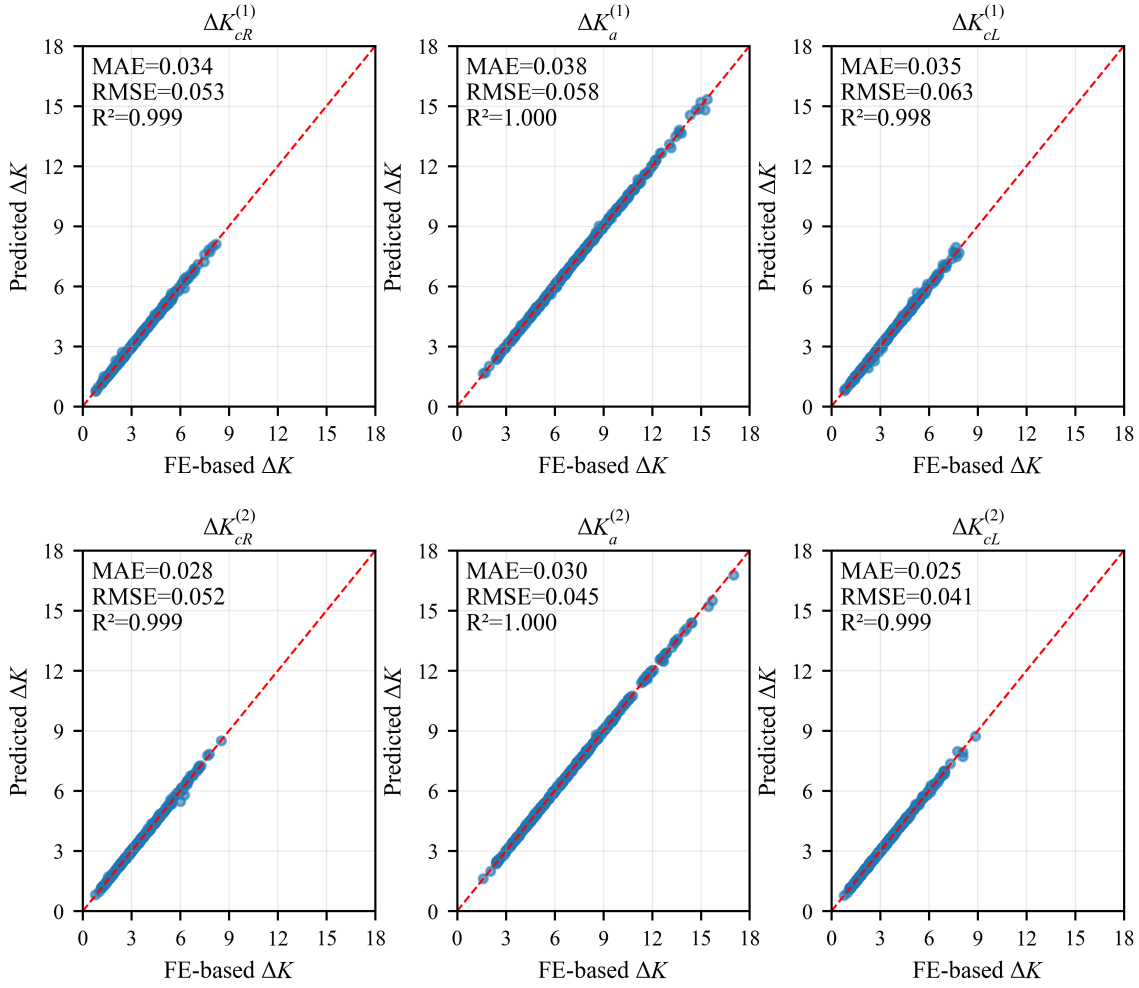

Fig. 5.7 Parity of MLP-predicted versus FE-computed SIF range (ΔK) at the three crack front locations for both cracks for the interacting configuration with angular separation $\beta = 0.003$ radians. The plots show the 20% hold-out test set for all six outputs together with a dashed $y = x$ reference line. Mean absolute error (MAE), root mean square error (RMSE), and R^2 for each output are reported within the subplots.

Similarly, for the post-coalescence single crack surrogate, Fig. 5.9 shows that across 250 held-out configurations, the predictions cluster tightly around $y = x$ with R^2 values ≥ 0.999, MAEs of 0.282-0.320, and RMSEs of 0.403-0.591, maintaining accuracy up to $\Delta K \approx 125$ MPa$\sqrt{\text{mm}}$. For the single offset crack surrogate, Fig. 5.10 reveals that 250 held-out cases over a ΔK range of [0, 122] align closely with $y = x$, with R^2 values ≥ 0.999, MAE of 0.283-0.337, and RMSE of 0.424–0.617, showing no bias at high ΔK.

Further validation of the two semi-elliptical cracks MLP surrogate is demonstrated by comparing crack growth trajectories obtained using SIFs predicted by the MLP against FE-based results, both integrated with an explicit Euler scheme over 20 years. Fig. 5.11 illustrates five representative

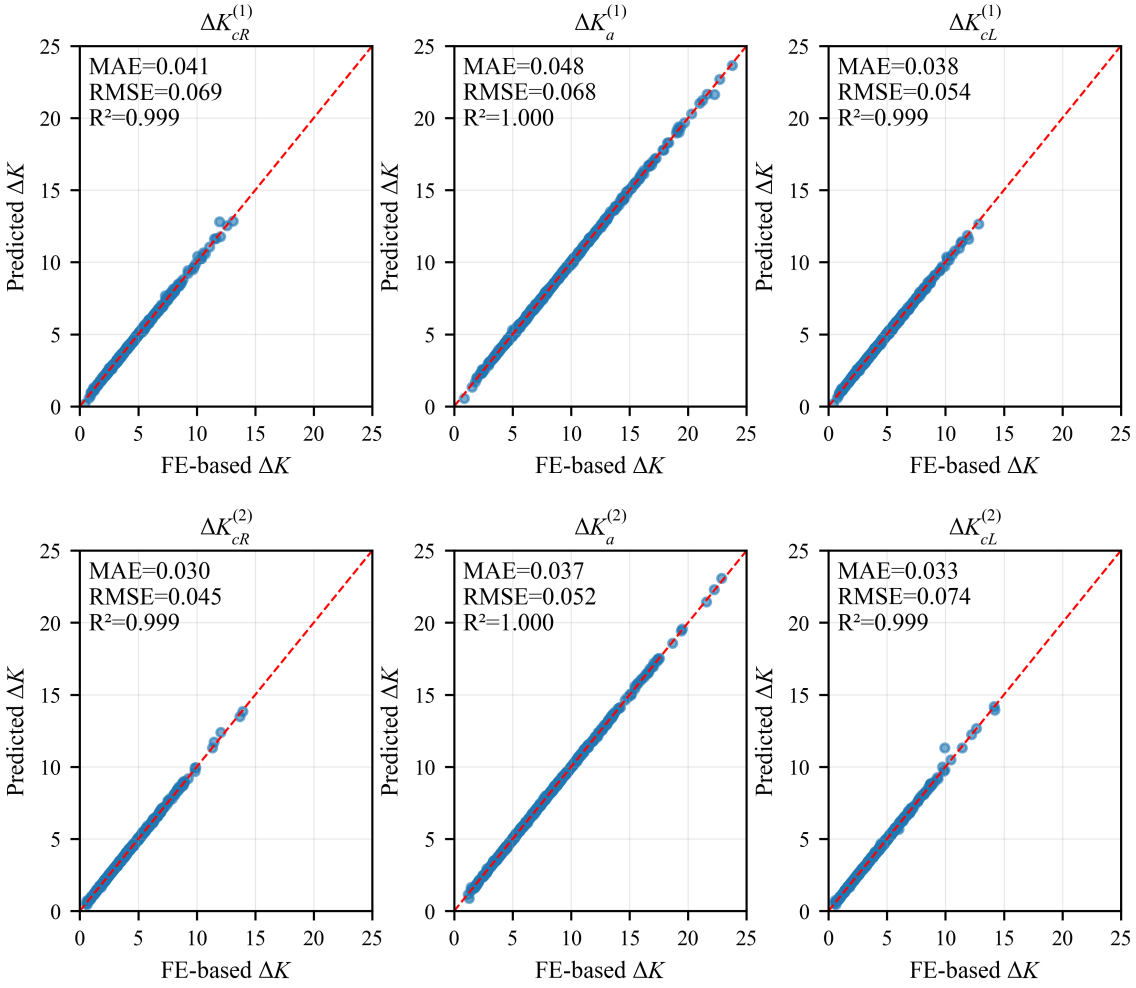

Fig. 5.8 Parity of MLP-predicted versus FE-computed SIF range (ΔK) at the three crack-front locations for both cracks for the interacting configuration with angular separation $\beta = 0.009$ radians. As in Fig. 5.7, the 20% hold-out test set is shown together with a dashed $y = x$ reference line. MAE, RMSE, and R^2 values for each output are reported in the subplots.

cases (S1–S5) spanning a range of growth rates, showing strong agreement between MLP and FE predictions, with a maximum RMSE of 0.141 mm for surface length $c^{(1)}$ and 0.045 mm for depth $a^{(1)}$, and mean average percentage errors below 2.1%. This confirms the MLP's fidelity in capturing the dynamics of interacting and coalescing cracks. Together with the high-fidelity SIF predictions validated in Figs. 5.7–5.10, these consistent crack growth trajectories affirm the surrogates' reliability for both SIF estimation and crack propagation.

Given the Paris law relation (Eq. 5.1), where m typically ranges from 2 to 4 for steel, the observed errors translate to modest growth rate perturbations of approximately $1 + m \cdot \varepsilon$ (with $\varepsilon \approx 0.005 - 0.01$), supporting their use in the subsequent RK4-based crack propagation. The validated MLP surrogates

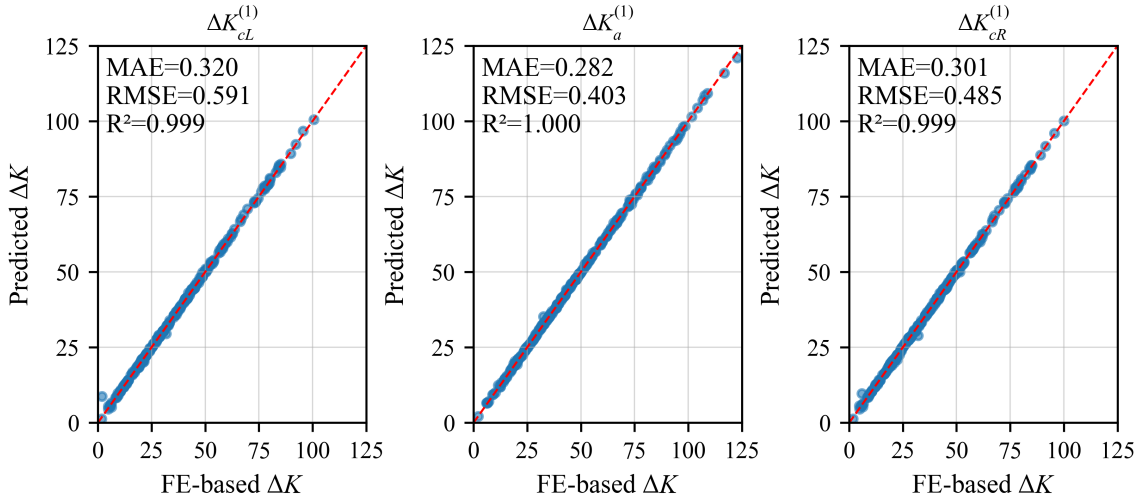

Fig. 5.9 Parity of MLP-predicted versus FE-computed SIF range (ΔK) at three crack front locations for the post-coalescence single semi-elliptical crack configuration: ΔK_{cL}, ΔK_a, and ΔK_{cR}. The test set (≈ 250 cases) is shown with a red dashed $y = x$ reference line. Mean absolute error (MAE), root mean square error (RMSE), and R^2 for each location are reported.

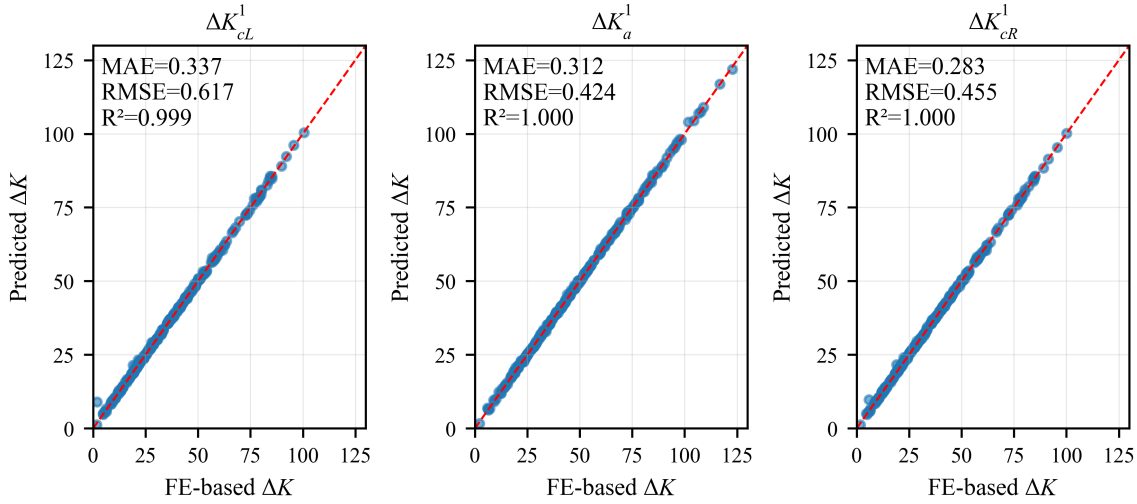

Fig. 5.10 Parity of MLP-predicted versus FE-computed SIF range (ΔK) at three crack front locations for the single semi-elliptical crack at a fixed angular offset $\beta = +0.0015$ radians configuration: ΔK_{cL}, ΔK_a, and ΔK_{cR}. The test set (≈ 250 cases) is shown with a red dashed $y = x$ reference line. Mean absolute error (MAE), root mean square error (RMSE), and R^2 for each location are reported.

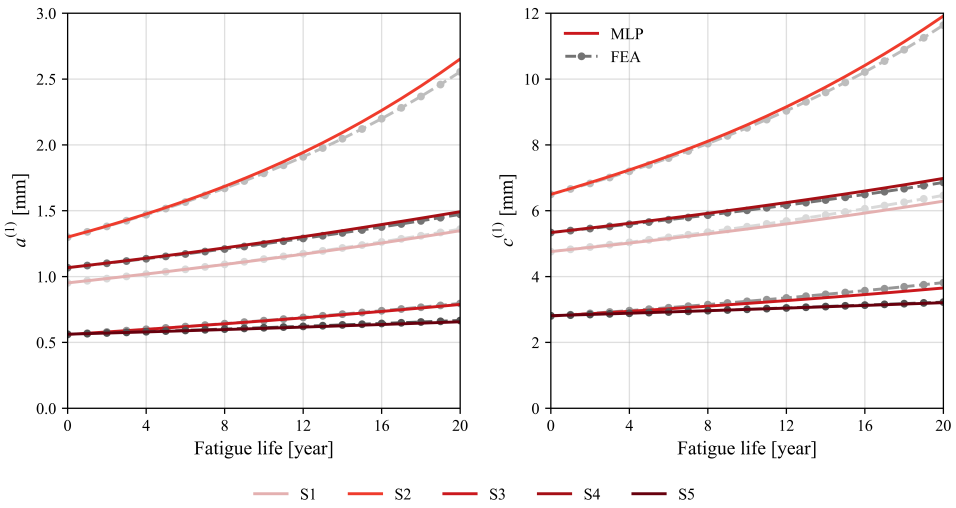

(a) First crack: $a^{(1)}$ (left) and $c^{(1)}$ (right).

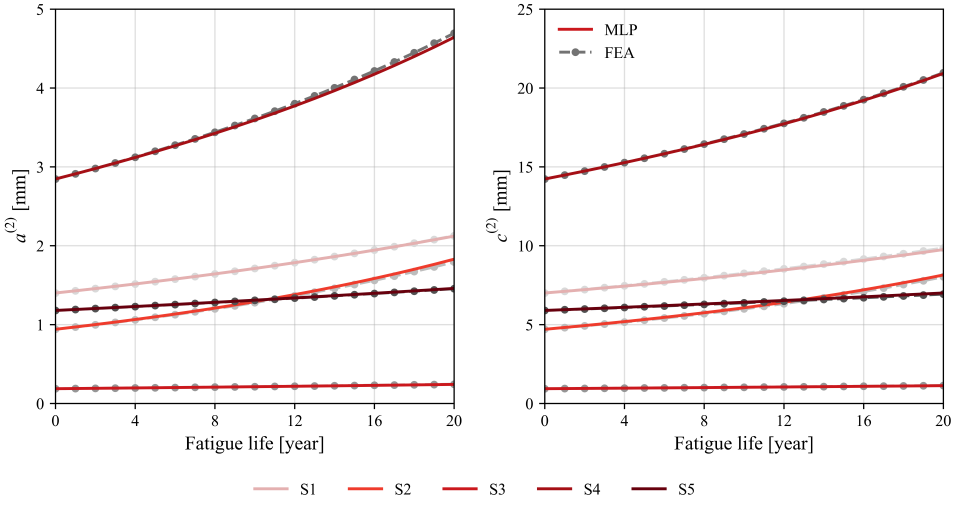

(b) Second crack: $a^{(2)}$ (left) and $c^{(2)}$ (right).

Fig. 5.11 Comparison of FE-based and MLP-based crack growth predictions over 20 years for five random samples.

reduce computational cost from hours per FE evaluation to milliseconds, enabling efficient MCS-based reliability analysis.

5.5.2 Probabilistic fatigue analysis

The first four configurations—(i) interacting cracks, (ii) single offset crack, (iii) two single cracks combined in series, and (iv) two single offset cracks with coalescence—share comparable loading and geometric baselines but differ in multiplicity, interaction modeling, and coalescence treatment, enabling a focused examination of how proximity-induced effects alter reliability.

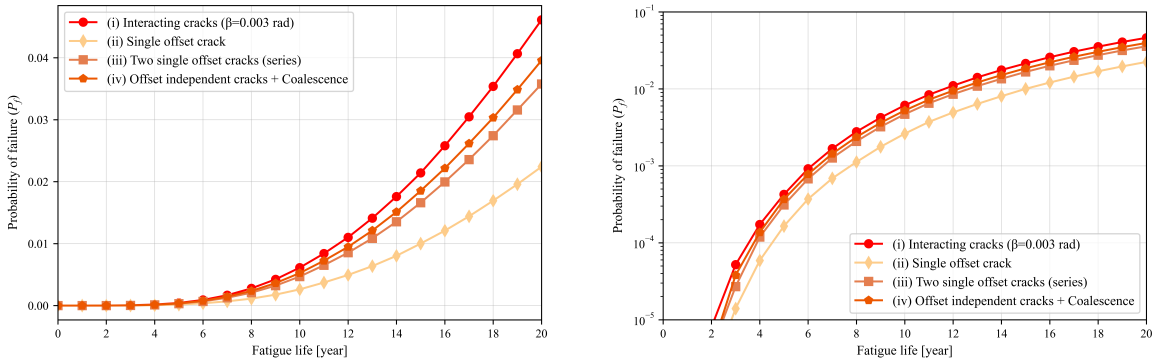

(a) Linear scale.

(b) Semi-log scale.

Fig. 5.12 Time evolution of probability of failure (P_f) for the interacting cracks, single offset crack, two single cracks in series, and two single offset cracks with coalescence (all at $\beta = 0.003$ radians).

Figure 5.12 compares the evolution of the probability of through-thickness failure over the 20-year life for four $\beta = 0.003$ radians configurations: interacting cracks (case (i)), a single offset crack (case (ii)), two single offset cracks combined in series without coalescence (case (iii)), and two single offset cracks that are allowed to coalesce once $\delta < 0.02$ mm (case (iv)). All curves exhibit a similar qualitative trend, with a gradual increase in P_f over the 20-year design life, but there are systematic differences in both the level and timing of failure probabilities.

At the end of the 20-year life, the interacting configuration (i) attains the largest probability of failure, $P_f^{(i)}(20) = 4.61 \times 10^{-2}$. The single offset crack (ii) gives $P_f^{(ii)}(20) = 2.24 \times 10^{-2}$, i.e. it underestimates the interaction-aware probability of failure by approximately 51%. The two crack series idealization without coalescence (iii) yields $P_f^{(iii)}(20) = 3.58 \times 10^{-2}$, about 60% higher than the single offset crack approximation and about 22% lower than the interacting case. Allowing the two offset cracks to coalesce while still using single offset crack SIFs before coalescence (case (iv)) produces an intermediate response, with $P_f^{(iv)}(20) = 3.96 \times 10^{-2}$: this is roughly 77% higher than the single offset crack, about 11% higher than the pure series model, and about 15% lower than the fully interacting configuration.

Differences between the four models are already visible at mid-life. At $t = 10$ years, the single crack (ii) has $P_f^{(ii)}(10) \approx 2.62 \times 10^{-3}$, whereas the interacting case (i) reaches $P_f^{(i)}(10) \approx 6.13 \times 10^{-3}$, around 134% higher. The series configuration (iii) and the coalescing two offset configuration (iv) give $P_f^{(iii)}(10) \approx 4.69 \times 10^{-3}$ and $P_f^{(iv)}(10) \approx 5.25 \times 10^{-3}$, corresponding to increases of approximately 79% and 100% relative to the single offset crack model, respectively. In terms of threshold levels, the interacting case (i), the series model (iii) and the coalescing two offset model (iv) all cross $P_f = 10^{-4}$ and 10^{-3} at years 4 and 7, respectively, and $P_f = 10^{-2}$ between years 12 and 13, whereas the single crack approximation (ii) reaches these thresholds at years 5, 8 and 15, respectively.

The ordering $P_f^{(ii)} < P_f^{(iii)} < P_f^{(iv)} < P_f^{(i)}$ is informative. Comparing cases (ii) and (iii) shows the effect of simply introducing multiple cracks without interaction or coalescence: the series idealization increases the 20-year probability of failure by about 60% relative to a single crack. Switching from

(iii) to (iv) isolates the role of coalescence under non-interacting SIFs: allowing the two offset cracks to merge increases P_f by roughly 11% at 20 years. Finally, comparing (iv) to the fully interacting case (i) highlights the additional influence of SIF interaction prior to coalescence: even when coalescence is treated consistently, neglecting interaction in the SIF model still reduces P_f by about 15% at the end-of-life. Taken together, these results show that (iv) provides the closest approximation to the interaction-aware probability of failure, while both the single offset crack model (ii) and the simple series idealization (iii) can significantly misrepresent the risk over the service life.

From a reliability viewpoint, moving from case (ii) to case (iii) converts a single-component system into a two-component series system subject to the same underlying loading and material uncertainties. For two independent, identically distributed cracks with small failure probability p, the series probability would be $P_f^{(iii)}(t) = 1-(1-p)^2 \approx 2p$, i.e. an approximately twofold increase. However, in the present case, the two cracks share the same random inputs (stress range, crack growth parameters, and initial size). Therefore, their failures are positively correlated, resulting in a more modest increase. Over the 20-year horizon, $P_f^{(iii)}(20) \approx 1.6\,P_f^{(ii)}(20)$, which corresponds to the observed 60% increase. Thus, case (iii) still exhibits the classical series system amplification of risk but with the effect tempered by the correlation between the two cracks. In case (iv), introducing coalescence adds an additional fracture mechanics effect. Once the cracks merge, the enlarged crack front experiences a higher global driving force proportional to a line integral of $[\Delta K]^m$ along the front [283]. This accelerates late-life growth and raises P_f above the pure series idealization.

The elevation of $P_f^{(i)}$ above $P_f^{(ii)}$ is consistent with the principles of fracture mechanics. At a spacing of 9 mm ($\beta = 0.003$ radians), the adjacent crack tips experience local ΔK amplification before coalescence, accelerating crack growth and reshaping the crack fronts. This behavior has been reported for adjacent semi-elliptical surface cracks (e.g., [19, 22, 29, 197]) and in our prior studies [204, 205].

In both case (i) and case (iv), all failed realizations experience coalescence before through-thickness failure because of the small initial spacing. Figure 5.13 summarizes the coalescence statistics for these two configurations, distinguishing between the fraction of samples that are already coalesced at a given year and those that coalesce for the first time in that year. At $t = 0$ the two models share the same initial population of coalesced realizations, with approximately 18.4% of samples already below the coalescence threshold and thus represented by an equivalent single crack. As crack growth proceeds, the interacting configuration (i) systematically produces more coalescence than the offset-based model (iv): by year 10, about 24.9% of samples are coalesced in case (i) versus 22.3% in case (iv), and by year 20 these fractions increase to approximately 37.1% and 30.2%, respectively. In annual terms, new coalescence in case (i) accounts for roughly 0.1–1.3% of the ensemble per year, compared with 0.1–0.8% in case (iv).

After coalescence, the system no longer behaves as two components. For coalesced realizations, the local welded detail effectively collapses to a single semi-elliptical crack for most of the remaining life. This truncates the period during which two concurrent failure paths are available in the system limit-state of Eq. 5.6. The higher $P_f(t)$ observed for the fully interacting configuration (i) is therefore

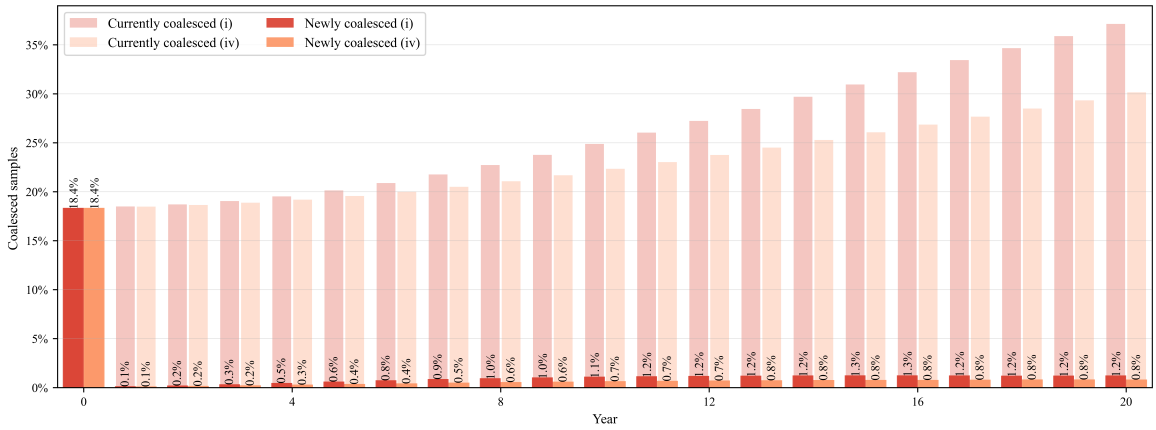

Fig. 5.13 Coalescence statistics for scenarios (i) interacting cracks and (iv) two single offset cracks with coalescence at angular separation $\beta = 0.003$ radians. For each year, the darker bars show the percentage of samples that coalesce for the first time in that year ('Newly coalesced'), while the lighter bars indicate the percentage of total samples that are coalesced at that year ('Currently coalesced').

the net result of two coupled effects: interaction-induced amplification of ΔK prior to coalescence, which accelerates crack growth and promotes earlier merging, and the subsequent evolution of a larger equivalent crack under the single crack limit-state. Case (iv), which neglects interaction in the SIFs but retains coalescence, captures the latter effect while underestimating the former, explaining why it provides the closest but still non-conservative approximation to the interaction-aware reliability curve.

Increasing the angular separation from $\beta = 0.003$ radians (case (i)) to $\beta = 0.009$ radians (case (v)) markedly reduces interaction between cracks and nearly eliminates the possibility of coalescence. In case (v), only about 0.1% of samples had already coalesced at year 0 and 2.6% by year 20, compared with 18.4% and 37.1% for case (i) (Fig. 5.15). The end-of-life probability of failure

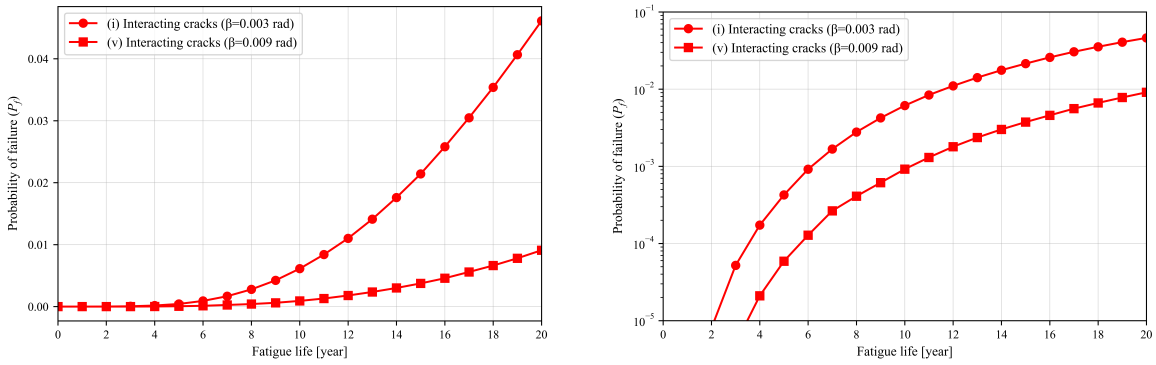

(a) Linear scale.

(b) Semi-log scale.

Fig. 5.14 Probability of failure (P_f) versus time for interacting cracks with angular separations $\beta = 0.003$ and $\beta = 0.009$ radians. Increasing the spacing substantially lowers the end-of-life P_f and delays the attainment of prescribed threshold levels.

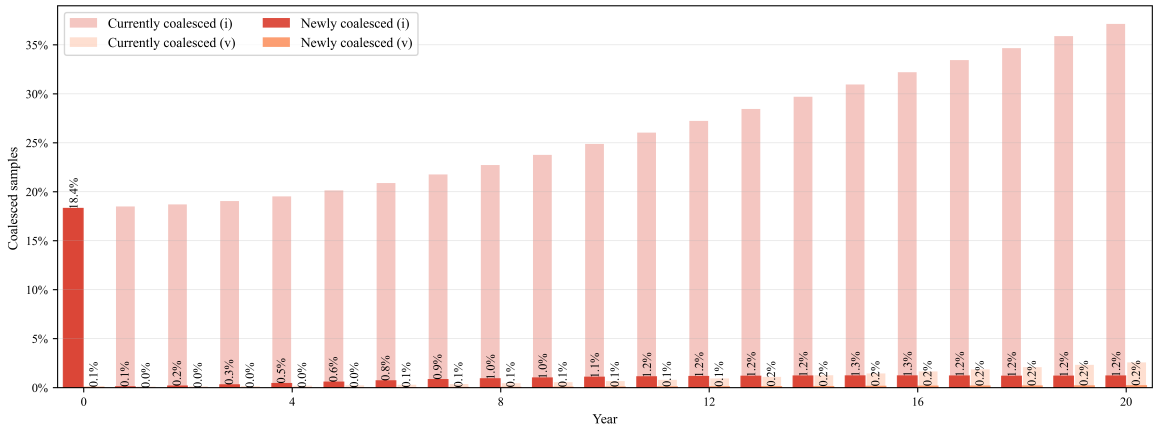

Fig. 5.15 Coalescence statistics for interacting cracks at angular separations $\beta = 0.003$ radians (case (i)) and $\beta = 0.009$ radians (case (v)). For each year, the darker bars show the percentage of samples that coalesce for the first time in that year ('Newly coalesced'), while the lighter bars indicate the percentage of total samples that are coalesced at that year ('Currently coalesced').

decreases from $P_f^{(i)}(20) = 4.61 \times 10^{-2}$ to $P_f^{(v)}(20) = 9.10 \times 10^{-3}$ (Fig. 5.14(a)), a reduction of about 80%; at $t = 10$ years, the wider spacing yields $P_f^{(v)}(10) \approx 9.2 \times 10^{-4}$, about seven times lower than $P_f^{(i)}(10) \approx 6.1 \times 10^{-3}$. Case (v) reaches $P_f = 10^{-4}$ and 10^{-3} in years 6 and 11, respectively, but does not reach 10^{-2} within 20 years (Fig. 5.14(b)). From a fracture mechanics viewpoint, larger β values reduce the near-tip amplification of ΔK on the neighboring crack fronts, making coalescence rare. As a result, the two cracks behave much more like independent single crack fronts throughout most of their lives, as reflected by the substantially lower $P_f(t)$.

These comparisons highlight the necessity of a state-adaptive reliability formulation that explicitly accounts for (a) pre-coalescence interaction, (b) the transition to a single merged crack front at coalescence, and (c) post-coalescence growth. Ignoring multiple cracks, as in the single offset crack scenario (case (ii)), underestimates P_f by about 51% at 20 years relative to the interacting configuration (case (i)). The simple series idealization (case (iii)) increases P_f by roughly 60% compared with the single offset crack model, yet still underestimates the interaction-aware P_f by about 22%. Incorporating coalescence while neglecting interaction (case (iv)) yields the closest approximation, but remains non-conservative, with an end-of-life P_f about 15% lower than case (i). The spacing study further shows that increasing the angular separation from $\beta = 0.003$ to $\beta = 0.009$ radians reduces the fraction of coalesced samples from $\sim 37\%$ to $\sim 3\%$ and lowers the 20 year P_f by about 80%. This emphasizes that closely spaced crack clusters in highly stressed regions dominate fatigue reliability, and it provides quantitative guidance for inspection planning in mid-life years (10–15) and for weld quality targets aimed at widening effective crack spacing.

5.6 Conclusions

This study presented a computational framework for probabilistic fatigue assessment of offshore wind monopile welds that integrates high-fidelity XFEM data with regime-specific MLP surrogates to capture crack interaction and coalescence effects. The surrogates reproduce stress intensity factor ranges (ΔK) with near-benchmark accuracy and negligible evaluation cost, making time-variant reliability analysis feasible.

Embedding the surrogates within a Runge–Kutta (RK)-based crack growth scheme and a Monte Carlo simulation loop captures the implicit dependency between adjacent cracks and the topology change at coalescence. In the welded circumferential joint studied, neglecting interaction and multiplicity (single offset crack model) underestimates end-of-life probability of failure by $\approx 51\%$. A simple two crack series idealization built from single crack surrogates also remains non-conservative, underestimating the interaction-aware P_f by $\approx 22\%$. A spacing study further shows that increasing angular separation from β=0.003 to 0.009 radians markedly suppresses coalescence (from about 37% to 2.6% of realizations) and reduces end-of-life P_f by $\sim 80\%$, providing quantitative guidance for inspection planning and weld quality targets.

The proposed state-adaptive surrogate framework provides a scalable pathway for realistic, system-level fatigue reliability assessment of large offshore structures. Future work will extend the framework to include inspection and repair strategies, adaptive surrogate enrichment during service life, and integration with digital twin platforms for condition-based monitoring.

Authorship Contribution Statement

Mishael, J: Conceptualization, Methodology, Literature Review, Data Curation, Writing – Original Draft, Visualization. **Morato, P. G.**: Conceptualization, Methodology, Writing – Review & Editing, Supervision **Rigo, P.**: Supervision, Project Administration.

Acknowledgement

The authors gratefully acknowledge the financial support provided by the Belgian Energy Transition Fund (ETF) through the MAXWind and FlexWind projects. The authors further acknowledge the computational resources provided by the Consortium des Équipements de Calcul Intensif (CÉCI), funded by the Fonds de la Recherche Scientifique de Belgique (F.R.S.-FNRS) under Grant No. 2.5020.11 and by the Walloon Region.

Declaration of generative AI in the writing process

During the preparation of this paper, the author(s) utilized ChatGPT, an AI tool developed by OpenAI, to assist in rewriting sentences for enhanced clarity and comprehension. Following the use of the tool,

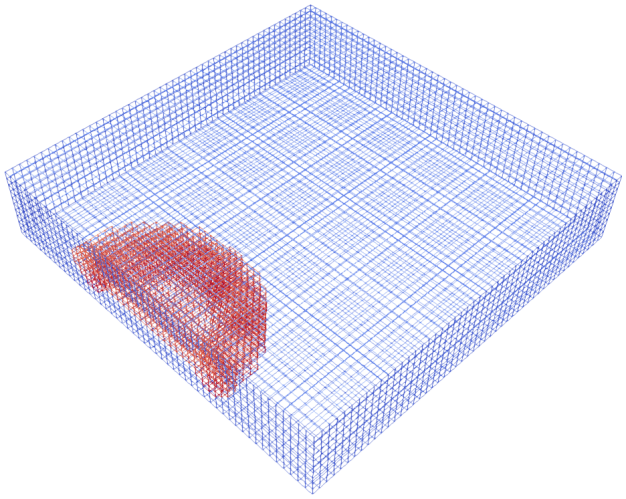

Fig. A1.1 Representation of a semi-elliptical crack on a plate using XFEM where the semi-elliptical crack is introduced into an existing mesh.

the author(s) thoroughly reviewed and edited the generated content as necessary to ensure its accuracy and alignment with the paper's objectives. The author(s) take full responsibility for the final content of this publication.

Appendix A1 XFEM formulation

The XFEM models cracks and discontinuities by enriching the standard degrees of freedom in the conventional finite element model. This enrichment introduces additional displacement fields that accurately represent the jump in displacement across the crack lips (called crack faces in three-dimensional models) as well as the stress singularity at the crack tip (crack front in three-dimensional models). Consequently, the crack geometry is represented explicitly and independently from the finite element mesh, as illustrated in Fig. A1.1, which shows a global finite element mesh with a semi-elliptical crack introduced as a separate entity. The displacement approximation in XFEM is expressed as follows:

$$u(x) = \sum_{i \in n} N_i(x)\, u_i + \sum_{j \in n_H} N_j(x)\, H(x)\, a_j + \sum_{k \in n_F} N_k(x) \sum_{l=1}^{4} F_l(x)\, b_k^l \tag{5.7}$$

where, N denotes the set of all nodes in the mesh, $N_i(x)$ represents the conventional finite element shape functions associated with node i, and u_i corresponds to the standard nodal degrees of freedom. The enriched degrees of freedom are defined as a_j, associated with the nodes n_H enriched by the Heaviside jump function $H(x)$, and b_k^l, corresponding to nodes n_F enriched by the crack-tip asymptotic functions $F_l(x)$.

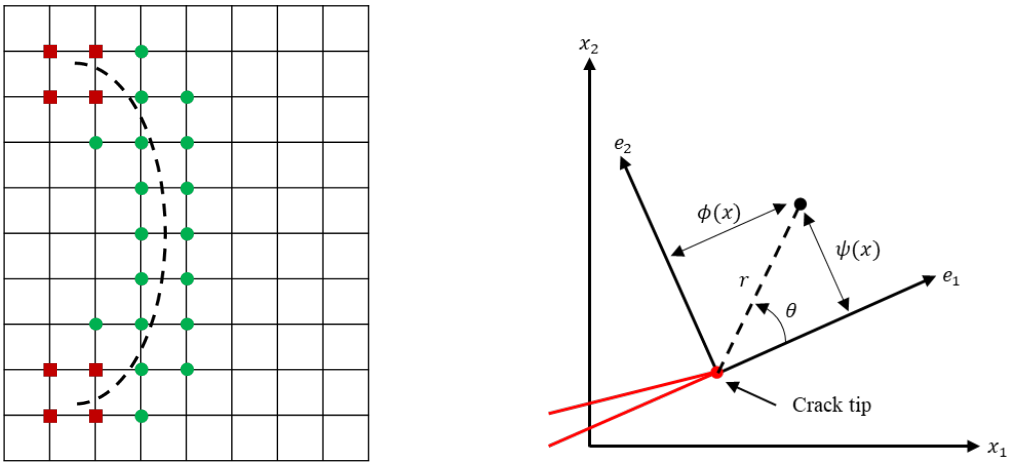

(a) (b)

Fig. A1.2 (a) Schematic representation of finite elements enriched by XFEM intersected by a curved crack (dashed line). Nodes enriched by the Heaviside function (displacement jump across crack faces) are indicated by green filled circles, while nodes enriched by crack-tip asymptotic functions (singular crack-tip fields) are represented by red filled squares. (b) Illustration of the local polar coordinate system (r,θ) defined at the crack tip, which specifies the orientation and distance used in asymptotic enrichment functions. Here, unit vectors e_1 and e_2 represent the local Cartesian coordinate axes oriented with respect to the crack faces.

XFEM introduces two distinct enrichments as shown schematically in Fig. A1.2 (a). The first is a discontinuity enrichment achieved using the Heaviside function, which models the displacement jump across the crack surfaces. The generalized Heaviside function $H(x)$ takes values depending on the position relative to the crack surfaces:

$$H(x) = \begin{cases} 1, & \text{if} \quad (x-x^*)\cdot e_{x^*} \geq 0, \\ -1, & \text{otherwise.} \end{cases} \tag{5.8}$$

where x^* denotes the closest point projection of x onto the crack surface, and e_{x^*} is the normal vector at the crack surface at point x^*.

The second enrichment is associated with the singular stress field near the crack tip. This enrichment uses four asymptotic functions, which capture the singular nature of the crack-tip stress and displacement fields. The crack-tip enrichment functions in polar coordinates (r,θ), defined locally at the crack tip, are given by:

$$F_l(r,\theta) = \sqrt{r}\left[sin\frac{\theta}{2}, cos\frac{\theta}{2}, sin\theta\ sin\frac{\theta}{2}, sin\theta\ cos\frac{\theta}{2}\right] \tag{5.9}$$

where (r,θ) represents the polar coordinates centered at the crack tip as illustrated in Fig. A1.2 (b), with the crack faces located at $\theta = \pm\pi$.

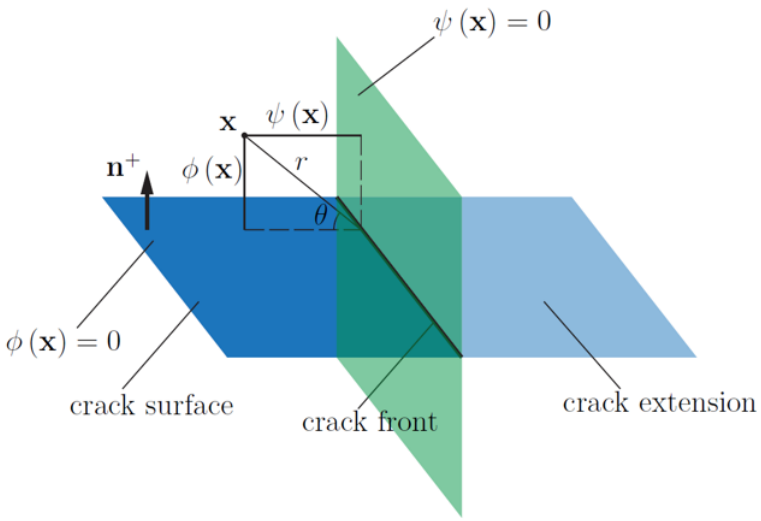

Fig. A1.3 Schematic representation of crack geometry using normal and tangent level set functions $\psi(x)$ and $\phi(x)$, respectively. Crack front and crack surface are also shown [284].

In XFEM, the crack geometry and position are typically managed using the level set method. The level set method represents discontinuities implicitly through scalar functions within the computational domain, where the zero-level set defines the discontinuity surface. Specifically, two signed distance functions, the normal level set function $\psi(x)$ and the tangent level set function $\phi(x)$, are defined at each node. The function $\psi(x)$ measures the shortest distance from the node to the crack surface, while $\phi(x)$ measures the distance from the node to a plane orthogonal to the crack surface containing the crack front. A schematic definition of these level sets in a 3D domain is illustrated in Fig. A1.3.

Using these level sets, the crack surface and crack front are defined implicitly as follows:

$$\begin{aligned} \text{Crack surface:} \quad & \phi(x) = 0 \quad \text{and} \quad \psi(x) < 0, \\ \text{Crack front:} \quad & \phi(x) = 0 \quad \text{and} \quad \psi(x) = 0 \end{aligned} \tag{5.10}$$

The local polar coordinates (r, θ), necessary for defining the enrichment functions, are also conveniently represented using level set functions as:

$$r = \sqrt{\phi(x)^2 + \psi(x)^2}, \quad \theta = \tan^{-1} \frac{\psi(x)}{\phi(x)} \tag{5.11}$$

For a given finite element, let $\psi_{\min}$ and $\psi_{\max}$ denote the minimum and maximum nodal values of $\psi(x)$, respectively, and similarly $\phi_{\min}$ and $\phi_{\max}$ denote the minimum and maximum nodal values of $\phi(x)$. Based on these nodal values, the necessary enrichments are determined as follows [285]:

If $\phi < 0$ and $\psi_{\min}\psi_{\max} \leq 0$, the crack intersects the element, and the element nodes are enriched using the Heaviside function $H(x)$.

If $\phi_{\min}\phi_{\max} \leq 0$ and $\psi_{\min}\psi_{\max} \leq 0$, a crack tip is located within the element, and the nodes are enriched using the asymptotic crack-tip functions $F_l(r,\theta)$.

Although crack propagation simulations are beyond the scope of the current study, XFEM allows for crack evolution through updating the level set functions without requiring remeshing. In such scenarios, level sets are updated based on an appropriate crack growth criterion, enabling efficient modeling of crack propagation in structural components.

Appendix A2 Mesh refinement algorithm around the crack front

Algorithm A2.1 Adaptive mesh refinement near interacting crack fronts

Define initial coarse element size h_0
Obtain crack depths a_1, a_2 and circumferential separation d_{tip}
if $\max(a_1, a_2) \geq 80$ mm **then**
  Set depth-based size $h_{\text{depth}} = 9/60$ mm
else if $70 \leq \max(a_1, a_2) < 80$ mm **then**
  Set $h_{\text{depth}} = 9/6$ mm
else
  Set $h_{\text{depth}} = \min(a_1, a_2)/40$
end if
if $d_{\text{tip}} \leq 2.5$ mm **then**
  Set separation-based size $h_{\text{sep}} = \max(d_{\text{tip}}/4,\ 0.005)$
else
  Set h_{sep} to a large default value
end if
Set target mesh size $h_c = \min(h_{\text{depth}},\ h_{\text{sep}})$
Compute number of refinement levels $n = \lceil (\ln(h_0) - \ln(h_c))/\ln(2) \rceil$
Obtain final element size $h = h_0/2^n$
Apply n uniform refinements near crack fronts

Appendix A3 Validation of FEA results

We validate the accuracy of SIFs computed with Code_Aster's XFEM by comparing predictions for single semi-elliptical surface cracks in wide, elastic plates of finite thickness against benchmark solutions from Newman and Raju [286] and the recent results of Coules and Probert [287].

Newman and Raju [286] examined semi-elliptical surface cracks in plates subjected to remote tensile loading, considering a broad range of crack geometries with depth-to-thickness ratios ($0.2 \leq$

$a/t \leq 0.8$) and depth-to-length ratios ($0.2 \leq a/c \leq 2.0$). The material was modeled with a Poisson's ratio of $\nu = 0.3$, and an arbitrary Young's modulus, since the SIF is independent of the elastic modulus. Although their study included both finite and infinite width plates, only the large plate case ($c/b = 0.2$, $c/h = 0.2$, where, b is the plate half width, and h is the plate half length.) is considered in this validation to eliminate boundary effects and focus only on the SIF computation accuracy. Pure tensile loading case is investigated by applying a unit magnitude of transverse loading to the crack plane.

Since Newman and Raju reported normalized SIFs, the Code_Aster results are also normalized as $K/\sqrt{\pi a/Q}$, where Q is the elliptical shape correction factor given by the empirical expression [189]:

$$Q = 1 + 1.464\left(\frac{a}{c}\right)^{1.65} \quad \text{for} \quad \frac{a}{c} \leq 1.0 \tag{5.12}$$

$$Q = 1 + 1.464\left(\frac{c}{a}\right)^{1.65} \quad \text{for} \quad \frac{a}{c} > 1.0 \tag{5.13}$$

Coules and Probert [287] provided additional numerical data for similar crack configurations, which are also used for comparison in this study. A summary of the results is shown in Fig. A3.1. Overall, good agreement is observed across all tested cases except for very wide cracks (a/c=0.2). This can be due to the low level of mesh refinement used by Newman and Raju [286]. The maximum deviation between Code_Aster and Newman and Raju's results is under 10% except a/c=0.2, and the discrepancy with Coules and Probert's results remains below 8% for all crack geometries analyzed.

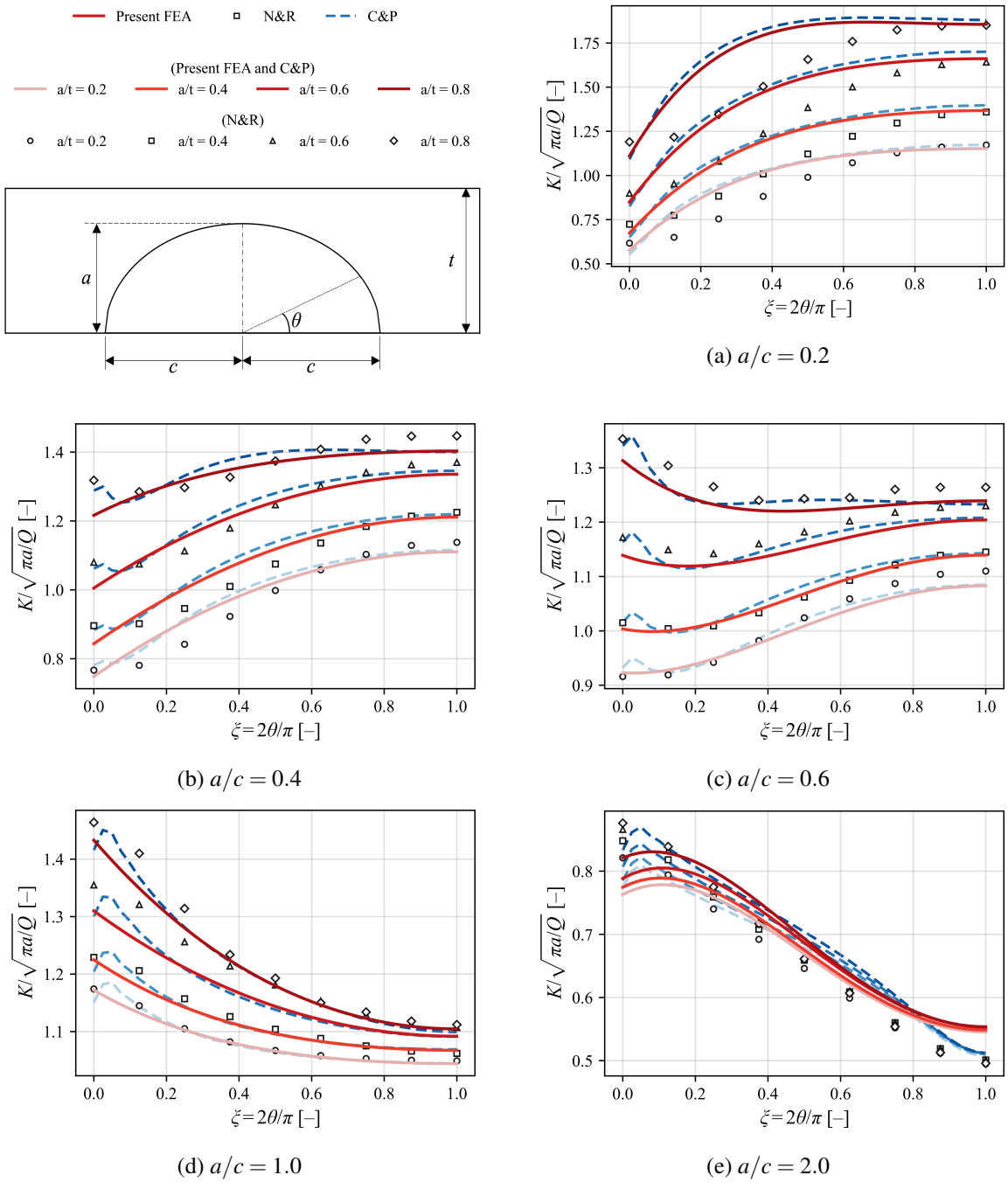

(a) $a/c = 0.2$

(b) $a/c = 0.4$

(c) $a/c = 0.6$

(d) $a/c = 1.0$

(e) $a/c = 2.0$

Fig. A3.1 Normalized stress intensity factor as a function of position along the crack front for semi-elliptical surface cracks with varying relative depths (a/t) and aspect ratios (a/c) in wide plates subjected to unit tensile stress. The top-left panel illustrates the plate geometry with a semi-elliptical surface crack and the legend used in all plots. N&R denotes the Newman & Raju results from [286], while C&P refers to the Coules & Probert results from [287].

CHAPTER 6

CONCLUSIONS AND OUTLOOK

6.1 Concluding remarks

This thesis presents a comprehensive approach that transforms the physics-based modeling of interacting surface cracks into a probabilistic, system-level reliability assessment of offshore wind turbine monopile welds. This approach combines evidence-based uncertainty characterization, deterministic interacting-crack simulation, and surrogate-accelerated reliability analysis.

Recognizing that design and assessment cannot rely on single nominal parameter values, Chapter 2 synthesizes corrosion fatigue evidence for monopile-relevant steels and load histories. The review documents substantial scatter in initial flaw sizes, crack growth parameters, and long-term stress ranges. This evidence justifies a stochastic approach to corrosion fatigue and offers reliable ranges and distributions for reliability analysis, connecting laboratory findings with field-relevant loading and environmental conditions.

Chapter 3 establishes the deterministic core, which is a generalized numerical methodology for fatigue crack growth of multiple surface cracks. This methodology explicitly represents interaction and coalescence, and it evaluates failure via two fracture mechanics endpoints: through-thickness penetration and exceedance of fracture toughness. This chapter also provides practical guidance on re-characterizing geometry after coalescence, designing meshes near approaching fronts, and extracting stable stress intensity factors (SIFs). It demonstrates the workflow on a realistic offshore structural connection.

Chapter 4 refines the core analysis by incorporating the weld profile. It quantifies how the local profile and constraint alter SIFs, shift the timing and sequence of coalescence, and change fatigue life predictions when multiple cracks interact. This is achieved by resolving the circumferential weld geometry in the finite element model of the monopile foundation. Case study demonstrates that weld fidelity is not merely a modeling detail; it can meaningfully impact reliability margins and should therefore be included whenever interaction effects are significant.

Building on those ingredients, Chapter 5 delivers a surrogate-enabled probabilistic framework that couples high-fidelity 3D SIF evaluations with efficient Paris law integration. Trained on targeted simulation campaigns, the MLP surrogates accelerate repeated SIF queries during numerical integra-

tion, reducing the computational cost from hours of finite element evaluation to milliseconds. This allows for the large-scale estimation of failure probabilities for components with multiple surface cracks, which supports scenario analyses and risk metrics suitable for design optimization, inspection prioritization, and farm-level decision-making. The probabilistic results demonstrate that neglecting crack interaction by treating each surface crack independently can lead to an inaccurate assessment of structural reliability. This emphasizes the importance of explicitly accounting for interaction and coalescence effects in welded joints.

This research work focuses on crack growth driven by interaction and coalescence under a tractable loading and failure formulation. Through-thickness penetration and fracture toughness exceedance are used as fracture mechanics endpoints. Natural extensions include coupled unstable fracture–plastic collapse assessment (e.g., via a failure assessment diagram (FAD)), multiaxial variable amplitude loading, and stochastic crack initiation locations and weld geometry variability. These are outlined as future research directions.

This thesis developed a methodology for circumferential welds in monopile foundations. The modular framework can be applied to other welded marine assets susceptible to corrosion fatigue and crack interaction. It is ready to incorporate mixed-mode crack growth, crack path prediction, and environment-dependent growth laws.

Finally, elements of this work directly underpin research activities in the Belgian Energy Transition Fund (ETF) funded MAXWind project. Specifically, the interaction-aware, surrogate-enabled, system-level reliability framework developed here provides a basis for risk-based optimization of inspection and maintenance decisions for offshore foundations. This framework can be extended to estimate tubular joint fatigue reliability, as addressed in the ETF-funded FlexWind project. This supports the development of strategies to extend the lifetime of jacket substructures for OWTs.

Original contributions

- A consolidated literature review on corrosion fatigue in OWT monopile foundations, identifying critical uncertainties in initial crack sizes, crack growth parameters, and long-term stress ranges—three major factors that govern reliability predictions and fatigue life modeling in marine environments.
- A generalized numerical methodology for simulating fatigue crack growth with multiple interacting surface cracks, with two fracture mechanics failure criteria: (i) through-thickness penetration and (ii) exceedance of fracture toughness.
- Practical finite element guidelines for modeling interacting surface cracks—geometry re-characterization after coalescence, meshing strategies near approaching fronts, and stable SIF extraction—validated on a realistic offshore structural connection.
- A detailed 3D finite element modeling strategy that explicitly accounts for weld geometry to analyze interaction and coalescence of surface cracks at circumferential welded joints in monopile-supported offshore wind turbines.

- An extension from deterministic interacting-crack modeling to probabilistic, system-level structural reliability by coupling FE-based crack propagation simulations with MLP surrogates, enabling large-scale Monte Carlo estimation of failure probabilities under uncertainty in loading, material properties, and crack interaction.

6.2 Suggestions for further research

The following directions would broaden the range of applications while maintaining the core interaction-aware reliability methodology developed in this thesis.

- Extend the framework to multiple interacting cracks (clusters) and quantify their combined influence on structural reliability, including coalescence sequences and competing failure modes.
- Incorporate coupled fracture-plastic collapse assessment by integrating failure assessment diagrams (FADs) with the current endpoints, enabling unified treatment of unstable fracture and ligament yielding.
- Generalize the loading representation by extending the current long-term statistical formulation (e.g., Weibull-based stress range modeling) to multiaxial and correlated loading effects, enabling reliability assessment under combined load actions and mixed-mode crack propagation.
- Model crack initiation locations and orientations as stochastic variables (including non-coplanar initiation), and propagate these uncertainties through the reliability assessment.
- Treat weld geometry and associated profile parameters as stochastic inputs, and quantify their contribution to uncertainty in SIFs, coalescence timing, and fatigue life.
- Incorporate weld residual stress effects into the framework (e.g., via representative through-thickness residual stress profiles), and assess their impact on SIFs, crack growth, and reliability outcomes.
- Incorporate crack path criteria (e.g., maximum tangential stress or energy-based criteria) to model propagation direction and deviations, particularly under mixed-mode conditions.
- Strengthen benchmarking by experimental validation, including targeted tests for interacting surface cracks and weld-profile effects in monopile-relevant geometries and environments.
- Assess surrogate-model robustness and generalization across broader ranges of geometries, crack configurations, and loading scenarios (e.g., domain adaptation, uncertainty-aware surrogates, and systematic out-of-domain testing).
- Develop sequence-to-sequence surrogates that predict full crack growth histories (including path) directly, reducing reliance on per-step SIF queries and Paris law integration.

REFERENCES

[1] R. Baboian, editor. *Corrosion Tests and Standards: Application and Interpretation-Second Edition*. ASTM International, West Conshohocken, PA, 2005.

[2] N. O. Larrosa, R. Akid, and R. A. Ainsworth. Corrosion-fatigue: a review of damage tolerance models, jul 2018.

[3] A. Jacob and A. Mehmanparast. Crack growth direction effects on corrosion-fatigue behaviour of offshore wind turbine steel weldments. *Marine Structures*, 75:102881, 2021.

[4] A. Fajuyigbe and F. Brennan. Fitness-for-purpose assessment of cracked offshore wind turbine monopile. *Marine Structures*, 77:102965, 2021.

[5] Bureau of Safety and Environmental Enforcement (BSEE). Offshore operators pressed on pipeline integrity: BSEE pipeline and decommissioning workshop. News Release, December 13, 2017. Accessed: 2025-01-27.

[6] P. Veers, C. L. Bottasso, L. Manuel, J. Naughton, L. Pao, J. Paquette, A. Robertson, M. Robinson, S. Ananthan, T. Barlas, A. Bianchini, H. Bredmose, S. G. Horcas, J. Keller, H. A. Madsen, J. Manwell, P. Moriarty, S. Nolet, and J. Rinker. Grand challenges in the design, manufacture, and operation of future wind turbine systems. *Wind Energy Science*, 8(7):1071–1131, 2023.

[7] R. Biswal, A. Al Mamun, and A. Mehmanparast. On the performance of monopile weldments under service loading conditions and fatigue damage prediction. *Fatigue and Fracture of Engineering Materials and Structures*, 44:1–15, 2021.

[8] Trading update Q1 2025: Ramp-up of new factory steadily improving. https://sif-group.com/imager/images/236467/MP-kopie_93cdd80cd58cdc322d03200db9620990.webp, 2025. Accessed: 2025-07-23.

[9] Jaroslav Mencik. *Chapter 5: Reliability of Systems, Concise Reliability for Engineers*. IntechOpen, Rijeka, Apr 2016.

[10] Quang A. Mai, John D. Sørensen, and Philippe Rigo. Updating Failure Probability of a Welded Joint in Offshore Wind Turbine Substructures. volume Volume 3: Structures, Safety and Reliability of *International Conference on Offshore Mechanics and Arctic Engineering*, page V003T02A059, 06 2016.

[11] Felipe Giro, Jose Mishael, Pablo G. Morato, and Philippe Rigo. INSPECTION AND MAINTENANCE PLANNING FOR OFFSHORE WIND SUPPORT STRUCTURES: MODELLING RELIABILITY AND INSPECTION COSTS AT THE SYSTEM LEVEL. In *Proceedings of the ASME 2022 41st International Conference on Ocean, Offshore and Arctic Engineering*, pages 1–10, Hamburg, 2022. ASME.

[12] Nandar Hlaing, Pablo G Morato, Jannie S Nielsen, Peyman Amirafshari, Athanasios Kolios, and Philippe Rigo. Inspection and maintenance planning for offshore wind structural components: integrating fatigue failure criteria with Bayesian networks and Markov decision processes. *Structure and Infrastructure Engineering*, 18(7):983–1001, 2022.

[13] P.G. Morato, C.P. Andriotis, K.G. Papakonstantinou, and P. Rigo. Inference and dynamic decision-making for deteriorating systems with probabilistic dependencies through bayesian networks and deep reinforcement learning. *Reliability Engineering & System Safety*, 235:109144, 2023.

[14] K.Y. Lam and S.P. Phua. Multiple crack interaction and its effect on stress intensity factor. *Engineering Fracture Mechanics*, 40(3):585–592, 1991.

[15] X. Wang, M. Modarres, and P. Hoffman. Analysis of crack interactions at adjacent holes and onset of multi-site fatigue damage in aging airframes. *International Journal of Fracture*, 156(1):155–163, 2009.

[16] Rahman Seifi, Oshin Ghadimian, and Milad Ranjbaran. Study on life and path of fatigue cracks in multiple site damage plates. *International Journal of Fatigue*, 80:449–458, 2015.

[17] Huijin Jin, Bing Cui, and Ling Mao. Fatigue Growth Behaviour of Two Interacting Cracks with Different Crack Offset. *Materials*, 12(21), 2019.

[18] Peng Xu, Renshu Yang, Yang Guo, Cheng Chen, Yang Yang, and Jinjing Zuo. Investigation of the interaction mechanism of two dynamic propagating cracks under blast loading. *Engineering Fracture Mechanics*, 259:108112, 2022.

[19] K. Kishimoto, W.O. Soboyejo, J.F. Knott, and R.A. Smith. A numerical investigation of the interaction and coalescence of twin coplanar semi-elliptical fatigue cracks. *International Journal of Fatigue*, 11(2):91–96, 1989.

[20] W.O. Soboyejo, J.F. Knott, M.J. Walsh, and K.R. Cropper. Fatigue crack propagation of coplanar semi-elliptical cracks in pure bending. *Engineering Fracture Mechanics*, 37(2):323–340, 1990.

[21] Xiaobin Lin. *Numerical Simulation of Fatigue Crack Growth*. PhD thesis, University of Sheffield, United Kingdom, 1994.

[22] Masayuki Kamaya. Growth evaluation of multiple interacting surface cracks. Part I: Experiments and simulation of coalesced crack. *Engineering Fracture Mechanics*, 75(6):1336–1349, 2008.

[23] P. E. O'Donoghue, T. Nishioka, and S. N. Atluri. Multiple surface cracks in pressure vessels. *Engineering Fracture Mechanics*, 20(3):545–560, 1984.

[24] T. H. Leek and I. C. Howard. An examination of methods of assessing interacting surface cracks by comparison with experimental data. *International Journal of Pressure Vessels and Piping*, 68(2):181–201, 1996.

[25] C.J. Bayley and R. Bell. Experimental and numerical investigation of coplanar fatigue crack coalescence. *International Journal of Pressure Vessels and Piping*, 74(1):33–37, 1997.

[26] Susan Pitt and Rhys Jones. Multiple-site and widespread fatigue damage in aging aircraft. *Engineering Failure Analysis*, 4(4):237–257, 1997.

[27] Masayuki Kamaya and Nobuo Totsuka. Influence of interaction between multiple cracks on stress corrosion crack propagation. *Corrosion science*, 44(10):2333–2352, 2002.

[28] Kimberli Jones, Sachin R Shinde, Paul N Clark, and David W Hoeppner. Effect of prior corrosion on short crack behavior in 2024-T3 aluminum alloy. *Corrosion Science*, 50(9):2588–2595, 2008.

[29] Masayuki Kamaya, Eiichi Miyokawa, and Masanori Kikuchi. Growth prediction of two interacting surface cracks of dissimilar sizes. *Engineering Fracture Mechanics*, 77(16):3120–3131, 2010.

[30] J.T. Tan and B.K. Chen. Coalescence and growth of two coplanar short cracks in AA7050-T7451 aluminium alloys. *Engineering Fracture Mechanics*, 102:324–333, 2013.

[31] John H.L. Pang, Hsin Jen Hoh, Kin Shun Tsang, Jason Low, Shawn Caleb Kong, and Wen Guo Yuan. Fatigue crack propagation analysis for multiple weld toe cracks in cut-out fatigue test specimens from a girth welded pipe. *International Journal of Fatigue*, 94:158–165, 2017.

[32] DNV GL. RP-C210 - Probabilistic methods for planning of inspection for fatigue cracks in offshore structures. Technical Report DNVGL-RP-C210, DNV GL, 2019.

[33] British Standards. BS7910:2013+A1:2015 Guide to methods for assessing the acceptability of flaws in metallic structures. Technical report, BSI Standards Publication, 389 Chiswick High Rd,Chiswick, London W4 4AL, United Kingdom, 2015.

[34] *Comparing a Fracture Mechanics Model to the SN-Curve Approach for Jacket-Supported Offshore Wind Turbines: Challenges and Opportunities for Lifetime Prediction*, volume Volume 6: Ocean Space Utilization; Ocean Renewable Energy of *International Conference on Offshore Mechanics and Arctic Engineering*, 06 2016.

[35] P. Amirafshari, F. Brennan, and A. Kolios. A fracture mechanics framework for optimising design and inspection of offshore wind turbine support structures against fatigue failure. *Wind Energy Science*, 6(3):677–699, 2021.

[36] X.B. Lin and R.A. Smith. A numerical simulation of fatigue growth of multiple surface initially semicircular defects under tension. *International Journal of Pressure Vessels and Piping*, 62(3):281–289, 1995.

[37] Yanmei Zhang, Zhongmin Xiao, and Jun Luo. Fatigue crack growth investigation on offshore pipelines with three-dimensional interacting cracks. *Geoscience Frontiers*, 9(6):1689–1697, 2018. Reliability Analysis of Geotechnical Infrastructures.

[38] Kaihua Zhang and Matthew Collette. Predicting growth and interaction of multiple cracks in structural systems using Dynamic Bayesian Networks. *Marine Structures*, 86:103271, 2022.

[39] Behrooz Tafazzoli Moghaddam, Ali Mahboob Hamedany, Jessica Taylor, Ali Mehmanparast, Feargal Brennan, Catrin Mair Davies, and Kamran Nikbin. Structural integrity assessment of floating offshore wind turbine support structures. *Ocean Engineering*, 208:107487, 2020.

[40] V. Giannella, F. Bardozzo, A. Postiglione, R. Tagliaferri, R. Sepe, and E. Armentani. Neural networks for fatigue crack propagation predictions in real-time under uncertainty. *Computers & Structures*, 288:107157, 2023.

[41] Demetrio Cristiani, Claudio Sbarufatti, Francesco Cadini, and Marco Giglio. Fatigue damage diagnosis and prognosis of an aeronautical structure based on surrogate modelling and particle filter. *Structural Health Monitoring*, 20(5):2726–2746, 2021.

[42] Wenyue Zhang, Yiming Su, Yufeng Jiang, Zhiqiang Hu, Jingtao Bi, and Wentao He. Data-driven fatigue crack propagation and life prediction of tubular T-joint: A fracture mechanics based machine learning surrogate model. *Engineering Fracture Mechanics*, 311:110556, 2024.

[43] Keji Pang and Huang Yuan. Assessment of three-dimensional multi-crack propagation for fatigue life prediction. *International Journal of Pressure Vessels and Piping*, 198:104660, 2022.

[44] H. E. Coules. Stress intensity interaction between dissimilar semi-elliptical surface cracks. *International Journal of Pressure Vessels and Piping*, 146:55–64, 2016.

[45] DNV GL. RP-C203 - Fatigue design of offshore steel structures. Technical Report DNVGL-RP-C203, DNV GL, 2016.

[46] Nandar Hlaing, Pablo Gabriel Morato, Philippe Rigo, Peyman Amirafshari, Athanasios Kolios, and Jannie S Nielsen. The effect of failure criteria on risk-based inspection planning of offshore wind support structures. In *Proc. of the 7th International Symposium on Life-Cycle Civil Engineering (IALCCE), Shanghai, China*, 2020.

[47] P.G. Morato, K. G. Papakonstantinou, C. P. Andriotis, J. S. Nielsen, and P. Rigo. Optimal inspection and maintenance planning for deteriorating structural components through dynamic Bayesian networks and Markov decision processes. *Structural Safety*, 94:102140, 01 2022.

[48] ABS. Guide for Fatigue Assessment of Offshore Structures. Technical report, American Bureau of Shipping, ABS Plaza, 16855 Northchase Drive, Houston, TX 77060 USA., 2018.

[49] D. Radaj, C.M. Sonsino, and W. Fricke. Chapter 6 - Crack propagation approach for seam-welded joints. In D. Radaj, C.M. Sonsino, and W. Fricke, editors, *Fatigue Assessment of Welded Joints by Local Approaches*, page 233–295. Woodhead Publishing, Sawston, 2006.

[50] T. Lassen and N. Recho. Proposal for a more accurate physically based S-N curve for welded steel joints. *International Journal of Fatigue*, 31(1):70–78, 2009.

[51] Oyewole Adedipe and Feargal Brennan. A study of fatigue crack growth in offshore wind monopile parent steel in air and seawater. In Soares Guedes, editor, *Proceedings of the 1st International Conference on Renewable Energies Offshore (RENEW 2014)*, pages 825–834, 11 2014.

[52] Oyewole Adedipe, Feargal Brennan, and Athanasios Kolios. Corrosion fatigue load frequency sensitivity analysis. *Marine Structures*, 42:115–136, 2015.

[53] O. Adedipe, F. Brennan, A. Mehmanparast, A. Kolios, and I. Tavares. Corrosion fatigue crack growth mechanisms in offshore monopile steel weldments. *Fatigue & Fracture of Engineering Materials & Structures*, 40(11):1868–1881, 2017.

[54] A. Mehmanparast, F. Brennan, and I. Tavares. Fatigue crack growth rates for offshore wind monopile weldments in air and seawater: SLIC inter-laboratory test results. *Materials & Design*, 114:494–504, 2017.

[55] A. Mehmanparast, J. Taylor, F. Brennan, and I. Tavares. Experimental investigation of mechanical and fracture properties of offshore wind monopile weldments: SLIC interlaboratory test results. *Fatigue & Fracture of Engineering Materials & Structures*, 41(12):2485–2501, 2018.

[56] Hasan Saeed, Somsubhro Chaudhuri, and Wim De Waele. Experimental evaluation of the short and long fatigue crack growth rate of S355 structural steel offshore monopile weldments in air and synthetic seawater. *Applied Ocean Research*, 149:104063, 2024.

[57] D Bowness and MMK Lee. Prediction of weld toe magnification factors for semi-elliptical cracks in T–butt joints. *International Journal of Fatigue*, 22(5):369–387, 2000.

[58] S.T. Lie, H.S. Zhao, and S.P. Vipin. New weld toe magnification factors for semi-elliptical cracks in plate-to-plate butt-welded joints. *Fatigue & Fracture of Engineering Materials & Structures*, 40:207–220, 2017.

[59] Linxian Zhi, Yuyang Zhu, Hai Wang, Zhengming Xu, and Zhihong Man. A recurrent neural network for modeling crack growth of aluminium alloy. *Neural Computing and Applications*, 27(1):197–203, January 2016.

[60] Patrick E Leser, Jacob D Hochhalter, James E Warner, John A Newman, William P Leser, Paul A Wawrzynek, and Fuh-Gwo Yuan. Probabilistic fatigue damage prognosis using surrogate models trained via three-dimensional finite element analysis. *Structural Health Monitoring*, 16(3):291–308, 2017.

[61] Xinran Ma, Xiaofan He, and Z.C. Tu. Prediction of fatigue–crack growth with neural network-based increment learning scheme. *Engineering Fracture Mechanics*, 241:107402, 2021.

[62] Arvind Keprate, RM Chandima Ratnayake, and Shankar Sankararaman. Adaptive gaussian process regression as an alternative to fem for prediction of stress intensity factor to assess fatigue degradation in offshore pipeline. *International Journal of Pressure Vessels and Piping*, 153:45–58, 2017.

[63] Arvind Keprate, R. M. Chandima Ratnayake, and Shankar Sankararaman. Experimental Validation of the Adaptive Gaussian Process Regression Model Used for Prediction of Stress Intensity Factor as an Alternative to Finite Element Method. *Journal of Offshore Mechanics and Arctic Engineering*, 141(2):021606, 10 2018.

[64] Eurocode. *Eurocode 3: Design of steel structures - Part 1-9: Fatigue, European Standard, EN 1993-1-9:2005*. European Committee for Standardisation, Brussels, 2005.

[65] Philipp Beiter, Aubryn Cooperman, Eric Lantz, Tyler Stehly, Matt Shields, Ryan Wiser, Thomas Telsnig, Lena Kitzing, Volker Berkhout, and Yuka Kikuchi. Wind power costs driven by innovation and experience with further reductions on the horizon. *WIREs Energy and Environment*, 10(5):e398, 2021.

[66] Sergio Sánchez, José Santos López-Gutiérrez, Vicente Negro, and M. Dolores Esteban. Foundations in offshore wind farms: Evolution, characteristics and range of use. Analysis of main dimensional parameters in monopile foundations. *Journal of Marine Science and Engineering*, 7(12), 2019.

[67] Victor Igwemezie, Ali Mehmanparast, and Athanasios Kolios. Current trend in offshore wind energy sector and material requirements for fatigue resistance improvement in large wind turbine support structures – A review. *Renewable and Sustainable Energy Reviews*, 101(November 2018):181–196, 2019.

[68] Dan Kallehave, Byron W. Byrne, Christian LeBlanc Thilsted, and Kristian Kousgaard Mikkelsen. Optimization of monopiles for offshore wind turbines. *Philosophical Transactions of the Royal Society A: Mathematical, Physical and Engineering Sciences*, 373(2035):20140100, 2015.

[69] EEW SPC Rolls Out World's Heaviest Monopile. https://www.offshorewind.biz/2016/03/03/eew-spc-rolls-out-worlds-heaviest-monopile/, 2025. Accessed: 2025-07-24.

[70] Anais Jacob, Ali Mehmanparast, Riccardo D'Urzo, and Joe Kelleher. Experimental and Numerical Investigation of Residual Stress Effects on Fatigue Crack Growth Behaviour of S355 Steel Weldments. *International Journal of Fatigue*, 128:105196, 07 2019.

[71] Anais Jacob, Jeferson Oliveira, Ali Mehmanparast, Foroogh Hosseinzadeh, Joe Kelleher, and Filippo Berto. Residual Stress Measurements in Offshore Wind Monopile Weldments using Neutron Diffraction Technique and Contour Method. *Theoretical and Applied Fracture Mechanics*, 96, 06 2018.

[72] Dong-Hwan Kang, Sanghoon Kim, Changhee Lee, Jong-Kwan Lee, and Tae-Won Kim. Corrosion fatigue behaviors of HSB800 and its HAZs in air and seawater environments. *Materials Science and Engineering: A*, 559:751–758, 2013.

[73] Fidan Smaili, G. Lojen, and Tomaž Vuherer. Fatigue crack initiation and propagation of different heat affected zones in the presence of a microdefect. *International Journal of Fatigue*, 128:105191, 2019.

[74] Hongchi Ma, Jinbin Zhao, Yi Fan, Yunhua Huang, Zhiyong Liu, Cuiwei Du, and Xiaogang Li. Comparative study on corrosion fatigue behaviour of high strength low alloy steel and simulated HAZ microstructures in a simulated marine atmosphere. *International Journal of Fatigue*, 137:105666, 2020.

[75] Jun Gao, Ziyu Zhang, Jibo Tan, Xinqiang Wu, Xiang Wang, En-Hou Han, and Wei Ke. Differences of corrosion fatigue behaviors among 316LN base metal, 316LN heat-affected zone and 308L weld metal in a safe-end weld joint in borated and lithiated high-temperature water. *International Journal of Fatigue*, 148:106223, 2021.

[76] J. W. C. Thompson. *Phenomenological investigation of the influence of Cathodic protection on corrosion fatigue crack propagation behaviour, in a BS 4360 50D type structural steel and associated weldment microstructures, in a marine environment*. PhD thesis, Cranfield University, 1984.

[77] L. R. Hilbert, A. R. Black, F. Andersen, and T. Mathiesen. Inspection and monitoring of corrosion inside monopile foundations for offshore wind turbines. In *Eurocorr Conference*, Stockholm, September 2011. Paper no. 4730.

[78] T. Mathiesen, A. Black, and F. Grønvold. Monitoring and Inspection Options for Evaluating Corrosion in Offshore Wind Foundations. In *NACE Corrosion 2016*, Vancouver, BC, March 2016. Paper C2016-7702.

[79] W. Wallace, David Hoeppner, and P.V Kandachar. AGARD Corrosion Handbook. Volume 1. Aircraft Corrosion: Causes and Case Histories. Technical Report AGARD-AG-278 Volume 1, Advisory Group for Aerospace Research and Development, North Atlantic Treaty Organization, 07- 1985.

[80] J.J. De Luccia, R.D. Gergar, and E.J. Jankowsky. AGARD Corrosion Handbook. Volume 2. Aircraft Corrosion Control Documents: A Descriptive Catalogue. Technical Report AGARD-AG-278 Volume 2, Advisory Group for Aerospace Research and Development, North Atlantic Treaty Organization, 03- 1987.

[81] J. P. Chubb, T. A. Morad, B. S. Hockenhull, and J. W. Bristow. The Effect of Exfoliation Corrosion on the Fatigue Behavior of Structural Aluminium Alloys. In S. N. Atluri, S. G. Sampath, and Pin Tong, editors, *Structural Integrity of Aging Airplanes*, pages 87–97, Berlin, Heidelberg, 1991. Springer Berlin Heidelberg.

[82] D. Gary Harlow and Robert P. Wei. Probability approach for prediction of corrosion and corrosion fatigue life. *AIAA Journal*, 32(10):2073–2079, 1994.

[83] Sankaran Mahadevan and Pan Shi. Corrosion fatigue reliability of aging aircraft structures. *Progress in Structural Engineering and Materials*, 3(2):188–197, 2001.

[84] Q. Y. Wang, R. M. Pidaparti, and M. J. Palakal. Comparative study of corrosion-fatigue in aircraft materials. *AIAA journal*, 39(2):325–330, 2001.

[85] C.E. Jaske, J.H. Payer, and V.S. Balint. Corrosion Fatigue of Metals in Marine Environments. Technical report, Metals and Ceramics Information Center, Battelle Columbus Laboratories, Columbus, Ohio, 1981.

[86] Zaki Ahmad. CHAPTER 4 - TYPES OF CORROSION: Materials and Environments. In Zaki Ahmad, editor, *Principles of Corrosion Engineering and Corrosion Control*, pages 120–270. Butterworth-Heinemann, Oxford, 2006.

[87] R J Baxter, D P, Maddox, S J and Pargeter. CORROSION FATIGUE BEHAVIOUR OF WELDED RISERS AND PIPELINES. In *Proceedings of the 26th International Conference on Offshore Mechanics and Arctic Engineering*, pages 117–124, San Diego, California, 2007.

[88] Dmytrakh, I. Corrosion Fatigue Cracking and Failure Risk Assessment of Pipelines. In Guy Pluvinage and Mohamed Hamdy Elwany, editor, *Proceedings of the NATO Advanced Research Workshop on Safety, Reliability and Risks Associated with Water, Oil and Gas Pipelines*, pages 99—-113, Alexandria, 2007. NATO Science for Peace and Security Series.

[89] George V. Chilingar, Ryan Mourhatch, and Ghazi D. Al-Qahtani. CHAPTER 2 - TYPES OF CORROSION. In George V. Chilingar, Ryan Mourhatch, and Ghazi D. Al-Qahtani, editors, *The Fundamentals of Corrosion and Scaling for Petroleum & Environmental Engineers*, pages 35–48. Gulf Publishing Company, 2008.

[90] B. T. Lu. Crack growth model for pipeline steels exposed to near-neutral pH groundwater. *Fatigue & Fracture of Engineering Materials & Structures*, 36(7):660–669, 2013.

[91] Zhongyu Cui, Liwei Wang, Zhiyong Liu, Cuiwei Du, Xiaogang Li, and Xin Wang. Anodic dissolution behavior of the crack tip of X70 pipeline steel in near-neutral pH environment. *Journal of Materials Engineering and Performance*, 25:5468–5476, 2016.

[92] M.A. Mohtadi-Bonab. Effects of Different Parameters on Initiation and Propagation of Stress Corrosion Cracks in Pipeline Steels: A Review. *Metals*, 9(5), 2019.

[93] DNV GL. ST-0126 - Support structures for wind turbines. Technical Report DNVGL-ST-0126, DNV GL, 2018.

[94] Muhammad Arshad and Brendan O'Kelly. Offshore wind-turbine structures: A review. *Proceedings of the Instituion of Civil Engineers – Energy*, 166:139–152, 11 2013.

[95] Wenbin Dong, Torgeir Moan, and Zhen Gao. Fatigue reliability analysis of the jacket support structure for offshore wind turbine considering the effect of corrosion and inspection. *Reliability Engineering & System Safety*, 106:11–27, 2012.

[96] Yan Dong, Xiangyu Kong, Gansheng An, and Jichuan Kang. Fatigue reliability of single-sided girth welds in offshore pipelines and risers accounting for non-destructive inspection. *Marine Structures*, 86:103268, 2022.

[97] E.U. Lee. REVIEW OF CORROSION FATIGUE. Technical report, NAVAL AIR SYSTEMS COMMAND, Washington, D.C., 1981.

[98] Tianliang Zhao, Zhiyong Liu, Cuiwei Du, Chunduo Dai, Xiaogang Li, and Bowei Zhang. Corrosion fatigue crack initiation and initial propagation mechanism of E690 steel in simulated seawater. *Materials Science and Engineering: A*, 708:181–192, 2017.

[99] Xiaoxuan Liao, Yadong Li, Bin Qiang, Jun Wu, Changrong Yao, and Xing Wei. An improved crack growth model of corrosion fatigue for steel in artificial seawater. *International Journal of Fatigue*, 160:106882, 2022.

[100] Rajneesh Jaisawal, Vidit Gaur, and Shahnawaz Ahmed. The combined effect of corrosive media and its temperature on the fatigue performance of aa5086-h321 weld joints. *International Journal of Fatigue*, 188:108522, 2024.

[101] Xiaoqiang Zhang, Huiying Gao, and Hong-Zhong Huang. Total fatigue life prediction for welded joints based on initial and equivalent crack size determination. *International Journal of Damage Mechanics*, 27(7):1084–1104, 2018.

[102] Y. Kitsunai, M. Tanaka, and E. Yoshihisa. Influence of residual stresses and loading frequencies on corrosion fatigue crack growth behavior of weldments. *Metallurgical and Materials Transactions A*, 29(4):1289–1298, 1998.

[103] Victor Igwemezie and Ali Mehmanparast. Waveform and frequency effects on corrosion-fatigue crack growth behaviour in modern marine steels. *International Journal of Fatigue*, 134:105484, 2020.

[104] Ruonan Zhang, Pengyu Wei, Ke Wang, Peilong Song, Xin Guo, Qingbo Zeng, and Shengpeng Li. An accelerated corrosion-fatigue testing method for marine high-strength steel based on equivalence principle of fatigue crack growth. *Ocean Engineering*, 314:119706, 2024.

[105] F. P. Brennan. A framework for variable amplitude corrosion fatigue materials tests for offshore wind steel support structures. *Fatigue & Fracture of Engineering Materials & Structures*, 37(7):717–721, 2014.

[106] Yuko Ishibashi and Yoichi Kayamori. An Experimental Method to Evaluate the Effect of Welding Residual Stress on Corrosion Fatigue Properties of Structural Steel in Synthetic Seawater. In *THERMEC 2018*, volume 941 of *Materials Science Forum*, pages 1716–1721. Trans Tech Publications Ltd, 1 2019.

[107] Haohui Xin and Milan Veljkovic. Residual stress effects on fatigue crack growth rate of mild steel S355 exposed to air and seawater environments. *Materials & Design*, 193:108732, 2020.

[108] A. Khajeian, A.H. Mahmoudi, and R. Seifi. On the prediction of corrosion fatigue in the presence of residual stresses. *Engineering Failure Analysis*, 169:109211, 2025.

[109] R. S. Piascik and S. A. Willard. THE GROWTH OF SMALL CORROSION FATIGUE CRACKS IN ALLOY 2024. *Fatigue & Fracture of Engineering Materials & Structures*, 17(11):1247–1259, 1994.

[110] Victor Igwemezie, Ali Mehmanparast, and Feargal Brennan. The role of microstructure in the corrosion-fatigue crack growth behaviour in structural steels. *Materials Science and Engineering: A*, 803:140470, 2021.

[111] Yifan Dong, Denghui Liu, Hegang Du, Haoran Sun, and Xiurong Zuo. Effect of microstructure on the mechanical properties and corrosion resistance of a welded joint of 620-grade marine steel. *Frontiers in Materials*, 10, 2023.

[112] Joscha Weinert, Stefanos Gkatzogiannis, Imke Engelhardt, Peter Knoedel, and Thomas Ummenhofer. Investigation of corrosive influence on the fatigue behaviour of HFMI-treated and as-welded transverse non-load-carrying attachments made of mild steel S355. *International Journal of Fatigue*, 151:106225, 2021.

[113] T. W. Crooker, F. D. Bogar, and W. R. Cares. Effects of Flowing Natural Seawater and Electrochemical Potential on Fatigue-Crack Growth in Several High- Strength Marine Alloys. Technical report, Naval Research Laboratory, Washington, D.C., 1976.

[114] F. J. Radd, L H. Crowder, and L. H. Wolfe. Effect of pH in the Range 6.6–14.0+ On the Aerobic Corrosion Fatigue of Steel. *Corrosion*, 16(8):415–418, 01 2013.

[115] S. K. Kolawole, F. O. Kolawole, A. B. O. Soboyejo, and W. O. Soboyejo. Modeling studies of corrosion fatigue in a low carbon steel. *Cogent Engineering*, 6(1):1695999, 2019.

[116] Tetsuya Saito and Iku Uchiyama. Influence of Electrochemical Potential on Crack Growth Rate by Corrosion Fatigue in Synthetic Sea Water. *Transactions of the Iron and Steel Institute of Japan*, 22(8):586–592, 1982.

[117] A. Turnbull and D.H. Ferriss. Mathematical modelling of the electrochemistry in corrosion fatigue cracks in steel corroding in marine environments. *Corrosion Science*, 27(12):1323–1350, 1987.

[118] T.W. Thorpe, P.M. Scott, A. Rance, and D. Silvester. Corrosion fatigue of BS 4360:50D structural steel in seawater. *International Journal of Fatigue*, 5(3):123–133, 1983.

[119] James P. Thomas and Robert P. Wei. Corrosion fatigue crack growth of steels in aqueous solutions I: Experimental results and modeling the effects of frequency and temperature. *Materials Science and Engineering: A*, 159(2):205–221, 1992.

[120] Anthony Comer and Lisa Looney. Corrosion and fatigue characteristics of positively polarised Zeron 100 base & weld metal in synthetic seawater. *International Journal of Fatigue*, 28(8):826–834, 2006.

[121] Andreas Gericke, Michél Hauer, Benjamin Ripsch, Michael Irmer, Jonas Nehlsen, and Knuth-Michael Henkel. Fatigue Strength of Structural Steel-Welded Connections with Arc-Sprayed Aluminum Coatings and Corrosion Behavior of the Corresponding Coatings in Sea Water. *Journal of Marine Science and Engineering*, 10(11), 2022.

[122] Y. Kondo. Prediction of Fatigue Crack Initiation Life Based on Pit Growth. *Corrosion*, 45(1):7–11, 01 1989.

[123] J.A. Balbín, V. Chaves, and N.O. Larrosa. Pit to crack transition and corrosion fatigue lifetime reduction estimations by means of a short crack microstructural model. *Corrosion Science*, 180:109171, 2021.

[124] Muhammad Shamir, Jarryd Braithwaite, and Ali Mehmanparast. Fatigue life assessment of offshore wind support structures in the presence of corrosion pits. *Marine Structures*, 92:103505, 2023.

[125] S. Srivatsan and T. S. Sudarshan. Mechanisms of fatigue crack initiation in metals: role of aqueous environments. *Journal of Materials Science*, 23(5):1521–1533, 1988.

[126] S.N. Rosenbloom and C. Laird. Fatigue crack nucleation based on a random slip process—I. Computer model. *Acta Metallurgica et Materialia*, 41(12):3473–3482, 1993.

[127] S. Xu, X.Q. Wu, E.H. Han, W. Ke, and Y. Katada. Crack initiation mechanisms for low cycle fatigue of type 316ti stainless steel in high temperature water. *Materials Science and Engineering: A*, 490(1):16–25, 2008.

[128] Zhongyu Cui, Zhiyong Liu, Liwei Wang, Xiaogang Li, Cuiwei Du, and Xin Wang. Effect of plastic deformation on the electrochemical and stress corrosion cracking behavior of X70 steel in near-neutral pH environment. *Materials Science and Engineering: A*, 677:259–273, 2016.

[129] M. Müller. Theoretical Considerations on Corrosion Fatigue Crack Initiation. *Metallurgical Transactions A*, 13(4):649 – 655, 1982.

[130] Qian Xu, Fei Shao, Lin-yue Bai, Qing-na Ma, and Mei Shen. Corrosion fatigue crack growth mechanisms in welded joints of marine steel structures. *Journal of Central South University*, 28(1):58–71, 2021.

[131] Victor Okenyi, Mahdi Bodaghi, Neil Mansfield, Shukri Afazov, and Petros Siegkas. A review of challenges and framework development for corrosion fatigue life assessment of monopile-supported horizontal-axis offshore wind turbines. *Ships and Offshore Structures*, 19(1):1–15, 2024.

[132] Behrooz Moghaddam, Ali Mahboob Hamedany, Ali Mehmanparast, Feargal Brennan, Kamran Nikbin, and C.M. Davies. Numerical analysis of pitting corrosion fatigue in floating offshore wind turbine foundations. *Procedia Structural Integrity*, 17:64–71, 01 2019.

[133] Abdulhakim Adeoye Shittu, Ali Mehmanparast, Mahmood Shafiee, Athanasios Kolios, Phil Hart, and Karl Pilario. Structural reliability assessment of offshore wind turbine support structures subjected to pitting corrosion-fatigue: A damage tolerance modelling approach. *Wind Energy*, 23(11):2004–2026, 2020.

[134] S.A. Elahi, F. Mehri Sofiani, S. Chaudhuri, J.A. Balbín, N.O. Larrosa, and W. De Waele. Investigation of the effect of pitting corrosion on the fatigue strength degradation of structural steel using a short crack model. *Procedia Structural Integrity*, 51:30–36, 2023. 6th International Conference on Structural Integrity and Durability (ICSID 2022).

[135] Seyed Ahmad Elahi, Robbe De Coster, Somsubhro Chaudhuri, Hasan Saeed, Farid Mehri Sofiani, and Wim De Waele. Thermometric investigation of fatigue crack initiation from corrosion pits in structural steel used in offshore wind turbines. European Academy of Wind Energy 2023, 2023.

[136] F. Mehri Sofiani, J. Tacq, S.A. Elahi, S. Chaudhuri, and W. De Waele. A hybrid probabilistic-deterministic framework for prediction of characteristic size of corrosion pits in low-carbon steel following long-term seawater exposure. *Corrosion Science*, 232:112039, 2024.

[137] H.P. Hong. Application of the Stochastic Process to Pitting Corrosion. *Corrosion*, 55(1):10–16, 01 1999.

[138] Pan Shi and Sankaran Mahadevan. Damage tolerance approach for probabilistic pitting corrosion fatigue life prediction. *Engineering Fracture Mechanics*, 68(13):1493–1507, 2001.

[139] A. Valor, F. Caleyo, L. Alfonso, D. Rivas, and J.M. Hallen. Stochastic modeling of pitting corrosion: A new model for initiation and growth of multiple corrosion pits. *Corrosion Science*, 49(2):559–579, 2007.

[140] Marek Jakubowski. Influence of pitting corrosion on fatigue and corrosion fatigue of ship and offshore structures. Part II: Load-pit crack interaction. *Polish Maritime Research*, 22:57–66, 2015.

[141] Henk Slot, Stefan Jansen, Bert Sluys, Erik Schuring, Richard Pijpers, Jorrit Rodenburg, and Joke Luyten. Corrosion Fatigue & Life Optimalisation of Offshore Wind Turbine Monopiles: Summary Report of the C-FLO Project. Public report, C-FLO Project, October 2023.

[142] Victor Okenyi, Shukri Afazov, Neil Mansfield, Martin Alexander Eder, Asger Bech Abrahamsen, Søren Fæster, Christopher Gottlieb Klingaa, Petros Siegkas, and Mahdi Bodaghi. Corrosion surface morphology-based methodology for fatigue assessment of offshore welded structures. *Fatigue & Fracture of Engineering Materials & Structures*, 46(12):4663–4677, 2023.

[143] Chen Li, José M. Mogollón, Arnold Tukker, Jianning Dong, Dominic von Terzi, Chunbo Zhang, and Bernhard Steubing. Future material requirements for global sustainable offshore wind energy development. *Renewable and Sustainable Energy Reviews*, 164:112603, 2022.

[144] Dillinger - Pure Innovation - Our references. https://en.dillinger.de/references/, 2025. Accessed: 2025-04-29.

[145] Structural Steel - S235, S275, S355 Chemical Composition, Mechanical Properties and Common Applications. https://www.azom.com/article.aspx?ArticleID=6022, 2019. Accessed: 2025-05-06.

[146] Structural Steel 460 - Chemical Composition, Mechanical Properties and Common Applications. https://www.azom.com/article.aspx?ArticleID=8067, 2013. Accessed: 2025-05-06.

[147] S460ML STEEL – WIND AND SOLAR STEEL. https://steelprogroup.com/wind-and-solar-steel/s460ml/#description, 2025. Accessed: 2025-05-06.

[148] Building the foundation of tomorrow´s energy supply Monopiles. https://eew-group.com/products/structural-pipe-offshore-wind/monopiles/, 2017. Accessed: 2025-05-06.

[149] Dillinger heavy plate for the offshore wind farm Hornsea 2. https://en.dillinger.de/references/dillinger-heavy-plate-for-the-offshore-wind-farm-hornsea-2/?id=8157. Accessed: 2025-04-29.

[150] Heavy plate from Dillinger for the offshore wind farm Borssele I & II. https://en.dillinger.de/references/dillinger-heavy-plate-for-the-offshore-wind-farm-borssele-i-ii/?id=8174. Accessed: 2025-04-29.

[151] Dillinger. Dillinger makes offshore wind-power turbines stand tall. https://www.impetus-pr.de/fileadmin/media/Pressetexte/Dillinger/Dillinger_Dillinger_makes_offshore_wind-power_turbines_stand_tall.pdf, 2019. Press release distributed by Impetus PR, accessed on 23-04-2025.

[152] Offshore steel grades: Perfect for high toughness and low temperatures. https://www.unionstahl.com/assortment/offshore-steels/?lang=en, 2025. Accessed: 2025-07-17.

[153] Victor Igwemezie, Philip Dirisu, and Ali Mehmanparast. Critical assessment of the fatigue crack growth rate sensitivity to material microstructure in ferrite-pearlite steels in air and marine environment. *Materials Science and Engineering: A*, 754:750–765, 2019.

[154] Oyewole Adedipe, Feargal Brennan, and Athanasios Kolios. Review of corrosion fatigue in offshore structures: Present status and challenges in the offshore wind sector. *Renewable and Sustainable Energy Reviews*, 61:141–154, 2016.

[155] Victor Igwemezie, Ali Mehmanparast, and Athanasios Kolios. Materials selection for XL wind turbine support structures: A corrosion-fatigue perspective. *Marine Structures*, 61:381–397, 2018.

[156] COMPARISON OF STEEL GRADES. https://en.dillinger.de/app/uploads/2024/03/20160215042419-ki_stahlsortenvergleich_rev0_e.pdf, 2011. Accessed: 2025-05-08.

[157] R. Hubo, F. Martin, and F. Schröter. Heavy plates for economical constructional steelwork and offshore structures. Technical report, Dillinger Hüttenwerke GTS, 2016.

[158] XF Zhang, P Han, H Terasaki, M Sato, and Y Komizo. Analytical investigation of prior austenite grain size dependence of low temperature toughness in steel weld metal. *Journal of Materials Science & Technology*, 28(3):241–248, 2012.

[159] Yoshikazu Matsumura and Hiroshi Yada. Evolution of ultrafine-grained ferrite in hot successive deformation. *Transactions of the Iron and Steel Institute of Japan*, 27(6):492–498, 1987.

[160] Ruslan Z Valiev. Structure and mechanical properties of ultrafine-grained metals. *Materials Science and Engineering: A*, 234:59–66, 1997.

[161] Zhongmin Yang and Ruizhen Wang. Formation of ultra-fine grain structure of plain low carbon steel through deformation induced ferrite transformation. *ISIJ international*, 43(5):761–766, 2003.

[162] R. O. Ritchie. Near-threshold fatigue-crack propagation in steels. *International Metals Reviews*, 24(1):205–230, 1979.

[163] Abílio M.P. de Jesus, Rui Matos, Bruno F.C. Fontoura, Carlos Rebelo, Luis Simões da Silva, and Milan Veljkovic. A comparison of the fatigue behavior between S355 and S690 steel grades. *Journal of Constructional Steel Research*, 79:140–150, 2012.

[164] Carlos Albuquerque, R.M.C. Miranda, V. Richter-Trummer, Miguel de Figueiredo, Rui Calçada, and P.M.S.T. Castro. Fatigue crack propagation behaviour in thick steel weldments. *International Journal of Structural Integrity*, 3:184–203, 05 2012.

[165] Stefanos Gkatzogiannis, Joscha Weinert, Imke Engelhardt, Peter Knoedel, and Thomas Ummenhofer. Correlation of laboratory and real marine corrosion for the investigation of corrosion fatigue behaviour of steel components. *International Journal of Fatigue*, 126:90–102, 2019.

[166] Tomasz Ślęzak and Lucjan Śnieżek. A Comparative LCF Study of S960QL High Strength Steel and S355J2 Mild Steel. *Procedia Engineering*, 114:78–85, 2015. ICSI 2015 The 1st International Conference on Structural Integrity, Funchal, Madeira, Portugal, 1st to 4th September, 2015.

[167] British Standards. BS EN 10025-2:2019: Hot rolled products of structural steels- Part 2: Technical delivery conditions for non-alloy structural steels. Technical report, BSI Standards Publication, 389 Chiswick High Rd, Chiswick, London W4 4AL, United Kingdom, 2019.

[168] Giora Maymon. Chapter 4 - Data on Initial Crack Distribution. In Giora Maymon, editor, *Stochastic Crack Propagation*, pages 43–52. Academic Press, 2018.

[169] BS7608. BS 7608:2014+A1:2015 - Guide to fatigue design and assessment of steel products. Technical report, Standard, British Standards Institution (BSI) Publication, 2015.

[170] Oskar Skoglund and John Leander. Initial parameters to estimate the fatigue strength of welded structures using a fracture mechanical model. *Engineering Structures*, 260:114185, 2022.

[171] F Koenigsberger and HW Green. Load-carrying capacity of fillet weld connections. *The welding Journal*, pages 859–863, 1953.

[172] Pedro Albrecht and Ian M Friedland. Fatigue-limit effect on variable-amplitude fatigue of stiffeners. *Journal of the structural division*, 105(12):2657–2675, 1979.

[173] JL Otegui, HW Kerr, DJ Burns, and UH Mohaupt. Fatigue crack initiation from defects at weld toes in steel. *International journal of pressure vessels and piping*, 38(5):385–417, 1989.

[174] S J Maddox. Chapter 3 - Factors which affect fatigue of welded joints. In S J Maddox, editor, *Fatigue Strength of Welded Structures (Second Edition)*, Woodhead Publishing Series in Welding and Other Joining Technologies, pages 30–37. Woodhead Publishing, second edition edition, 2002.

[175] T Bokalrud and A Karlsen. Probabilistic fracture mechanics evaluation of fatigue failure from weld defects in butt welded joints. *Proceeding on Conference on Fitness for Purpose Validation of Welded Constructions, London, UK*, 1982.

[176] Knut M. Engesvik and Torgeir Moan. Probabilistic analysis of the uncertainty in the fatigue capacity of welded joints. *Engineering Fracture Mechanics*, 18(4):743–762, 1983.

[177] A Thayamballi, Yao Chen, and Dan Liu. Fracture mechanics based assessment of fatigue reliability in ship structures. In *Ship Structure Symposium,'84*, 1984.

[178] DO Harris. Probabilistic fracture mechanics. In *Probabilistic structural mechanics handbook: theory and industrial applications*, pages 106–145. Springer, 1995.

[179] Torgeir Moan, Ole T Vårdal, Nils-C Hellevig, and Knut Skjoldli. Initial crack depth and POD values inferred from in-service observations of cracks in North Sea jackets. *J. Offshore Mech. Arct. Eng.*, 122(3):157–162, 2000.

[180] TD Righiniotis and MK Chryssanthopoulos. Probabilistic fatigue analysis under constant amplitude loading. *Journal of Constructional Steel Research*, 59(7):867–886, 2003.

[181] Efren Ayala-Uraga and Torgeir Moan. Fatigue reliability-based assessment of welded joints applying consistent fracture mechanics formulations. *International Journal of Fatigue*, 29(3):444–456, 2007.

[182] Inge Lotsberg, Gudfinnur Sigurdsson, Arne Fjeldstad, and Torgeir Moan. Probabilistic methods for planning of inspection for fatigue cracks in offshore structures. *Marine Structures*, 46:167–192, 2016.

[183] Y. Dong, A.P. Teixeira, and C. Guedes Soares. Application of adaptive surrogate models in time-variant fatigue reliability assessment of welded joints with surface cracks. *Reliability Engineering & System Safety*, 195:106730, 2020.

[184] Peyman Amirafshari, Nigel Barltrop, Martyn Wright, and Athanasios Kolios. Weld defect frequency, size statistics and probabilistic models for ship structures. *International Journal of Fatigue*, 145:106069, 2021.

[185] Shankar Sankararaman, You Ling, and Sankaran Mahadevan. Statistical inference of equivalent initial flaw size with complicated structural geometry and multi-axial variable amplitude loading. *International Journal of Fatigue*, 32(10):1689–1700, 2010.

[186] Llewellyn Morse, Zahra Sharif Khodaei, and MH Aliabadi. A multi-fidelity modelling approach to the statistical inference of the equivalent initial flaw size distribution for multiple-site damage. *International Journal of Fatigue*, 120:329–341, 2019.

[187] M. Wahab and M. Alam. The significance of weld imperfections and surface peening on fatigue crack propagation life of butt-welded joints. *Journal of Materials Processing Technology*, 153-154:931–937, 2004.

[188] I. S. Raju and J. C. Newman. Stress-intensity factors for a wide range of semi-elliptical surface cracks in finite-thickness plates. *Engineering Fracture Mechanics*, 11(4):817–829, 1979.

[189] J. C. Newman and I. S. Raju. An empirical stress-intensity factor equation for the surface crack. *Engineering Fracture Mechanics*, 15(1-2):185–192, 1981.

[190] S.J. Maddox. An analysis of fatigue cracks in fillet welded joints. *International Journal of Fracture*, 11(2):221 – 243, 1975.

[191] Weidong Zhao, Bernt Johan Leira, Guoqing Feng, Chao Gao, and Ting Cui. A reliability approach to fatigue crack propagation analysis of ship structures in polar regions. *Marine Structures*, 80:103075, 2021.

[192] T. Nguyen and M. Wahab. The effect of butt weld geometry parameters on stress intensity factor and fatigue life. *Journal of Computational Mechanics*, page 883–888, 1993.

[193] J. Ferreira and C. Branco. Fatigue analysis and prediction in fillet welded joints in the low thickness range. *Fatigue & Fracture of Engineering Materials & Structures*, 13:201–212, 2007.

[194] B. Schork, P. Kucharczyk, M. Madia, U. Zerbst, J. Hensel, J. Bernhard, D. Tchuindjang, M. Kaffenberger, and M. Oechsner. The effect of the local and global weld geometry as well as material defects on crack initiation and fatigue strength. *Engineering Fracture Mechanics*, 198:103–122, 2018.

[195] A. Kolios, L. Wang, A. Mehmanparast, and F. Brennan. Determination of stress concentration factors in offshore wind welded structures through a hybrid experimental and numerical approach. *Ocean Engineering*, 178:38–47, 2019.

[196] T. L. Anderson. *Fracture Mechanics: Fundamentals and Applications*. CRC Press, 4 edition, 2017.

[197] M. Kamaya. Influence of the Interaction on Stress Intensity Factor of Semi-Elliptical Surface Cracks. In *Proceedings of ASME 2005 Pressure Vessels and Piping Conference*, volume Volume 3: Design and Analysis, pages 273–280, 07 2005.

[198] R. Bell and O. Vosikovsky. Fatigue Life Prediction of Welded Joints for Offshore Structures Under Variable Amplitude Loading. *Journal of Offshore Mechanics and Arctic Engineering*, 115:123–130, 1993.

[199] S. To, S. Lambert, and D. Burns. A multiple crack model for fatigue in welded joints. *International Journal of Fatigue*, 15:333–340, 1993.

[200] M. Madia, B. Schork, J. Bernhard, and M. Kaffenberger. Multiple crack initiation and propagation in weldments under fatigue loading. *Procedia Structural Integrity*, 7:423–430, 2017.

[201] I. S. Raju and J. C. Newman. Stress-Intensity Factors for Circumferential Surface Cracks in Pipes and Rods Under Tension and Bending Loads. In *Fracture Mechanics: Seventeenth Volume*, Seventeenth National Symposium on Fracture Mechanics , Albany, New York, pages 789–805, 1984.

[202] H. Navid, R.T. Fenner, F. Nadiri, and G.A. Webster. Stress intensity factors for internal and external cracks in pressurised thick-walled cylinders. *International Journal of Pressure Vessels and Piping*, 18(4):241–254, 1985.

[203] K.J. Kirkhope, R. Bell, and J. Kirkhope. Stress intensity factors for single and multiple semi-elliptical surface cracks in pressurized thick-walled cylinders. *International Journal of Pressure Vessels and Piping*, 47(2):247–257, 1991.

[204] J. Mishael, P.G. Morato, and P. Rigo. Numerical fatigue modeling and simulation of interacting surface cracks in offshore wind structural connections. *Marine Structures*, 92:1–17, 2023.

[205] J. Mishael, P. G. Morato, and P. Rigo. Propagation of Interacting Cracks in Offshore Wind Welded Structures through Numerical Analysis. In *Proceedings of the Thirty-fourth International Ocean and Polar Engineering Conference (ISOPE 2024)*, pages 3116–3123, 2024.

[206] Jiancheng Leng, Jiajia Zhang, Jinbo Zhang, and Zitong Chen. A Surrogate Model to Predict Stress Intensity Factor of Tubular Joint Based on Bayesian Optimization Gaussian Process Regression. *Journal of Offshore Mechanics and Arctic Engineering*, 147(2):021701, 09 2024.

[207] Mosbeh R. Kaloop, Pijush Samui, Jae-Joung Kim, Jong Wan Hu, and Ahmed Ramzy. Stress intensity factor prediction on offshore pipelines using surrogate modeling techniques. *Case Studies in Construction Materials*, 16:e01045, 2022.

[208] G Shen and G Glinka. Weight functions for a surface semi-elliptical crack in a finite thickness plate. *Theoretical and Applied Fracture Mechanics*, 15(3):247–255, 1991.

[209] R Goyal and G Glinka. Fracture mechanics-based estimation of fatigue lives of welded joints. *Welding in the World*, 57:625–634, 2013.

[210] Y Dong and C Guedes Soares. Stress distribution and fatigue crack propagation analyses in welded joints. *Fatigue & fracture of engineering materials & structures*, 42(1):69–83, 2019.

[211] A.F. Hobbacher. *Recommendations for Fatigue Design of Welded Joints and Components*. International Institute of Welding, Springer International Publishing, Switzerland, 2016.

[212] A.F. Hobbacher. Chapter 4 - The use of fracture mechanics in the fatigue analysis of welded joints. In K.A. Macdonald, editor, *Fracture and Fatigue of Welded Joints and Structures*, page 91–112. Woodhead Publishing, Sawston, United Kingdom, 2011.

[213] OH Burnside, SJ Hudak Jr, E Oelkers, K Chan, and RJ Dexter. Long-Term Corrosion Fatigue of Welded Marine Steels. Technical report, Ship Structure Committee, 1984.

[214] M Knop, J Heath, Z Sterjovski, and SP Lynch. Effects of cycle frequency on corrosion-fatigue crack growth in cathodically protected high-strength steels. *Procedia Engineering*, 2(1):1243–1252, 2010.

[215] Richard Joseph Appleton. *Corrosion fatigue of a C-Mn steel*. Phd thesis, University of Glasgow, October 1985.

[216] Knop Mark. *Effects of Cycle Frequency,Waveform, and Electrode Potential on Corrosion-Fatigue Crack Growth in High-Strength Tempered Martensitic Steels*. PhD thesis, Department of Materials Science and Engineering, Monash University, Melbourne, Australia, 2015.

[217] H Xin and M Veljkovic. Effects of residual stresses on fatigue crack initiation of butt-welded plates made of high strength steel. In *Advances in Engineering Materials, Structures and Systems: Innovations, Mechanics and Applications*, pages 1260–1265. CRC Press, 2019.

[218] Michael Rye Andersen. *Fatigue Crack Initiation and Growth in Ship Structures*. PhD thesis, Technical University of Denmark, Lyngby, Denmark, 1998.

[219] Bruno Pedrosa, José Correia, Grzegorz Lesiuk, Carlos Rebelo, and Milan Veljkovic. Fatigue crack growth modelling for s355 structural steel considering plasticity-induced crack-closure by means of unigrow model. *International Journal of Fatigue*, 164:107120, 2022.

[220] Helen Ryan and Ali Mehmanparast. Development of a new approach for corrosion-fatigue analysis of offshore steel structures. *Mechanics of Materials*, 176:104526, 2023.

[221] Apostolos Papanikolaou, E Alfred Mohammed, and Spyros E Hirdaris. Stochastic uncertainty modelling for ship design loads and operational guidance. *Ocean engineering*, 86:47–57, 2014.

[222] Pandeli Temarel, Wei Bai, Anne Bruns, Quentine Derbanne, Daniele Dessi, S Dhavalikar, Nuno Fonseca, T Fukasawa, X Gu, A Nestegård, et al. Prediction of wave-induced loads on ships: Progress and challenges. *Ocean Engineering*, 119:274–308, 2016.

[223] Yan Dong, Yordan Garbatov, and C. Guedes Soares. Review on uncertainties in fatigue loads and fatigue life of ships and offshore structures. *Ocean Engineering*, 264:112514, 2022.

[224] Yordan Garbatov and C Guedes Soares. Uncertainty assessment of fatigue damage of welded ship structural joints. *Engineering structures*, 44:322–333, 2012.

[225] Rasmus Folsø. Spectral fatigue damage calculation in the side shells of ships, with due account taken of the effect of alternating wet and dry areas. *Marine structures*, 11(7-8):319–343, 1998.

[226] Shanshan Li, Yan Dong, and C Guedes Soares. A procedure to generate design load-time histories for fatigue strength assessment of offshore structures. *Ocean Engineering*, 213:107707, 2020.

[227] Enzo Marino, Alessandro Giusti, and Lance Manuel. Offshore wind turbine fatigue loads: The influence of alternative wave modeling for different turbulent and mean winds. *Renewable Energy*, 102:157–169, 2017.

[228] Yi-Wen Cheng. The fatigue crack growth of a ship steel in seawater under spectrum loading. *International journal of fatigue*, 7(2):95–100, 1985.

[229] Eurocode 3. *Eurocode 3: Design of steel structures - Part 1-9: Fatigue*. Number EN 1993-1-9:2005. European Committee for Standardisation, Brussels, 2005.

[230] Quang A. Mai, Wout Weijtjens, Christof Devriendt, Pablo G. Morato, Philippe Rigo, and John D. Sørensen. Prediction of remaining fatigue life of welded joints in wind turbine support structures considering strain measurement and a joint distribution of oceanographic data. *Marine Structures*, 66:307–322, 2019.

[231] Lijia Long, Quang Anh Mai, Pablo Gabriel Morato, John Dalsgaard Sørensen, and Sebastian Thöns. Information value-based optimization of structural and environmental monitoring for offshore wind turbines support structures. *Renewable Energy*, 159:1036–1046, 2020.

[232] X. Wang. Stress intensity factors and weight functions for deep semi-elliptical surface cracks in finite-thickness plates. *Fatigue and Fracture of Engineering Materials and Structures*, 25(3):291–304, 2002.

[233] Mathieu Bocher, Ali Mehmanparast, Jarryd Braithwaite, and Mahmood Shafiee. New shape function solutions for fracture mechanics analysis of offshore wind turbine monopile foundations. *Ocean Engineering*, 160(January):264–275, 2018.

[234] S. Yoshimura, J.-S. Lee, and G. Yagawa. Automated System for Analyzing Stress Intensity Factors of Three-Dimensional Cracks: Its Application to Analyses of Two Dissimilar Semi-Elliptical Surface Cracks in Plate. *Journal of Pressure Vessel Technology*, 119(1):18–26, 02 1997.

[235] S. K. Patel, Bhagavatula Dattaguru, and K. Ramachandra. Multiple Interacting and Coalescing Semi-Elliptical Surface Cracks in Fatigue-Part-I: Finite Element Analysis. *Structural Longevity*, 3(1):37–57, 2010.

[236] Satoyuki Tanaka, Thin Thin Htut, Kengo Maeda, Kazuhisa Yagi, and Naoki Osawa. Fracture mechanics investigation of crack coalescence in a steel tubular T-joint specimen. *Engineering Failure Analysis*, 139:106504, 2022.

[237] T. Nishioka and S. N. Atluri. Analysis of Surface Flaw in Pressure Vessels by a New 3-Dimensional Alternating Method. *Journal of Pressure Vessel Technology*, 104(4):299–307, 11 1982.

[238] Y. Murakami and S. Nemat-Nasser. Interacting dissimilar semi-elliptical surface flaws under tension and bending. *Engineering Fracture Mechanics*, 16(3):373–386, 1982.

[239] N. A. Noda, K. Kobayashi, and T. Oohashi. Variation of the stress intensity factor along the crack front of interacting semi-elliptical surface cracks. *Archive of Applied Mechanics*, 71:43–52, 2001.

[240] Z. J. Zeng, S. H. Dai, and Y. M. Yang. Analysis of surface cracks using the line-spring boundary element method and the virtual crack extension technique. *International Journal of Fracture*, 60:157–167, 1993.

[241] T. Okawa, Y. Sumi, and M. Mohri. Simulation-based fatigue crack management of ship structural details applied to longitudinal and transverse connections. *Marine Structures*, 19(4):217–240, 2006.

[242] Kaihua Zhang and Matthew Collette. Experimental investigation of structural system capacity with multiple fatigue cracks. *Marine Structures*, 78:102943, 2021.

[243] Pablo G. Morato, Konstantinos G. Papakonstantinou, Charalampos P. Andriotis, and Philippe Rigo. Managing offshore wind turbines through Markov decision processes and dynamic Bayesian networks. In *Proc. of the 13th International Conference on Structural Safety & Reliability (ICOSSAR), Shanghai, China*, 11 2022.

[244] Yifan Huang, Xin Wang, and Xinjian Duan. Evaluation of crack opening displacement of through-wall circumferential-cracked pipe using direct weight function method. *Theoretical and Applied Fracture Mechanics*, 108:102595, 2020.

[245] A. Hosseini and M.A. Mahmoud. Evaluation of stress intensity factor and fatigue growth of surface cracks in tension plates. *Engineering Fracture Mechanics*, 22(6):957–974, 1985.

[246] M.A. Mahmoud and A. Hosseini. Assessment of stress intensity factor and aspect ratio variability of surface cracks in bending plates. *Engineering Fracture Mechanics*, 24(2):207–221, 1986.

[247] R. T. Davenport and R. Brook. THE THRESHOLD STRESS INTENSITY RANGE IN FATIGUE. *Fatigue & Fracture of Engineering Materials & Structures*, 1(2):151–158, 1979.

[248] M. Stern, E. B. Becker, and R. S. Dunham. A contour integral computation of mixed-mode stress intensity factors. *International Journal of Fracture*, 12(3):359–368, 1976.

[249] J. F. Yau, S. S. Wang, and H. T. Corten. A Mixed-Mode Crack Analysis of Isotropic Solids Using Conservation Laws of Elasticity. *Journal of Applied Mechanics*, 47(2):335–341, 06 1980.

[250] Hongjun Yu and Meinhard Kuna. Interaction integral method for computation of crack parameters K–T – A review. *Engineering Fracture Mechanics*, 249:107722, 2021.

[251] Timothy Lewis and Xin Wang. The T-stress solutions for through-wall circumferential cracks in cylinders subjected to general loading conditions. *Engineering Fracture Mechanics*, 75(10):3206–3225, 2008.

[252] Thomas Stenberg. *Fatigue properties of cut and welded high strength steels: Quality aspects in design and production*. PhD thesis, KTH School of Engineering Sciences, Stockholm, Sweden, 2016.

[253] JCSS. JCSS Probabilistic Model Code Part 3- Resistance Models. Technical report, Joint Committee on Structural Safety, April 2011.

[254] J Jonkman and W Musial. Offshore Code Comparison Collaboration (OC3) for IEA Task 23 Offshore Wind Technology and Deployment. Technical Report December, NREL, 2010.

[255] DNV GL. ST-0126 - Support structures for wind turbines. Technical Report DNVGL-ST-0126, DNV GL, 2018.

[256] ANSYS Inc. Mechanical user's guide, 2020.

[257] W. Dong, T. Moan, and Z. Gao. Long-term fatigue analysis of multi-planar tubular joints for jacket-type offshore wind turbine in time domain". *Enginreeing Structures*, 33(6):1–13, 2011.

[258] J.M. Melenk and I. Babuška. The partition of unity finite element method: Basic theory and applications. *Computer Methods in Applied Mechanics and Engineering*, 139(1):289–314, 1996.

[259] Ivo Babuška and Jens M Melenk. The partition of unity method. *International journal for numerical methods in engineering*, 40(4):727–758, 1997.

[260] N. Sukumar and J.-H. Prévost. Modeling quasi-static crack growth with the extended finite element method Part I: Computer implementation. *International Journal of Solids and Structures*, 40(26):7513–7537, 2003.

[261] R. Huang, N. Sukumar, and J.-H. Prévost. Modeling quasi-static crack growth with the extended finite element method Part II: Numerical applications. *International Journal of Solids and Structures*, 40(26):7539–7552, 2003.

[262] Christophe Daux, Nicolas Moës, John Dolbow, Natarajan Sukumar, and Ted Belytschko. Arbitrary branched and intersecting cracks with the extended finite element method. *International Journal for Numerical Methods in Engineering*, 48(12):1741–1760, 2000.

[263] J.C. Sobotka and R.C. McClung. Stress-intensity factors solutions for straight through cracks in C-sections. *Engineering Fracture Mechanics*, 271:108593, 2022.

[264] Xinyu Zhang, Tingting Zhao, Yifan Liu, Qingqing Chen, Zhiyong Wang, and Zhihua Wang. A data-driven model for predicting the mixed-mode stress intensity factors of a crack in composites. *Engineering Fracture Mechanics*, 288:109385, 2023.

[265] Mohamed El Amine Ben Seghier, Hermes Carvalho, Behrooz Keshtegar, José A. F. O. Correia, and Filippo Berto. Novel hybridized adaptive neuro-fuzzy inference system models based particle swarm optimization and genetic algorithms for accurate prediction of stress intensity factor. *Fatigue & Fracture of Engineering Materials & Structures*, 43(11):2653–2667, 2020.

[266] Wentao He, Jingxi Liu, and De Xie. Probabilistic life assessment on fatigue crack growth in mixed-mode by coupling of Kriging model and finite element analysis. *Engineering Fracture Mechanics*, 139:56–77, 2015.

[267] Jonas Merrell, John Emery, Robert M. Kirby, and Jacob Hochhalter. Stress intensity factor models using mechanics-guided decomposition and symbolic regression. *Engineering Fracture Mechanics*, 310:110432, 2024.

[268] Glen H. Besterfield, Wing Kam Liu, Mark A. Lawrence, and Ted Belytschko. Fatigue crack growth reliability by probabilistic finite elements. *Computer Methods in Applied Mechanics and Engineering*, 86(3):297–320, 1991.

[269] Shuming Xiao, Yang Han, Yi Zhang, Qikun Wei, Yifan Wang, Na Wang, Haodong Wang, Jingxi Liu, and Yan Liu. A Reliability Analysis Framework of Ship Local Structure Based on Efficient Probabilistic Simulation and Experimental Data Fusion. *Metals*, 12(5), 2022.

[270] B. Echard, N. Gayton, and M. Lemaire. AK-MCS: An active learning reliability method combining Kriging and Monte Carlo Simulation. *Structural Safety*, 33(2):145–154, 2011.

[271] N. Roussouly, F. Petitjean, and M. Salaun. A new adaptive response surface method for reliability analysis. *Probabilistic Engineering Mechanics*, 32:103–115, 2013.

[272] A.A. Chojaczyk, A.P. Teixeira, L.C. Neves, J.B. Cardoso, and C. Guedes Soares. Review and application of Artificial Neural Networks models in reliability analysis of steel structures. *Structural Safety*, 52:78–89, 2015.

[273] J.-M. Bourinet, F. Deheeger, and M. Lemaire. Assessing small failure probabilities by combined subset simulation and Support Vector Machines. *Structural Safety*, 33(6):343–353, 2011.

[274] Nicolas Moës, John Dolbow, and Ted Belytschko. A finite element method for crack growth without remeshing. *International Journal for Numerical Methods in Engineering*, 46(1):131–150, 1999.

[275] Matthew Pais, Nam-Ho Kim, and Timothy Davis. Reanalysis of the extended finite element method for crack initiation and propagation. In *51st AIAA/ASME/ASCE/AHS/ASC Structures, Structural Dynamics, and Materials Conference 18th AIAA/ASME/AHS Adaptive Structures Conference 12th*, page 2536, 2010.

[276] Jianxu Shi, David Chopp, Jim Lua, N Sukumar, and Ted Belytschko. Abaqus implementation of extended finite element method using a level set representation for three-dimensional fatigue crack growth and life predictions. *Engineering fracture mechanics*, 77(14):2840–2863, 2010.

[277] Guido Dhondt. Automatic 3-D mode I crack propagation calculations with finite elements. *International Journal for Numerical Methods in Engineering*, 41(4):739–757, 1998.

[278] Zhang, Jie and Hertelé, Stijn and Micone, Nahuel and De Waele, Wim. Modelling framework for 3D fatigue crack propagation in welds of offshore steel structures. In Silva Gomes, Joaquim and Meguid, Shaker, editor, *IRF2016: 5TH INTERNATIONAL CONFERENCE INTEGRITY-RELIABILITY-FAILURE*, pages 751–762. INEGI/FEUP (2016), 2016.

[279] Matthew J. Pais, Felipe A.C. Viana, and Nam H. Kim. Enabling high-order integration of fatigue crack growth with surrogate modeling. *International Journal of Fatigue*, 43:150–159, 2012.

[280] M.N. Vu, S. Geniaut, P. Massin, and J.J. Marigo. Numerical investigation on corner singularities in cracked plates using the G-theta method with an adapted θ field. *Theoretical and Applied Fracture Mechanics*, 77:59–68, 2015.

[281] Wenbin Dong, Torgeir Moan, and Zhen Gao. Long-term fatigue analysis of multi-planar tubular joints for jacket-type offshore wind turbine in time domain. *Engineering Structures*, 33(6):2002–2014, 2011.

[282] T. Lucht. Finite element analysis of three dimensional crack growth by the use of a boundary element sub model. *Engineering Fracture Mechanics*, 76(14):2148–2162, 2009.

[283] Masayuki Kamaya. Growth evaluation of multiple interacting surface cracks. Part II: Growth evaluation of parallel cracks. *Engineering Fracture Mechanics*, 75(6):1350–1366, 2008.

[284] Said El Fakkoussi, Sorin Vlase, Marin Marin, Ouadie Koubaiti, Ahmed Elkhalfi, and Hassane Moustabchir. Predicting Stress Intensity Factor for Aluminum 6062 T6 Material in L-Shaped Lower Control Arm (LCA) Design Using Extended Finite Element Analysis. *Materials*, 17(1), 2024.

[285] Abdelaziz Yazid, Nabbou Abdelkader, and Hamouine Abdelmadjid. A state-of-the-art review of the X-FEM for computational fracture mechanics. *Applied Mathematical Modelling*, 33(12):4269–4282, 2009.

[286] Jr. Newman, J. C. and I. S. Raju. Analyses of Surface Cracks in Finite Plates Under Tension or Bending Loads. NASA Technical Paper NASA-TP-1578, NASA Langley Research Center, Hampton, VA, United States, December 1979. Report Number: L-13053, Accession Number: 80N13512.

[287] H.E. Coules and M.A. Probert. Studying the interaction of crack-like flaws using the MATLAB toolbox int_defects. *Engineering Fracture Mechanics*, 227:106733, 2020.